UNIWERSYTET
IM. ADAMA MICKIEWICZA
W POZNANIU

mgr Marta Jędrzejczyk

Rozprawa doktorska

Synteza, analiza strukturalna i badanie aktywności biologicznej pochodnych salinomycyny

Synthesis, structural analysis, and biological activity evaluation of salinomycin derivatives

Promotor
prof. dr hab. Adam Huczyński

Poznań, 2025

„Results were unexpected, but within an acceptable margin of panic.”

– Anonymous

Podziękowania

Kilka razy w życiu usłyszałam, że mam szczęście do dobrych ludzi, z czym niezaprzeczalnie się zgadzam i mam wielką nadzieję, że to szczęście mnie nigdy nie opuści. Zatem na wstępie tej pracy pragnę z głębi serca podziękować osobom, które towarzyszyły mi przez te niemal sześć ostatnich lat, a ich obecność dodawała mi sił i otuchy oraz pomagała przetrwać najtrudniejsze momenty.

Szczególne podziękowania kieruję do mojego promotora – prof. dr. hab. Adama Huczyńskiego. Dziękuję za wsparcie merytoryczne, inspiracje naukowe oraz możliwość rozwoju i zaufanie. Za stworzenie przestrzeni, którą wypełniała nie tylko praca, ale i ludzie, z którymi tworzyliśmy zgrany zespół.

Pragnę także podziękować najlepszemu *lab mate* jaki mógł mi się trafić – Michałowi Sulikowi. Praca z Tobą to była wielka przyjemność. Dziękuję za wsparcie, cenne wskazówki i wspólne szukanie rozwiązań. Za wyrozumiałość do mojego zapominalstwa, wspólne koncertowanie i granie w *Latające chomiki* (w trakcie przerw obiadowych rzecz jasna) oraz za każdy moment śmiechu – a było ich sporo.

Dziękuję całemu Zakładowi Chemii Medycznej, a w szczególności Michałowi i Jackowi, za wszystkie wspólne kawy i dyskusje – nie tylko na tematy chemiczne. Greto i Dominiko, podziękowania należą się również Wam, dziękuję za każdą cenną radę i rozmowę. W tym miejscu chciałabym również wymienić studentki, z którymi miałam okazję pracować – Roksanę i Weronikę – dziękuję Wam za zaufanie i możliwość rozwoju moich umiejętności pedagogicznych.

Chciałabym również podziękować wszystkim, z którymi miałam okazję współpracować podczas realizacji mojego projektu doktorskiego – prof. Janowi Janczakowi, prof. Piotrowi Bednarczykowi i prof. Marcie Strudze, a także ich zespołom badawczym. Dziękuję również prof. Jackowi A. Tuszyńskiemu za możliwość realizacji dwóch staży pod jego opieką na Politechnice Turyńskiej w Turynie.

I would also like to express my gratitude to Prof. Yuri N. Antonenko for his valuable contribution to this interdisciplinary project.

Wyrazy wdzięczności kieruję również do mojej Rodziny, a w szczególności moich Rodziców. Dziękuję Wam za ogromne wsparcie oraz wiarę we mnie przez cały okres studiów. Oficjalnie to już koniec, kolejnych lat studiów (w najbliższym czasie) nie planuję.

Jest też część bliskich mi osób, która wiernie kibicowała mi przez ten cały okres. Domka – dziękuję Ci za wsparcie i przypominanie mi, że bycie naukowcem i praca w laboratorium to coś niestandardowego, coś co zapewne będzie jednym z najciekawszych doświadczeń w moim życiu. Dziękuję również całemu teamowi z Os. Zwycięstwa - Basi, Magdzie, Martynce, Ewci i Dajanie – za każdy doping, wspólny wypad i wysłuchiwanie moich gorzkich żali. Karolu, Tobie dziękuję szczególnie za jedną rozmowę, która miała miejsce w momencie mojego największego zwątpienia i która mnie zmotywowała.

Pragnę także serdecznie podziękować Narodowemu Centrum Nauki za wsparcie finansowe udzielone w ramach projektu OPUS nr 2021/41/B/ST4/00088, które umożliwiło realizację badań przedstawionych w niniejszej rozprawie doktorskiej.

NARODOWE CENTRUM NAUKI

Dziękuję również za możliwość realizacji dwóch staży zagranicznych na Politechnice Turyńskiej, w ramach projektów nr 048/13/UAM/0004; 003/13/UAM/0010, które były finansowane z programu „Inicjatywa doskonałości – uczelnia badawcza”.

UCZELNIA
BADAWCZA
INICJATYWA DOSKONAŁOŚCI

Na sam koniec chciałabym podziękować i pogratulować sobie. Brawo Ty! Możesz być z siebie dumna, zawsze mogłaś, ale teraz już w szczególności.

Spis treści

1. Streszczenie w języku polskim

Salinomycyna jest związkiem pochodzenia naturalnego, wytwarzanym przez bakterie *Streptomyces albus*. Związek ten jest zaliczany do grupy antybiotyków jonoforowych, zdolnych do transportowania kationów metali przez błony komórkowe. Salinomycyna znalazła szerokie zastosowanie w weterynarii jako kokcydiostatyk ze względu na silne właściwości przeciwpierwotniakowe. Ponadto w ciągu ostatnich dwóch dziesięcioleci niejednokrotnie potwierdzono potencjał terapeutyczny salinomycyny wobec komórek nowotworowych, w tym również macierzystych komórek nowotworowych.

Przedmiotem rozprawy doktorskiej zatytułowanej: *„Synteza, analiza strukturalna i badanie aktywności biologicznej pochodnych salinomycyny”* była chemiczna modyfikacja antybiotyku jonoforowego, przebadanie właściwości jonoforetycznych otrzymanych pochodnych oraz ocena ich aktywności biologicznej.

W skład rozprawy doktorskiej wchodzą trzy publikacje, w których opisano reakcję rozkładu cząsteczki salinomycyny w warunkach kwasowych oraz syntezę jej koniugatów z kationami fosfoniowymi, otrzymanych w wyniku modyfikacji cząsteczki w pozycji C1 oraz C20. W celu określenia i potwierdzenia struktury zsyntezowanych pochodnych wykorzystano szereg technik analitycznych takich jak spektrometria mas z jonizacją przez elektrorozpylenie (ESI-MS), wysokorozdzielcza spektrometria mas (HR-MS), spektroskopia w podczerwieni (FT-IR), analiza elementarna (EA), dyfrakcja rentgenowska (XRD) oraz spektroskopia magnetycznego rezonansu jądrowego (^{1}H NMR, ^{13}C NMR, ^{31}P NMR, 2D NMR).

Badania w zakresie chemii medycznej mają charakter interdyscyplinarny, zatem analiza krystalograficzna produktu rozkładu salinomycyny została wykonana we współpracy z prof. Janem Janczakiem z Instytutu Niskich Temperatur i Badań Strukturalnych im. Włodzimierza Trzebiatowskiego Polskiej Akademii Nauk we Wrocławiu.

We współpracy z prof. Yurim N. Antonenko z Moskiewskiego Uniwersytetu Państwowego im. M.W. Łomonosowa, przeprowadzono badania nad właściwościami jonoforetycznymi otrzymanych koniugatów, badając ich wpływ na sztuczne i naturalne błony biologiczne oraz zdolność do translokacji przez warstwy dwulipidowe.

Aktywność przeciwnowotworowa koniugatów otrzymanych w publikacji III, została szczegółowo przebadana przez zespół badawczy prof. Marty Strugi

z Warszawskiego Uniwersytetu Medycznego. Przeprowadzono testy *in vitro* z wykorzystaniem pięciu linii ludzkich komórek nowotworowych takich jak: linia gruczolaka jelita grubego (SW480), gruczolaka jelita grubego z przerzutami (SW620), nowotworu prostaty (PC3), nowotworu piersi (MDA-MB-231) oraz niedrobnokomórkowego raka płuc (A549). Do oceny cytotoksyczności otrzymanych związków wykorzystano dwie normalne linie komórkowe: linia ludzkich keratynocytów (HaCaT) oraz linia fibroblastów płuc chomika chińskiego (V79). Ponadto przebadano wpływ wybranych pochodnych na mitochondria komórek nowotworowych, potencjał błony mitochondrialnej oraz wpływ na cykl komórkowy, indukowanie apoptozy i reaktywnych form tlenu.

Badania biologiczne obejmowały także analizę właściwości przeciwbakteryjnych otrzymanych koniugatów. Związki przebadano wobec bakterii Gram-dodatnich: *Staphylococcus epidermidis* i *Staphylococcus aureus* oraz Gram-ujemnych: *Pseudomonas aeruginosa* i *Escherichia coli*.

W końcowym etapie badań właściwości biologicznych salinomycyny i jej pochodnych przetestowano ich wpływ na oddychanie komórkowe oraz zdolność do transportowania kationów z wykorzystaniem techniki czarnych błon lipidowych. Badania te przeprowadzono we współpracy z prof. Piotrem Bednarczykiem ze Szkoły Głównej Gospodarstwa Wiejskiego w Warszawie.

Przeprowadzone badania biologiczne udowodniły, że cytotoksyczność większości pochodnych była kilkukrotnie większa w porównaniu do niemodyfikowanej salinomycyny, a także leku referencyjnego (doksorubicyny). Udowodniono, że obecność kationu trifenylofosfoniowego w cząsteczce antybiotyku wpływa na funkcjonalność mitochondriów i szybkość przenikania przez błony komórkowe. Ponadto wybrane pochodne wykazywały zdolność do wywoływania apoptozy komórek nowotworowych.

Wyniki zaprezentowane w niniejszej rozprawie potwierdziły, że koniugowanie bioaktywnych cząsteczek prowadzi do obiecujących rezultatów oraz że jest to dobry kierunek w poszukiwaniu nowych i skuteczniejszych związków o aktywności przeciwnowotworowej.

2. Streszczenie w języku angielskim

Salinomycin is a naturally occurring compound produced by the bacterium *Streptomyces albus*. It belongs to the group of ionophore antibiotics, which are capable of transporting metal cations across cell membranes. Salinomycin has been widely used in veterinary medicine as a coccidiostat due to its strong antiparasitic properties. Moreover, over the past two decades, its therapeutic potential against cancer cells, including cancer stem cells, has been repeatedly confirmed.

The subject of the doctoral dissertation titled *"Synthesis, structural analysis, and biological activity evaluation of salinomycin derivatives"* was the chemical modification of ionophore antibiotic, the examination of the ionophoretic properties of the obtained derivatives, and the assessment of their biological activity.

The dissertation includes three publications that describe the decomposition reaction of the salinomycin molecule under acidic conditions and the synthesis of its conjugates with phosphonium cations, obtained by modifying the molecule at positions C1 and C20. To determine and confirm the structures of the synthesized derivatives, a range of analytical techniques were conducted, including electrospray ionization mass spectrometry (ESI-MS), high-resolution mass spectrometry (HR-MS), infrared spectroscopy (FT-IR), elemental analysis (EA), X-ray diffraction (XRD), and nuclear magnetic resonance spectroscopy (^{1}H NMR, ^{13}C NMR, ^{31}P NMR, 2D NMR).

Research in medicinal chemistry is interdisciplinary; therefore, the crystallographic analysis of the salinomycin degradation product was conducted in collaboration with Prof. Jan Janczak from the Institute of Low Temperature and Structure Research of the Polish Academy of Sciences in Wrocław.

In collaboration with Prof. Yuri N. Antonenko from the Moscow State University, studies were carried out on the ionophoretic properties of the obtained conjugates, examining their effect on artificial and natural biological membranes, as well as their ability to translocate through lipid bilayers.

The anticancer activity of the conjugates obtained in Publication III was thoroughly investigated by the research team of Prof. Marta Struga from the Medical University of Warsaw. *In vitro* tests were conducted using five human cancer cell lines: colorectal adenocarcinoma (SW480), metastatic colorectal adenocarcinoma (SW620), prostate cancer (PC3), breast cancer (MDA-MB-231), and non-small cell lung cancer (A549). To assess the cytotoxicity of the obtained compounds, two normal cell lines were used: human

keratinocytes (HaCaT) and Chinese hamster lung fibroblasts (V79). Additionally, the effect of selected derivatives on cancer cell mitochondria, mitochondrial membrane potential, and their influence on the cell cycle, apoptosis induction, and reactive oxygen species production were investigated.

The biological studies also included an analysis of the antibacterial properties of the obtained conjugates. The compounds were tested against Gram-positive bacteria (*Staphylococcus epidermidis* and *Staphylococcus aureus*) and Gram-negative bacteria (*Pseudomonas aeruginosa* and *Escherichia coli*).

At the final stage of biological research on salinomycin and its derivatives, their effect on cellular respiration and their ability to transport cations were tested using the black lipid membrane technique. These studies were conducted in collaboration with Prof. Piotr Bednarczyk from the Warsaw University of Life Sciences.

The conducted biological studies demonstrated that the cytotoxicity of most derivatives was several times higher compared to unmodified salinomycin as well as the reference drug (doxorubicin). It was proven that the presence of a triphenylphosphonium cation in the antibiotic molecule affects mitochondrial functionality and the rate of membrane penetration. Furthermore, selected derivatives exhibited the ability to induce apoptosis in cancer cells.

The results presented in this dissertation confirmed that conjugation of bioactive molecules leads to promising outcomes and represents a valuable approach in the search for new and more effective anticancer compounds.

3. Cel pracy

Spośród antybiotyków jonoforowych salinomycyna wyróżnia się wysoką wrażliwością na środowisko kwasowe i wysokie temperatury. Podczas prac z salinomycyną, zaobserwowano, że cząsteczka z łatwością ulega rozpadowi w wyniku zbyt niskiego pH. Zatem jednym z celów rozprawy doktorskiej była szczegółowa analiza reakcji rozkładu salinomycyny w warunkach kwasowych oraz zaprojektowanie, synteza i ocena aktywności biologicznej jej nowych pochodnych.

Jako, że proces rozpadu cząsteczki salinomycyny nie był do tej pory wnikliwie przebadany, zdecydowano przeprowadzić dokładną analizę procesu rozpadu salinomycyny wraz z charakterystyką produktów rozkładu. Dodatkowo, powszechnie wiadomo, że stabilność substancji jest kluczowym kryterium przy projektowaniu leków, zwłaszcza tych o podaniu drogą doustną, podczas której związki są szczególnie narażone na kwaśne środowisko żołądka. Dlatego też celem moich badań było sprawdzenie czy produkt rozpadu salinomycyny w środowisku kwaśnym wykazuje nadal właściwości jonoforetyczne, kluczowe dla zachowania aktywności biologicznej. Aby potwierdzić te założenia, postanowiono wykrystalizować produkt rozkładu, a także jego sól potasową. Do potwierdzenia struktury obu związków wykorzystano szereg technik analitycznych, m.in. dyfrakcję rentgenowską przeprowadzoną przez prof. Jana Janczaka z Instytutu Niskich Temperatur i Badań Strukturalnych im. Włodzimierza Trzebiatowskiego Polskiej Akademii Nauk we Wrocławiu.

Ze względu na bardzo niską selektywność konwencjonalnych metod leczenia nowotworów takich jak chemioterapia, w ciągu ostatnich lat skupiono uwagę na rozwoju terapii celowanej, opartej na precyzyjnym działaniu na kluczowe szlaki sygnałowe i cele molekularne komórek nowotworowych. Mitochondria jako centra energetyczne komórek, pełnią ważną rolę w procesie metabolizmu komórkowego, a w przypadku komórek nowotworowych wykazują one szereg dysfunkcji mitochondrialnych, które sprzyjają ich wzmożonej proliferacji. Zatem organelle te stały się atrakcyjnym celem dla terapii przeciwnowotworowych, co otwiera nowe perspektywy leczenia, zwłaszcza w przypadku nowotworów opornych na standardowe metody terapii. Kolejnym celem mojego projektu doktorskiego było przeprowadzenie regioselektywnej modyfikacji salinomycyny i jej koniugacja z kationem trifenylofosfoniowym, który jest powszechnie znaną cząsteczką ukierunkowaną na mitochondria. Pierwszym krokiem było zaplanowanie wydajnej metody syntezy, a następnie optymalizacja warunków metody oczyszczania otrzymanych związków. Postanowiono sprawdzić czy otrzymane koniugaty będą zdolne do celowania w mitochondria komórek nowotworowych i będą wpływać na ich funkcjonalność. Dodatkowo, aby określić aktywność biologiczną otrzymanych pochodnych, większość z nich została przebadana pod kątem właściwości przeciwnowotworowych i przeciwbakteryjnych we współpracy z zespołem prof. Marty Strugi z Warszawskiego Uniwersytetu Medycznego. Weryfikacja właściwości elektrofizjologicznych otrzymanych analogów oraz ich zdolności do przenikania przez błony biologiczne została przeprowadzona we współpracy z prof. Yurim N. Antonenko z Moskiewskiego Uniwersytetu im. M.W. Łomonosowa oraz prof. Piotrem Bednarczykiem ze Szkoły Głównej Gospodarstwa Wiejskiego w Warszawie.

Realizacja zaplanowanych syntez i badań pozwoliła znaleźć korelację między strukturą pochodnych salinomycyny a ich aktywnością biologiczną (zależność struktura-aktywność, SAR). Uzyskane wyniki mogą w przyszłości przyczynić się do racjonalnego projektowania nowych leków, zwłaszcza tych ukierunkowanych na mitochondria.

4. Ankieta dorobku naukowego

A. Wykaz opublikowanych i powiązanych tematycznie artykułów naukowych stanowiących rozprawę doktorską pt. *„Synteza, analiza strukturalna i badanie aktywności biologicznej pochodnych salinomycyny”*:

I. **M. Jędrzejczyk**, J. Janczak, A. Huczyński, *“Molecular structure and spectroscopic studies of the product of acidic degradation of salinomycin and its potassium salt”*, **Journal of Molecular Structure**, 2022; 1263:133129; IF_{2022} = 3,8; punkty MNiSW = 70.

Mój udział w publikacji obejmował izolację salinomycyny oraz syntezę, oczyszczenie i krystalizację zdegradowanej pochodnej salinomycyny i syntezę soli potasowej tej pochodnej. W celu określenia struktury i czystości otrzymanego związku, przeprowadziłam szczegółową analizę spektrometryczną i spektroskopową. Mój udział obejmował przygotowanie próbek do pomiarów (FT-IR, NMR, ESI-MS) oraz analizę i opracowanie otrzymanych wyników spektroskopowych. Odpowiadałam za przygotowanie manuskryptu i suplementu, a także brałam aktywny udział w dyskusji z recenzentami.

Mój udział procentowi stanowi: 70%

Udział procentowy współautorów wynosi: Jan Janczak 15%, Adam Huczyński 15%.

II. Y. N. Antonenko, **M. Jędrzejczyk**, T. I. Rokitskaya, L. S. Khailova, E. A. Kotova, A. Huczyński, *“Rate of translocation across lipid bilayer of triphenylphosphonium-linked salinomycin derivatives contributes significantly to their* K^+/H^+ *exchange activity on membranes”*, **Bioelectrochemistry**, 2022; 145:108089. IF_{2022} = 5,0; punkty MNiSW = 100.

Mój udział w publikacji obejmował wieloetapową syntezę i oczyszczenie pochodnych salinomycyny, przygotowanie próbek do pomiarów (NMR, ESI-MS) oraz analizę i opracowanie otrzymanych wyników badań spektroskopowych. Odpowiadałam za przygotowanie części manuskryptu i suplementu oraz brałam aktywny udział w dyskusji z recenzentami.

Mój udział procentowi stanowi: 40%

Udział procentowy współautorów wynosi: Yuri N. Antonenko 20%, Tatyana I. Rokitskaya 10%, Ljudmila S. Khailova 10%, Elena A. Kotova 10%, Adam Huczyński 10%.

III. **M. Jędrzejczyk**, M. Sulik, M. Mielczarek-Puta, G. Y. Lim, M. Podsiad, J. Hoser, P. Bednarczyk, M. Struga, A. Huczyński, *"Anticancer activity of salinomycin quaternary phosphonium salts"*, **European Journal of Medicinal Chemistry**, 2024; 282:117055. IF_{2023} = 6,0; punkty MNiSW = 140.

Mój udział w publikacji obejmował izolację salinomycyny, przygotowanie substratu do reakcji oraz syntezę i oczyszczenie pochodnych salinomycyny. Przeprowadziłam szczegółową analizę spektrometryczną i spektroskopową otrzymanych pochodnych. Mój udział obejmował przygotowanie próbek do pomiarów (NMR, ESI-MS, HR-MS) oraz analizę i opracowanie otrzymanych wyników badań spektroskopowych. Odpowiadałam za przygotowanie manuskryptu i suplementu, oraz brałam aktywny udział w dyskusji z recenzentami.

Mój udział procentowi stanowi: 40%

Udział procentowy współautorów wynosi: Michał Sulik 5%, Magdalena Mielczarek-Puta 15%, Gwan Y. Lim 5%, Małgorzata Podsiad 5%, Jakub Hoser 10%, Piotr Bednarczyk 5%, Marta Struga 5%, Adam Huczyński 10%.

B. Publikacje naukowe niebędące częścią rozprawy doktorskiej:

- powstałe podczas studiów doktorskich:

1. **M. Jędrzejczyk**, J. Janczak, M. Sulik, A. Huczyński, *"Comparative analysis of the crystal structures of hydrates and sodium salts of monensin and its new C-26 succinate ester"*, **Journal of Molecular Structure**, 2024; 1312: 138489. doi:10.1016/j.molstruc.2024.138489. IF_{2023} = 4,0; punkty MNiSW = 70.
2. A. Torun, A. Zdanowicz, N. Miazek-Zapala, P. Zapala, B. Pradhan, **M. Jedrzejczyk**, A. Ciechanowicz, Z. Pilch, M. Skorzynski, M. Słabicki, G. Rymkiewicz, J. Barankiewicz, C. Martines, L. Laurenti, M. Struga, M. Winiarska, J. Golab, M. Kucia, M. Z. Ratajczak, A. Huczynski, D. P. Calado, D. G. Efremov, A. Zerrouqi, B. Pyrzynska, *"Potassium/sodium cation carriers robustly up-regulate CD20 antigen by targeting MYC, and synergize with anti-CD20 immunotherapies to eliminate malignant B cells"*, **Haematologica**, 2024. doi:10.3324/haematol.2024.285826. IF_{2023} = 8,2; punkty MNiSW = 140.

3. **M. Jędrzejczyk**, B. Morabito, B. Żyżyńska-Granica, M. Struga, J. Janczak, M. Aminpour, J. A. Tuszynski, A. Huczyński, *"Novel Combretastatin A-4 Analogs-Design, Synthesis, and Antiproliferative and Anti-Tubulin Activity"*, **Molecules**, 2024; 29(10):2200. doi:10.3390/molecules29102200. IF_{2023} = 4,2; punkty MNiSW = 140.
4. **M. Jędrzejczyk**, N. Stępczyńska, G. Klejborowska, M. Podsiad, J. Stefańska, D. Steverding, A. Huczyński, *"Synthesis and evaluation of antibacterial and trypanocidal activity of derivatives of monensin A"*, **Bioorganic & Medicinal Chemistry Letters**, 2022, 58, 128521. doi:10.1016/j.bmcl.2021.128521. IF_{2022} = 2,77; punkty MNiSW = 70.
5. A. Urbaniak, M. R. Reed, Heflin, B. Heflin, J. Gaydos, S. Piña-Oviedo, **M. Jędrzejczyk**, G. Klejborowska, N. Stępczyńska, T. C. Chambers, A. J. Tackett, A. Rodriguez, A. Huczyński, R.L. Eoff, A.M. MacNicol, *"Monensin and its analogues show anti-glioblastoma activity in an organoid model of cancer"*, **The FASEB Journal**, 2022; 36: S1. doi: 10.1096/fasebj.2022.36.S1.R5150. IF_{2022} = 4,8; punkty MNiSW = 140.
6. A. Urbaniak, M. R. Reed, B. Heflin, J. Gaydos, S. Piña-Oviedo, **M. Jędrzejczyk**, G. Klejborowska, N. Stępczyńska, T. C. Chambers, A. J. Tackett, A. Rodriguez, A. Huczyński, R. L. Eoff, A. M. MacNicol, *"Anti-glioblastoma activity of monensin and its analogs in an organoid model of cancer"*, **Biomedicine & Pharmacotherapy**, 2022; 153: 113440. doi:10.1016/j.biopha.2022. IF_{2022} = 7,5; punkty MNiSW = 100.

- powstałe przed rozpoczęciem studiów doktorskich:

1. G. Klejborowska, M. Jędrzejczyk, N. Stępczyńska, E. Maj, J. Wietrzyk, A. Huczyński, *"Antiproliferative activity of ester derivatives of monensin A at the C-1 and C-26 positions"*, **Chemical Biology & Drug Design**, 2019; 94(4):1859-1864. doi:10.1111/cbdd.13581. IF_{2019} = 2,5, punkty MNiSW = 70.

C. Staże naukowe:

1. **2-tygoniowy** staż na **Politechnice Turyńskiej (Turyn, Włochy)** w ramach projektu Inicjatywa Doskonałości – Uczelnia Badawcza. Tytuł projektu: *"Design and*

synthesis of novel combretastatin A-4 analogues as new mitotic inhibitors", wykonany pod opieką prof. Jacka A. Tuszyńskiego (25.09.2021 – 09.10. 2021).

2. **2-tygoniowy** staż na **Politechnice Turyńskiej (Turyn, Włochy)** w ramach projektu Inicjatywa Doskonałości – Uczelnia Badawcza. Tytuł projektu: *"Analogs of combretastatin A-4 as new tubulin polymerization destabilizers"*, wykonany pod opieką prof. Jacka A. Tuszyńskiego (09.09.2022 – 23.09. 2022).

D. Konferencje naukowe:

- międzynarodowe:

1. The 4th MMCS: Harnessing the Power of New Drug Modalities, Barcelona, 24.04 – 26.04.2024; **Marta Jędrzejczyk**, Michał Sulik, Magdalena Mielczarek-Puta, Jakub Hoser, Piotr Bednarczyk, Marta Struga, Adam Huczyńsk „*Triphenylphosphonium salts of salinomycin as antiproliferative agents targeting the mitochondria"* – wystąpienie,
2. The 2nd French-Polish Chemistry Congress, National School of Chemistry Montpellier, Montpellier, 28.08. – 31.08.2023; **Marta Jędrzejczyk**, Magdalena Mielczarek-Puta, Małgorzata Podsiad, Marta Struga, Adam Huczyński „*Synthesis, cytotoxicity, and antimicrobial activity of triphenylphosphonium salts of salinomycin"* – poster,
3. The 30th Young Research Fellows Meeting - SCT 2023, Paryż, 01.02. – 03.02.2023; **Marta Jędrzejczyk**, Natalia Stępczyńska, Greta Klejborowska, Alicja Urbaniak, Alan T. Jackett, Dietmar Steverding, Joanna Stefańska, Adam Huczyński, „*Synthesis and evaluation of biological activity of monensin A esters and urethanes"* – poster,
4. The 9th EFMC Young Medicinal Chemists' Symposium, Nicea, 08.09. – 09.09.2022; **Marta Jędrzejczyk**, Yuri N. Antonenko, Tatyana I. Rokitskaya, Ljudmila S. Khailova, Elena A. Kottowa, Adam Huczyński, *„New derivatives of salinomycin as mitochondria-targeting conjugates"* – poster,

- krajowe:

1. XVII Ogólnopolskie Seminarium dla Doktorantów i Studentów, Na pograniczu chemii i biologii, Jastrzębia Góra, 12.05 – 15.05.2019; **Marta Jędrzejczyk**, Greta

Klejborowska, Joanna Wietrzyk, Adam Huczyński, *„Synteza i aktywność przeciwproliferacyjna pochodnych monenzyny A modyfikowanych w pozycji C-1”* – wystąpienie.

E. Zrealizowane projekty badawcze:

1. Grant Narodowego Centrum nauki OPUS nr 2021/41/B/ST4/00088 *„Koniugaty celujące w mitochondria jako nowe środki przeciwnowotworowe”* – wykonawca,
2. Grant Narodowego Centrum nauki OPUS nr 2019/35/B/NZ5/01445 *„Testowanie pochodnych nośników kationowych jako potencjalnych terapeutyków w leczeniu nowotworów wywodzących się od limfocytów B”* – wykonawca,
3. Projekt finansowany z programu Inicjatywa Doskonałości – Uczelnia Badawcza nr 048/13/UAM/0004 *„Analogs of combretastatin A-4 as new tubulin polymerization destabilizers”* – kierownik projektu,
4. Projekt finansowany z programu Inicjatywa Doskonałości – Uczelnia Badawcza nr 003/13/UAM/0010 *„Design and synthesis of novel combretastatin A-4 analogues as new mitotic inhibitors”* – kierownik projektu.

5. Wprowadzenie

Substancje pochodzenia naturalnego odgrywają kluczową rolę w procesie odkrywania leków, gdyż stanowią one istotną część obecnie stosowanych produktów leczniczych [4,5]. W 2012 roku oszacowano, że ponad 50 % zatwierdzonych leków wywodziło się z surowców naturalnych [5]. W porównaniu do konwencjonalnych środków syntetycznych, produkty naturalne charakteryzują się unikatowymi właściwościami takimi jak: wysoka biofunkcjonalność, różnorodność molekularna oraz niska toksyczność [4,6]. Ponadto, szacuje się, że pomiędzy 1981 a 2019 rokiem, spośród nowo zatwierdzonych leków przeciwnowotworowych około 25% stanowią związki pochodzenia naturalnego i ich pochodne [7].

Choroby nowotworowe są drugą najczęstszą przyczyną zgonów u ludzi. Według danych Światowej Organizacji Zdrowia, w 2022 roku odnotowano około 20 milionów nowych przypadków zachorowań oraz blisko 10 milionów zgonów z powodu nowotworu [8]. Przewiduje się, że do 2040 roku liczba zachorowań wzrośnie nawet o 47% w porównaniu z 2020 rokiem [9]. Ze względu na złożoność chorób nowotworowych, badania naukowe w tym obszarze zawsze były ogromnym wyzwaniem. Termin „nowotwór" obejmuje liczną grupę schorzeń, charakteryzujących się niekontrolowaną proliferacją nieprawidłowych komórek, które posiadają zdolność do inwazji oraz przemieszczania się do innych partii ciała [4]. Współczesne strategie terapeutyczne w leczeniu nowotworów obejmują kilka głównych metod, takich jak chemioterapia, terapia celowana, immunoterapia, radioterapia oraz chirurgiczne usuwanie zmian nowotworowych. Radioterapia i leczenie chirurgiczne są terapiami miejscowymi, ukierunkowanymi na eliminację nowotworu w obrębie zmienionych tkanek. Z kolei chemioterapia, terapia celowana oraz immunoterapia należą do metod systemowych, pozwalających na oddziaływanie na komórki nowotworowe w całym organizmie. Chemioterapia działa niespecyficznie, atakując szybko dzielące się komórki, podczas gdy terapia celowana blokuje konkretne szlaki molekularne istotne dla proliferacji nowotworu, natomiast immunoterapia mobilizuje układ odpornościowy do eliminacji komórek nowotworowych [10–12]. Warto dodać, że w przypadku chemioterapii pacjenci doświadczają szeregu skutków ubocznych wynikających z cytotoksycznego działania na zdrowe i prawidłowo dzielące się komórki. Spośród najczęściej występujących działań niepożądanych możemy wyróżnić: nudności, wymioty, zapalanie błon śluzowych jamy ustnej, utrata włosów oraz zaburzenia czynności szpiku z leukemią, małopłytkowością i anemią [13]. Ze względu na wyniszczające skutki terapii z użyciem klasycznych leków cytostatycznych, w ciągu ostatnich dwóch dekad intensywnie rozwijano terapie celowane jako alternatywną strategię leczenia nowotworów. Liczne badania wykazały ich wyższą skuteczność oraz lepszy profil bezpieczeństwa w porównaniu z konwencjonalną chemioterapią, co przyczyniło się do ich ugruntowania jako jednej z kluczowych metod terapeutycznych w onkologii [14–16]. Biorąc pod uwagę rozmiar cząsteczki, spośród leków ukierunkowanych molekularnie możemy wyróżnić dwie grupy związków: małe cząsteczki i makrocząsteczki (przeciwciała monoklonalne), a porównując te obie grupy, można zaobserwować, że te mniejsze wykazują więcej zalet w kilku aspektach: niższe koszty produkcji, korzystniejszy profil farmakokinetyczny, przestrzeganie zaleceń przez pacjentów, a także łatwiejsze warunki przechowywania i transportu. Pierwszym lekiem z tej grupy wprowadzonym na rynek jest imatyrib, który trafił do obrotu w 2001 roku [17]. A już do stycznia 2021 roku Agencja Żywności i Leków, FDA (ang. *Food and Drug Administration*), odpowiedzialna za dopuszczanie leków do obrotu w Stanach Zjednoczonych, zaaprobowała łącznie 89 leków z tej grupy [15]. Ta liczba świadczy o dynamicznym rozwoju w obszarze onkologii, potwierdzając potencjał terapii celowanej jako obiecującego kierunku w odkrywaniu i opracowywaniu nowych leków przeciwnowotworowych. Jednakże, podobnie jak w przypadku klasycznych chemioterapeutyków, kluczowym wyzwaniem w terapii celowanej pozostaje problem wielolekooporności. Pomimo licznych innowacji, w trakcie leczenia zaobserwowano rozwój oporności nowotworów na stosowane substancje, co istotnie ogranicza ich skuteczność [18]. Wzrost zachorowalności na nowotwory oraz ograniczenia konwencjonalnych metod leczenia stanowią zatem jedno z największych wyzwań współczesnej onkologii, wciąż wymagając opracowywania alternatywnych strategii terapeutycznych, w tym również zdolnych do przezwyciężania mechanizmów lekooporności.

W ramach realizacji projektu doktorskiego obiektem mojego zainteresowania była salinomycyna, związek należący do grupy antybiotyków jonoforowych. Polieterowe antybiotyki jonoforowe to związki pochodzenia naturalnego, wykazujące szerokie spektrum aktywności biologicznej, w tym silne właściwości przeciwnowotworowe. Ich wysoka bioaktywność wynika ze specyficznej struktury molekularnej, obejmującej hydrofilową kieszeń zdolną do koordynowania kationów metali oraz hydrofobowy płaszcz, który umożliwia przenikanie przez błony lipidowe i transport kationów ze środowiska zewnątrzkomórkowego do wnętrza komórki [19].

Salinomycyna (Rys. 1) po raz pierwszy została wyizolowana ze szczepu bakterii *Streptomyces albus* w 1974 roku, podczas badań przesiewowych prowadzonych w poszukiwaniu nowych antybiotyków [20].

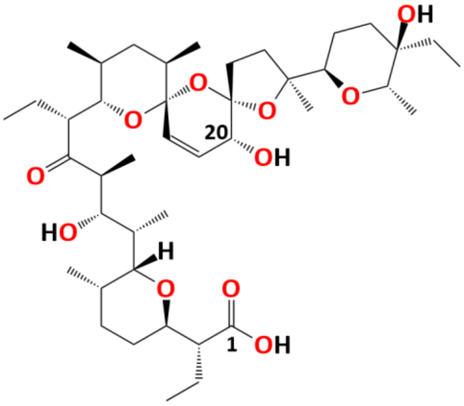

Rysunek 1. Wzór strukturalny salinomycyny.

Mimo swojej otwartołańcuchowej budowy, salinomycyna i jej sole potrafią przyjąć pseudocykliczną strukturę w wyniku utworzenia wewnątrzcząsteczkowych wiązań wodorowych między grupą karboksylową a grupami hydroksylowymi znajdującym się po przeciwnej stronie cząsteczki [21]. Taki układ szkieletu polieterowego umożliwia kompleksowanie kationów metali, z największym powinowactwem wobec kationów sodu i potasu [22]. Skoordynowany kation jest transportowany i uwalniany we wnętrzu komórki zaburzając naturalny gradient stężeń Na^+/K^+ i wewnątrzkomórkowe pH, co w konsekwencji prowadzi do obrzęku komórki, uszkodzenia mitochondriów oraz indukowania apoptozy – zaprogramowanej śmierci komórki [23].

Salinomycyna wykazuje szerokie spektrum bioaktywności, obejmujące działanie przeciwwirusowe, przeciwbakteryjne – ze szczególną skutecznością wobec bakterii Gram-dodatnich – a także właściwości przeciwgrzybicze i przeciwpasożytnicze [24]. Warto również dodać, że salinomycyna znalazła zastosowanie jako niehormonalny stymulator wzrostu i kokcydiostatyk w przemysłowej hodowli drobiu i bydła [23].

Rok 2009 był przełomowy w kontekście badań nad aktywnością salinomycyny. Piyush B. Gupta i współpracownicy przeprowadzili badania screeningowe obejmujące blisko 16 000 biologicznie czynnych związków, w tym leków przeciwnowotworowych, w celu oceny ich skuteczności wobec macierzystych komórek raka piersi (ang. *Cancer Stem Cells*, CSCs) [25]. Badania wykazały, że zaledwie 32 związki, co stanowi 0,2% analizowanej puli, były zdolne do hamowania rozwoju CSCs, a spośród nich to salinomycyna wykazała największą aktywność przeciwnowotworową. Ponadto, w porównaniu z powszechnie stosowanym cytostatykiem – paklitaksel – antybiotyk jonoforowy wykazał aż 100-krotnie większą skuteczność.

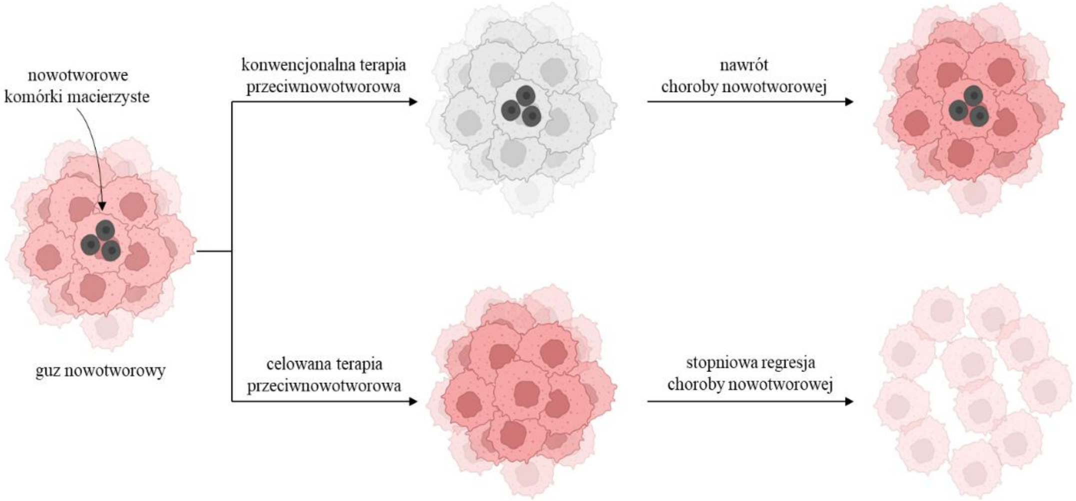

Rysunek 2. Zasady działania konwencjonalnej i celowanej w komórki macierzyste terapii przeciwnowotworowej.

Odkrycie to przyczyniło się do postrzegania salinomycyny jako obiecujący związek o wysokim potencjale przeciwnowotworowym [25]. Aby w pełni zrozumieć przełomowość tego badania, warto wyjaśnić jak kluczową rolę w rozwoju choroby onkologicznej pełnią nowotworowe komórki macierzyste. Stanowią one jedynie 2–10% masy guza oraz są ukryte w jego wnętrzu, co znacząco utrudnia zlokalizowanie ich oraz zwalczanie podczas terapii. Ponadto CSCs wykazują zdolność do samoodnawiania i pluripotencji, a także do inicjowania wzrostu guza, proliferacji, migracji (przerzutowania) oraz rozwijania oporności na leczenie przeciwnowotworowe [26,27]. Zaobserwowano, że konwencjonalna chemioterapia nie jest zdolna do zniszczenia nowotworowych komórek macierzystych, co najczęściej skutkuje nawrotami choroby. Zatem zaczęto badać możliwość opracowania różnych strategii terapii celowanej na CSCs, takie jak terapia z wykorzystaniem małych cząsteczek czy przeciwciał monoklonalnych [28].

W tym miejscu warto również wspomnieć o stosowaniu terapii skojarzonej, łączącej dwie metody zwalczania nowotworu. Jako przykład może posłużyć koniugat trastuzumab derukstekan (Enhertu®), który jest połączeniem leku cytostatycznego z przeciwciałem monoklonalnym działającym na receptor HER2. Lek ten został zatwierdzony w leczeniu pacjentów z nieoperacyjnym HER2-dodatnim i HER2-ujemnym rakiem piersi, rakiem żołądka i niedrobnokomórkowym rakiem płuc [29]. Istnieją doniesienia literaturowe, które świadczą o synergistycznym działaniu salinomycyny z takimi lekami jak AZD3463 lub już wcześniej wspomniany trastuzumab, które są stosowane w terapii celowanej. Badania *in vitro* w obu przypadkach wykazały hamowanie proliferacji komórek rakowych znacznie skuteczniej niż w przypadku stosowania monoterapii [30,31]. Zatem powyższe doniesienia potwierdzają, że terapia skojarzona może zwiększać skuteczność leczenia nowotworów poprzez wykorzystanie różnych mechanizmów działania leków.

Spośród wszystkich badań naukowych poświęconych salinomycynie, sporą część stanowią prace nad jej chemiczną modyfikacją i analizą aktywności biologicznej otrzymanych pochodnych. Jednym z przykładów modyfikacji salinomycyny są jej biokoniugaty, które stanowią niewielką część wszystkich analogów, jednak dotychczasowe wyniki badań wskazują na ich obiecujący potencjał terapeutyczny. W ciągu ostatnich dziesięciu lat, prof. Huczyński wraz ze swoim zespołem badawczym zsyntezował szereg biokoniugatów salinomycyny między innymi z floksurydyną, azydotymidyną, sylibiną, alkaloidami kory chinowca oraz estrami metylowymi aminokwasów [32–36]. Wszystkie z modyfikacji dotyczyły grupy karboksylowej znajdującej się w pozycji C1. Spośród nich najaktywniejszym analogiem okazał się ester z floksurydyną, pochodną 5-fluorouracylu, stosowaną w leczeniu raka jelita grubego. Zsyntezowany koniugat wykazał większą aktywność przeciwprolifercyjną *in vitro* wobec komórek białaczki promielocytowej (HL-60 i HL-60/vinc) niż niemodyfikowana salinomycyna i powszechnie stosowana cisplatyna [32].

Opierając się na powyższych doniesieniach, można było wysnuć wniosek, że koniugowanie cząsteczki salinomycyny z innym związkiem bioaktywnym, może mieć pozytywny wpływ na jej aktywność biologiczną.

Doskonałym przykładem tego rodzaju cząsteczki jest kation trifenylofosfoniowy (TPP^+), który pełni kluczową rolę jako związek nakierowujący na mitochondria. Jon TPP^+ posiada stabilizowany ładunek dodatni, który jest zdelokalizowany na trzech pierścieniach fenylowych. Dodatkowo, jego lipofilowy charakter zwiększa zdolność do przenikania przez hydrofobową błonę mitochondrialną [37]. Jako, że błona mitochondriów w komórkach nowotworowych jest hiperpolaryzowana (-220 mV) w porównaniu do mitochondriów zdrowych komórek (-160 mV), przenikanie dodatnio naładowanych cząsteczek do mitochondriów komórek proliferujących patologicznie jest znacznie łatwiejsze [38]. Warto podkreślić, że mitochondria należą do kluczowych organelli komórkowych, odgrywając fundamentalną rolę w metabolizmie energetycznym oraz regulacji procesu apoptozy. Udowodniono, że metabolizm w mitochondriach komórek nowotworowych różni się od tego w zdrowych komórkach, a proces proliferacji zachodzi znacznie szybciej niż w zdrowych organellach [39]. Wynika to z dysfunkcji mitochondrialnych, które sprzyjają namnażaniu komórek i rozwijaniu oporności na apoptozę. Efekt Warburga jest jednym z przykładów wspomnianych dysfunkcji, który polega na tym, że komórki nowotworowe preferencyjnie wykorzystują glikolizę do produkcji dużych ilości energii, mimo obecności tlenu. Prowadzi to do wzmożonej produkcji kwasu mlekowego, co zapewnia kwaśne mikrośrodowisko komórkom nowotworowym, sprzyjające nie tylko szybszej proliferacji, ale także rozwijaniu lekooporności [40]. Zatem badania nad rozwojem strategii terapeutycznej ukierunkowanej na mitochondria wydaje się być obiecującym kierunkiem w zwalczaniu nowotworów.

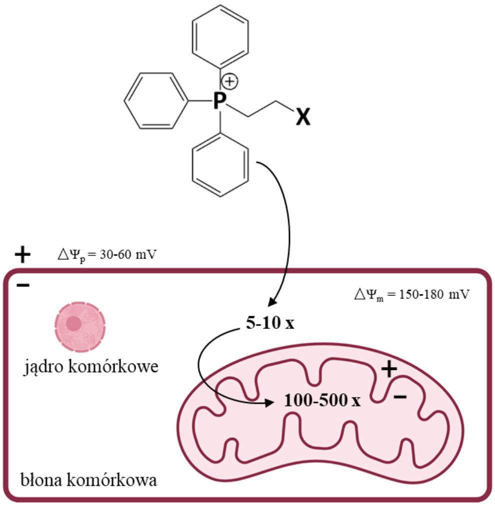

Rysunek 3. Wychwyt związku z ugrupowaniem TPP$^+$ przez mitochondria.

Korzyści wynikające z koniugacji bioaktywnych cząsteczek z kationem trifenylofosfoniowym zostały już niejednokrotnie udowodnione. W 2013 roku, zsyntezowano koniugat chlorambucylu i kationu trifenylofosfoniowego oraz przebadano jego aktywność przeciwnowotworową wobec linii komórkowych raka piersi oraz trzustki, wykazujących oporność na niezmodyfikowany lek. Wyniki testów *in vitro* wykazały, że pochodna TPP$^+$ cechowała się nawet 12-krotnie wyższą skutecznością wobec komórek raka piersi w porównaniu do niezmodyfikowanego chlorambucylu, a ponadto skutecznie przezwyciężała oporność na lek zarówno w liniach komórkowych nowotworu piersi, jak i trzustki [41]. Kolejnym przykładem są analogi chloramfenikolu z TPP$^+$, które zostały przebadane pod kątem aktywności przeciwbakteryjnej. Chloramfenikol jest znanym antybiotykiem, którego skuteczność znacznie zmalała ze względu na rozwój lekooporności u bakterii [42]. W badaniu udowodniono, że dwa z zsyntezowanych koniugatów wykazują znaczące działanie przeciwbakteryjne wobec szczepu *Staphylococcus aureus* opornego na metycylinę, MRSA (ang. *methicyllin-resistant Staphylococcus aureus*), podczas gdy niemodyfikowany chloramfenikol nie wykazywał aktywności wobec badanych szczepów MRSA. Ponadto, w testach *in vivo* wykazano, że jedna z pochodnych podawana myszom zakażonym klinicznym izolatem MRSA, wykazała porównywalną, a nawet lepszą skuteczność przeciwko MRSA niż standardowy antybiotyk – wankomycyna [43]. Przytoczone wyniki badań nad koniugatami potwierdzają, iż przyłączanie kationu TPP^+ do związków biologicznie aktywnych, zwiększa ich potencjał terapeutyczny, co więcej, przełamuje lekooporność. W trakcie realizacji mojego projektu doktorskiego skupiłam więc uwagę na koniugacji salinomycyny z kationem trifenylofosfoniowym.

6. Omówienie wyników badań

A. Badania nad rozkładem cząsteczki salinomycyny

Przy modyfikowaniu salinomycyny należy szczególnie pamiętać o jej wrażliwości na środowisko kwasowe. Zatem podczas planowania syntezy, trzeba uważnie dobierać warunki reakcji aby zapobiec rozkładowi cząsteczki [21]. W trakcie realizowania projektu doktorskiego niejednokrotnie salinomycyna uległa rozpadowi w wyniku nieprawidłowo dobranych warunków środowiska reakcji. Ponadto, postrzegając salinomycynę i jej pochodne jako środki o wysokim potencjale terapeutycznym, należy się zastanowić jaki wpływ na trwałość cząsteczki miałaby doustna metoda administracji potencjalnego leku. Zdecydowana większość leków jest podawana drogą doustną, zatem przy projektowaniu ich należy wziąć pod uwagę silnie kwaśne środowisko żołądka człowieka (pH = 1,5 – 2,0), które może być kluczowym czynnikiem wpływającym na stabilność, wchłanianie i rozpuszczalność substancji aktywnej [44]. Dlatego też przeanalizowanie procesu rozpadu salinomycyny pod wpływem środowiska kwasowego stał się również celem mojej pracy [1].

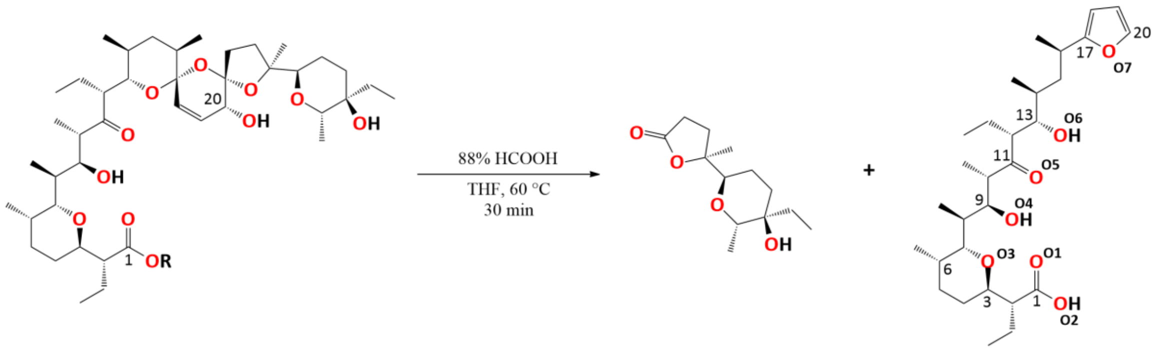

salinomycyna, R = H
sól sodowa salinomycyny, R = Na

I-1

I-2

Rysunek 4. Reakcja rozkładu salinomycyny.

Pierwsza publikacja opisuje badania nad procesem rozkładu cząsteczki salinomycyny w środowisku kwasowym [1]. W swoich badaniach brałam pod uwagę doniesienia Wellsa z 1988 roku, w których użyto kwasu mrówkowego jako czynnika wywołującego rozpad cząsteczki (Rys. 4)[a] [45]. Dodatkowo przetestowano rozkład salinomycyny pod wpływem innych kwasów o różnych wartościach pK_a – kwasu fosforowego(V) ($pK_a = 2,12$) oraz kwasu octowego ($pK_a = 4,76$). Do kontrolowania przebiegu reakcji zastosowano chromatografię cienkowarstwową (ang. *thin-layer chromatography,* TLC). W przypadku

---

[a] W rozprawie doktorskiej zastosowano oznaczenie, które będzie zgodne z opisami kryształu.

kwasu fosforowego(V) o stężeniu 85% zaobserwowano natychmiastową zmianę barwy roztworu z jasnożółtej na ciemnoczerwoną, co świadczyło o całkowitym rozkładzie salinomycyny. Natomiast w obecności kwasu octowego o stężeniu 99% po upływie 24h zaobserwowano znikomy rozkład cząsteczki. Użycie kwasu mrówkowego ($pK_a = 3{,}74$) umożliwiło kontrolowanie procesu rozpadu salinomycyny. Za pomocą chromatografii cienkowarstwowej obserwowano stopniowe zanikanie substratu i tworzenie produktów degradacji (**I-1** i **I-2**). Po upływie 30 minut zaobserwowano zanik większości substratu i przerwano reakcję degradacji, rozcieńczając mieszaninę reakcyjną chlorkiem metylenu i przystępując do ekstrakcji z wodą, w celu usunięcia pozostałości kwasu mrówkowego.

Dotychczas, struktura głównego produktu rozpadu **I-2** nie została szczegółowo przebadana, w tym celu wykrystalizowano związek **I-2** i przeprowadzono analizę strukturalną. Ponadto, opierając się na doświadczeniu, wysnuto hipotezę, że ze względu na obecność grupy karboksylowej, ketonowej i grup hydroksylowych, związek **I-2** zachował właściwości jonoforetyczne i jest zdolny do kompleksowania jonów metali. W celu weryfikacji tej hipotezy, otrzymano kryształ soli potasowej związku **I-2** (Rys. 5) i przeanalizowano go w stanie stałym oraz w roztworze. Do weryfikacji struktury i czystości związków **I-2** i **I-2-K** użyto szeregu metod analitycznych.

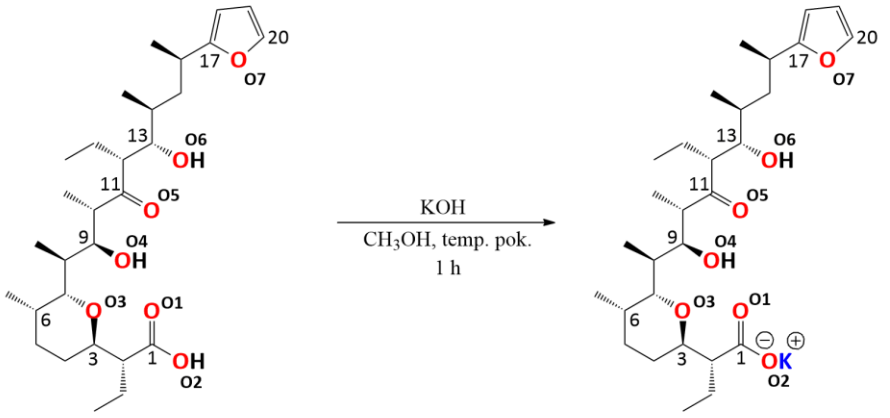

I-2 **I-2-K**

Rysunek 5. Synteza soli potasowej **I-2-K**.

Pierwszą metodą były pomiary rentgenowskiej dyfrakcji pojedynczego kryształu związków **I-2** i **I-2-K**. Analiza kryształu produktu **I-2** wykazała, że kwasowy rozpad nie wpłynął na absolutną konfigurację na asymetrycznych atomach węgla i została ona zachowana tak jak w cząsteczce niemodyfikowanej salinomycyny. Zaobserwowano, że pierścień furanowy jest płaski, natomiast pierścień tetrahydropyranowy wykazuje konformację krzesełkową. Cała konformacja jest stabilizowana przez wewnątrzcząsteczkowe wiązania wodorowe O–H···O utworzone pomiędzy grupą hydroksylową (O4) i grupą karboksylową (O1) (Rys. 6). Układ cząsteczek w krysztale jest w głównej mierze determinowany przez międzycząsteczkowe wiązania wodorowe, oddziaływania elektrostatyczne oraz siały van der Waalsa.

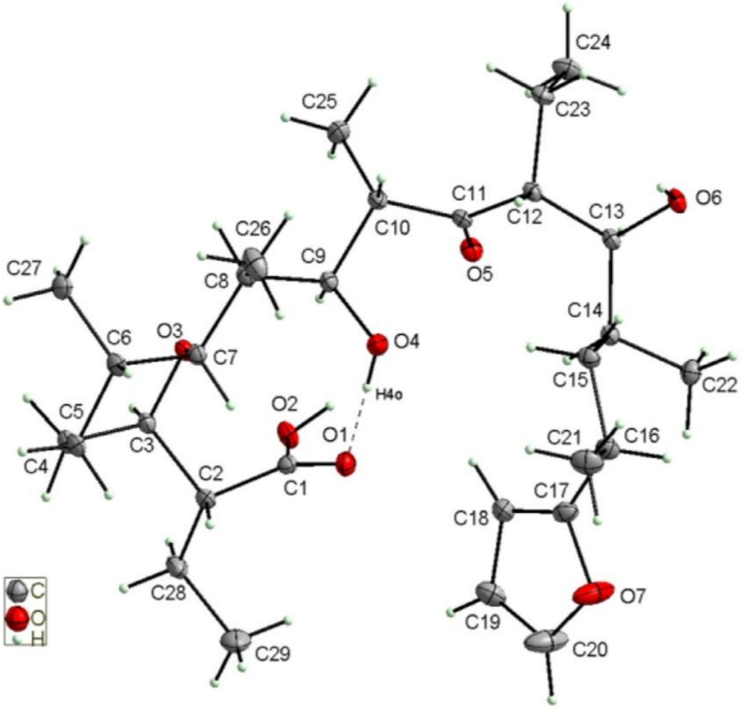

Rysunek 6. Struktura molekularna związku **I-2**, obliczona metodą dyfrakcji rentgenowskiej.

Aby zweryfikować hipotezę, że produkt degradacji zachował zdolność do kompleksowania jonów, obliczono i przeanalizowano mapy molekularnego potencjału elektrostatycznego (MESP) cząsteczki neutralnej oraz zdeprotonowanej (Rys. 7).

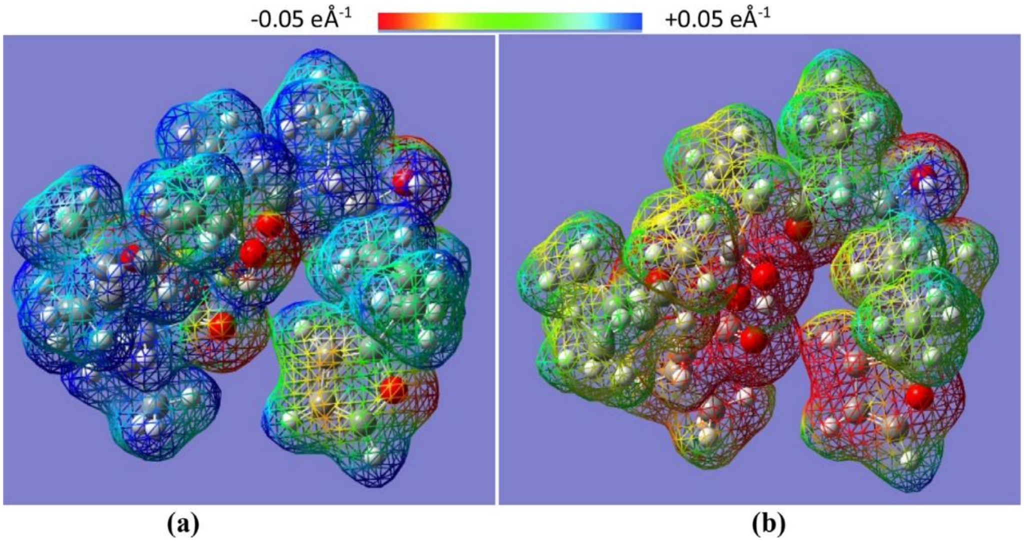

Rysunek 7. Trójwymiarowy potencjał elektrostatyczny cząsteczek przedstawiony na izopowierzchni całkowitej gęstości elektronowej (0,008 eÅ^{-3}) dla **I-2** (a) i jego zdeprotonowanego anionu (b). Kod koloru: –0,05 eÅ^{-1} (czerwony) do +0,05 eÅ^{-1} (niebieski).

Analiza potencjału elektrostatycznego cząsteczek jest uznawana za skuteczne narzędzie umożliwiające zrozumienie i interpretację właściwości chemicznych i reaktywności układów molekularnych oraz pokazuje rozmieszczenie ładunku elektrostatycznego w cząsteczce [46]. Przy użyciu programu GaussView 5.0 potwierdzono jonoforetyczne właściwości produktu degradacji kwasowej salinomycyny, zgodnie z oczekiwaniami ujemny potencjał elektrostatyczny anionowej formy związku **I-2** rozciąga się na znacznie większym obszarze w porównaniu do cząsteczki obojętnej oraz ma bardziej ujemną wartość.

Następnym krokiem do potwierdzenia właściwości jonoforetycznych była analiza kryształu zsyntezowanej soli **I-2-K** (Rys. 8). Wykazano, że otrzymana sól posiada bardziej złożoną strukturę, gdyż asymetryczna jednostka **I-2-K** składa się z sześciu cząsteczek soli potasowej i trzech cząsteczek wody, przy czym jedna z nich jest nieuporządkowana.

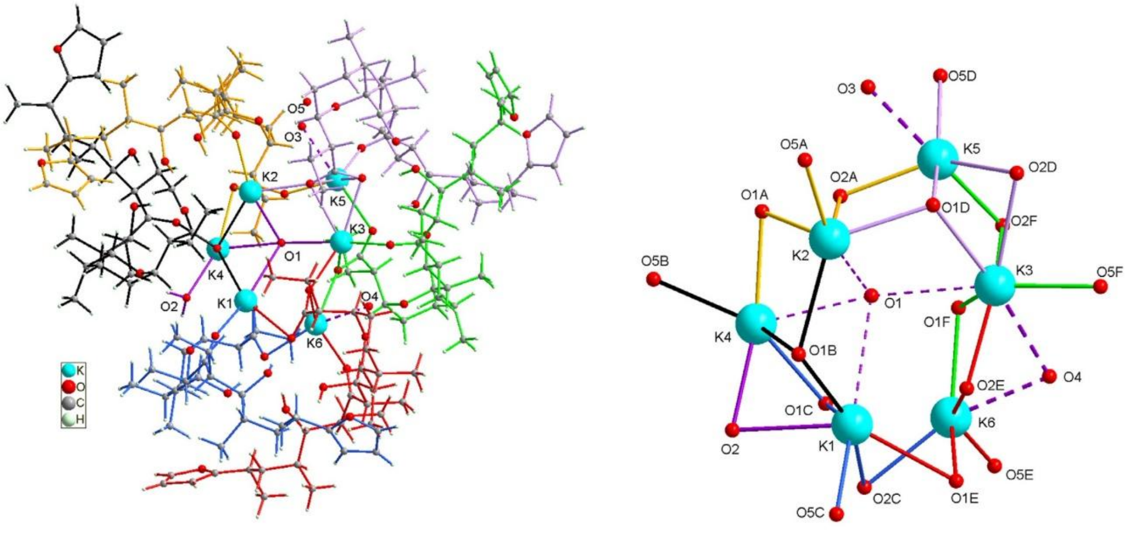

(a) **(b)**

Rysunek 8. Asymetryczna jednostka soli składająca się z sześciu kationów potasu i sześciu zdeprotonowanych form anionowych cząsteczki **I-2**.

Na Rysunku 8a przedstawiono asymetryczną jednostkę soli, gdzie każdą cząsteczkę zdeprotonowanego związku **I-2**, oznaczono innym kolorem. Sześć kationów potasu oddziałuje z sześcioma anionami oraz centralnie położoną cząsteczką wody (O1), która tworzy wiązania z czterema jonami potasu (K1, K2, K3 i K4), prowadząc do powstania supramolekularnego kompleksu K_6. Każdy z sześciu anionów w asymetrycznej jednostce oddziałuje z trzema kationami potasu za pośrednictwem atomów tlenu zdysocjowanej grupy karboksylowej (COO^{-}) oraz atomu tlenu (O5) grupy karbonylowej (Rys. 8b). W Tabeli 1 zestawiono cechy struktur krystalicznych związku **I-2** i **I-2-K**.

Tabela 1. Zestawienie cech kryształów związków **I-2** i **I-2-K**.

Cecha	**I-2**	**I-2-K**
Układ krystalograficzny	jednoskośny	rombowy
Grupa przestrzenna	$P2_1$	$P2_12_12_1$
Liczba cząsteczek w komórce elementarnej (Z)	2	4
Stabilizacja cząsteczki	Wiązania wodorowe	Wiązania wodorowe i oddziaływania $K^+\cdots O$

Kolejną techniką analityczną była spektroskopia w podczerwieni z transformacją Fourier'a (FT-IR). Technika ta pozwala na weryfikację obecności charakterystycznych grup funkcyjnych w cząsteczce oraz ich oddziaływania z otoczeniem [47]. W badaniu wykonano widma obu związków **I-2** i **I-2-K** w stanie stałym oraz w roztworze dichlorometanu CH_2Cl_2. W przypadku związku **I-2** największe zmiany zaobserwowano w obszarze drgań rozciągających ν(OH) i ν(C=O) (Rys. 9). Porównując widma IR kryształu **I-2** (linia ciągła) i jego roztworu w CH_2Cl_2 (linia przerywana) widzimy różnice między tymi dwiema strukturami, szczególnie w tworzeniu wiązań wodorowych. Jak wynika z tego porównania, wiązania wodorowe są różne w ciele stałym i w roztworze. Umiarkowanie silne międzycząsteczkowe wiązanie wodorowe O6-H···O5 ulega zerwaniu w roztworze dichlorometanu, co potwierdza zanik pasma przy częstotliwości 3338 cm^{-1} i wzrastająca intensywność pasma przy 3500 cm^{-1} (linia przerywana) (Rys. 9b). Warto również przyjrzeć się obszarowi drgań rozciągających pochodzących od grupy karbonylowej ν(C=O) (Rys. 9c). W widmie kryształu **I-2** oddziaływanie atomu tlenu grupy karboksylowej COOH w obrębie międzycząsteczkowego wiązania wodorowego (O2—H···O6) jest pokazane przez pasmo ν(C=O) przy 1696 cm^{-1}. Pasmo przypisane drganiom ν(C=O) grupy ketonowej jest pokazane przy 1706 cm^{-1}. W tym samym obszarze widma związku **I-2** w roztworze dichlorometanu (linia przerywana) możemy zauważyć różnice, oprócz pasma przy 1708 cm^{-1} pojawia się nowe, mniej intensywne pasmo przy ok. 1735 cm^{-1}. Obecność tego pasma sugeruje, że karbonylowy atom tlenu grupy karboksylowej COOH nie bierze udziału w tworzeniu wiązania wodorowego w odróżnieniu od tego co zaobserwowano w krysztale.

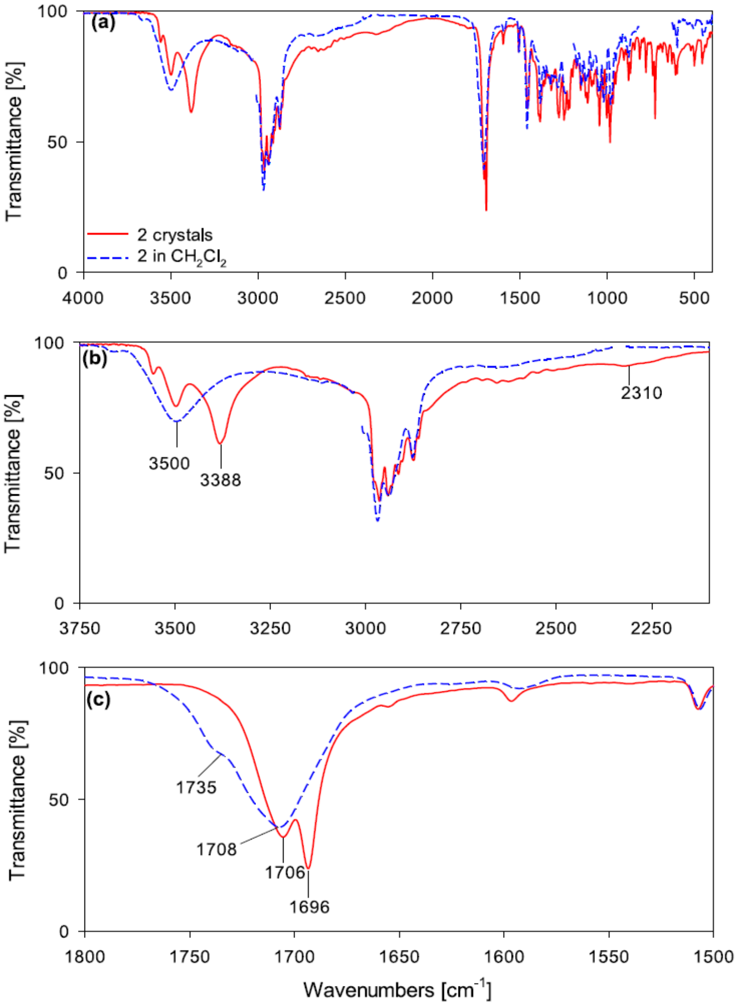

Rysunek 9. Widma IR związku **I-2** w formie kryształu (linia ciągła) i w formie roztworu w CH_2Cl_2 (linia przerywana) w obszarach: (a) 4000–400 cm^{-1}, (b) 3750–2100 cm^{-1} i (c) 1800–1500 cm^{-1}.

Porównując widma IR soli **I-2-K** w ciele stałym i w roztworze, zaobserwowano niewielkie zmiany w kształcie pasm w obszarach 3050 cm^{-1} oraz 1800–1350 cm^{-1} (Rys. 10). Na przykładzie obliczonej różnicy pomiędzy pasmami $\nu_{asym.}(COO^{-})$ a $\nu_{sym.}(COO^{-})$, która wynosi $\Delta\nu = 171$ cm^{-1} dla kryształu, jak i roztworu, można wywnioskować, że grupa karboksylanowa powinna być koordynowana w podobny sposób.

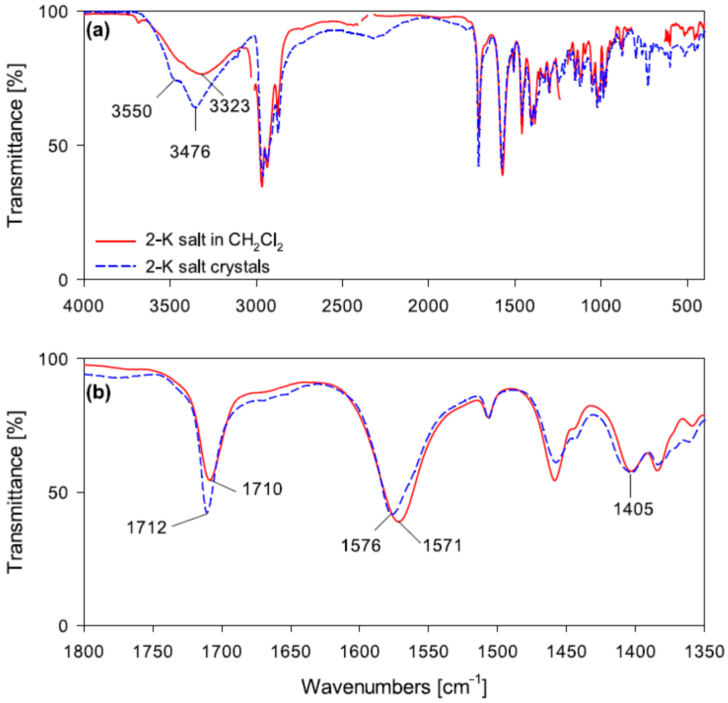

Rysunek 10. Widma FT-IR kryształu soli **I-2-K** (linia przerywana) i soli **I-2-K** w roztworze CH_2Cl_2 (linia ciągła) w obszarach: (a) 4000–400 cm^{-1} i (b) 1800–1350 cm^{-1}.

Dodatkowo, zdolność do koordynowania jonów sprawdzono przy użyciu spektrometrii masowej z jonizacją przez elektrorozpylenie (ESI-MS) [48]. Wyniki wykazały, że związek **I-2** jest w stanie tworzyć stabilne kompleksy z kationami metali jednowartościowych, takimi jak Na^+, K^+ i Rb^+ o stechiometrii 1:1 i 2:1 (Rys. 11).

Preferencja tworzenia kompleksów $(L+M)^+$ i $(2L+M)^+$ z różnymi kationami jednowartościowymi zmienia się w następującej kolejności: $Na^+ > K^+ \geq Rb^+$. Analiza ESI-MS pokazuje również, że związek **I-2** nie utworzył kompleksów z Li^+ i Cs^+, co prawdopodobnie wynika ze zbyt małego lub zbyt dużego rozmiaru kationu i niedopasowania do hydrofilowej kieszeni związku **I-2**.

Dla pełnej charakterystyki otrzymanych związków przeprowadzono również analizę elementarną związków **I-2** i **I-2-K**. Wyniki eksperymentalne pokrywają się z obliczoną zawartością procentową poszczególnych pierwiastków dla badanych związków.

W badaniach wykorzystano również spektroskopię magnetycznego rezonansu jądrowego w celu potwierdzenia i charakterystyki struktury otrzymanych związków. Widma ^1H NMR, ^{13}C NMR i dwuwymiarowe widma (2D NMR) ^1H – ^{13}C HETCOR, ^1H – ^{13}C HMBC oraz ^1H – ^1H COSY umieszczono w suplemencie do publikacji I (Figures S1 – S10).

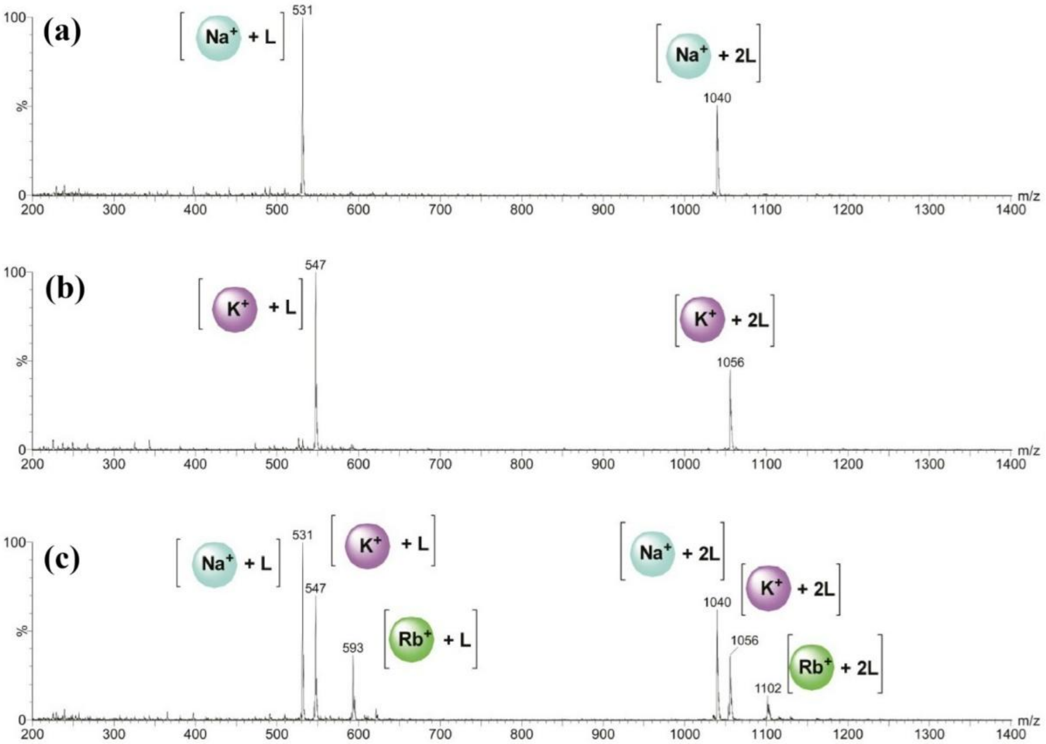

Rysunek 11. Widmo masowe ESI mieszaniny związku **I-2** w stosunku 1:1 z: (a) $NaClO_4$, (b) $KClO_4$, (c) widmo masowe ESI mieszaniny związku **I-2** w stosunku 3:1:1:1 z $NaClO_4$, $KClO_4$ i $RbClO_4$ (cv = 30V).

B. Synteza i badania pochodnych salinomycyny z kationem trifenylofosfoniowym

Druga i trzecia publikacja obejmują badania nad koniugacją salinomycyny z kationem trifenylofosfoniowym (TPP^+) oraz aktywnością biologiczną zsyntezowanych pochodnych [2,3]. Dodatkowo, znaczącą część badań stanowią testy biofizyczne z wykorzystaniem sztucznych i naturalnych błon biologicznych oraz mitochondriów.

Większość modyfikacji dotyczy grupy karboksylowej w pozycji C1. Warto podkreślić, że pierwsze próby syntezy koniugatów TPP^+ wymagały optymalizacji warunków reakcji. Zaobserwowano, że wydajności otrzymywanych estrów i triazolu, były niższe w porównaniu do wcześniej przeprowadzanych modyfikacji [49,50]. Dodatkowo, na etapie oczyszczania otrzymanych związków napotkano wiele przeszkód. Czas poświęcony optymalizowaniu warunków rozdziału chromatograficznego stanowi sporą część tego projektu. Po wielu próbach doboru rozpuszczalników, tempa przepływu rozpuszczalnika, długości drogi rozdziału, opracowano metody rozdziału dla koniugatów TPP^+.

W publikacji II omówiono syntezę oraz właściwości jonoforetyczne koniugatów salinomycyny, otrzymanych w wyniku chemicznej modyfikacji w pozycji C1 i w pozycji C20 (Rys. 12).[b] Właściwości jonoforetyczne przebadano we współpracy z prof. Yurim Antonenko z Moskiewskiego Uniwersytetu Państwowego im. M. W. Łomonosowa. W wyniku przeprowadzonych modyfikacji otrzymano dwie pochodne estrowe **II-6**, **II-8** oraz triazolowy analog **II-5** zsyntezowany za pomocą dipolarnej 1,3-cykloaddycji Huisgena (CuAAC), jednej z reakcji klik [51]. Otrzymanie pochodnej **II-5** wymagało przeprowadzenia kilkuetapowej syntezy, począwszy od zablokowania grupy karboksylowej przy użyciu trimetylosililoetanolu [52]. Następnym etapem była reakcja Mitsunobu, w wyniku której dochodzi do wprowadzenia grupy azydkowej o odwróconej konfiguracji w pozycji C20. Otrzymany azydek *epi*-salinomycyny poddajemy reakcji odblokowania za pomocą fluorku tetrabutyloamoniowego, TBAF. Ostatnim etapem jest synteza 1,2,3-triazolu, katalizowana jonami miedzi (I). To jedna z kilku koncepcji chemii klik, opracowanej przez Sharplessa i Meldala, która została nagrodzona nagrodą Nobla w 2022 roku [53]. Reakcja katalizowana jonami miedzi gwarantuje otrzymanie 1,4-podstawionego triazolu, ponadto metoda ta charakteryzuje się szybkim tempem reakcji oraz całkowitą regioselektywnością [54]. Wszystkie z otrzymanych produktów były poddane analizie spektrometrycznej (ESI-MS, HR-MS) i spektroskopowej (^{1}H NMR,

---

[b] W trakcie analizy wyników badań zastosowano nowe oznaczenia związków X-Y, gdzie X to cyfra rzymska odwołująca się do numeru publikacji wg spisu treści, a Y to cyfra arabska odpowiadająca oryginalnemu oznaczeniu związków w publikacji.

^{13}C NMR) w celu potwierdzenia ich struktury. Opisy widm umieszczono w suplemencie do publikacji II.

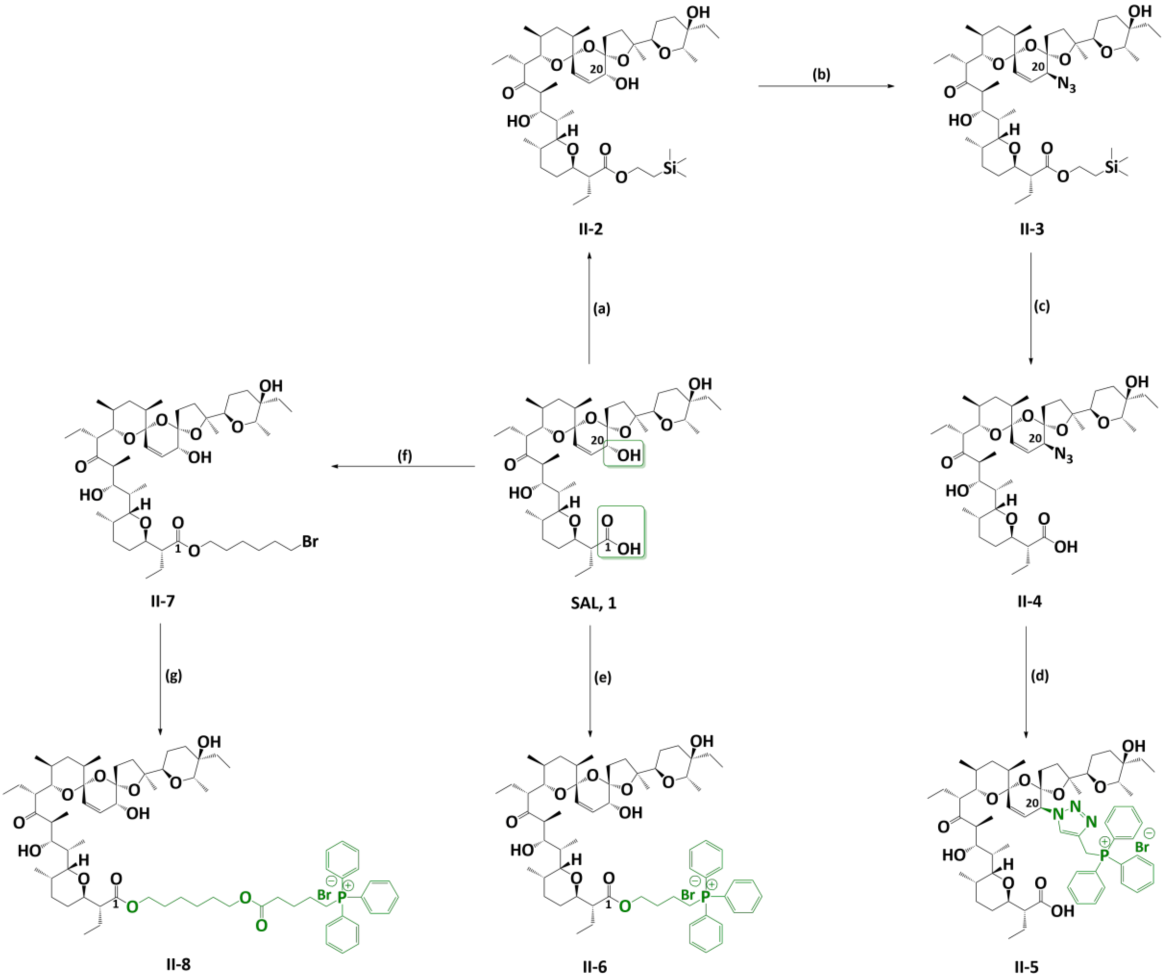

Rysunek 12. Synteza pochodnych SAL-TPP$^+$. Warunki reakcji: (a) 2-TMS etanol, TCFH, DMAP, CH_2Cl_2, 0°→tp; (b) PPh_3, DIAD, DPPA, bezwod. THF, tp; (c) TBAF, THF, tp; (d) bromek trifenylopropargilofosfoniowy, CuI, CH_3CN, tp; (e) bromek (4-bromobutylo)trifenylofosfoniowy, DBU, DMF, 100°C; (f) 1,6-dibromoheksan, DBU, toluen, 100°C; (g) bromek 4-(karboksybutylo)trifenylofosfoniowy, DBU, DMF, 100°C.

W pierwszym badaniu przetestowano właściwości jonoforetyczne salinomycyny i jej pochodnych przy użyciu liposomów obciążonych fluorescencyjnym wskaźnikiem pH – pyraniną. W eksperymencie wykorzystano liposomy, w których pH wewnętrzne wynosiło 6, a zewnętrzne 8. Po dodaniu wodorotlenku potasu do buforu zewnętrznego (zawierającego 100 mM KCl), monitorowano zmiany fluorescencji pyraniny, wskazujące na równoważenie pH w wyniku transportu protonów. W warunkach kontrolnych zmiana pH buforu zewnętrznego nie wpływała na pH wnętrza liposomów, natomiast obecność efektywnego transportera jonów powodowała wymianę K^+/H^+, prowadząc do wyrównania pH. Zaobserwowano, że związek **II-5** powodował szybką wymianę K^+/H^+, co prowadziło do wyrównania pH w liposomach. Niemodyfikowana salinomycyna transportowała jony nieco wolniej, jednak równie skutecznie co jej triazolowa pochodna **II-5**. Uzyskany wynik potwierdził, że koniugacja salinomycyny z kationem TPP^+ w pozycji C20 nie osłabia jej właściwości jonoforetycznych i minimalnie zwiększa zdolność do transportowania jonów przez dwuwarstwową błonę lipidową.

Kolejne eksperymenty zostały przeprowadzone z wykorzystaniem izolowanych mitochondriów. W jednym z testów użyto mitochondriów, które nie wykazywały aktywnego potencjału błonowego i nie generowały ATP. Aktywność jonoforów oceniono stosując metodę monitorowania pęcznienia mitochondriów w medium zawierającym octan potasu. Wpływ badanych analogów i niemodyfikowanego antybiotyku na pęcznienie mitochondriów monitorowano poprzez mierzenie zmian absorbancji światła przy długości fali 540 nm. Spośród testowanych pochodnych, ponownie związek **II-5** i salinomycyna okazały się najbardziej aktywne powodując wyraźne pęcznienie mitochondriów, co potwierdza ich zdolność do transportu K^+/H^+ przez błony mitochondrialne. Ze wszystkich badanych związków, pochodna **II-8** wypadła w tym eksperymencie najgorzej. W przypadku testów z użyciem mitochondriów z aktywnym potencjałem błonowym, zmierzono zmiany potencjału błonowego za pomocą selektywnej elektrody tetrafenylofosfoniowej (P-TPP^+). Do zawiesiny mitochondriów dodano bursztynian (substrat kompleksu II łańcucha oddechowego) oraz rotenon (inhibitor kompleksu I łańcucha oddechowego), co pozwoliło na stabilne wytworzenie potencjału błonowego i stworzenie jednolitych warunków do pomiaru wpływu salinomycyny i jej koniugatów na potencjał błonowy mitochondriów [55]. Test potwierdził, że pochodna **II-5** wykazuje największą aktywność i działa silniej niż salinomycyna, co sugeruje, że może akumulować się w mitochondriach dzięki obecności grupy TPP^+ w pozycji C20 i przyciąganiu cząsteczki przez ujemny potencjał błonowy mitochondrium.

W ostatnim badaniu testowano zdolność salinomycyny i jej pochodnych do przemieszczania się przez dwuwarstwowe błony lipidowe. Mierzono czas relaksacji prądu (τ) – im szybsza relaksacja prądu, tym szybciej dany związek przechodzi przez błonę. Według otrzymanych wyników, pochodna **II-5** przenika przez błony najszybciej spośród testowanych związków (τ < 1 s). Pochodna **II-6** wykazała umiarkowanie szybkie przenikanie (τ_{on} = 2,05 s, τ_{off} = 3,55 s), natomiast koniugat **II-8** okazał się najwolniejszy spośród pochodnych (τ_{on} = 21 s, τ_{off} = 46 s). Salinomycyna sama w sobie nie wykazuje elektrycznej aktywności w błonie lipidowej, co potwierdza, że działa jako jonofor w sposób elektroneutralny.

Wszystkie z wykonanych eksperymentów wskazują na wyjątkowe właściwości jonoforetyczne triazolowej pochodnej **II-5**. Ponadto udowodniono, że analog **II-5** zachowuje aktywność niemodyfikowanego związku, ale działa szybciej i skuteczniej, zwłaszcza w mitochondriach. Związek **II-6** w większości wykonanych testów, nie wykazał silnych właściwości jonoforetycznych, jednakże przenikał przez błony biologicznie umiarkowanie szybko, aczkolwiek znacznie szybciej niż pochodna **II-8**. Słabą aktywność analogu **II-8** może tłumaczyć obecność dodatkowego estrowego wiązania w cząsteczce, jak i długość linkera między cząsteczką antybiotyki a kationem TPP$^+$.

W publikacji III, omówiono syntezę 13 estrów salinomycyny otrzymanych w wyniku modyfikacji grupy karboksylowej w pozycji C1 (Rys. 13) [3]. Pomimo mało obiecujących wyników estrowych pochodnych w publikacji II, zdecydowano poszerzyć bibliotekę tego typu związków, syntezując 11 całkowicie nowych analogów, różniących się długością łańcucha węglowego i rodzajem kationu trifenylofosfoniowego w grupie estrowej.[c]

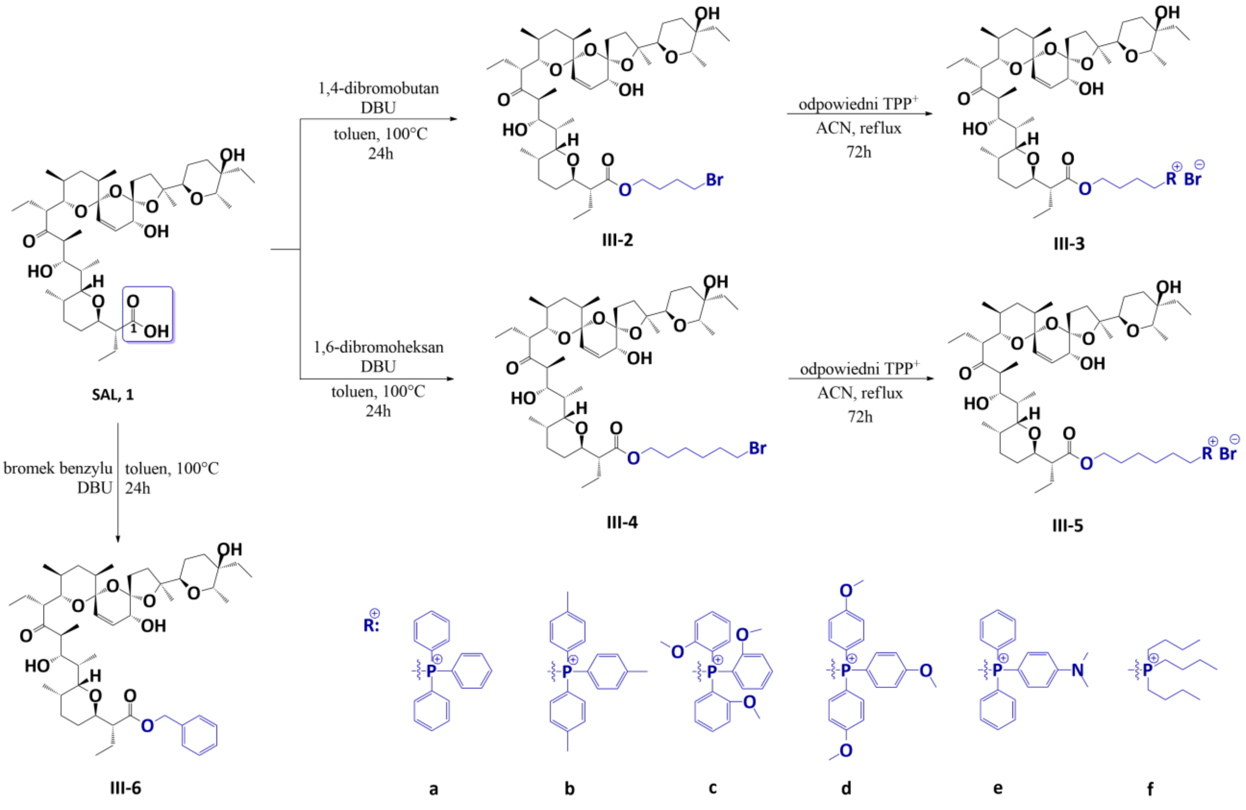

Rysunek 13. Synteza pochodnych salinomycyny z kationami fosfoniowymi.

W celu zweryfikowania czy obecność kationu TPP$^+$ jest kluczowa, zsyntezowano również ester benzylowy **III-6** i wraz z resztą analogów przetestowano jego aktywność biologiczną

---

[c] W tym badaniu ponownie zsyntezowano związek **II-6**, jednakże przy użyciu innej metodologii. Przy omawianiu wyników publikacji III, związek ten będzie występować pod oznaczeniem **III-3a**.

i wpływ na oddychanie komórkowe. Podczas projektowania serii pochodnych wzięto pod uwagę doniesienia literaturowe, które dowodziły, że typ oraz długość linkera łączącego kation TPP^+ z cząsteczką może wpływać na aktywność biologiczną koniugatu [36,37]. Dodatkowo, Rokitskaya ze współpracownikami niejednokrotnie dowiedli, że szybkość penetracji przez błony komórkowe pochodnych TPP^+ jest warunkowana przez rodzaj podstawnika przy pierścieniach aromatycznych kationu TPP^+ [56,57]. Tym samym, w omawianym badaniu zastosowano dwa typy linkerów oraz pięć różnych kationów trifenylofosfoniowych i jeden kation fosfoniowy podstawiony łańcuchami alkilowymi. Dzięki wdrożeniu sześciu różnych ugrupowań możliwe było określenie zależności struktury i aktywności (SAR) pochodnych oraz zbadanie, w jaki sposób wpływa to na zdolność przenikania przez błony biologiczne.

Estry salinomycyny otrzymano w wyniku dwuetapowej syntezy. Związki **III-2**, **III-4** i **III-6** zsyntezowano w reakcji salinomycyny z odpowiednim bromkiem w obecności mocnej zasady 1,8-diazabicyklo[5.4.0]undek-7-enu (DBU) [58]. Następnie, pochodne **III-2** i **III-4** zostały poddane reakcji substytucji S_N2, używając odpowiedniej fosfiny. Wszystkie produkty końcowe zostały oczyszczone za pomocą systemu CombiFlash®Rf$^+$ (chloroform/aceton, wzrastający gradient stężeń) sprzężonego z detektorem rozproszenia światła, ELS (ang. *Evaporative Light Scattering Detector*) i spektrometrią masową ESI.

Aktywność przeciwproliferacyjna salinomycyny i jej pochodnych została przebadana w testach *in vitro* na pięciu liniach ludzkich komórek nowotworowych: gruczolaka jelita grubego (SW480), gruczolaka jelita grubego z przerzutami (SW620), raka prostaty (PC3), raka piersi (MDA-MB-231) oraz niedrobnokomórkowego raka płuc (A549). Dodatkowo, w celu zbadania toksyczności badanych związków użyto dwóch zdrowych linii komórkowych: ludzkich keratynocytów (HaCaT) oraz fibroblastów płuc chomika chińskiego (V79). Aktywność cytotoksyczną określono przy użyciu testu kolorymetrycznego z bromkiem 3-[4,5-dimetylotiazol-2-yl]-2,5-difenylotetrazoliowym (MTT), a wyniki testów wyrażono jako stężenia hamujące wzrost 50% badanej populacji komórek (IC_{50}) [59]. Jako związek referencyjny użyto doksorubicynę (DOX), która jest szeroko stosowanym lekiem w chemioterapii nowotworów. W Tabeli 2 zestawiono wyniki wybranych pochodnych, niemodyfikowanego antybiotyku i doksorubicyny.

Z wyjątkiem linii PC3, pochodne salinomycyny sprzężone z kationem TPP^+ wykazywały wysoką aktywność cytotoksyczną wobec komórek nowotworowych, z wartościami stężenia IC_{50} poniżej 1 µM. Zdecydowana większość analogów TPP^+ wykazała silniejsze działanie przeciwproliferacyjne niż niemodyfikowana salinomycyna.

Ponadto pochodne **III-3a** i **III-3e** okazały się aktywniejsze wobec komórek SW620 i MDA-MB-231 niż sama doksoroubicyna.

Tabela 2. Cytotoksyczność (IC_{50}, µM) badanych związków.

	Linie komórek nowotworowych					**Zdrowe komórki**	
	SW480	**SW620**	**PC3**	**MDA-MB-231**	**A549**	**HaCaT**	**V79**
SAL, 1	1,36 ± 0,01	1,81 ± 0,08	3,00 ± 0,34	1,22 ± 0,19	1,86 ± 0,04	0,80 ± 0,19	1,44 ± 0,33
III-3a	0,39 ± 0,15	0,14 ± 0,01	1,35 ± 0,19	0,74 ± 0,01	0,67 ± 0,07	1,23 ± 0,02	0,13 ± 0,03
III-3b	0,44 ± 0,09	0,50 ± 0,04	2,21 ± 1,77	0,83 ± 0,17	0,81 ± 0,05	1,02 ± 0,33	3,77 ± 0,24
III-3e	0,57 ± 0,13	0,11 ± 0,05	2,52 ± 1,27	0,78 ± 0,17	0,75 ± 0,11	1,28 ± 0,08	0,37 ± 0,10
III-3f	0,49 ± 0,09	0,52 ± 0,05	1,45 ± 0,31	0,90 ± 0,09	0,86 ± 0,05	0,70 ± 0,12	0,59 ± 0,01
III-5a	0,71 ± 0,07	2,57 ± 0,45	1,85 ± 0,11	2,65 ± 1,15	0,72 ± 0,17	0,78 ± 0,17	0,63 ± 0,06
III-5b	0,61 ± 0,04	0,72 ± 0,08	1,58 ± 0,19	0,83 ± 0,27	0,98 ± 0,01	1,05 ± 0,27	0,67 ± 0,09
III-5e	0,58 ± 0,09	0,71 ± 0,01	1,47 ± 0,26	0,88 ± 0,01	0,85 ± 0,05	0,71 ± 0,05	0,60 ± 0,11
III-5f	0,50 ± 0,09	0,67 ± 0,14	2,89 ± 0,17	1,02 ± 0,04	1,05 ± 0,21	0,62 ± 0,06	0,65 ± 0,07
III-6	3,48 ± 0,20	7,77 ± 0,45	8,79 ± 0,20	16,54 ± 2,82	7,52 ± 1,52	8,00 ± 1,36	5,83 ± 1,46
DOX	0,29 ± 0,08	0,31 ± 0,08	0,59 ± 0,02	0,83 ± 0,03	0,63 ± 0,20	0,29 ± 0,01	2,01 ± 0,03

Aby określić selektywność otrzymanych związków, obliczono również współczynnik selektywności SI (ang. *selectivity index*). SI jest miarą umożliwiającą weryfikację czy badany związek potrafi selektywnie atakować komórki nowotworowe, bez wpływu na zdrowe komórki. Im wyższa wartość indeksu SI, tym lepsza selektywność i potencjał działania wobec komórek nowotworowych. Przyjmuje się, że związki o wartości $SI \geq 1$ charakteryzują się niską toksycznością, natomiast te, których wartość wskaźnika $SI > 3$, są uznawane za wysoce selektywne. W Tabeli 3 zestawiono wartości SI dla wybranych związków. Kolorem czerwonym zaznaczono wartości, które świadczą o wysokiej selektywności związków **III-3a**, **III-3b** i **III-3e**. Warto dodać, że dla większości koniugatów SAL-TPP$^+$, wartość współczynnika SI była wyższa niż dla estru benzylowego **III-6**, salinomycyny i doksorubicyny.

Tabela 3. Wartości indeksu selektywności (SI).

	HaCaT					**V79**				
	SW480	SW620	PC3	MDA-MB-231	A549	SW480	SW620	PC3	MDA-MB-231	A549
SAL, 1	0,6	0,4	0,3	0,66	0,4	1,1	0,8	0,5	1,2	0,8
III-3a	**3,2**	**8,8**	0,9	1,7	1,8	0,3	0,9	0,1	0,2	0,2
III-3b	2,3	2,0	0,5	1,2	1,3	**8,6**	**7,5**	1,7	**4,5**	**4,7**
III-3e	2,2	**11,6**	0,5	1,6	1,7	0,6	3,4	0,1	0,5	0,5
III-3f	1,4	1,3	0,5	0,8	0,8	1,2	1,1	0,4	0,7	0,7
III-5a	1,1	0,3	0,4	0,3	1,1	0,9	0,2	0,3	0,2	0,9
III-5b	1,7	1,5	0,7	1,3	1,1	1,1	0,9	0,4	0,8	0,7
III-5e	1,2	1,0	0,5	0,8	0,8	1,0	0,8	0,4	0,7	0,7
III-5f	1,2	0,9	0,2	0,6	0,6	1,3	1,0	0,2	0,6	0,6
III-6	2,3	1,0	0,9	0,5	1,1	1,7	0,8	0,7	0,3	0,8
DOX	1,0	0,9	0,5	0,3	0,46	6,9	6,5	3,4	2,4	3,2

Kolejna seria testów biologicznych była wykonana z użyciem salinomycyny i jej koniugatów **III-3a**, **III-3f** oraz estru benzylowego **III-6**.

Przebadano wpływ wybranych związków na mitochondria komórek nowotworu płuc A549 i nowotworu piersi MDA-MB-231. Do testów wykorzystano dwa rodzaje barwników: MitoTracker Green FM (MTGreen) i MitoTracker Red CMX Ros (MTRed), które są stosowane do oceny zarówno masy mitochondriów, jak i ich funkcjonalności. W badaniu mierzono średnią intensywność fluorescencji, MFI (ang. *mean fluorescence intensity*). W przypadku barwnika MTGreen, pod wpływem pochodnych **III-3a** i **III-3f** odnotowano nawet 8-krotny wzrost intensywności fluorescencji w porównaniu do próby kontrolnej. Pochodne **III-3a** i **III-3f** wywoływały istotny wzrost masy mitochondriów, co może wynikać z intensywnej fizji mitochondrialnej, czyli fragmentacji mitochondriów. Wzrost intensywności fluorescencji zaobserwowano również stosując barwnik MTRed, co może wskazywać na wzmożoną aktywność mitochondriów pod wpływem analogów **III-3a** i **III-3f**. Salinomycyna i związek **III-6** nie wywoływały żadnych istotnych zmian w intensywności fluorescencji, co potwierdzałoby, że obecność ugrupowania TPP$^+$ gwarantuje zdolność do wpływania na mitochondria i zakłócania funkcji mitochondrialnych.

Następnym krokiem była ocena oddziaływania pochodnych **III-3a**, **III-3f**, **III-6** i niemodyfikowanego antybiotyku na cykl komórkowy oraz indukcję apoptozy w komórkach nowotworowych. Wykazano, że koniugaty z TPP^+ hamują cykl komórkowy w fazie G0/G1 w obu badanych liniach komórkowych (A549 i MDA-MB-231), natomiast salinomycyna wykazuje znaczące działanie przeciwproliferacyjne tylko w przypadku linii komórkowej nowotworu piersi. Dodatkowo, udowodniono, że tylko pochodne **III-3a** i **III-3f** skutecznie indukowały apoptozę. Pod wpływem pochodnej **III-3a**, zaobserwowano 35-krotny wzrost liczby komórek w trakcie apoptozy w porównaniu do próby kontrolnej. Testy wykazały, że obie pochodne SAL-TPP^+ hamują rozwój komórek nowotworowych poprzez promowanie apoptozy i zakłócanie regulacji cyklu komórkowego, podczas gdy salinomycyna i ester benzylowy **III-6** wykazały niższą aktywność przeciwnowotworową.

Test JC-10, który umożliwia zbadanie wpływu na potencjał błony mitochondrialnej, MMP (ang. *mitochondrial membrane potential*) również jest dobrą metodą na określenie funkcjonalności mitochondriów pod wpływem testowanych związków. Udowodniono, że pochodne **III-3a** i **III-3f** wywoływały znaczny spadek potencjału błony mitochondrialnej w komórkach nowotworowych, co silnie wiąże się z inicjowaniem apoptozy. Analogi TPP^+ w odróżnieniu od salinomycyny i związku **III-6**, skutecznie destabilizowały funkcjonalność mitochondriów. Zaobserwowano także, że mitochondria komórek nowotworu piersi były znacznie bardziej podatne na działanie związków **III-3a** i **III-3f** niż w przypadku nowotworu płuc. Uzyskane wyniki świadczą, że celowanie i zaburzenie potencjału błony mitochondrialnej może być skuteczną strategią terapeutyczną.

Dodatkowo przeprowadzono testy na obecność reaktywnych form tlenu, ROS (ang. *reactive oxygen species*) w komórkach nowotworowych linii A549 i MDA-MB-231. Badania dowiodły, że koniugaty **III-3a** i **III-3f** zwiększają produkcję reaktywnych form tlenu przez komórki nowotworowe w obu liniach komórkowych (szczególnie **III-3a** w komórkach nowotworu piersi), podczas gdy salinomycyna i ester benzylowy **III-6** wywoływały znikomy wzrost ROS. Jako że wysoki poziom ROS może doprowadzić do uszkodzenia DNA i błony mitochondrialnej, prowadząc do śmierci komórki, otrzymane wyniki potwierdzają aktywność przeciwnowotworową zsyntezowanych pochodnych TPP^+.

W ramach badań nad aktywnością biologiczną, wykonano również testy *in vitro* sprawdzające właściwości przeciwbakteryjne. W badaniu wykorzystano sześć szczepów bakterii Gram-dodatnich i dwa szczepy bakterii Gram-ujemnych oraz cyprofloksacynę jako lek referencyjny. Mimo że większa część koniugatów wykazała wyższą aktywność przeciw bakteriom Gram-dodatnim niż modelowy ester benzylowy **III-6**, żaden z otrzymanych analogów TPP$^+$ nie wykazał wyższej aktywności przeciwbakteryjnej niż niemodyfikowana salinomycyna i cyprofloksacyna. Wszystkie pochodne były nieaktywne przeciw bakteriom Gram-ujemnym, podobnie jak salinomycyna.

Kolejna część badania składała się z dwóch testów biofizycznych. W pierwszym z nich przeanalizowano zmiany szybkości oddychania komórkowego w komórkach nowotworu płuc (A549) wywoływanych pod wpływem pochodnych **III-3a**, **III-3b**, **III-3e**, **III-3f**, **III-6** i salinomycyny. Eksperyment wykonano za pomocą wysokorozdzielczego respirometru tlenowego, mierzącego tempo zużycia tlenu przez komórki. Test wykazał, że koniugaty **III-3a**, **III-3b** i **III-3e** zwiększały tempo oddychania nawet 2,5-krotnie przy stężeniu równym 1 μM, jednakże przy wyższych stężeniach (≥10 μM) prowadziły do spadku szybkości oddychania, co wynikało prawdopodobnie z destabilizacji mitochondriów. Ponadto potwierdzono, że salinomycyna i ester benzylowy **III-6** nie wpływają na tempo oddychania komórkowego, a pochodna **III-3f** powoduje niewielki wzrost zużycia tlenu. Uzyskane wyniki świadczą o zaburzeniu funkcjonalności mitochondriów przez pochodne **III-3a**, **III-3b** i **III-3e** co w konsekwencji indukuje większe zużycie tlenu przez komórki.

W drugim eksperymencie wykorzystano technikę czarnych błon lipidowych w celu przebadania zdolności elektrofizjologicznych pochodnych TPP$^+$ i niemodyfikowanego antybiotyku [60,61]. Sztucznie wygenerowana błona lipidowa jest umieszczona między dwoma roztworami elektrolitów, w których mierzone są zmiany potencjału elektrycznego i przepływ prądu powstający pod wpływem badanych związków. W badaniu wykazano, że pochodne **III-3a**, **III-3b** i **III-3e** indukowały przepływ prądu przez błonę lipidową, a związek **III-3b** generował 2,5-krotnie większy przepływ prądu przy stężeniu 10 mM niż związek **III-3a**. Salinomycyna nie wpływała na zmianę przepływu prądu w całym zakresie stosowanych stężeń, co wynika z elektroneutralnego transportu. Warto dodać, że przepływ prądu był płynny i jednostajny, mimo że nie zaobserwowano tworzenia kanałów jonowych wewnątrz błony, umożliwiających przepływ jonów. Zatem, otrzymane wyniki świadczą o tym, że obecność kationu TPP$^+$ w cząsteczce gwarantuje lepszą przepuszczalność błon, w konsekwencji umożliwiając płynny i efektywniejszy przepływ jonów.

7. Podsumowanie

- Dokonano dokładnej analizy reakcji rozkładu salinomycyny w środowisku kwaśnym.
- Za pomocą technik krystalograficznych (XDR), spektrometrycznych (ESI-MS), spektroskopowych (FT-IR, NMR, 2DNMR) potwierdzono strukturę produktu rozkładu **I-2** i jego soli potasowej **I-2-K**.
- Wykazano, że struktura związku **I-2** różni się w formie stałej i w formie roztworu w dichlorometanie, podobne obserwacje odnotowano w przypadku struktury **I-2-K**.
- Udowodniono zachowanie zdolności kompleksujących przez zdegradowaną cząsteczkę salinomycyny **I-2**, związek skutecznie koordynuje jony metali jednowartościowych Na^+, K^+ oraz Rb^+ tworząc kompleksy o stechiometrii 1:1 i 2:1.
- Po raz pierwszy otrzymano koniugaty salinomycyny z kationem TPP^+ poprzez modyfikację cząsteczki w pozycji C1 i w pozycji C20.
- Opracowano wieloetapową metodę syntezy triazolowej pochodnej **II-5**, obejmującą etapy: blokowania grupy karboksylowej, reakcji Mitsunobu, reakcji odblokowania grupy karboksylowej i dipolarnej 1,3-cykloaddycji Huisgena.
- Struktury zsyntezowanych koniugatów potwierdzono przy użyciu technik spektrometrycznych (ESI-MS, HR-MS), i spektroskopowych (^{1}H NMR, ^{13}C NMR, ^{31}P NMR).
- Po wielu nieudanych próbach skutecznie zoptymalizowano metodę oczyszczania związków wykorzystując system CombiFlash®Rf+ sprzężony z detektorem rozproszenia światła ELS i spektrometrią masową ESI,
- Nowo otrzymane pochodne **II-5**, **II-6** i **II-8** zostały przebadane pod kątem właściwości jonoforetycznych przy użyciu metod z wykorzystaniem sztucznych i naturalnych błon biologicznych.
- Wykazano, że koniugat **II-5** zachował zdolność do transportowania kationów w poprzek błon biologicznych, w niewielkim stopniu lepiej w porównaniu do niemodyfikowanej salinomycyny.
- Triazolowa pochodna **II-5** przenikała przez błony biologicznie znacznie szybciej niż salinomycyna i analogi **II-6** i **II-8**.

- Poszerzono bibliotekę pochodnych salinomycyny z kationem fosfoniowym TPP^+ przyłączonym w pozycji C1, używając dwóch długości linkera i sześciu typów kationów fosfoniowych,
- Salinomycyna i wszystkie zsyntezowane estry z publikacji III, przebadano w testach *in vitro* wobec pięciu linii ludzkich komórek nowotworowych: gruczolaka jelita grubego (SW480), gruczolaka jelita grubego z przerzutami (SW620), raka prostaty (PC3), raka piersi (MDA-MB-231) oraz niedrobnokomórkowego raka płuc (A549). Wszystkie z pochodnych TPP^+ wykazały większą aktywność przeciwproliferacyjną niż niemodyfikowana salinomycyna i ester benzylowy **III-6**. Analogi **III-3a** i **III-3e** były bardziej aktywne wobec komórek gruczolaka jelita grubego z przerzutami (SW620) i komórek raka piersi (MDA-MB-231) niż doksorubicyna.
- Wyznaczono współczynniki selektywności dla salinomycyny i pochodnych z publikacji III. Były one dla większości pochodnych TPP^+ wyższe niż dla estru benzylowego **III-6**, salinomycyny i doksorubicyny. Analogi **III-3a**, **III-3b** i **III-3e** okazały się wysoce selektywnymi związkami, ich wartości SI wahały się w zakresie 3,2 – 11,6.
- W badaniu wpływu na aktywność mitochondriów przy użyciu barwników MitoTracker wykazano, że pochodne **III-3a** i **III-3f** wykazały zdolność do zakłócania funkcjonalności mitochondriów w komórkach nowotworowych, a ich oddziaływanie na mitochondria były silniejsze niż w przypadku salinomycyny i związku **III-6**.
- Przebadano wpływ wybranych pochodnych na cykl komórkowy i indukowanie apoptozy w komórkach nowotworowych raka piersi i płuc. Wykazano, że analogi **III-3a** i **III-3f** hamują rozwój komórek nowotworowych poprzez promowanie apoptozy i zakłócanie regulacji cyklu komórkowego znacznie skuteczniej niż niemodyfikowany antybiotyk i ester benzylowy **III-6**.
- Udowodniono, że koniugaty **III-3a** i **III-3f** wywołują utratę potencjału błonowego przez mitochondria komórek nowotworowych, co wiąże się z promowaniem apoptozy czego nie zaobserwowano w przypadku związku wyjściowego i **III-6**.
- W testach na obecność reaktywnych form tlenu, wykazano, że pochodne **III-3a** i **III-3f** znacznie zwiększają produkcję ROS, co destabilizuje funkcjonalność komórek.

- Pochodne SAL-TPP$^+$ wykazały aktywność przeciwbakteryjną wobec bakterii Gram-dodatnich znacznie większą niż ester benzylowy **III-6**, jednakże były niewiele mniej aktywne w porównaniu do salinomycyny i cyprofloksacyny.
- Testy badające wpływ na szybkość oddychania komórkowego, dowiodły, że obecność ugrupowania TPP$^+$ jest kluczowa. Zaobserwowano, że pochodne SAL-TPP$^+$ inicjowały większe zużycie tlenu w komórkach raka płuc, zwiększając tempo 2,5-krotnie przy stężeniu równym 1 μM.
- W testach z wykorzystaniem czarnych błon lipidowych udowodniono, że związki TPP$^+$ generują przepływ prądu jonowego przez błonę dwuwarstwową zależnie od dawki, podczas gdy salinomycyna nie wykazała takich właściwości.
- Uzyskane wyniki dowodzą, że racjonalna koniugacja cząsteczki salinomycyny z kationami TPP$^+$ prowadzi do otrzymania aktywnych pochodnych o wysokim potencjale terapeutycznym, a obecność ugrupowania TPP$^+$ warunkuje wpływ na funkcjonalność mitochondriów w komórkach nowotworowych.
- Ponadto lepszą aktywność biologiczną zaobserwowano w przypadku związków z krótszym linkerem, a spośród podstawionych kationów TPP$^+$, szczególnie wysoką aktywność wykazywał koniugat **III-3e** z podstawnikiem dimetyloaminowym.

8. Bibliografia

[1] M. Jędrzejczyk, J. Janczak, A. Huczyński, Molecular structure and spectroscopic studies of the product of acidic degradation of salinomycin and its potassium salt, J. Mol. Struct. 1263 (2022) 133129. https://doi.org/10.1016/j.molstruc.2022.133129.

[2] Y.N. Antonenko, M. Jędrzejczyk, T.I. Rokitskaya, L.S. Khailova, E.A. Kotova, A. Huczyński, Rate of translocation across lipid bilayer of triphenylphosphonium-linked salinomycin derivatives contributes significantly to their K^+/H^+ exchange activity on membranes, Bioelectrochemistry 145 (2022). https://doi.org/10.1016/J.BIOELECHEM.2022.108089.

[3] M. Jędrzejczyk, M. Sulik, M. Mielczarek-Puta, G.Y. Lim, M. Podsiad, J. Hoser, P. Bednarczyk, M. Struga, A. Huczyński, Anticancer activity of salinomycin quaternary phosphonium salts, Eur. J. Med. Chem. 282 (2025) 117055. https://doi.org/10.1016/j.ejmech.2024.117055.

[4] A. Naeem, P. Hu, M. Yang, J. Zhang, Y. Liu, W. Zhu, Q. Zheng, Natural Products as Anticancer Agents: Current Status and Future Perspectives, Molecules 27 (2022) 8367. https://doi.org/10.3390/molecules27238367.

[5] D.A. Dias, S. Urban, U. Roessner, A Historical Overview of Natural Products in Drug Discovery, Metabolites 2 (2012) 303–336. https://doi.org/10.3390/metabo2020303.

[6] A.G. Atanasov, S.B. Zotchev, V.M. Dirsch, I.E. Orhan, M. Banach, J.M. Rollinger, D. Barreca, W. Weckwerth, R. Bauer, E.A. Bayer, M. Majeed, A. Bishayee, V. Bochkov, G.K. Bonn, N. Braidy, F. Bucar, A. Cifuentes, G. D'Onofrio, M. Bodkin, M. Diederich, A.T. Dinkova-Kostova, T. Efferth, K. El Bairi, N. Arkells, T.-P. Fan, B.L. Fiebich, M. Freissmuth, M.I. Georgiev, S. Gibbons, K.M. Godfrey, C.W. Gruber, J. Heer, L.A. Huber, E. Ibanez, A. Kijjoa, A.K. Kiss, A. Lu, F.A. Macias, M.J.S. Miller, A. Mocan, R. Müller, F. Nicoletti, G. Perry, V. Pittalà, L. Rastrelli, M. Ristow, G.L. Russo, A.S. Silva, D. Schuster, H. Sheridan, K. Skalicka-Woźniak, L. Skaltsounis, E. Sobarzo-Sánchez, D.S. Bredt, H. Stuppner, A. Sureda, N.T. Tzvetkov, R.A. Vacca, B.B. Aggarwal, M. Battino, F. Giampieri, M. Wink, J.-L. Wolfender, J. Xiao, A.W.K. Yeung, G. Lizard, M.A. Popp, M. Heinrich, I. Berindan-Neagoe, M. Stadler, M. Daglia, R. Verpoorte, C.T. Supuran, Natural products in drug discovery: advances and opportunities, Nat. Rev. Drug Discov. 20 (2021) 200–216. https://doi.org/10.1038/s41573-020-00114-z.

[7] D.J. Newman, G.M. Cragg, Natural Products as Sources of New Drugs over the Nearly Four Decades from 01/1981 to 09/2019, J. Nat. Prod. 83 (2020) 770–803. https://doi.org/10.1021/acs.jnatprod.9b01285.

[8] Global cancer burden growing, amidst mounting need for services, (n.d.). https://www.who.int/news/item/01-02-2024-global-cancer-burden-growing--amidst-mounting-need-for-services (accessed February 6, 2025).

[9] H. Sung, J. Ferlay, R.L. Siegel, M. Laversanne, I. Soerjomataram, A. Jemal, F. Bray, Global Cancer Statistics 2020: GLOBOCAN Estimates of Incidence and Mortality

Worldwide for 36 Cancers in 185 Countries, CA Cancer J. Clin. 71 (2021) 209–249. https://doi.org/10.3322/caac.21660.

[10] H.-Y. Min, H.-Y. Lee, Molecular targeted therapy for anticancer treatment, Exp. Mol. Med. 54 (2022) 1670–1694. https://doi.org/10.1038/s12276-022-00864-3.

[11] N. McCarthy, Twisting BMI1, Nat. Rev. Cancer 10 (2010) 667–667. https://doi.org/10.1038/nrc2940.

[12] A.H. Partridge, J.G. Elmore, D. Saslow, W. McCaskill-Stevens, S.J. Schnitt, Challenges in ductal carcinoma in situ risk communication and decision-making, CA Cancer J. Clin. 62 (2012) 203–210. https://doi.org/10.3322/caac.21140.

[13] E. Dickens, S. Ahmed, Principles of cancer treatment by chemotherapy, Surgery (Oxford) 36 (2018) 134–138. https://doi.org/10.1016/j.mpsur.2017.12.002.

[14] P.L. Bedard, D.M. Hyman, M.S. Davids, L.L. Siu, Small molecules, big impact: 20 years of targeted therapy in oncology, The Lancet 395 (2020) 1078–1088. https://doi.org/10.1016/S0140-6736(20)30164-1.

[15] L. Zhong, Y. Li, L. Xiong, W. Wang, M. Wu, T. Yuan, W. Yang, C. Tian, Z. Miao, T. Wang, S. Yang, Small molecules in targeted cancer therapy: advances, challenges, and future perspectives, Signal Transduct. Target. Ther. 6 (2021) 201. https://doi.org/10.1038/s41392-021-00572-w.

[16] P.L. Bedard, D.M. Hyman, M.S. Davids, L.L. Siu, Small molecules, big impact: 20 years of targeted therapy in oncology, The Lancet 395 (2020) 1078–1088. https://doi.org/10.1016/S0140-6736(20)30164-1.

[17] D.G. Savage, K.H. Antman, Imatinib Mesylate — A New Oral Targeted Therapy, New England Journal of Medicine 346 (2002) 683–693. https://doi.org/10.1056/NEJMra013339.

[18] M. Qian, B. Zhu, X. Wang, M. Liebman, Drug resistance in ALK-positiveNon-small cell lungcancer patients, Semin. Cell Dev. Biol. 64 (2017) 150–157. https://doi.org/10.1016/j.semcdb.2016.09.016.

[19] A. Huczyński, Polyether ionophores - Promising bioactive molecules for cancer therapy, Bioorg. Med. Chem. Lett. 22 (2012) 7002–7010. https://doi.org/10.1016/j.bmcl.2012.09.046.

[20] Y. MIYAZAKI, M. SHIBUYA, H. SUGAWARA, O. KAWAGUCHI, C. HIROSE, J. NAGATSU, S. ESUMI, Salinomycin, a new polyether antibiotic., J. Antibiot. (Tokyo) 27 (1974) 814–821. https://doi.org/10.7164/antibiotics.27.814.

[21] M. Antoszczak, A comprehensive review of salinomycin derivatives as potent anticancer and anti-CSCs agents, Eur. J. Med. Chem. 166 (2019) 48–64. https://doi.org/10.1016/j.ejmech.2019.01.034.

[22] A. Huczynski, Salinomycin - A New Cancer Drug Candidate, Chem. Biol. Drug Des. 79 (2012) 235–238. https://doi.org/10.1111/j.1747-0285.2011.01287.x.

[23] M. Antoszczak, J. Rutkowski, A. Huczyński, Structure and Biological Activity of Polyether Ionophores and Their Semisynthetic Derivatives, in: Bioactive Natural Products, Wiley, 2014: pp. 107–170. https://doi.org/10.1002/9783527684403.ch6.

[24] D.A. Kevin II, D.A. Meujo, M.T. Hamann, Polyether ionophores: broad-spectrum and promising biologically active molecules for the control of drug-resistant bacteria and parasites, Expert Opin. Drug Discov. 4 (2009) 109–146. https://doi.org/10.1517/17460440802661443.

[25] P.B. Gupta, T.T. Onder, G. Jiang, K. Tao, C. Kuperwasser, R.A. Weinberg, E.S. Lander, Identification of Selective Inhibitors of Cancer Stem Cells by High-Throughput Screening, Cell 138 (2009) 645–659. https://doi.org/10.1016/j.cell.2009.06.034.

[26] X. Chu, W. Tian, J. Ning, G. Xiao, Y. Zhou, Z. Wang, Z. Zhai, G. Tanzhu, J. Yang, R. Zhou, Cancer stem cells: advances in knowledge and implications for cancer therapy, Signal Transduct. Target. Ther. 9 (2024) 170. https://doi.org/10.1038/s41392-024-01851-y.

[27] E. Batlle, H. Clevers, Cancer stem cells revisited, Nat. Med. 23 (2017) 1124–1134. https://doi.org/10.1038/nm.4409.

[28] L. Yang, P. Shi, G. Zhao, J. Xu, W. Peng, J. Zhang, G. Zhang, X. Wang, Z. Dong, F. Chen, H. Cui, Targeting cancer stem cell pathways for cancer therapy, Signal Transduct. Target. Ther. 5 (2020) 8. https://doi.org/10.1038/s41392-020-0110-5.

[29] Enhertu | European Medicines Agency (EMA), (n.d.). https://www.ema.europa.eu/en/medicines/human/EPAR/enhertu (accessed February 5, 2025).

[30] P.S. Oak, F. Kopp, C. Thakur, J.W. Ellwart, U.R. Rapp, A. Ullrich, E. Wagner, P. Knyazev, A. Roidl, Combinatorial treatment of mammospheres with trastuzumab and salinomycin efficiently targets HER2-positive cancer cells and cancer stem cells, Int. J. Cancer 131 (2012) 2808–2819. https://doi.org/10.1002/ijc.27595.

[31] A. Asik, N.P.O. Ay, B.G. Bagca, H.O. Caglar, C. Gunduz, C.B. Avci, Combination of Salinomycin and AZD3463 Reveals Synergistic Effect on Reducing the Viability of T98G Glioblastoma Cells, Anticancer Agents Med. Chem. 20 (2020) 2267–2273. https://doi.org/10.2174/1871520620666200721121517.

[32] A. Huczyński, M. Antoszczak, N. Kleczewska, M. Lewandowska, E. Maj, J. Stefańska, J. Wietrzyk, J. Janczak, L. Celewicz, Synthesis and biological activity of salinomycin conjugates with floxuridine, Eur. J. Med. Chem. 93 (2015) 33–41. https://doi.org/10.1016/j.ejmech.2015.01.045.

[33] M. Antoszczak, M. Sobusiak, E. Maj, J. Wietrzyk, A. Huczyński, Synthesis and antiproliferative activity of new bioconjugates of Salinomycin with amino acid esters, Bioorg. Med. Chem. Lett. 25 (2015) 3511–3514. https://doi.org/10.1016/j.bmcl.2015.06.086.

[34] M. Antoszczak, E. Maj, N. Kleczewska, J. Wietrzyk, L. Celewicz, A. Huczynski, Differences in Antiproliferative Activity Between Salinomycin-AZT Conjugates

Obtained via ‘Click’ and Esterification Reactions, Med. Chem. (Los Angeles) 13 (2017) 127–136. https://doi.org/10.2174/1573406412666160823165522.

[35] I. Skiera, M. Antoszczak, J. Trynda, J. Wietrzyk, P. Boratyński, K. Kacprzak, A. Huczyński, Antiproliferative Activity of Polyether Antibiotic – *Cinchona* Alkaloid Conjugates Obtained *via* Click Chemistry, Chem. Biol. Drug. Des. 86 (2015) 911–917. https://doi.org/10.1111/cbdd.12523.

[36] D. V. Tsyganov, A. V. Samet, E.A. Silyanova, V.I. Ushkarov, A.E. Varakutin, N.B. Chernysheva, R.N. Chuprov-Netochin, A.A. Khomutov, A.S. Volkova, S. V. Leonov, M.N. Semenova, V. V. Semenov, Synthesis and Antiproliferative Activity of Triphenylphosphonium Derivatives of Natural Allylpolyalkoxybenzenes, ACS Omega 7 (2022) 3369–3383. https://doi.org/10.1021/acsomega.1c05515.

[37] J. Zielonka, J. Joseph, A. Sikora, M. Hardy, O. Ouari, J. Vasquez-Vivar, G. Cheng, M. Lopez, B. Kalyanaraman, Mitochondria-Targeted Triphenylphosphonium-Based Compounds: Syntheses, Mechanisms of Action, and Therapeutic and Diagnostic Applications, Chem. Rev. 117 (2017) 10043–10120. https://doi.org/10.1021/acs.chemrev.7b00042.

[38] M.T. Jeena, S. Kim, S. Jin, J.H. Ryu, Recent progress in mitochondria-targeted drug and drug-free agents for cancer therapy, Cancers (Basel) 12 (2020). https://doi.org/10.3390/cancers12010004.

[39] K. Klein, K. He, A.I. Younes, H.B. Barsoumian, D. Chen, T. Ozgen, S. Mosaffa, R.R. Patel, M. Gu, J. Novaes, A. Narayanan, M.A. Cortez, J.W. Welsh, Role of Mitochondria in Cancer Immune Evasion and Potential Therapeutic Approaches, Front. Immunol. 11 (2020). https://doi.org/10.3389/fimmu.2020.573326.

[40] D. Niu, Y. Wu, Z. Lei, M. Zhang, Z. Xie, S. Tang, Lactic acid, a driver of tumor-stroma interactions, Int. Immunopharmacol. 106 (2022) 108597. https://doi.org/10.1016/j.intimp.2022.108597.

[41] M. Millard, J.D. Gallagher, B.Z. Olenyuk, N. Neamati, A selective mitochondrial-targeted chlorambucil with remarkable cytotoxicity in breast and pancreatic cancers, J. Med. Chem. 56 (2013) 9170–9179. https://doi.org/10.1021/jm4012438.

[42] S. Schwarz, C. Kehrenberg, B. Doublet, A. Cloeckaert, Molecular basis of bacterial resistance to chloramphenicol and florfenicol, FEMS Microbiol. Rev. 28 (2004) 519–542. https://doi.org/10.1016/j.femsre.2004.04.001.

[43] T. Li, X. He, W. Tao, R. Zhang, Q. He, H. Gong, Y. Liu, D. Luo, M. Zhang, C. Zou, S.-L. Zhang, Y. He, Development of membrane-targeting TPP+-chloramphenicol conjugates to combat methicillin-resistant staphylococcus aureus (MRSA) infections, Eur. J. Med. Chem. 264 (2024) 115973. https://doi.org/10.1016/j.ejmech.2023.115973.

[44] D.E. Beasley, A.M. Koltz, J.E. Lambert, N. Fierer, R.R. Dunn, The Evolution of Stomach Acidity and Its Relevance to the Human Microbiome, PLoS One 10 (2015) e0134116. https://doi.org/10.1371/journal.pone.0134116.

[45] J.L. Wells, J. Bordner, P. Bowles, J.W. McFarland, Novel degradation products from the treatment of salinomycin and narasin with formic acid, J. Med. Chem. 31 (1988) 274–276. https://doi.org/10.1021/jm00396a045.

[46] C.H. Suresh, G.S. Remya, P.K. Anjalikrishna, Molecular electrostatic potential analysis: A powerful tool to interpret and predict chemical reactivity, WIREs Computational Molecular Science 12 (2022). https://doi.org/10.1002/wcms.1601.

[47] P.R. Griffiths, J.A. de Haseth, Fourier Transform Infrared Spectrometry, Wiley, 2007. https://doi.org/10.1002/047010631X.

[48] J.H. Gross, Mass Spectrometry, Springer Berlin Heidelberg, Berlin, Heidelberg, 2011. https://doi.org/10.1007/978-3-642-10711-5.

[49] M. Antoszczak, K. Popiel, J. Stefańska, J. Wietrzyk, E. Maj, J. Janczak, G. Michalska, B. Brzezinski, A. Huczyński, Synthesis, cytotoxicity and antibacterial activity of new esters of polyether antibiotic - Salinomycin, Eur. J. Med. Chem. 76 (2014) 435–444. https://doi.org/10.1016/j.ejmech.2014.02.031.

[50] M. Sulik, E. Maj, J. Wietrzyk, A. Huczyński, M. Antoszczak, Synthesis and Anticancer Activity of Dimeric Polyether Ionophores, Biomolecules 10 (2020) 1039. https://doi.org/10.3390/biom10071039.

[51] M. Meldal, C.W. Tornøe, Cu-Catalyzed Azide−Alkyne Cycloaddition, Chem. Rev. 108 (2008) 2952–3015. https://doi.org/10.1021/cr0783479.

[52] B. Borgström, X. Huang, M. Pošta, C. Hegardt, S. Oredsson, D. Strand, Synthetic modification of salinomycin: selective O-acylation and biological evaluation, Chemical Communications 49 (2013) 9944. https://doi.org/10.1039/c3cc45983g.

[53] F.P.J.T. Rutjes, ed., Click Chemistry, Georg Thieme Verlag KG, Stuttgart, 2022. https://doi.org/10.1055/b000000077.

[54] C.D. Hein, X.-M. Liu, D. Wang, Click Chemistry, A Powerful Tool for Pharmaceutical Sciences, Pharm. Res. 25 (2008) 2216–2230. https://doi.org/10.1007/s11095-008-9616-1.

[55] A. Managò, L. Leanza, L. Carraretto, N. Sassi, S. Grancara, R. Quintana-Cabrera, V. Trimarco, A. Toninello, L. Scorrano, L. Trentin, G. Semenzato, E. Gulbins, M. Zoratti, I. Szabò, Early effects of the antineoplastic agent salinomycin on mitochondrial function, Cell Death Dis. 6 (2015) e1930–e1930. https://doi.org/10.1038/cddis.2015.263.

[56] T.I. Rokitskaya, V.B. Luzhkov, G.A. Korshunova, V.N. Tashlitsky, Y.N. Antonenko, Effect of methyl and halogen substituents on the transmembrane movement of lipophilic ions, Physical Chemistry Chemical Physics 21 (2019) 23355–23363. https://doi.org/10.1039/C9CP03460A.

[57] T.I. Rokitskaya, R.S. Kirsanov, L.S. Khailova, A.A. Panteleeva, K.G. Lyamzaev, G.A. Korshunova, E.A. Kotova, Y.N. Antonenko, Methylation of Phenyl Rings in Ester-Stabilized Phosphorus Ylides Vastly Enhances Their Protonophoric Activity, ChemBioChem 25 (2024). https://doi.org/10.1002/cbic.202300848.

[58] A. Huczyński, J. Stefańska, P. Przybylski, B. Brzezinski, F. Bartl, Synthesis and antimicrobial properties of Monensin A esters, Bioorg. Med. Chem. Lett. 18 (2008) 2585–2589. https://doi.org/10.1016/j.bmcl.2008.03.038.

[59] F. Denizot, R. Lang, Rapid colorimetric assay for cell growth and survival, J. Immunol. Methods 89 (1986) 271–277. https://doi.org/10.1016/0022-1759(86)90368-6.

[60] J. Hoser, A. Dabrowska, M. Zajac, P. Bednarczyk, Changes in Ion Transport across Biological Membranes Exposed to Particulate Matter, Membranes (Basel) 13 (2023) 763. https://doi.org/10.3390/membranes13090763.

[61] K.U. Prasad, S. Alonso-Romanowski, C.M. Venkatachalam, T.L. Trapane, D.W. Urry, Synthesis, characterization, and black lipid membrane studies of [7-L-Alanine]gramicidin A, Biochemistry 25 (1986) 456–463. https://doi.org/10.1021/bi00350a027.

KOPIE OPUBLIKOWANYCH I POWIĄZANYCH TEMATYCZNIE ARTYKUŁÓW NAUKOWYCH

PUBLIKACJA I
wraz z suplementem

Marta Jędrzejczyk, Jan Janczak, Adam Huczyński

„Molecular structure and spectroscopic studies of the product of acidic degradation of salinomycin and its potassium salt"

Journal of Molecular Structure 1263 (2022) 133129

Journal of Molecular Structure 1263 (2022) 133129

Contents lists available at ScienceDirect

Journal of Molecular Structure

journal homepage: www.elsevier.com/locate/molstr

Molecular structure and spectroscopic studies of the product of acidic degradation of salinomycin and its potassium salt

Marta Jędrzejczyk[a], Jan Janczak[b], Adam Huczyński[a,*]

[a] Department of Medical Chemistry, Faculty of Chemistry, Adam Mickiewicz University, Uniwersytetu Poznańskiego 8, 61-614, Poznań, Poland
[b] Institute of Low Temperature and Structure Research, Polish Academy of Sciences, Okólna 2 str., 50–422, Wrocław, Poland

ARTICLE INFO

Article history:
Received 15 February 2022
Revised 5 April 2022
Accepted 19 April 2022
Available online 21 April 2022

Keywords:
Ionophores
Complexes
Supramolecular structure
Chemical degradation, Natural product

ABSTRACT

Salinomycin (SAL), a monocarboxylic polyether antibiotic isolated from *Streptomyces albus* is widely used in veterinary medicine as a growth promoter and as a supplement in poultry feed to control infection with coccidia. SAL exhibits also potent activity against the proliferation of various cancer cells, including those that display multidrug resistance (MDR), and can precisely kill cancer stem cells (CSCs). The compound **2** – a product of the acidic degradation of SAL has been isolated and structurally characterized by X-ray, FT-IR, NMR, and DFT methods. Additionally, to check the ionophoretic properties of this compound its potassium salt (**2-K**) has been also obtained and the crystal structures of these two compounds as well as their structures in solution were studied in detail. It was found that the structures of **2** and **2-K** salt were different in the solid and in the solution. Using ESI MS method it was demonstrated that that compound **2** was also able to form 1:1 and 2:1 complexes with Na^+, K^+, and Rb^+ cations. For the first time we have demonstrated that the product of salinomycin degradation still shows ionophoretic properties.

1. Introduction

Salinomycin (**SAL –** Scheme 1) is a polyether ionophore antibiotic, isolated from *Streptomyces albus* [1]. Nowadays, **SAL** is commercially used in veterinary medicine as a coccidiostatic agent and a non-hormonal growth promotor. **SAL,** similarly to the other ionophore antibiotics, exhibits a wide spectrum of biological properties, which is due to its ability of coordination of metal cations and transporting them into the cellular environment. For a few decades, much evidence has been collected proving significant biological activity of **SAL** against Gram-positive bacteria, parasites, and fungi [2,3]. Furthermore, the breakthrough in the perception of **SAL** took place in 2009, when Gupta *et al.* identified **SAL** as the most promising chemotherapeutic drug candidate against breast cancer stem cells (CSCs), from among 16,000 bioactive compounds. **SAL** exhibited even 100-fold greater activity than the well-known anticancer drug paclitaxel, which is commonly used in the fight against breast CSCs [4,5].

In 1988, Wells *et al.* studied degradation of **SAL** sodium salt upon treatment with formic acid. As a result, they obtained partially decomposed compounds **1** and **2** (Scheme 1). Compound **2** was modified by formylation and acylation of the furan ring. The results of biological tests showed that the obtained derivatives did not exhibit significant anticoccidial activity [6]. Because salinomycin is widely used in the livestock industry and may enter the environment through landfills with animal waste and agricultural runoff, Sun and co-workers [7] identified also the propensity of salinomycin to undergo acid-catalysed transformation in mildly acidic aquatic systems and characterized in depth the reactions involved.

As yet no scientific group has reported investigation of the crystal structure of **2** and its ability to form complexes with metal cations. Based on our many years of experience with ionophore antibiotics and their derivatives as well as their complexes with metal cations, we have put forward a hypothesis that compound **2** obtained by the acidic degradation of **SAL** is still able to form complexes with metal cations. Therefore, the aim of this study was the characterization of degradation of **SAL**, in different acidic conditions, and investigation of the complex formation of the degradation product. Our studies proved that the product obtained by the acidic degradation of **SAL** can still participate in the complexation of the metal ions and exhibits ionophoretic properties. The molecular structure of **2** has never been examined in detail, therefore, we focused here on the detailed spectroscopic, structural, and spectrometric studies of **2**, its potassium salt in solid-state and in

---

[*] Corresponding author.
E-mail address: adhucz@amu.edu.pl (A. Huczyński).

https://doi.org/10.1016/j.molstruc.2022.133129

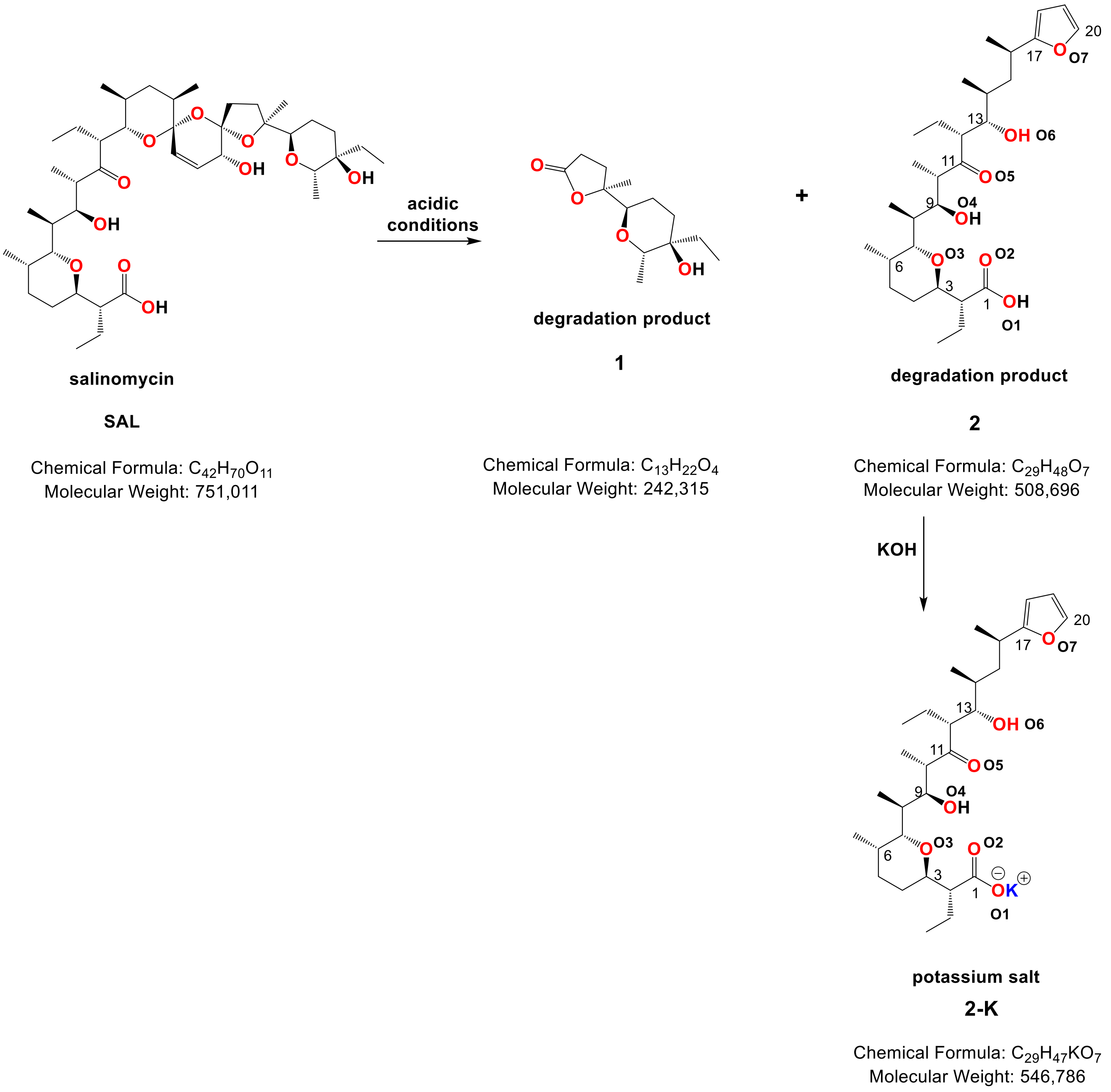

Scheme 1. The acidic degradation of salinomycin.

solution, using various methods such as spectroscopic (FT-IR, ^{1}H and ^{13}C NMR, 2D NMR), spectrometric (ESI MS) and single crystal X-ray diffraction.

2. Experimental

2.1. General

All commercially available reagents and solvents were purchased from two independent sources (Merck (Germany) or Trimen Chemicals S.A. (Poland) and used in the experiments without further purification. Detailed description of general procedures, used equipment (NMR spectrometer, FT-IR spectrophotometer, mass spectrometer), measurement parameters, and software can be found in the Supplementary material. The ^{1}H and ^{13}C NMR signals were assigned using the gradient-enhanced version of the 2D experiments (^{1}H–^{13}C HETCOR, ^{1}H–^{13}C HMBC, and ^{1}H–^{1}H COSY) and are shown in the Supplementary material. The 2D spectra were recorded using standard pulse sequences from Bruker pulse-sequence libraries.

2.2. Acidic degradation of salinomycin – synthesis of 2

Salinomycin sodium salt (SAL-Na) was obtained conveniently by isolation of its sodium salt from the commercially available veterinary premix SACOX® using the procedure described by us previously [8]. The degradation of salinomycin sodium salt (SAL-Na) was conducted using the modified Wells procedure [6].

To a solution of SAL-Na (774 mg, 1 mmol) in 15 mL THF, 12 mL formic acid (88% ACS Reagent, Sigma-Aldrich) was added and the mixture was stirred at 60°C for 30 minutes. The reaction mixture was subsequently diluted with CH_2Cl_2 and washed three times with deionized water. The organic phases of the reaction mixture were combined and concentrated under reduced pressure to give clear oils. The product of degradation (**2**) was easily isolated on silica gel using the CombiFlash®Rf$^+$ (hexane/ethyl acetate, increasing concentration gradient 0 → 50%) using Evaporative Light Scattering Detector (ELSD) as a colourless solid (45% yield). The ^{1}H, ^{13}C NMR as well as 2D NMR spectra of **2** can be found in the Supplementary material (Figs. S1-S2 and Figs. S3-S5, respectively). The parallelepiped colourless X-ray quality single crystals of **2** were grown by slow evaporation from hexane/ethyl acetate solution (252 mg, 50% yield). Mp = 133-136°C.

^{1}H NMR (400 MHz, CD_2Cl_2) δ (ppm) 12.80 (bs, 1H), 7.29 (dd, J = 1.9, 0.8 Hz, 1H), 6.26 (dd, J = 3.2, 1.8 Hz, 1H), 6.04 (dt, J = 3.2, 0.8 Hz, 1H), 4.09 (dd, J = 10.3, 1.4 Hz, 1H), 3.97 (dd, J = 11.0, 5.7 Hz, 1H), 3.74 (dd, J = 9.5, 1.9 Hz, 1H), 3.58 (dd, J = 10.0, 2.1 Hz, 1H), 3.03 – 2.85 (m, 3H), 2.68 (dt, J = 10.5, 2.4 Hz, 1H), 2.21 (ddd, J = 13.6, 10.7, 2.9 Hz, 1H), 2.00 – 1.87 1.70 (m, 6H), 1.60 – 1.35 (m, 5H), 1.33 – 1.23 (m, 2H), 1.22 (d, J = 6.9 Hz, 3H), 0.94 (td, J = 7.1, 4.4 Hz, 6H), 0.84 (dd, J = 6.9, 3.3 Hz, 6H), 0.79 (t, J = 7.4 Hz, 3H), 0.75 (d, J = 6.9 Hz, 3H).

^{13}C NMR (101 MHz, CD_2Cl_2) δ (ppm) 218.5, 178.6, 160.8, 140.8, 110.2, 104.1, 75.2, 74.4, 71.9, 70.7, 57.4, 48.9, 48.4, 40.2, 36.7, 34.1, 31.3, 28.5, 26.4, 22.9, 21.4, 20.1, 16.1, 16.0, 13.2, 12.9, 12.1, 11.1, 7.3.

FT-IR (2 mg/200mg KBr) ν (cm^{-1}) 3500, 3308, 2969, 1706, 1696, 1508,1045, 984, 726.

Elemental analysis for $C_{29}H_{48}O_7$ calculated: C, 68.47; H, 9.51; found: C, 68.24; H, 9.83;

2.3. Synthesis of 2-K salt

A mixture of **2** (153 mg, 0.3 mmol), and potassium hydroxide (20 mg, 0.36 mmol) in methanol was stirred vigorously for 1 h. After this time, the solvent was evaporated under reduced pressure, to dryness. The residue was dissolved in dried acetonitrile. The solution was allowed to evaporate at room temperature. After three weeks, crystals were formed in 45% yield. The crystals suitable for X-ray diffraction analysis were obtained by recrystallization from dried acetonitrile. Mp = 165-168°C. The ^{1}H, ^{13}C NMR as well as 2D NMR, and spectra of **2** can be found in the Supplementary material (Figs. S6-S7 and Figs. S8-S10, respectively).

^{1}H NMR (401 MHz, CD_2Cl_2) δ 7.30 (dd, J = 1.8, 0.8 Hz, 1H), 6.27 (dd, J = 3.2, 1.9 Hz, 1H), 6.08 (dt, J = 3.2, 0.7 Hz, 1H), 4.62 (s, 4H), 4.14 (dd, J = 10.3, 1.6 Hz, 1H), 3.90 (dd, J = 10.9, 4.4 Hz, 1H), 3.74 (ddd, J = 9.8, 8.1, 1.9 Hz, 2H), 3.04 – 2.75 (m, 2H), 2.61 (dt, J = 11.3, 2.0 Hz, 1H), 2.23 (ddd, J = 13.7, 10.9, 2.9 Hz, 1H), 1.90 – 1.74 (m, 2H), 1.57 – 1.35 (m, 3H), 1.31 – 1.17 (m, 4H), 1.00 – 0.87 (m, 6H), 0.82 (dd, J = 9.1, 6.9 Hz, 5H), 0.78 – 0.64 (m, 5H).

^{13}C NMR (151 MHz, CD_2Cl_2) δ 218.3, 182.8, 160.8, 140.8, 110.3, 104.2, 76.3, 73.6, 71.5, 68.9, 57.8, 50.3, 48.4, 40.3, 36.4, 35.0, 31.3, 28.5, 26.8, 23.5, 21.6, 20.4, 16.1, 15.2, 13.2, 12.8, 12.6, 11.3, 7.2.

FT-IR (2 mg/200mg KBr) ν (cm^{-1}) 3355, 2969, 1712, 1696, 1596, 1405.

Elemental analysis for $C_{174}H_{288}K_6O_{45}$ calculated: C, 62.67; H, 8.71; found: C, 62.45; H, 8.95;

2.4. X-ray measurements

The single crystals of the product of salinomycin degradation **2** (acid) and its hydrated potassium salt **2-K** were used for data collection using graphite monochromatic MoKa radiation (λ = 0.71073 Å) and ω-scan technique ($\Delta\omega$ = 1°) in a four circle κ geometry Xcalibur diffractometer with a Sapphire2 area CCD detector. Data collection was made using the CrysAlis CCD program [9]. Integration, scaling of the reflections, correction for Lorenz and polarization effects, and absorption corrections were included using the CrysAlis Red program [9]. The structure was solved by the direct method using SHELXT-2014/7 [10] and refined using SHELXL-2018/3 program [11]. The hydrogen atoms were introduced in their geometrical positions and treated as rigid. Two of the three water molecules in the hydrated crystal of potassium salt **2-K** were ordered and one water molecule was disordered. The H atoms of water could be localized from the difference Fourier maps only for one water molecule (O2) that acts as a donor in the hydrogen bonds, for the other ordered one and for the third disordered one the hydrogen atoms were impossible to localize. The final difference Fourier maps showed no peaks of chemical significance. Details of the data collection parameters, crystallographic data, and final agreement parameters are collected in Table 1. Visualization of the structure was made with the Diamond 3.0 program [12]. The structures have been deposited with the Cambridge Crystallographic Data Centre in the CIF format, no. CCDC 2151164 and 2151165 for **2 and 2-K** salt, respectively. Copies of this information can be obtained free of charge from The Director, CCDC, 12 Union Road, Cambridge, CB2 1EZ, UK (fax: +44 1223 336 033); email: deposit@ccdc.cam.ac.uk or www: http://www.ccdc.cam.ac.uk).

Table 1
Crystal data and refinement parameters for **2** and **2-K**.

	2	2-K
Formula	$C_{29}H_{48}O_7$	$C_{174}H_{288}O_{45}K_6$
Molecular weight	508.67	3334.63
Temperature (K)	100(1)	100(1)
Crystal system	monoclinic	orthorhombic
Space group	P 2_1	P $2_12_12_1$
a (Å)	11.6532(3)	13.5032(5)
b (Å)	9.8185(2)	36.1758(16)
c (Å)	13.8944(3)	37.6916(15)
α (°)	90	90
β (°)	113.419(3)	90
γ (°)	90	90
V (Å^3)	1458.80(6)	18411.9(13)
Z	2	4
F(000)	556	7224
D_{cal} (g·cm^{-1})	1.158	1.203
θ range(°)	2.935 ÷ 29.291	2.437 ÷ 27.999
μ (mm^{-1})	0.081	0.216
Crystal size (mm)	0.306 × 0.242 × 0.213	0.382 × 0.103 × 0.101
T_{min} / T_{max}	0.9876 / 1.000	0.96855 / 1.000
Total / unique / obs refls	63092 / 7470 / 6997	184564 / 43094 / 21698
R_{int}	0.0276	0.0620
R [$F^2>2\sigma(F^2)$][a]	0.0316	0.0787
wR [F^2 all refls][a]	0.0795	0.0996
S	1.028	0.983
$\Delta\rho_{max}$, $\Delta\rho_{min}$ (eÅ^{-3})	+0.238, -0.171	+0.600, -0.323
Flack parameter	0.10(19)	0.04(2)

[a] $R=\Sigma\ ||F_o|-|F_c||/\Sigma F_o$, $wR=\{\Sigma\ [w(F_o^2-F_c^2)^2]/\Sigma wF_o^4\}^{½}$; $w^{-1}=\sigma^2(F_o^2)+(aP)^2+bP$ where $P=(F_o^2+2F_c^2)/3$, $a=0.0449$ and $b=0.2252$ for **2**, and $a=0.0102$ and $b=0$ for **2-K**.

2.5. DFT calculations of the structure of 2 and its anion

Molecular orbital calculations with full geometry optimization of **2** and its deprotonated anion were performed with the Gaussian09 program package [13]. All calculations were carried out at the DFT level using the Becke3-Lee–Yang–Parr correlation functional (B3LYP) [14, 15, 16] with the 6-31G(d,p) basis set assuming the geometry resulting from the X-ray diffraction study as the starting structure. As convergence criteria, the threshold limits of 0.00025 and 0.0012 a.u. were applied for the maximum force and the displacement, respectively. The three-dimensional molecular

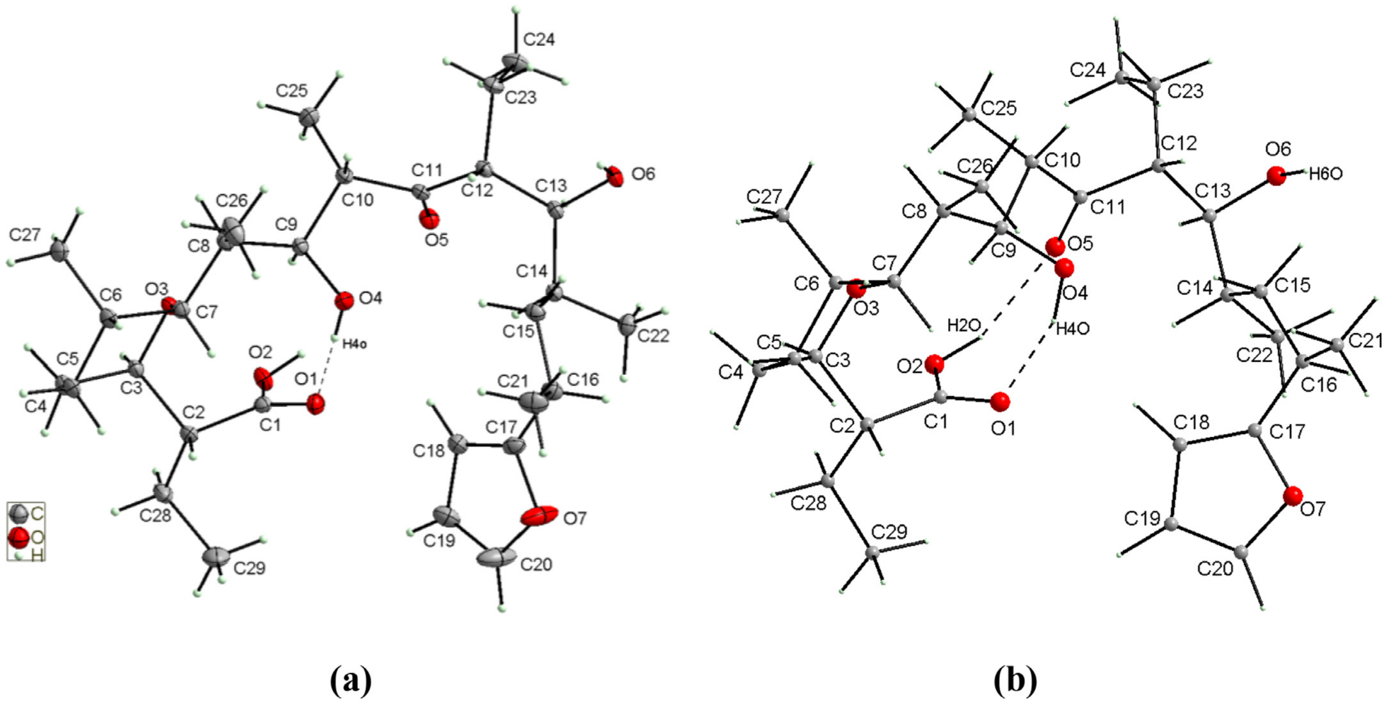

Fig. 1. View of X-ray (a) and DFT optimized (b) molecular structure of **2** with the labelling scheme. Displacement ellipsoids are shown at the 50% probability level, H atoms with arbitrary radii (for X-ray).

electrostatic potential (3D MESP) maps were obtained on the basis of the DFT (B3LYP/6-31G) and optimized. The calculated 3D MESP was mapped onto the total electron density isosurface (0.008 e$Å^{-3}$) for the neutral molecule and its anion.

2.6. Calculations of the structure of 2 and 2-K complex present in solution

The initial models for calculations were built on the basis of the determined here X-ray structure of compound **2** and its potassium salt (**2-K**). Structures of **2** and **2-K** complex were at first optimized by MM3, after assuming appropriate limitations resulting from spectroscopic studies resulting from the type of hydrogen bonds or the cation complexation method, and the energetically most favourable structures were calculated using the semi-empirical MO-G PM6 large molecule geometry algorithm, suitable for calculations of large systems, using SCIGRES package (SCIGRESS version FQ 3.4.4). Finally the structures of the energetically most favourable structures of **2** and **2-K** complex were calculated using the DFT B88-LYP method (SCIGRESS version FQ 3.4.4).

3. Results and discussion

3.1. Chemistry

The degradation of **SAL** leading to compound **2** was realized in three ways, using different acids. The use of phosphoric acid led to very fast complete disintegration of **SAL** and it was impossible to control the reaction. In contrast, the reaction with acetic acid led to very slow degradation of SAL and the main product was formed in a small amount. The most effective among the three reactions proved to be that with formic acid. The degradation of **SAL** using formic acid was efficient and gave the expected product **2** as an amorphous white solid in 50% yield. Then, the crystal of **2** was obtained by slow evaporation from hexane/ethyl acetate solution. The **2-K** salt was obtained from an equimolar methanol solution of **2** and KOH after evaporation of the solvent under reduced pressure. The crystals suitable for X-ray single crystal analysis were obtained by recrystallization from dried acetonitrile.

3.2. Description of the crystal structure of 2 and its potassium salt (2-K salt)

Acidic degradation of salinomycin using formic acid leads to the formation of compound **2**. The polyether compound **2** crystallizes in the non-centrosymmetric space group $P2_1$ of the monoclinic system with two molecules per unit cell. The space group $P2_1$ is chiral since compound **2** contains several asymmetric carbon atoms. The absolute configuration at the asymmetric carbon atoms is: C2 (R), C3 (R), C6 (S), C7 (R), C8 (S), C9 (S), C12 (R), C13 (S), C14 (S) and C16 (R). Thus, the absolute configuration at these atoms is the same as in salinomycin [18], so its acidic degradation does not change the absolute configuration at these atoms. The X-ray selected geometrical parameters together with the optimized DFT are listed in Table 2 and the fully optimized DFT parameters are listed in Table S1 (in SI). The pyran ring exhibits chair conformation and the furan ring is planar. The whole conformation is stabilized by the intramolecular O–H···O hydrogen bond formed between the hydroxyl group and the carboxyl group (Fig. 1).

The optimized DFT parameters (bond lengths and angles) for molecule **2** are comparable with the values obtained from X-ray diffraction, however, the conformation of the whole molecule is slightly different from that following from the X-ray diffraction patterns. The differences are particularly pronounced in torsion angles (Table 2), which is caused by a change in the conformation due to the intramolecular interaction and the formation of an O–H···O hydrogen bond between the carboxyl group and the carbonyl oxygen atom (O5).

Small differences between the X-ray and DFT conformations of the studied molecule result from the fact that the parameters following from the X-ray diffraction patterns refer to the conformation of molecules in crystals, in which interactions between the molecules play a significant role and lead to crystallization and

Table 2
Selected geometrical parameters (Å,°) for molecule **2** together with DFT values.

X-ray	DFT				
C1–O1	1.2146(19)	1.223			
C1–O2	1.3291(19)	1.338			
C3–O3	1.4404(18)	1.429			
C7–O3	1.4442(18)	1.443			
C9–O4	1.4366(17)	1.433			
C11–O5	1.2179(19)	1.227			
C13–O6	1.4442(17)	1.434			
C1–C2–C3–O3	-40.41(16)	-25.41			
C2–C3–O3–C7	-72.95(15)	-74.80			
C3–O3–C7–C8	173.41(11)	-169.83			
C7–C8–C9–C10	167.64(12)	151.92			
C8–C9–C10–C11	171.34(12)	-174.56			
C11–C12–C13–C14	-62.88(16)	-63.41			
C13–C14–C15–C16	-164.78(13)	-162.12			
C15–C16–C17–C18	-16.20(13)	-15.20			
D–H•••A	D–H	H•••A	D•••A	D–H•••A	
O4–H4O•••O1	0.80 (3)	2.07 (3)	2.8245 (18)	157 (2)	(X-ray)
O2–H2O•••O6^{i}	0.85 (2)	1.79 (2)	2.6368 (15)	170 (2)	(X-ray)
O6–H6O•••O5^{ii}	0.84 (2)	1.95 (2)	2.7738 (16)	168 (2)	(X-ray)
O4–H4O•••O1	0.971	1.941	2.834	151.85	(DFT)
O2–H2O•••O5	0.983	2.094	3.031	158.72	(DFT)

Symmetry codes: (i) −x+1, y−1/2, −z+1; (ii) −x+1, y+1/2, −z+1.

specific crystal packing, while the DFT values refer to a single isolated molecule in the gas state, neglecting the interactions between molecules.

The arrangement of the molecules of **2** in the crystal is mainly determined by the intermolecular O–H···O hydrogen bonds, electrostatic interaction, and the van der Waals forces. The molecules related by the screw 2_1 axis are interconnected by O–H···O hydrogen bonds into chains along the *b*-axis (Fig. 2). The van der Waals and dispersive forces are the main ones between the chains and they stabilize the architecture of the crystal. In order to verify the hypothesis that the product obtained as a result of acidic degradation of **SAL** can still participate in the complexation of metal ions and exhibit ionophoretic properties, a three-dimensional electrostatic potential map was calculated and its salt with potassium was synthesized. Geometry optimization calculations of the neutral molecule as well as its deprotonated anion were performed using the DFT method, starting with the geometry of the molecule in the crystal. Selected optimized DFT parameters for the deprotonated anion of **2** are listed in Table 3 and the fully optimized DFT parameters are listed in Table S2 (in SI).

The molecular electrostatic potential map (MESP) is related to the electronic density in the studied molecules and can be a powerful tool for analysing the interactions, both between the molecules of the same compound and provides vital information on the possibility of host-guest complexes formation both in biological systems and in ionophoretic systems [17–19].

The three-dimensional MESP map for **2** and its deprotonated anion mapped onto the total electron density isosurface (0.008 eÅ^{-3}) was obtained using the GaussView 5.0 program (Fig. 3). For the neutral molecule of **2,** the regions of negative MESP are associated with the lone pair of electronegative oxygen atoms, whereas the regions of positive MESP are associated with the electropositive atoms, mainly H atoms. Additionally, lees negative EP are found on both sides of the furan ring (Fig. 3a). For the anionic form of the molecule **2**, as expected, the negative electrostatic potential extends over an area much wider than that for the neutral molecule and also has a more negative magnitude (Fig. 3b). Thus, the obtained 3D MESP maps confirmed the ionophoretic properties of the product of the acidic degradation of salinomycin. Therefore, the ionophoretic properties in relation to potassium cations were checked.

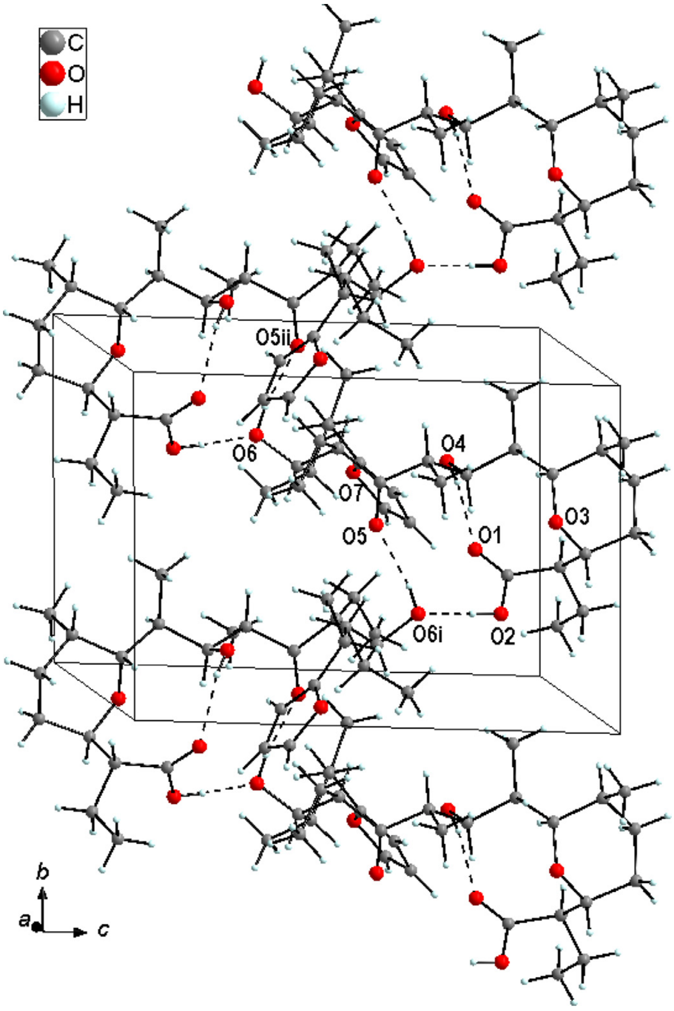

Fig. 2. The arrangement of molecules in a unit cell showing a chain of intermolecular O–H···O hydrogen bonds. (Red dashed lines represent intra and black dashed lines represent intermolecular O–H···O).

Table 3
Selected geometrical parameters (Å, °) for **2-K** together with DFT values of the deprotonated molecule of **2**.

	Anion 2A	2B	2C	2D	2E	2F	DFT
C1–O1	1.257(6)	1.247(6)	1.270(7)	1.265(6)	1.284(6)	1.258(6)	1.276
C1–O2	1.257(6)	1.275(7)	1.269(6)	1.277(6)	1.257(6)	1.273(7)	1.247
C3–O3	1.442(6)	1.457(6)	1.457(6)	1.467(6)	1.461(6)	1.447(6)	1.437
C7–O3	1.448(6)	1.463(6)	1.451(6)	1.450(5)	1.455(6)	1.449(6)	1.434
C9–O4	1.429(6)	1.440(6)	1.435(6)	1.425(6)	1.440(6)	1.448(7)	1.415
C11–O5	1.225(6)	1.224(6)	1.221(7)	1.220(6)	1.217(7)	1.231(6)	1.222
C13–O6	1.442(7)	1.432(6)	1.435(6)	1.425(7)	1.413(6)	1.438(6)	1.443
C1–C2–C3–O3	-56.5(6)	-51.1(6)	-48.7(6)	-52.6(6)	-45.3(6)	-47.5(6)	103.77
C2–C3–O3–C7	-67.4(6)	-71.5(5)	-71.0(5)	-70.2(5)	-71.7(5)	-69.9(6)	-67.55
C3–O3–C7–C8	171.2(4)	171.3(4)	174.2(4)	177.7(4)	178.0(4)	173.2(4)	170.29
C7–C8–C9–O4	-68.1(6)	-62.0(6)	-65.2(6)	-59.5(6)	-58.5(6)	-62.0(6)	107.06
C7–C8–C9–C10	170.2(4)	174.5(5)	175.2(5)	-179.0(5)	-177.8(5)	180.0(5)	163.12
C8–C9–C10–C11	172.9(4)	165.7(5)	-168.4(5)	-170.1(5)	-176.7(5)	177.1(5)	158.61
C9–C10–C11–O5	50.6(7)	64.3(7)	39.4(7)	40.7(8)	40.3(7)	48.2(8)	-73.49
C11–C12–C13–C14	-160.4(5)	-167.3(5)	-159.8(5)	-144.5(5)	-157.0(5)	-149.1(5)	-54.51
C13–C14–C15–C16	162.7(6)	159.4(5)	100.2(6)	-172.4(5)	100.5(6)	176.1(5)	-176.95
C15–C16–C17–C18	-1.0(12)	0.1(10)	-4.9(9)	120.3(8)	-15.1(10)	-94.4(9)	-77.94
Closest contacts K-O							
K1–O1B	2.600(4)	K2–O1D	2.622(4)	K3–O2E	2.611(4)	K4–O2	2.699(4)
K1–O5C	2.633(4)	K2–O5A	2.654(4)	K3–O5F	2.664(4)	K4–O1A	2.724(4)
K1–O1C	2.762(4)	K2–O1A	2.734(4)	K3–O1F	2.830(4)	K4–O5B	2.790(4)
K1–O1E	2.842(4)	K2–O1B	2.876(4)	K3–O1D	2.842(4)	K4–O1C	2.915(4)
K1–O2E	2.889(4)	K2–O2B	2.929(4)	K3–O2D	2.875(4)	K4–O1B	2.982(4)
K1–O2	2.926(3)	K2–O2A	3.387(5)	K3–O4	3.023(15)	K4–O2B	3.163(4)
K1–O1	3.321(4)	K2–O1	2.933(4)	K3–O1	3.075(3)	K4–O1	2.851(3)
			K3–O2F	3.062(4)			
K5–O2A	2.532(4)		K6–O4	2.613(14)			
K5–O5D	2.592(4)		K6–O5E	2.620(4)			
K5–O2F	2.686(4)		K6–O1F	2.673(4)			
K5–O3	2.734(13)		K6–O2C	2.702(4)			
K5–O2D	2.814(4)		K6–O2E	2.782(4)			
K5–O1D	2.869(4)		K6–O1C	3.035(4)			
K5–O4D	3.114(4)		K6–O1E	3.044(4)			

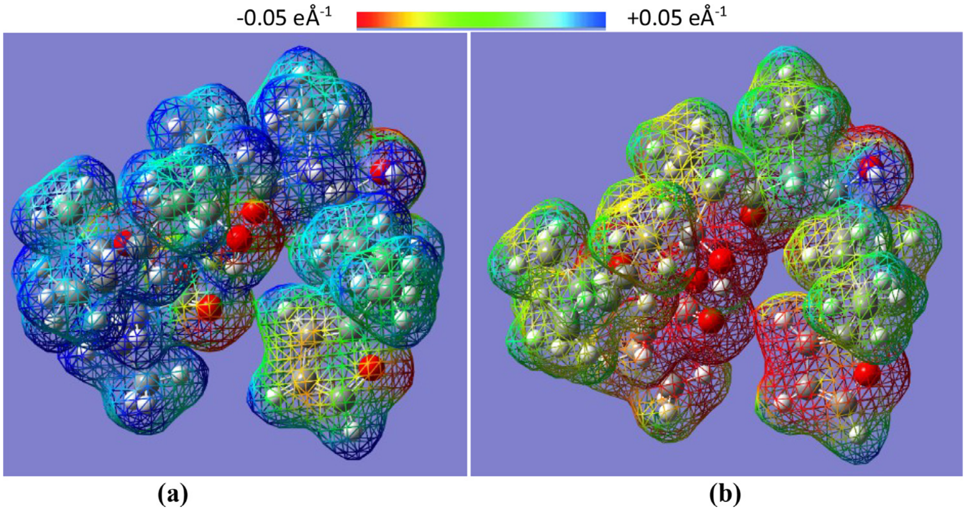

Fig. 3. Three-dimensional molecular electrostatic potential mapped onto the total electron density isosurface (0.008 eÅ^{-3}) for **2** (a) and its deprotonated anion (b). Colour code: −0.05 eÅ^{-1} (red) to +0.05 eÅ^{-1} (blue).

Investigating the ionophoretic properties of the SAL acid degradation product (**2**) in relation to potassium cations, good quality single crystals of potassium cations of **2-K** potassium salt were obtained. The obtained **2-K** potassium salt crystallizes similarly to **2** in the chiral non-centrosymmetric space group $P2_12_12_1$ of the orthorhombic system. The asymmetric **2-K** unit consists of six molecules of potassium salt and three molecules of water, one of them is disordered (O3, O4, and O5 with the occupation factors of 0.40, 0.32, and 0.28, respectively). The structure of the asymmetric unit is illustrated in Fig. 4, where each of the six deprotonated molecules of **2** is marked with a different colour.

Six potassium cations interact with six deprotonated anions and, additionally, with the centrally located water molecule (O1), which interacts with four potassium ions (K1, K2, K3, and K4), forming a supramolecular K_6-complex (Fig. 4). Each anion of the six in the asymmetric unit interacts with the three potassium cations through the oxygen atoms of the dissociated carboxyl group (COO^-) and the oxygen atom (O5) of the carbonyl group. Additionally, two anions (2D and 2E) out of six also interact *via* a hydroxyl group linked to C4 carbon (Fig. S11 in SI).

The interactions of potassium ions with the anions of **2** in the **2-K** crystal imply that the conformation of the above anions cal-

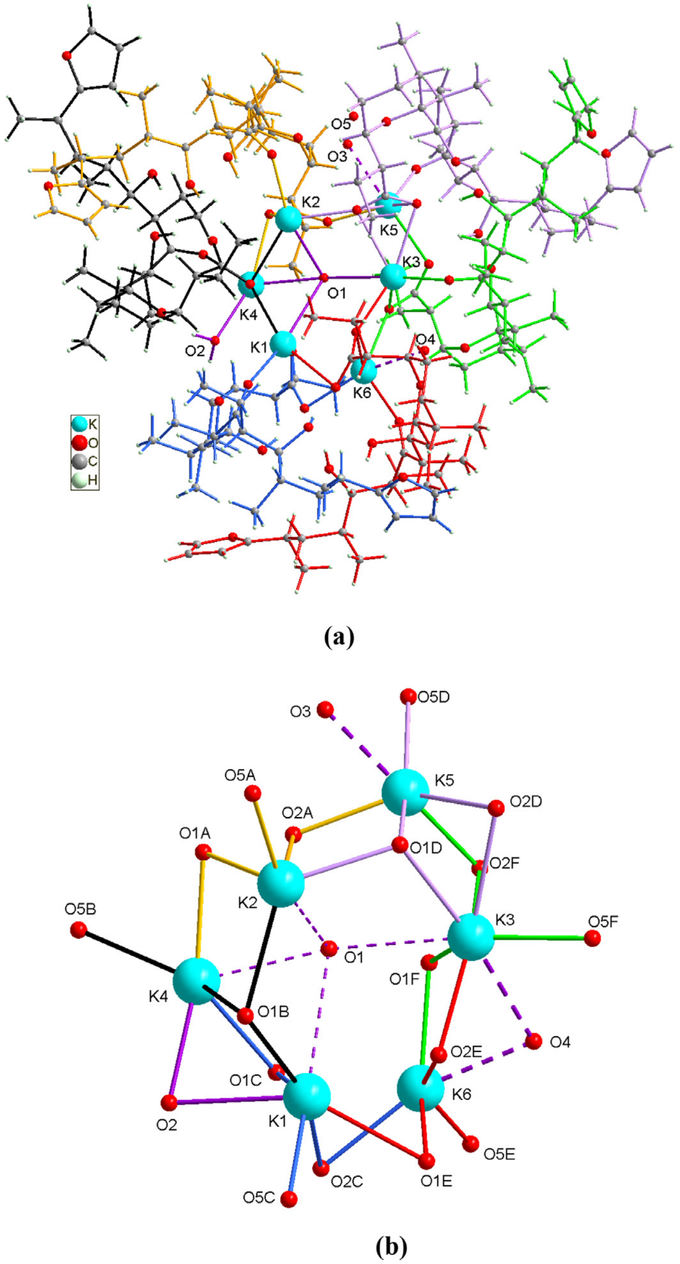

Fig. 4. View of the asymmetric **2-K** salt unit showing the six potassium cations and the six deprotonated anionic forms of the molecule of **2**, each marked with different colour (a) and a view of the nearest oxygen neighbours around K^+ cations (b).

culated by the DFT method is different from that obtained in the crystal.

The conformation of the non-interacting anion (form DFT) is stabilized by the almost linear bond O–H•••O (see Table S2). The surroundings of the potassium cations in the crystal structure are slightly more complicated. The potassium cations K1, K2, K4, K5, and K6 have 7 oxygen atoms with different K-O contacts in their surroundings, while the K3 cation has 8 oxygen atoms in its environment with the K–O contact lengths ranging from 2.611(4) to 3.075(3) Å (Table 3, Fig. 4). Within each supramolecular K_6-complex aggregate, besides the K–O interactions, also the O–H•••O interactions play an important role in the stabilization of the K_6-aggregate (Table 4). The arrangement of the supramolecular K_6-complex aggregates in the crystal is mainly determined by the electrostatic interaction and by the van der Waals forces, *e.g.* H•••H dispersive forces, since there are no directional interactions (like hydrogen bonds) between the aggregates (Figure S13 in SI).

Table 4
Hydrogen-bond geometry (Å,°) for **2-K**.

D–H•••A	D–H	H•••A	D•••A	D–H•••A
O4A–H4A•••O1A	0.84	1.95	2.780 (5)	168
O6A–H6AA•••O2B	0.84	1.99	2.766 (5)	152
O4B–H4B•••O2B	0.84	1.89	2.702 (5)	164
O6B–H6BA•••O4B	0.84	2.08	2.819 (6)	146
O4C–H4C•••O2C	0.84	1.98	2.820 (5)	172
O6C–H6CA•••O1E	0.84	2.02	2.835 (5)	163
O6D–H6DA•••O2F	0.84	2.12	2.928 (5)	161
O6E–H6EA•••O2C	0.84	1.99	2.811 (5)	166
O4F–H4F•••O2F	0.84	1.98	2.803 (5)	168
O6F–H6FA•••O2D	0.84	1.92	2.748 (5)	167
O2–H2G•••O3C	0.99	1.81	2.750 (5)	158
O2–H2H•••O3B	0.99	1.82	2.792 (5)	165

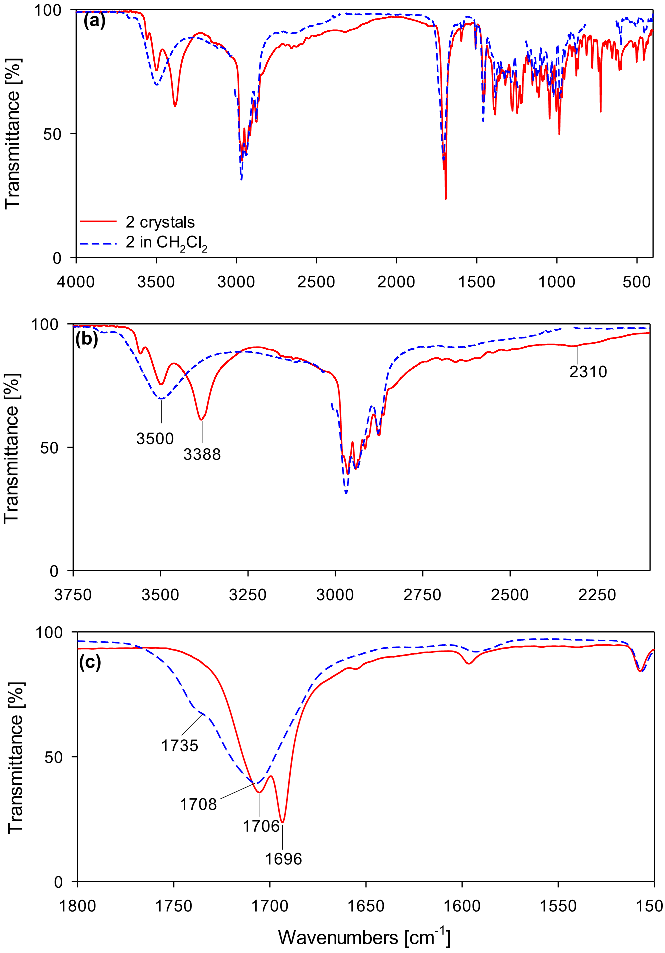

Fig. 5. FT-IR spectra of the crystals of **2** in nujol/fluorolube mulls (–) and **2** in dichloromethane solution (- - -) in the ranges: (a) 4000–400 cm^{-1}, (b) 3750–2100 cm^{-1} and (c) 1800–1500 cm^{-1}.

3.3. Molecular structure of 2 and 2-K salt in solution

The combination of X-ray analysis and FT-IR spectroscopy is a powerful tool to study hydrogen-bonded systems. In this study, this combination was applied to examine **2** and its potassium salt **2-K** in the solid-state and in dichloromethane solution (a hydrophobic solvent mimicking the cell membrane).

A comparison of the IR spectrum of **2** in dichloromethane with that in the solid-state (Fig. 5) shows that in solution the

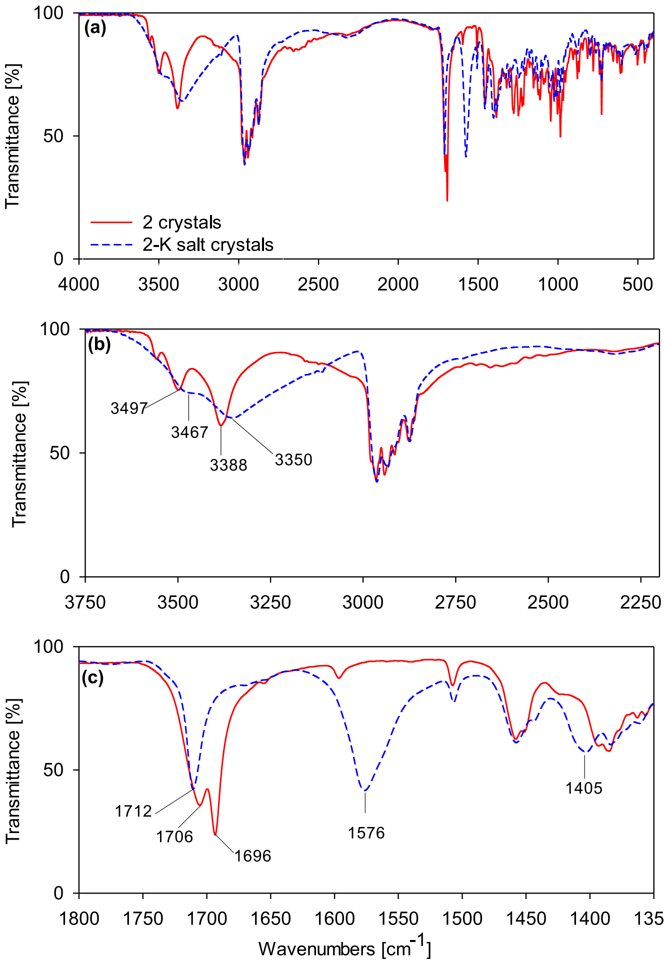

Fig. 6. FT-IR spectra in nujol/fluorolube mulls of crystals of **2** (—) and **2-K** salt crystals **(- - -)** in the ranges: (a) 4000–400 cm^{-1}, (b) 3750–2100 cm^{-1} and (c) 1800–1500 cm^{-1}.

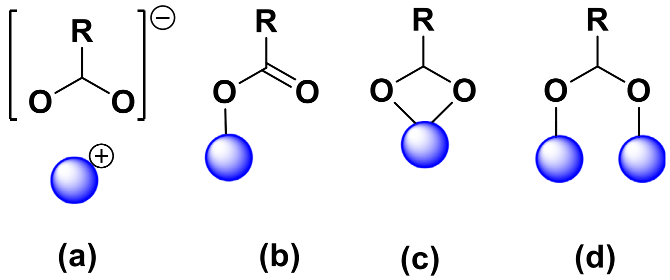

Fig. 7. Structure of metal carboxylates according to the type of metal–ligand interaction: (a) ionic or uncoordinated form, (b) unidentate coordination, (c) bidentate chelating coordination, (d) bidentate bridging coordination.

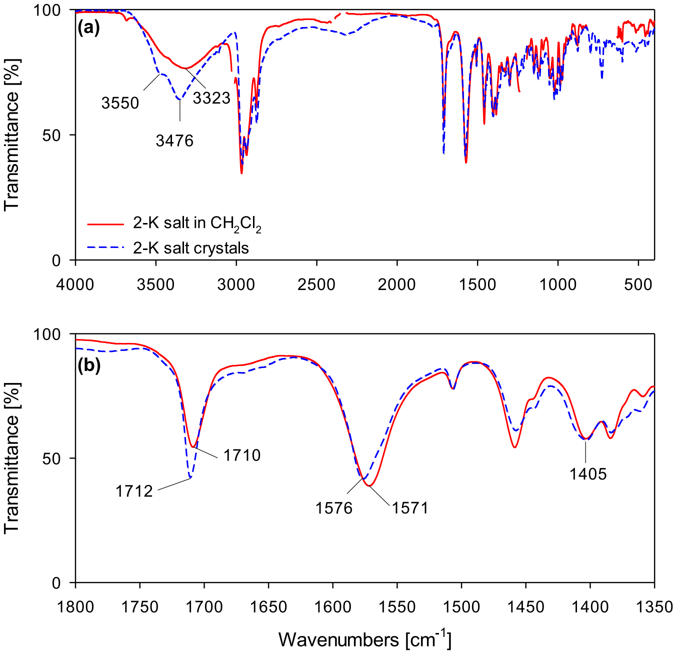

Fig. 8. FT-IR spectra of the crystals of **2-K** salt in nujol/fluorolube mulls (- - -) and **2-K** salt in dichloromethane solution (—): (a) 4000–400 cm^{-1} and (b) 1800–1350 cm^{-1}.

crystal structure of **2** is not conserved. In Fig. 5 the FT-IR spectrum of crystalline **2** compiled from nujol and fluorolube mulls is compared with the corresponding spectrum of **2** (dashed line) in dichloromethane. The regions of the ν(OH) and ν(C=O) vibrations are additionally shown in Fig. 5b and c, in an expanded scale, because the most significant changes are observed in these spectral regions. The strongest intermolecular hydrogen bond between the COOH and OH group (O2—H•••O6^{i}; D···A = 2.64 Å and the D–H···A angle of 170°) is manifested in the spectrum by a broad and low intensity band in the region ca. 3200-2000 cm^{-1}. The spectrum substructure in the range from about 2600 cm^{-1} to 2300 cm^{-1}, can be explained on the basis of the Fermi resonance between the νOH with the overtone 2δOH and skeletal vibrations [20]. The appearance of the shoulder near 2310 cm^{-1} is characteristic of the hydrogen-bonded COOH group. In the CH$_2$Cl$_2$ solution (dashed line, Fig. 5) the range and intensity of this band are decreased, which must be related to the breaking of the intermolecular hydrogen bond. The hydrogen atom of the COOH group is, therefore, not involved in the formation of the strong hydrogen bond in dichloromethane solution.

The IR spectrum of the crystalline **2** shows a complex band with two maxima, at 3500 cm^{-1} and 3338 cm^{-1}, assigned to different inter- and intra-molecular hydrogen bonds within the crystal structure of this compound. These hydrogen bonds and their parameters are shown in Table 2. According to the hydrogen bonds parameters, the first band at 3500 cm^{-1} should be assigned to the ν(OH) vibrations of O4H which is engaged in a weak intramolecular hydrogen bond with the oxygen atom of the carboxylic group (O4—H•••O1; D···A = 2.82; D-H···A = 157°). The second band at 3338 cm^{-1} should be assigned to the ν(OH) vibrations of O4H which is engaged in a relatively stronger intermolecular hydrogen bond between the O6H hydroxyl group and the oxygen atom of the ketone group (O6—H•••O5^{ii}; D···A = 2.77; D-H···A = 168°).

A comparison of the IR spectra of crystalline **2** (solid line), and its CH$_2$Cl$_2$ solution (dashed line) reveals differences between the two structures, especially in the formation of hydrogen bonds. As follows from this comparison, the hydrogen bonds are different in the solid and in the solution. The moderately strong intermolecular hydrogen bond O6—H•••O5^{ii} is broken in the dichloromethane solution, which is confirmed by the vanishing of the band at 3338 cm^{-1} and increasing intensity of the band at 3500 cm^{-1} (dashed line, Fig. 5).

The stretching vibration of carbonyl group ν(C=O) is important in the IR spectrum because of its strong intensity and high sensitivity towards relatively minor changes in its environment, *e.g.* hydrogen bond formation. The C=O stretching bands of the acids are considerably more intensive than the ketone C=O stretching bands. The carbonyl stretching frequency of the hydrogen-bonded COOH group is decreased by 25 cm^{-1} or more than in the non-hydrogen-bonded COOH group. In the spectrum of crystalline **2,** the interaction of the oxygen atom of the COOH group within the intermolec-

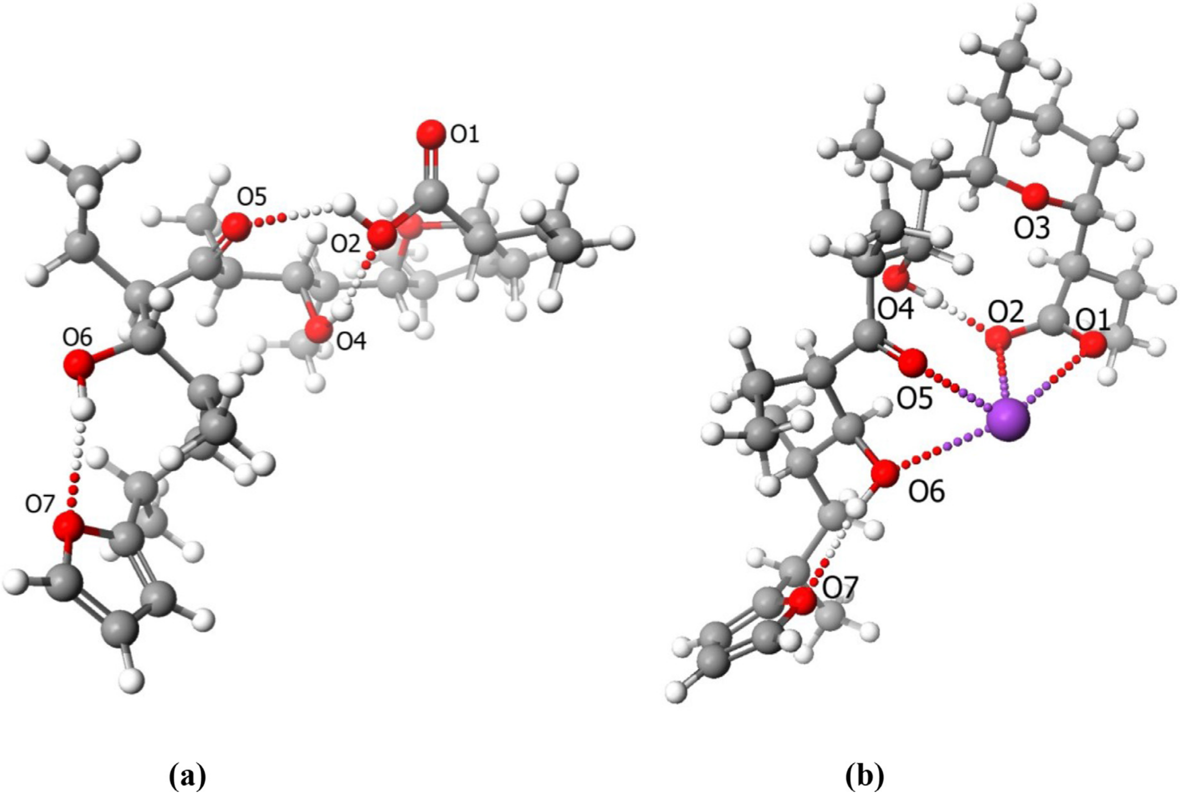

Fig. 9. Structures of compound **2** (a) and **2-K** salt complex (b) calculated by DFT B88-LYP method being in full agreement with the FT-IR and ^{1}H NMR spectra measured in solution.

ular hydrogen bond (O2—H•••O6^{i}) is demonstrated by the band of the ν(C=O) at 1696 cm^{-1}.

The band assigned to the ν(C=O) vibrations of the ketone group is shown at 1706 cm^{-1}. The IR spectrum of **2** in dichloromethane solution (dashed line) is quite different from that in solid-state; besides the band at 1696 cm^{-1}, a new, less intensive band appears at ca. 1735 cm^{-1}. The presence of this band suggests that in the structure in the solution the carbonyl group of COOH is not engaged in the hydrogen bond formation. This observation is in agreement with the ^{1}H NMR data.

The ^{1}H and ^{13}C NMR data of **2** and its potassium salt **2-K**, all in CD_2Cl_2, are shown in Supplementary materials, along with two-dimensional COSY, HETCOR, HMBC spectra (Figures S1-S10). In the ^{1}H NMR spectrum of **2,** the signals assigned to the protons of the O4H and O6H groups overlap at 1.90 ppm. Thus, these OH groups are involved in weak intramolecular hydrogen bonds. The most significantly shifted signal of the OH groups is found in the ^{1}H NMR spectrum of **2** at 12.0 ppm and is assigned to the COOH proton, involved in the weak hydrogen bond.

A simple comparison of the FT-IR spectra of the crystalline **2** (solid line) and its crystalline potassium salt **2-K** (dashed line) (Fig. 6) indicates differences between their structures. The most informative region of the FT-IR spectrum of crystalline **2-K** salt is that from 1800 cm-1 to 1350 cm-1, Fig. 6c. In this spectrum, two bands at 1576 cm^{-1}and 1405 cm^{-1} are assigned to the ν_{as}(COO^{-}) and ν_{as}(COO^{-}) of the carboxylate group. The first band appears as a very strong and generally broad band, while the second band is less intensive. In the spectrum of **2-K** salt (dashed line), the band assigned to the ν(C=O) vibration of the carboxylic group in the spectrum of crystalline **2** at 1696 cm^{-1}, disappears and two new bands assigned to ν_{as}(COO^{-}) and ν_{as}(COO^{-}) appear with maxima at about 1576 cm^{-1}and 1405 cm^{-1}, respectively. The appearance of these new bands together with the disappearance of the broad absorption between 3200-2000 cm^{-1} indicate the formation of the potassium salt of compound **2**.

Extensive IR spectra of carboxylate salts have been studied in the last decades [21, 22]. These studies proved that the carboxylate anion may coordinate with the metal cation in one of the modes presented in Fig 7. It has been postulated that the separation ($\Delta\nu$) between the IR spectra bands assigned to the symmetric and asymmetric carboxylic group vibration, calculated as $\Delta\nu = \nu_{as}(COO^{-}) - \nu_{s}(COO^{-})$, indicates the type of the metal-carboxylate bonding, *i.e.* ionic ($\Delta\nu \sim 200$ cm^{-1}), unidentate ($\Delta\nu >> 200$ cm^{-1}), bidentate ($50 < \Delta\nu < 150$ cm^{-1}) or bridging ($130 < \Delta\nu < 200$ cm^{-1}). Therefore, the separation of the bands ($\Delta\nu$) can be useful for the solution of the carboxylate structures.

In the unit cell of **2-K** crystal, the carboxyl group is deprotonated, whereas the carboxylate group is engaged in the coordination of three K^{+} cations as shown in Fig. 4 and also in the formation of intramolecular hydrogen bond with the O4H group (D···A ~ 2.80; D–H···A ~ 168°) and intermolecular hydrogen bonds with the O6H group (D···A ~ 2.75; D–H···A ~ 167°). The IR spectra of **2-K** salt in dichloromethane and in solid are compared in Fig. 8. A comparison of these spectra shows only small changes in the shape of the band complex in the region close to 3050 cm^{-1} (Fig. 8a) as well as in the region between 1800–1350 cm^{-1} (Fig. 8b). For example, the calculated $\Delta\nu = 171$ cm^{-1} for **2-K** in solid-state and $\Delta\nu = 171$ cm^{-1} for **2-K** in the dichloromethane solution (Fig. 8) indicate that the carboxylate group should be coordinated in a similar mode (bidentate bridging coordination). Thus, in the structure of **2-K** salt in the solution, the carboxylic group should be engaged in the coordination of K^{+} cation and also it should form hydrogen bonds with the OH group (bidentate bridging). In the ^{1}H NNR spectrum, the signals assigned to the other O4H and O6H groups overlap at 4.60 ppm, Fig. S6. Thus, these OH groups are involved in hydrogen bonds of similar, relatively weak strength.

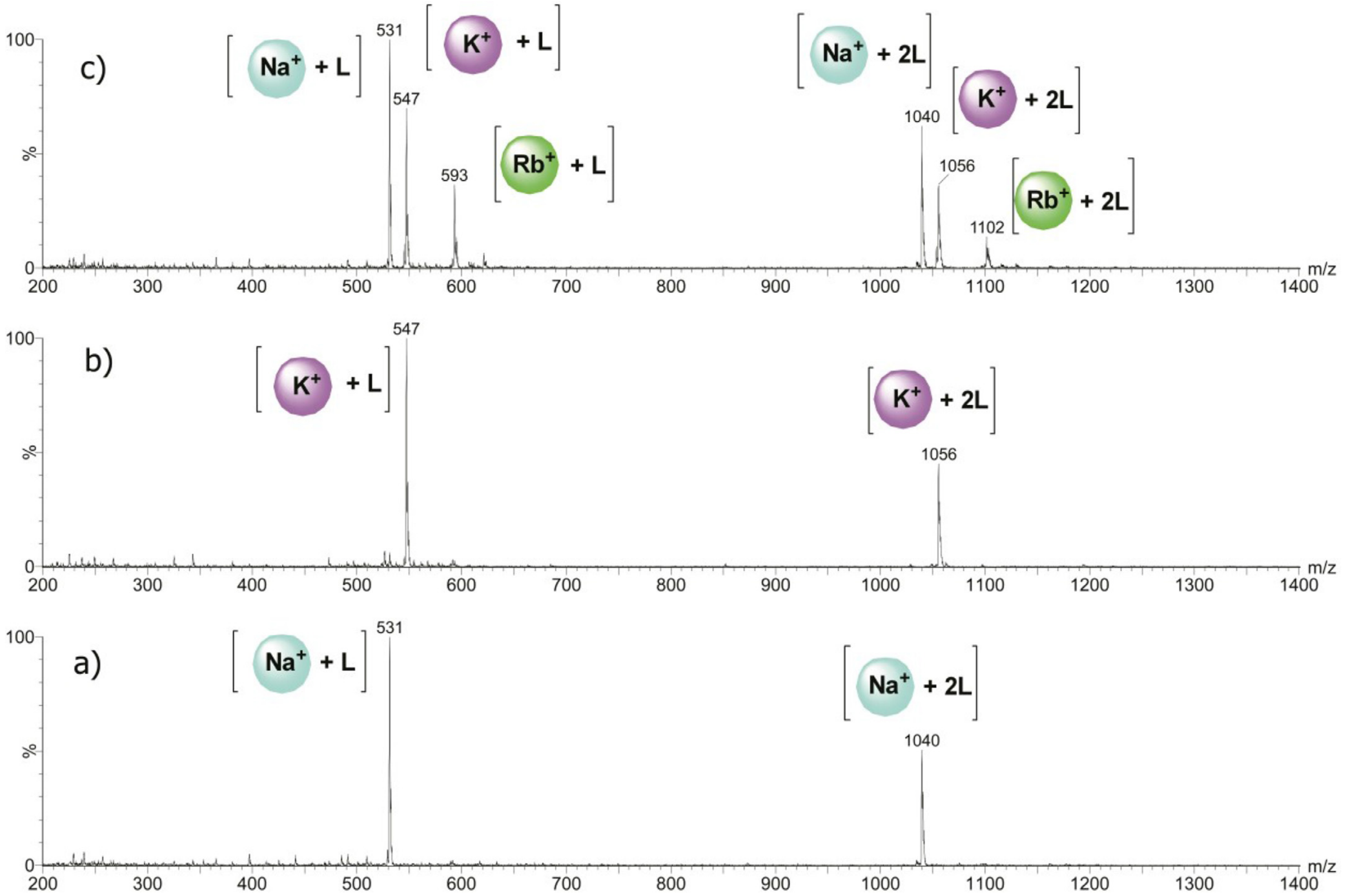

Fig. 10. ESI mass spectrum of a 1:1 mixture of **2** with: (a) $NaClO_4$ (b) $KClO_4$. ESI mass spectrum of a 3:1:1:1 mixture of **2** with $NaClO_4$, $KClO_4$, and $RbClO_4$ (*cv* = 30V) (c).

Table 5
The lengths (Å) and angles (°) of the hydrogen bonds for **2** and its **2-K** complex calculated by B88-LYP DFT method (SCIGRESS version FQ 3.4.4).

	D—H•••A	D—H	H•••A	D•••A	D—H•••A
2	O4—H•••O1	0.984	1.974	2.896	155.10
	O2—H•••O5	0.993	2.246	2.939	125.73
	O6—H•••O7	0.981	2.284	3.137	144.17
2-K	O4—H•••O2	1.006	1.722	2.694	161.12
	O6—H•••O7	0.983	2.334	3.217	149.05

Table 6
The interatomic distances (Å) and partial charges on oxygen atoms of **2-K** complex structures calculated by B88-LYP DFT method (SCIGRESS version FQ 3.4.4).

Coordinating atom			Monovalent cation partial charge
Number	Partial charge	Distance (Å) O → K^+	
O1	-0.486	2.71	+0.638
O2	-0.562	2.77	
O3	-0.381	–	
O4	-0.619	–	
O5	-0.370	2.77	
O6	-0.601	2.85	
O7	-0.256	–	

On the basis of the above discussed X-ray results as well as FT-IR and NMR spectra analysis, the possible structures of **2** and **2-K** complex in solution were calculated by the B88-LYP DFT method. The most favourable structures of **2** and its **2-K** salt are compared in Fig. 9 and Table 5, respectively. The structures of **2** and **2-K** complex calculated by DFT in solution are different from the corresponding ones in the crystals. In the structure of **2** (Fig. 9) the three intramolecular hydrogen bond proton are formed: O4H••• O1, O1H••• O5, and O6H••• O7. The hydrogen bonds existing in this structure are marked by dots. The calculated lengths of these hydrogen bonds are shown in Table 5. The structure with the hydrogen bonds and the parameters of these bonds is in better agreement with the above discussed spectroscopic data.

The most probable structure of **2-K** salt complex calculated by the DFT method, which is in the best agreement with the spectroscopic data, is presented in Fig. 9. The interatomic distances and angles of hydrogen bonds stabilizing the **2-K** structure are collected in Table 5. The calculations indicate the possibility of forming two intramolecular hydrogen bonds, with the O4H and O6–H protons bonded to the oxygen atoms of the carboxylate or furan moiety. According to the parameters of these intramolecular hydrogen bonds, they are very weak. This observation is in very good agreement with the spectroscopic data discussed above. On the other hand, it should be also taken into account that the conformation in solid-state does not always resemble that in solution in which the OH hydroxyl groups are not involved in intermolecular interactions with other molecules but rather make intramolecular hydrogen bonds stabilizing the pseudo-cyclic structure of the ionophore molecules. Additionally, the structure in the solid-state is more complicated because it is hydrated.

The interatomic distances between the oxygen atoms of **2** and the K^+ cation are collected in Table 6. Analysis of these values shows that some oxygen atoms such as O1, O2, O5, and O6 are involved in the coordination of the metal cation, whereas the atoms O3, O4 and O7 play no role in this coordination process. It is also consistent with the spectroscopic data presented above.

3.4. ESI mass spectrometry evidence of the complex formation between 2 and monovalent metal cations

The cation transport by polyether ionophores is attributed to their ability to exchange protons and cations in an electroneutral process [23, 24]. The crystal and spectroscopic data disused above clearly show that the anion of compound **2** forms stable electroneutral complexes with K^+ in the solid-state as well as in the solution. Moreover, the alternative electrogenic mode of cation transport could be also realized by polyether ionophores. In the electrogenic cation transport, the carboxylic group remains protonated (COOH) [24-25]. Therefore, the possibility of forming compound **2** complexes with metal cations was also checked using the positive ion-mode Electrospray Ionization Mass Spectrometry (ESI MS).

The *m/z* data observed in the ESI mass spectra of the complexes formed between $MClO_4$ (M = Na, K and Rb) salts and **2** (acidic form) are shown in Fig. 9. The ESI-MS spectra of **2** with Na^+ and K^+ cations (Fig. 10a and b) show two characteristic signals at m/z of 531 and 547, respectively, proving the formation of the 1:1 ratio host-guest complexes $(L+M)^+$, where L is compound **2.** Another series of signals is observed in the ESI-MS spectra at *m/z* = 1040 and 1056. These peaks are assigned to the 2:1 complex cations $(2L+M)^+$ built from two molecules of compound **2** and one monovalent metal cation.

The ESI spectrum of the mixture of Na^+, K^+, and Rb^+ cations with compound **2** at a concentration of 33% of the equivalent concentration recorded at *cv* =30 V, is shown in Fig 9c. The spectrum shows three characteristic signals at *m/z*=531, 547, and 593 assigned to the 1:1 complexes $(L+M)^+$ and three signals at m/z=1040, 1056, and 1102 assigned to the $(2L + M)^+$ complex species. The intensity of the first group of signals is higher than that of the other group of signals, indicating that the formation of the $(L+M)^+$ complexes is favoured. These results are comparable to the ESI results obtained for the complexes of selected cations by compound **2** (Fig. 9a and b). In both groups of *m/z* signals, the highest intensity is observed of the signal assigned to the complex with Na^+ indicating clearly that compound **2** preferentially forms complexes with this cation. The preference for formation of the $(L+M)^+$ and $(2L + M)^+$ complexes with other cations changes in the following order: $Na^+ > K^+ \gg Rb^+$. ESI-MS also shows that compound **2** did not form complexes with Li^+ and Cs^+, possibly due to too small or too large cation size and mismatch with the hydrophilic interior of compound **2**.

4. Conclusions

Salinomycin (**SAL**), a well-known agricultural antibiotic used mainly to prevent coccidiosis in poultry, exhibits also activities against gram-positive bacteria. Recently, **SAL** has been also identified as a selective inhibitor of human cancer stem cells (CSC) in a variety of cancer types. **SAL** and its derivatives are recognized as very promising anticancer drug candidates due to their activity against various types of human cancer cells. For the first time, compound **2** – a product of the acidic degradation of salinomycin has been obtained in the crystalline form. Detailed spectroscopic, crystallographic, and DFT studies provided the evidence showing that the structure of **2** is different in the solid-state and in dichloromethane solution. The crystal structure contains a neutral molecule **2** and is stabilized by several inter- and intra-hydrogen bonds but in the solution, the characteristic pseudo-cyclic structure of **2** is stabilized exclusively by intramolecular hydrogen bonds. From the chemical point of view, the product of salinomycin decomposition **2** can be still a potential ionophore able to bind metal cation due to the presence of oxygen atoms of various types (carboxylic, ether, hydroxyl) in its structure. Thus, we have obtained for the first time the potassium salt of **2**. The structure of this **2-K** salt has been studied in solid-state and in solution. In the crystal of **2-K** salt, the six K^+ cations interact with six anions of **2** and the centrally located H_2O molecule. Each anion of the six ones in the asymmetric unit interacts with the three K^+ cations through the oxygen atoms of the COO^- group and the oxygen atom of the C=O group. The spectroscopic studies show that in the dichloromethane solution the structure of **2-K** salt is different than that in the solid-state. In the solution, the K^+ cation is surrounded by four oxygen atoms, two from the COO^- group, one from the C=O group and one from the C5-OH group. The pseudo-cyclic structure of this complex is also stabilized by weak intramolecular hydrogen bond between C4OH and the oxygen atom of the carboxylic group. The structures of **2** and **2-K** salt were visualized using the DFT calculations.

The results of ESI mass spectrometry studies have shown that compound **2** is able to form stable complexes with monovalent metal cations such as Na^+, K^+, and Rb^+ with 1:1 and 2:1 ratios. The most preferred complex is formed between **2** and Na^+ cation.

Compound **2** is a lipophilic cation-complexing agent (electroneutral and electrogenic carrier type ionophore) able to form 1:1 and 2:1 host-guest supramolecular complexes with Na^+, K^+, and Rb^+ cations.

Declaration of Competing Interest

The authors declare that they have no known competing financial interests or personal relationships that could have appeared to influence the work reported in this paper.

Supplementary materials

Supplementary material associated with this article can be found, in the online version, at doi:10.1016/j.molstruc.2022.133129.

References

[1] M. Antoszczak, J. Rutkowski, A. Huczyński, Structure and biological activity of polyether ionophores and their semisynthetic derivatives, in: Bioact. Nat. Prod., Wiley-VCH Verlag GmbH & Co. KGaA, Weinheim, Germany, 2015, pp. 107–170, doi:10.1002/9783527684403.ch6.

[2] M. Antoszczak, A. Huczyński, Salinomycin and its derivatives – a new class of multiple-targeted “magic bullets, Eur. J. Med. Chem. 176 (2019) 208–227, doi:10.1016/j.ejmech.2019.05.031.

[3] A. Huczynski, Salinomycin – A New Cancer Drug Candidate, Chem. Bio.l Drug Des. 79 (2012) 235–238, doi:10.1111/j.1747-0285.2011.01287.x.

[4] P.B. Gupta, T.T. Onder, G. Jiang, K. Tao, C. Kuperwasser, R.A. Weinberg, E.S. Lander, Identification of selective inhibitors of cancer stem cells by high-throughput screening, Cell 138 (2009) 645–659, doi:10.1016/j.cell.2009.06.034.

[5] M. Antoszczak, A comprehensive review of salinomycin derivatives as potent anticancer and anti-CSCs agents, Eur. J. Med. Chem. 166 (2019) 48–64, doi:10.1016/J.EJMECH.2019.01.034.

[6] J.L. Wells, J. Bordner, P. Bowles, J.W. McFarland, Novel degradation products from the treatment of salinomycin and narasin with formic acid, J. Med. Chem. 31 (1988) 274–276, doi:10.1021/jm00396a045.

[7] P. Sun, H. Yao, D. Minakata, J.C. Crittenden, S.G. Pavlostathis, C.H. Huang, Acid-catalyzed transformation of ionophore veterinary antibiotics: Reaction mechanism and product implications, Environ. Sci. Technol. 47 (2013) 6781–6789, doi:10.1021/es3044517.

[8] A. Huczyński, J. Janczak, M. Antoszczak, J. Stefańska, B. Brzezinski, FT-IR X-ray, NMR and PM5 structural studies and antibacterial activity of unexpectedly stable salinomycin-benzotriazole intermediate ester, J. Mol. Struct. 1022 (2012) 197–203, doi:10.1016/j.molstruc.2012.05.019.

[9] CrysAlis CCD and CrysAlis Red 1.171.38.43, Rigaku Oxford Diffraction, Oxford, U.K., 2015.

[10] G.M. Sheldrick, SHELXT - integrated space-group and crystal-structure determination, Acta Crystallogr. Sect. A Found. Crystallogr. 71 (2015) 3–8, doi:10.1107/S2053273314026370.

[11] G.M. Sheldrick, Crystal structure refinement with SHELXL, Acta Crystallogr. Sect. C Struct. Chem. 71 (2015) 3–8, doi:10.1107/S2053229614024218.

[12] K. Brandenburg, H. Putz, DIAMOND Version 3.0, Crystal Impact GbR, Bonn, Germany, 2006.
[13] M.J. Frisch, G.W. Trucks, H.B. Schlegel, Gaussian 16, Revision C.01, Gaussian, Inc., Wallin, 2016.
[14] A.D. Becke, Density-functional thermochemistry. IV. A new dynamical correlation functional and implications for exact-exchange mixing, J. Chem. Phys. 104 (1996) 1040–1046, doi:10.1063/1.470829.
[15] C. Lee, W. Yang, R.G. Parr, Development of the Colle-Salvetti correlation-energy formula into a functional of the electron density, Phys. Rev. B. 37 (1988) 785–789, doi:10.1103/PhysRevB.37.785.
[16] R.G. Parr, Y. Weitao, Density-Functional Theory of Atoms and Molecules, Density-Functional Theory Atoms Mol. (1995). doi:10.1093/OSO/9780195092769.001.0001.
[17] P. Politzer, P.R. Laurence, K. Jayasuriya, Molecular electrostatic potentials: an effective tool for the elucidation of biochemical phenomena, Environ. Health Perspect. VOL. 61 (1985) 191–202, doi:10.2307/3430072.
[18] P. Politzer, D.G. Thular (Eds.), Chemical Applications of Atomic and Molecular Electrostatic Potentials, Springer-Verlag, Boston, 1981, doi:10.1007/978-1-4757-9634-6.
[19] J.S. Murray, P. Politzer, J.S. Murray, P. Politzer, The electrostatic potential: an overview, Wiley Interdiscip. Rev. Comput. Mol. Sci. 1 (2) (2011) 153–163 The electrostatic potential: An overview, Wiley Interdiscip. Rev. Comput. Mol. Sci. 1 (2011) 153–163. doi:10.1002/wcms.19.
[20] S. Bratos, H. Ratajczak, P. Viot, Properties of H-bonding in the infrared spectral range, Hydrog. Liq. (1991) 221–235, doi:10.1007/978-94-011-3274-9_18.
[21] G.B. Deacon, R.J. Phillips, Relationships between the carbon-oxygen stretching frequencies of carboxylato complexes and the type of carboxylate coordination, Coord. Chem. Rev. 33 (1980) 227–250, doi:10.1016/S0010-8545(00)80455-5.
[22] C.C.R. Sutton, G. Da Silva, G.V. Franks, Modeling the IR spectra of aqueous metal carboxylate complexes: correlation between bonding geometry and stretching mode wavenumber shifts, Chem. – A Eur. J. 21 (2015) 6801–6805, doi:10.1002/CHEM.201406516.
[23] M. Antoszczak, A medicinal chemistry perspective on salinomycin as a potent anticancer and anti-CSCs agent, Eur. J. Med. Chem. 164 (2019) 366–377, doi:10.1016/J.EJMECH.2018.12.057.
[24] A. Huczyński, J. Janczak, D. Łowicki, B. Brzezinski, Monensin a acid complexes as a model of electrogenic transport of sodium cation, Biochim. Biophys. Acta - Biomembr. 1818 (2012) 2108–2119, doi:10.1016/j.bbamem.2012.04.017.

Molecular structure and spectroscopic studies of the product of acidic degradation of salinomycin and its potassium salt

Marka Jędrzejczyk [a], Jan Janczak [b], Adam Huczyński [a, *]

[a]*Department of Medical Chemistry, Faculty of Chemistry, Adam Mickiewicz University, Uniwersytetu Poznańskiego 8, 61-614, Poznań, Poland*

[b]*Institute of Low Temperature and Structure Research, Polish Academy of Sciences, PO Box 1410, 50–950, Wrocław, Poland*

Supplementary data

Spectroscopic and spectrometric measurements

The ^{1}H and ^{13}C NMR spectra of **2** and **2-K salt** in dichloromethane-d2 were recorded on a Bruker Avance DRX 600 spectrometer or Agilent VNMRS 400 MHz spectrometer. The ^{1}H NMR measurement of **2** and **2-K salt** (0.07 M in dichloromethane-d2) was performed at the operating frequency 600.055 MHz; flip angle, pw = 45°; spectral width, sw = 4500 Hz; acquisition time, at = 2.0 s; relaxation delay, d1 = 1.0 s; number of scans, nt = 64; T = 293.0 K, and using TMS as an internal standard. No window function or zero filling was used. The digital resolution was 0.2 Hz per point. The error in the chemical shift value was 0.01 ppm. The ^{13}C NMR spectrum of **2** and **2-K salt** (0.07 M in dichloromethane-d2) was recorded at the operating frequency 150.899 MHz; flip angle, pw = 60°; spectral width, sw = 19.000 Hz; acquisition time, at = 1.8 s; relaxation delay, d1 = 1.0 s; number of scans, nt = 1024; T = 293.0 K, and using TMS as an internal standard. The line broadening parameters were 0.5 or 1.0 Hz. The error in the chemical shift value was 0.1 ppm. For Agilent VNMRS 400 MHz spectrometer: the operating frequencies for ^{1}H measurements was 402.65 MHz; pulse width corresponding to the flip angle of 45^{0}; spectral width swh = 8064.5 Hz; acquisition time at= 5 sec; relaxation delay d_1=1.0 s; T = 293.0 K, TMS was used as the internal standard. No window function or zero filling were used. Digital resolution was 0.2 Hz/point. ^{13}C NMR spectra were recorded at the operating frequency 101.26 MHz; pulse width corresponding to the flip angle of 60^{0}; sw = 26041.7 Hz; at = 1.3 s; d_1=1.0 s; T = 293.0 K and TMS as the internal standard. Line broadening parameters of 0.5 or 1 Hz were applied.

All spectra were locked to deuterium resonance of dichloromethane-d2. The ^{1}H and ^{13}C NMR signals of **2** and **2-K salt** were assigned using the gradient-enhanced version of the 2D experiments (^{1}H-^{1}H COSY, ^{1}H-^{13}C HMQC and ^{1}H-^{13}C HMBC) shown in the Supplementary material (see below). The 2D spectra were recorded using standard pulse sequences from Bruker pulse-sequence libraries.

The FT-IR spectra of **2**, its potassium salt (**2-K salt**) were recorded in dichloromethane solution (0.07 mol dm^{-3}) and nujol/fluorolube mulls. A cell with silicon (Si) windows and wedge-shaped layers were used to avoid interferences (mean layer thickness 170 μm). The spectra were taken with an IFS 113v FT-IR spectrophotometer (Bruker, Karlsruhe) equipped with a DTGS detector; resolution 2 cm–1, NSS = 125.

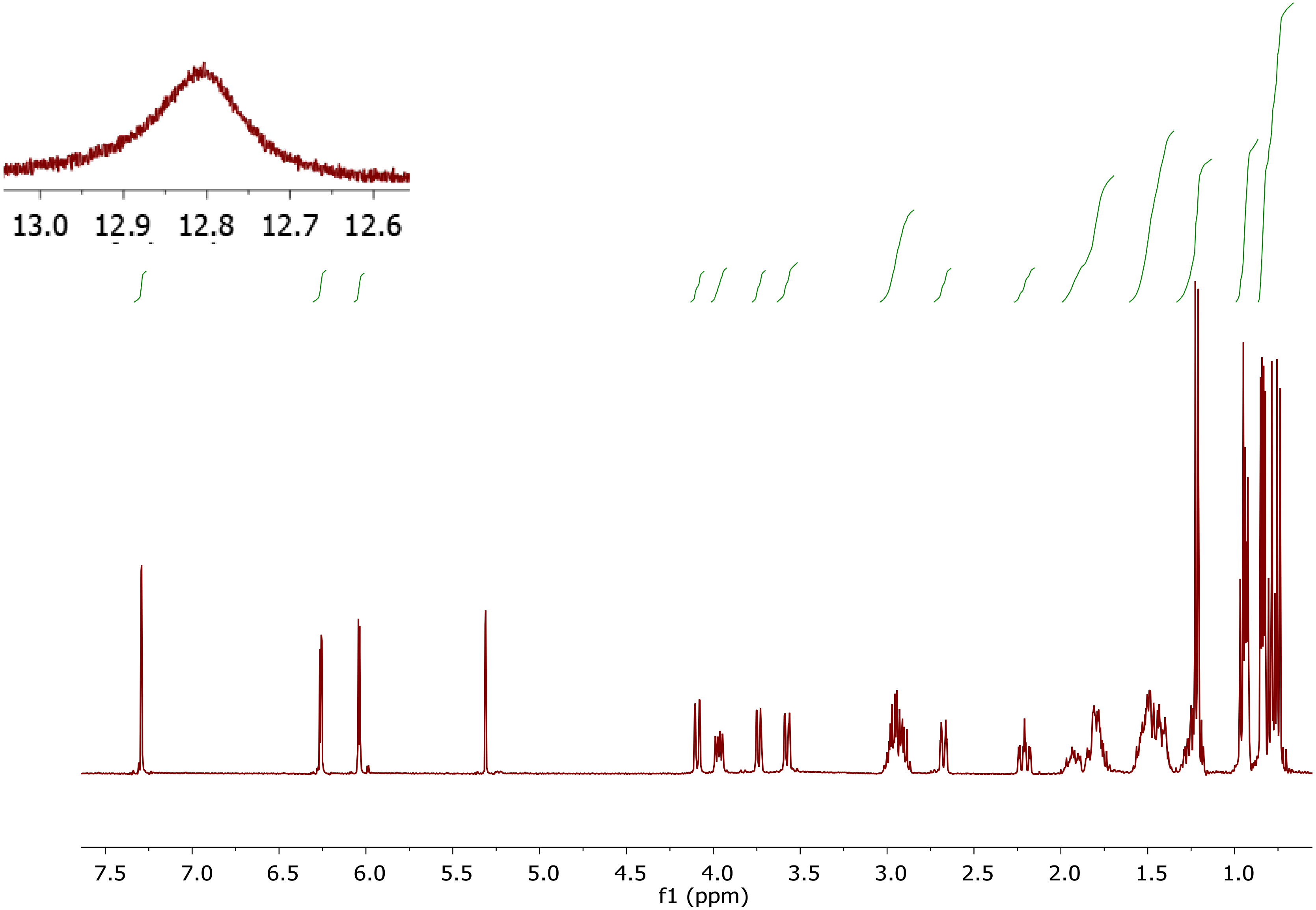

Fig. S1. ^{1}H NMR spectrum of **2** (400MHz, CD_2Cl_2).

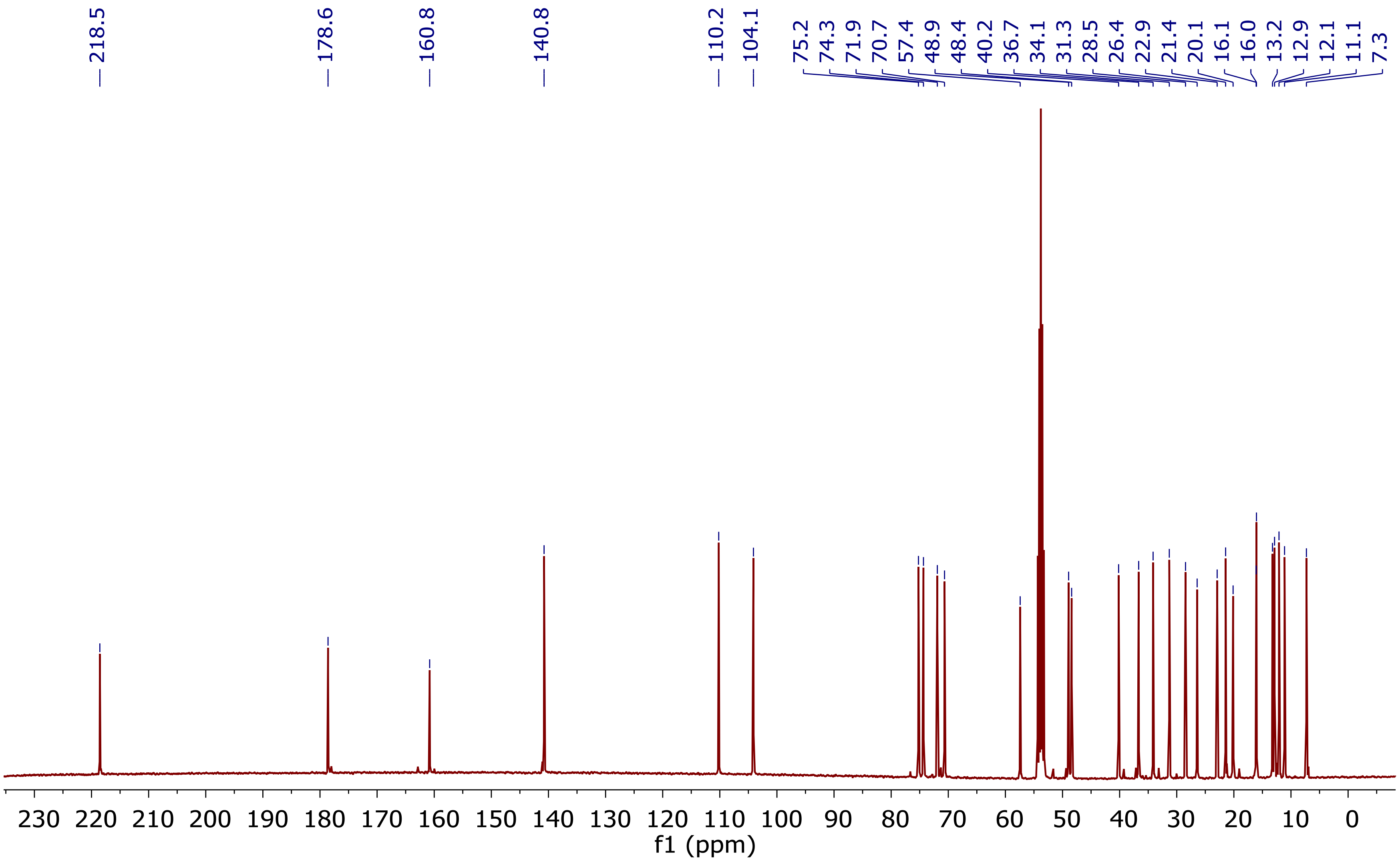

Fig. S2. ^{13}C NMR spectrum of **2** (101 MHz, CD_2Cl_2).

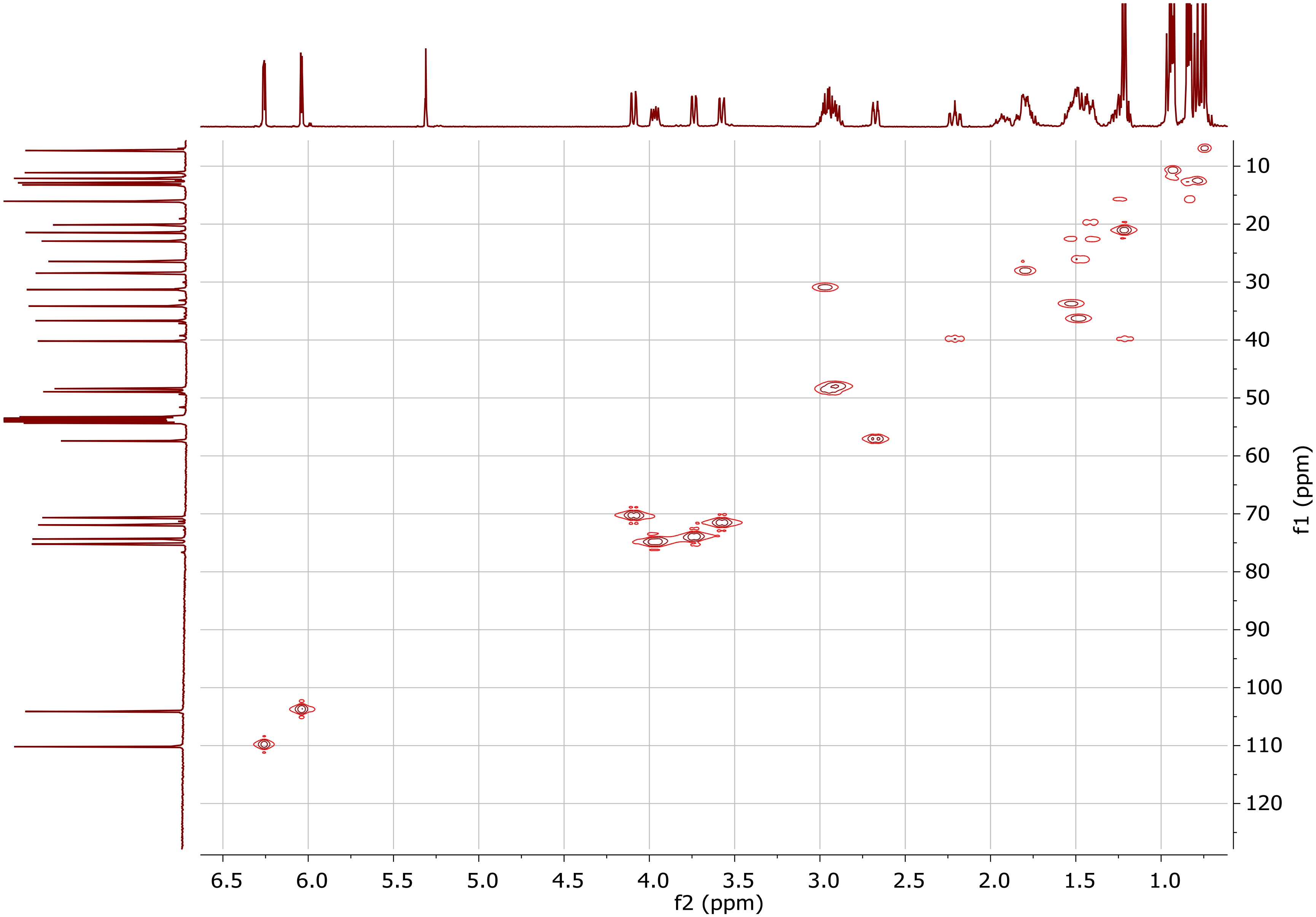

Fig. S3. ^{1}H ^{13}C HETCOR spectrum of **2** (CD_2Cl_2).

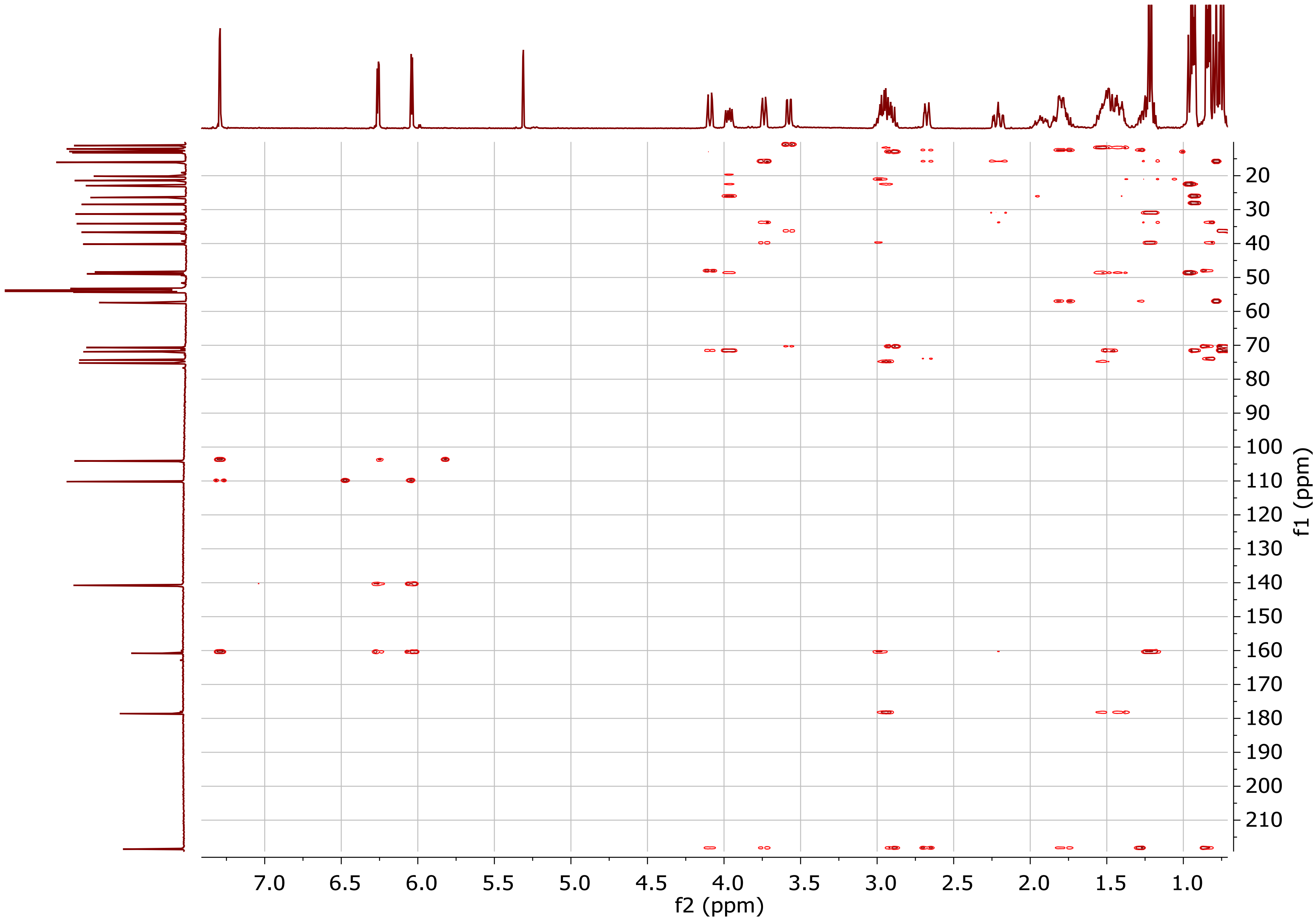

Fig. S4. ^{1}H ^{13}C HMBC spectrum of **2** (CD_2Cl_2).

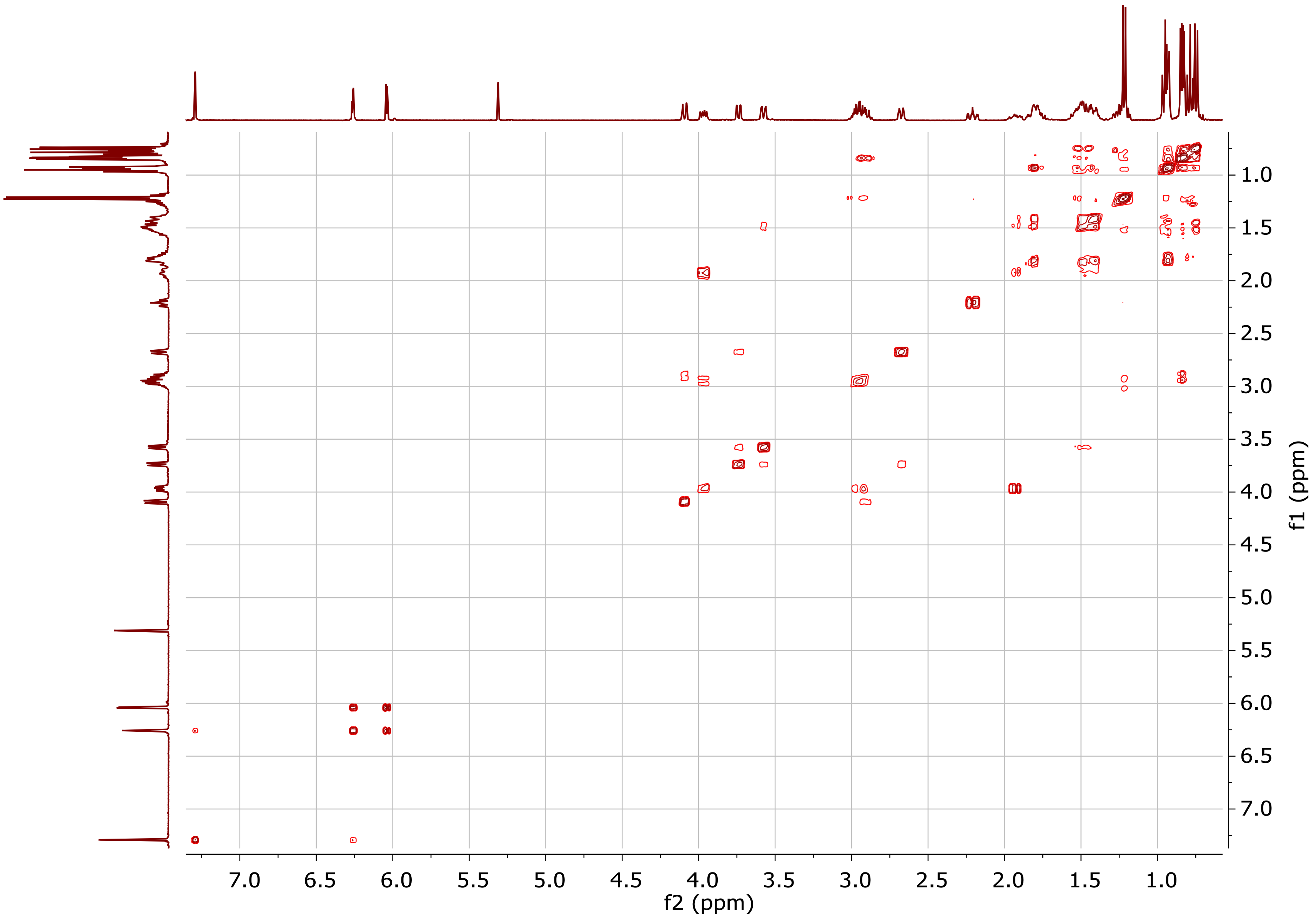

Fig. S5. ^{1}H ^{1}H COSY spectrum of **2** (CD_2Cl_2).

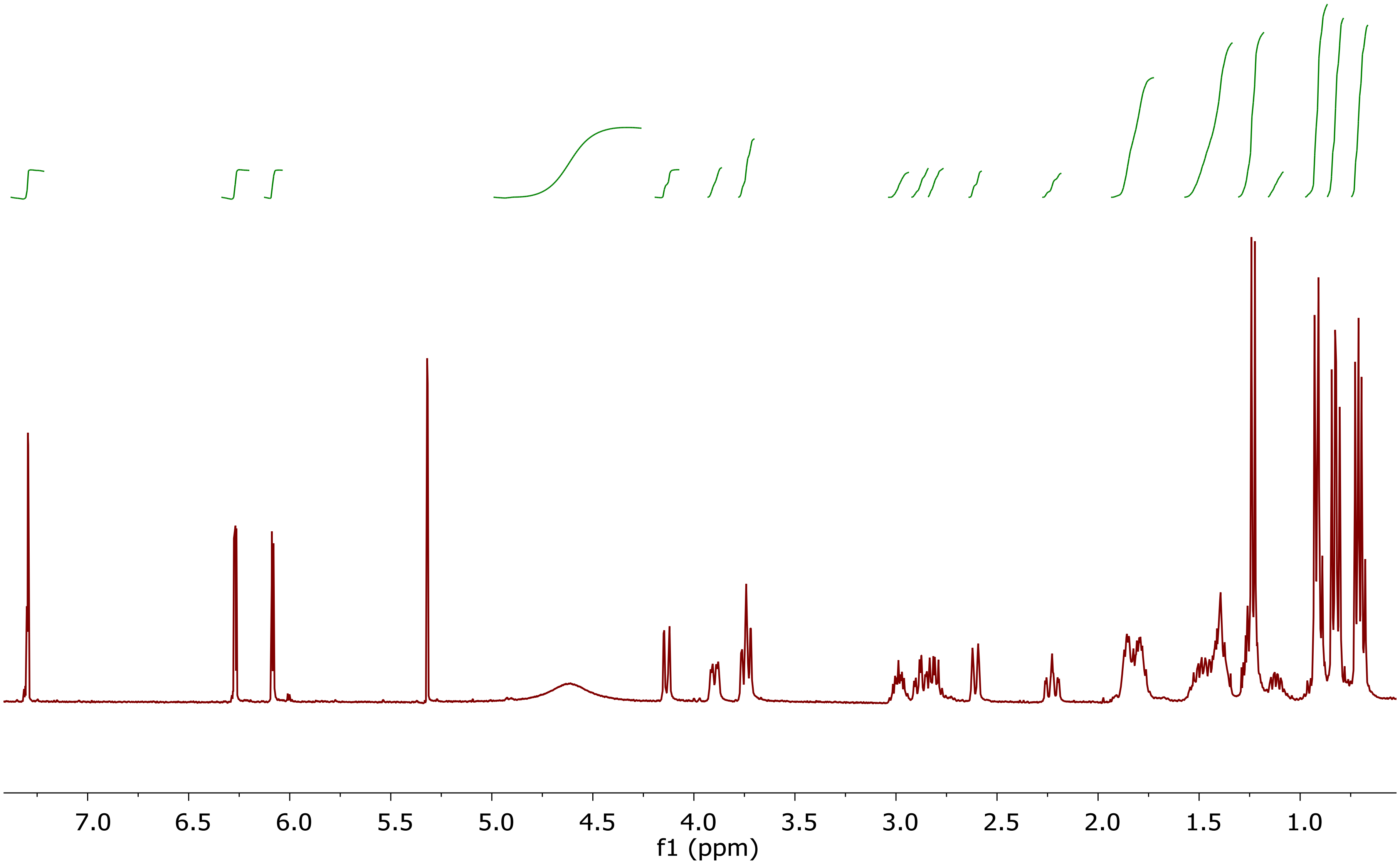

Fig. S6. ^{1}H NMR spectrum of **2-K salt** (400MHz, CD_2Cl_2)

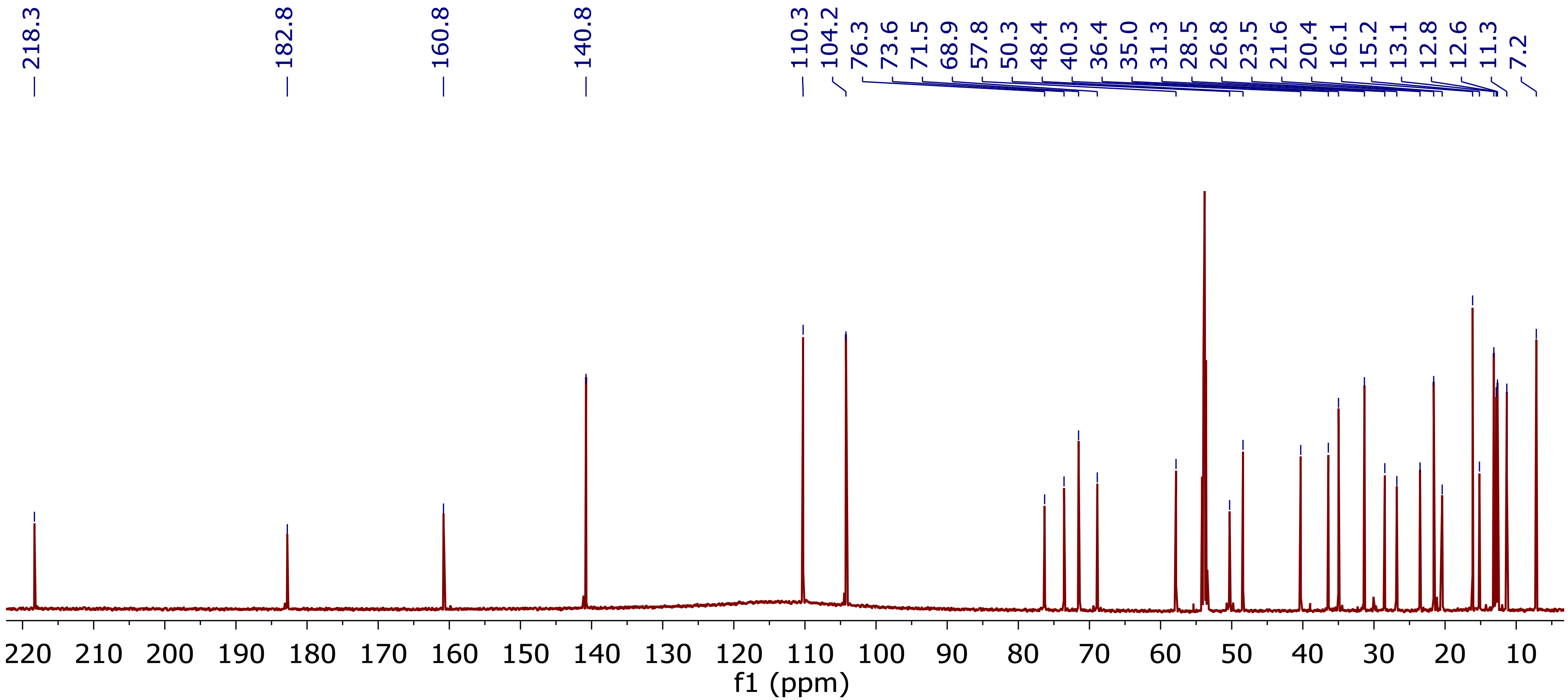

Fig. S7. ^{13}C NMR spectrum of **2-K salt** (101 MHz, CD_2Cl_2)

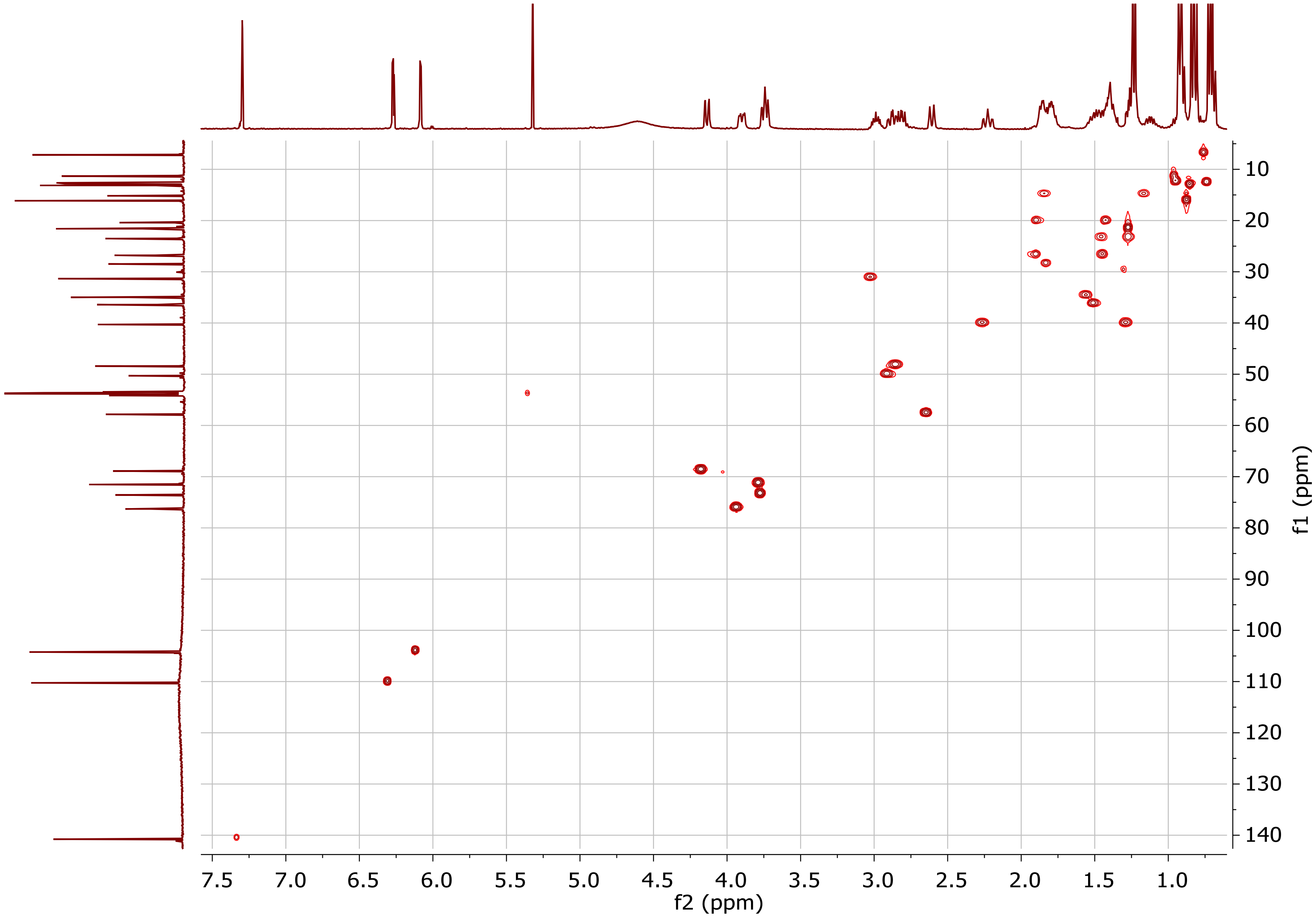

Fig. S8. ^{1}H ^{13}C HETCOR spectrum of **2-K salt** (CD_2Cl_2).

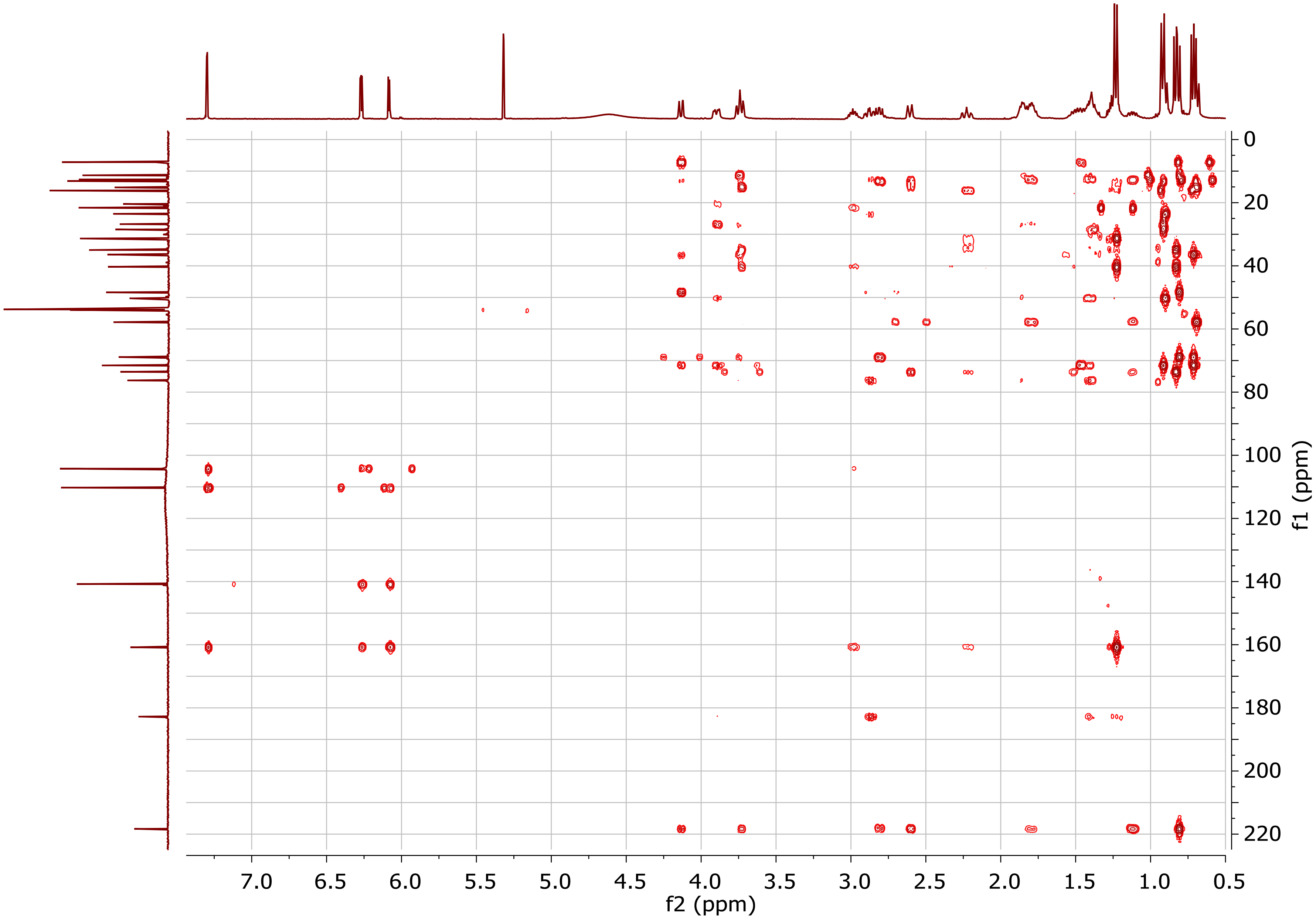

Fig. S9. ^{1}H ^{13}C HMBC spectrum of **2-K salt** (CD_2Cl_2).

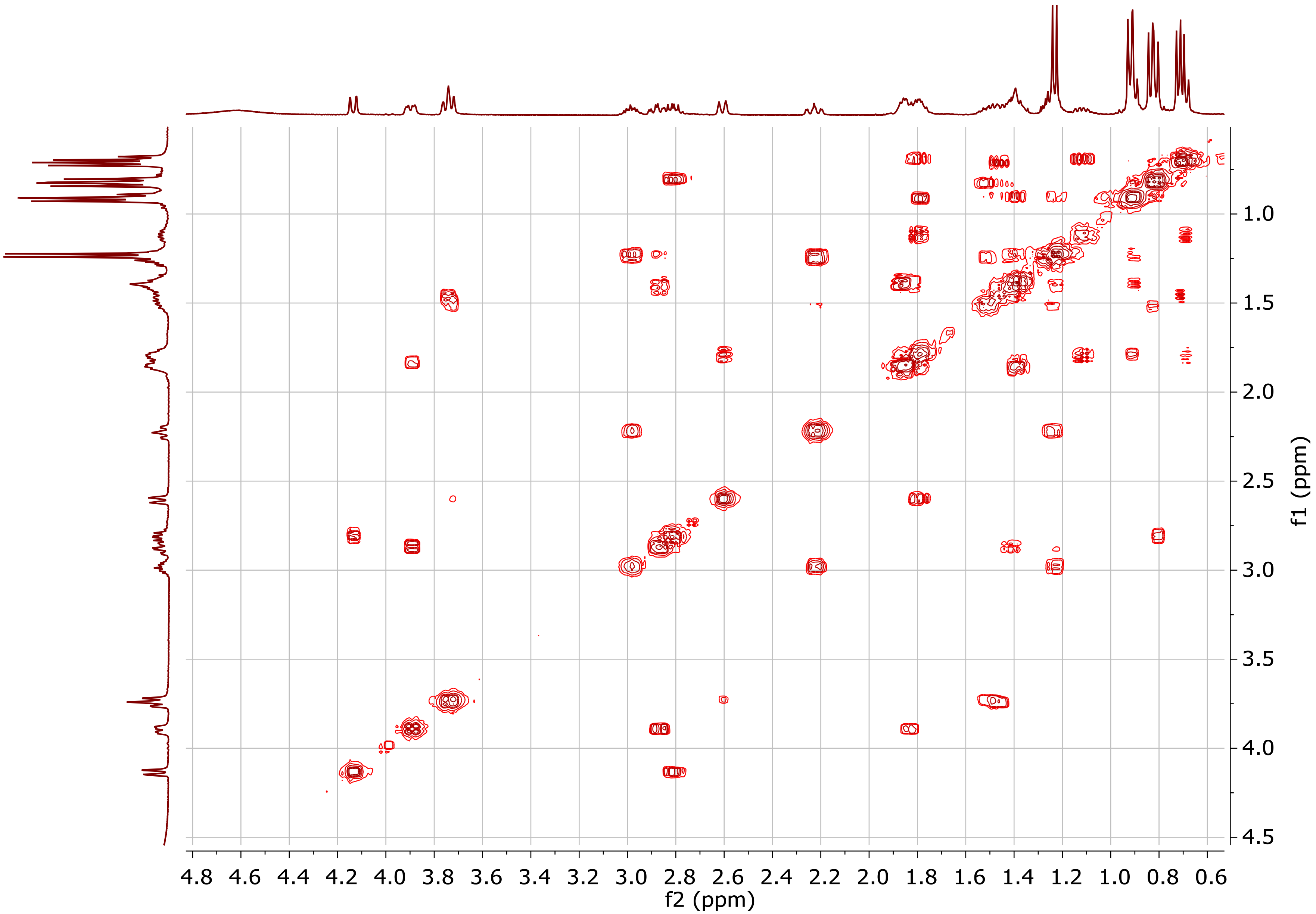

Fig. S10. ^{1}H ^{1}H COSY spectrum of **2-K salt** (CD_2Cl_2).

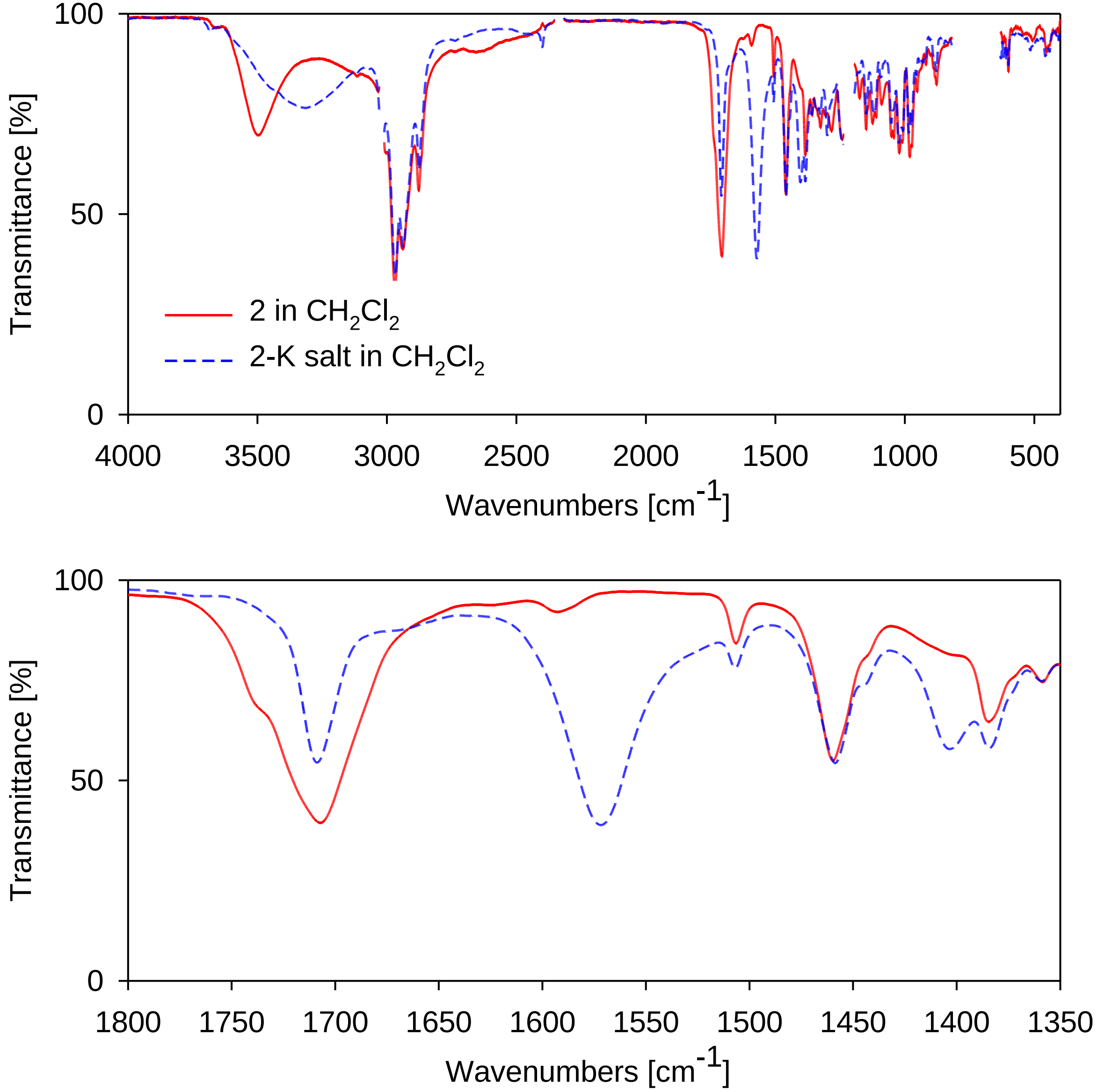

Fig. S11. FTIR spectra of the dichloromethane solutions of 2 and 2 potassium salt.

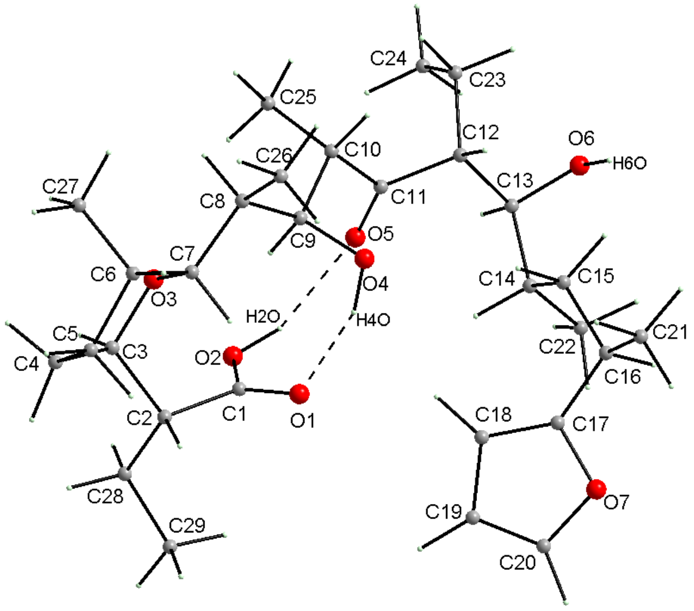

Table S1. DFT optimized parameters for **2**.

C1–O1	1.223	C1–O2	1.338	C1–C2	1.520	C2–C3	1.564	C3–C4	1.540
C4–C5	1.539	C5–C6	1.547	C6–C7	1.539	C7–C8	1.546	C8–C9	1.552
C9–C10	1.537	C9–O4	1.433	C10–C11	1.544	C11–O5	1.227	C11–C12	1.523
C12–C13	1.549	C13–O6	1.434	C13–C14	1.555	C14–C15	1.550	C15–C16	1.543
C16–C17	1.500	C17–O7	1.375	C17–C18	1.364	C18–C19	1.435	C19–C20	1.358
C20–O7	1.366	C16–C21	1.544	C14–C22	1.550	C12–C23	1.560	C23–C24	1.532
C10–C25	1.542	C8–C26	1.533	C6–C27	1.536	C2–C28	1.543	C28–C29	1.532
C–H (CH$_3$)	1.095	C–H (CH$_2$)	1.097	C–H (CH)	1.096	for C18,C19,C20:		C–H	1.079
O2–H2O	0.983	O4–H4O	0.971	O6–H6O	0.967				

O1–C1–O2	123.20	O1–C1–C2	122.87	C1–C2–C3	109.34	C2–C3–C4	111.57
C3–C4–C5	112.44	C4–C5–C6	112.38	C5–C6–C7	106.67	C6–C7–O3	109.27
C6–C7–C8	118.51	C7–C8–C9	107.26	C8–C9–C10	118.29	C9–C10–C11	106.87
C10–C11–O5	120.43	C10–C11–C12	117.81	C11–C12–C13	113.76	C12–C13–C14	116.14
C13–C14–C15	112.16	C14–C15–C16	117.69	C15–C16–C17	113.40	C16–C17–C18	135.36
C17–C18–C19	106.79	C18–C19–C20	106.19	C19–C20–O7	110.32	C17–O7–C20	107.33
C17–C16–C21	110.50	C15–C16–C21	110.23	C14–C14–C22	113.46	C13–C14–C22	108.95
C12–C13–O6	109.69	C11–C12–C23	109.68	C12–C23–C24	114.91	C12–C11–O5	121.73
C10–C11–O5	120.43	C9–C10–C25	112.48	C8–C9–O4	111.29	C7–C8–C26	113.41
C5–C6–C27	112.60	C3–C2–C28	111.00	C2–C28–C29	113.70		

O1–C1–C2–C3	111.76	C1–C2–C3–C4	-152.21	C2–C3–C4–C5	82.78	C3–C4–C5–C6	49.83
C4–C5–C6–C7	-55.76	C2–C3–O3–C7	-74.80	C5–C6–C7–C8	178.86	C6–C7–C8–C9	175.06
C7–C8–C9–C10	151.92	C7–C8–C9–O4	-83.63	C8–C9–C10–C11	-174.55	C9–C10–C11–O5	51.43
C9–C10–C11–C12	-130.56	C10–C11–C12–C13	166.16	C11–C12–C13–C14	-63.41	C11–C12–C13–O6	169.36
C12–C13–C14–C15	-53.81	C13–C14–C15–C16	-162.12	C14–C15–C16–C17	-60.12	C15–C16–C17–C18	-15.20
C16–C17–C18–C19	-177.35	C17–C18–C19–C20	0.01	C18–C19–C20–O7	0.01	C19–C20–O7–C17	-0.01
O7–C17–C16–C21	-68.08	C14–C15–C16–C21	175.40	C14–C13–C12–C23	171.75	C13–C12–C23–C24	59.98
C11–C12–C23–C24	-67.10	C12–C11–C10–C25	107.94	C8–C9–C10–C25	-54.96	C10–C9–C8–C26	-82.88
C6–C7–C8–C26	50.57	C8–C7–C6–C27	54.36	C4–C5–C6–C27	69.23	C4–C2–C2–C28	83.47
O3–C3–C2–C28	-149.72	C3–C2–C28–C28	-174.56				

D—H···A	D—H	H···A	D···A	D—H···A
O4—H4O···O1	0.971	1.941	2.834	151.85

O2—H2O···O5	0.983	2.094	3.031	158.72

Table S2. DFT optimized parameters for deprotonated anion **2**.

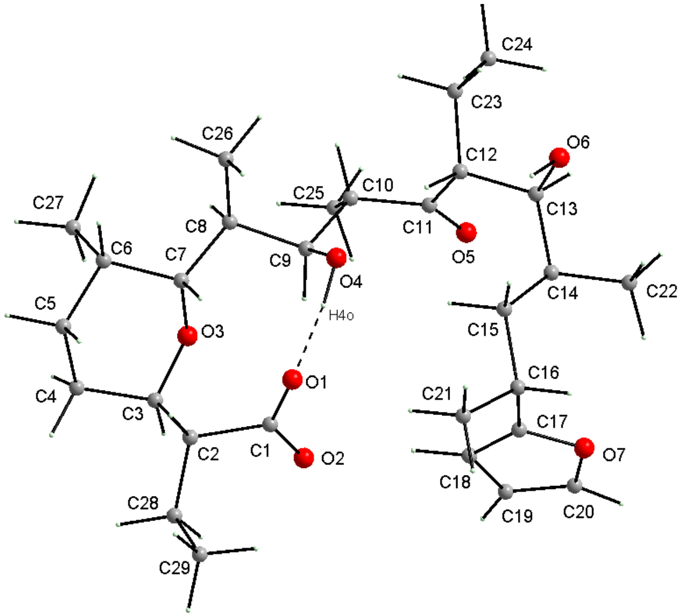

C1–O1	1.276	C1–O2	1.247	C1–C2	1.559	C2–C3	1.552	C3–C4	1.541
C4–C5	1.537	C5–C6	1.545	C6–C7	1.550	C7–C8	1.544	C8–C9	1.563
C9–C10	1.565	C9–O4	1.415	C10–C11	1.541	C11–O5	1.222	C11–C12	1.531
C12–C13	1.551	C13–O6	1.443	C13–C14	1.552	C14–C15	1.541	C15–C16	1.553
C16–C17	1.504	C17–O7	1.382	C17–C18	1.365	C18–C19	1.436	C19–C20	1.360
C20–O7	1.366	C16–C21	1.542	C14–C22	1.539	C12–C23	1.559	C23–C24	1.534
C10–C25	1.535	C8–C26	1.537	C6–C27	1.537	C2–C28	1.538	C28–C29	1.532
C–H (CH_3)	1.095	C–H (CH_2)	1.097	C–H (CH)	1.096	for C18,C19,C20:	C–H	1.079		
O4–H4O	1.004	O6–H6O	0.968						

O1–C1–O2	123.20	O1–C1–C2	122.87	C1–C2–C3	109.34	C2–C3–C4	111.57
C3–C4–C5	112.44	C4–C5–C6	112.38	C5–C6–C7	106.67	C6–C7–O3	109.27
C6–C7–C8	118.51	C7–C8–C9	107.26	C8–C9–C10	118.29	C9–C10–C11	106.87
C10–C11–O5	120.43	C10–C11–C12	117.81	C11–C12–C13	113.76	C12–C13–C14	116.14
C13–C14–C15	112.16	C14–C15–C16	117.69	C15–C16–C17	113.40	C16–C17–C18	135.36
C17–C18–C19	106.79	C18–C19–C20	106.19	C19–C20–O7	110.32	C17–O7–C20	107.33
C17–C16–C21	110.50	C15–C16–C21	110.23	C14–C14–C22	113.46	C13–C14–C22	108.95
C12–C13–O6	109.69	C11–C12–C23	109.68	C12–C23–C24	114.91	C12–C11–O5	121.73
C10–C11–O5	120.43	C9–C10–C25	112.48	C8–C9–O4	111.29	C7–C8–C26	113.41
C5–C6–C27	112.60	C3–C2–C28	111.00	C2–C28–C29	113.70		

O1–C1–C2–C3	103.77	C1–C2–C3–C4	-159.86	C2–C3–C4–C5	76.54	C3–C4–C5–C6	51.82
C4–C5–C6–C7	-53.20	C2–C3–O3–C7	-74.80	C5–C6–C7–C8	176.96	C6–C7–C8–C9	-178.53
C7–C8–C9–C10	163.12	C7–C8–C9–O4	-73.49	C8–C9–C10–C11	158.61	C9–C10–C11–O5	107.06
C9–C10–C11–C12	-77.91	C10–C11–C12–C13	168.11	C11–C12–C13–C14	-54.51	C11–C12–C13–O6	178.88
C12–C13–C14–C15	-54.68	C13–C14–C15–C16	-176.95	C14–C15–C16–C17	-51.93	C15–C16–C17–C18	-77.94
C16–C17–C18–C19	179.89	C17–C18–C19–C20	0.06	C18–C19–C20–O7	0.06	C19–C20–O7–C17	-0.16
O7–C17–C16–C21	-134.27	C14–C15–C16–C21	-176.46	C14–C13–C12–C23	-179.01	C13–C12–C23–C24	70.92
C11–C12–C23–C24	-55.96	C12–C11–C10–C25	157.43	C8–C9–C10–C25	-77.41	C10–C9–C8–C26	-73.29
C6–C7–C8–C26	57.61	C8–C7–C6–C27	52.70	C4–C5–C6–C27	77.78	C4–C2–C2–C28	78.22
O3–C3–C2–C28	-156.29	C3–C2–C28–C28	-173.07				

D—H···A	D—H	H···A	D···A	D—H···A
O4—H4O···O1	1.004	1.612	2.611	172.76

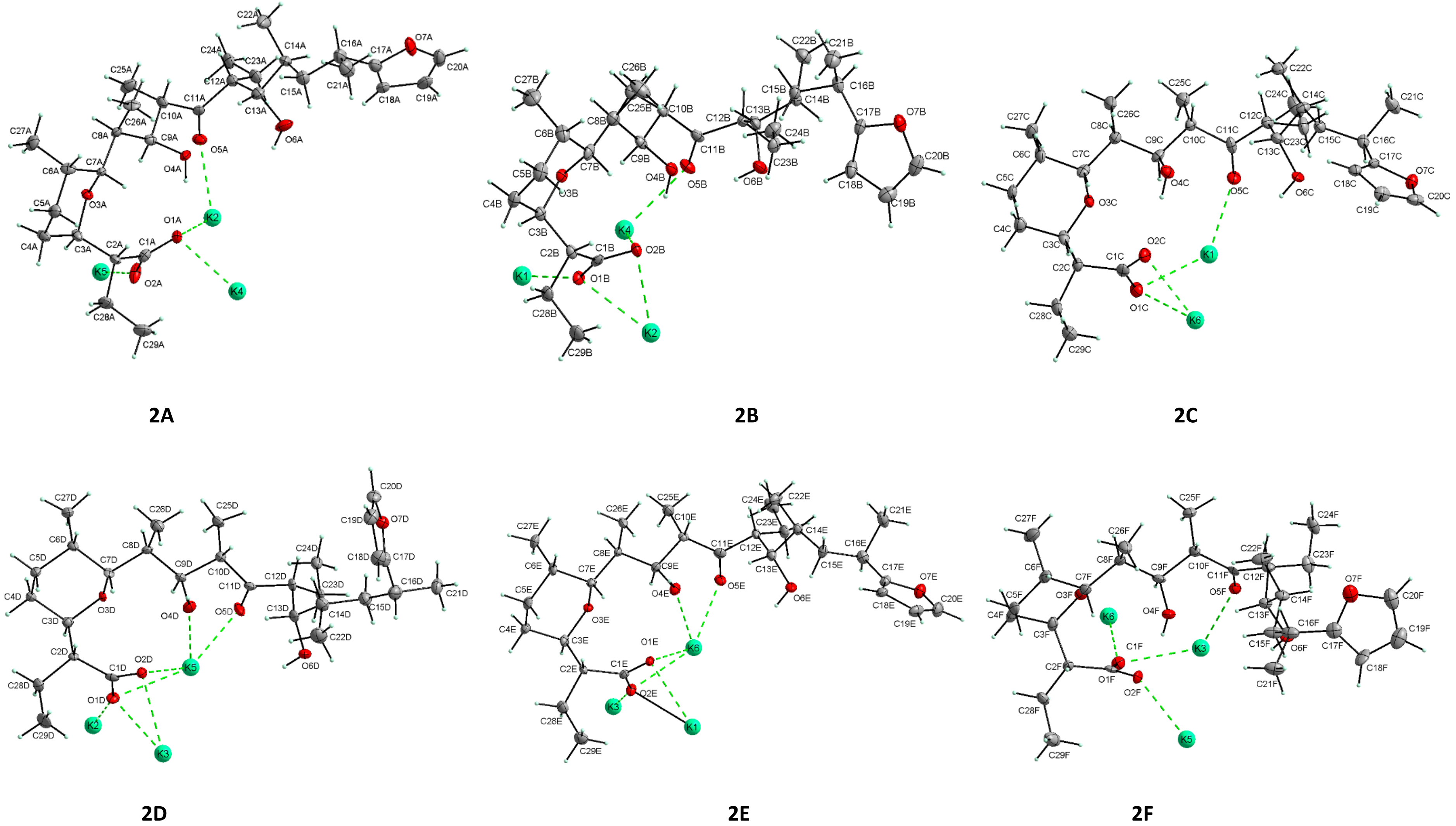
2A 2B 2C

2D 2E 2F

Fig. S11. View of the interactions of individual anions **2** with potassium ions.

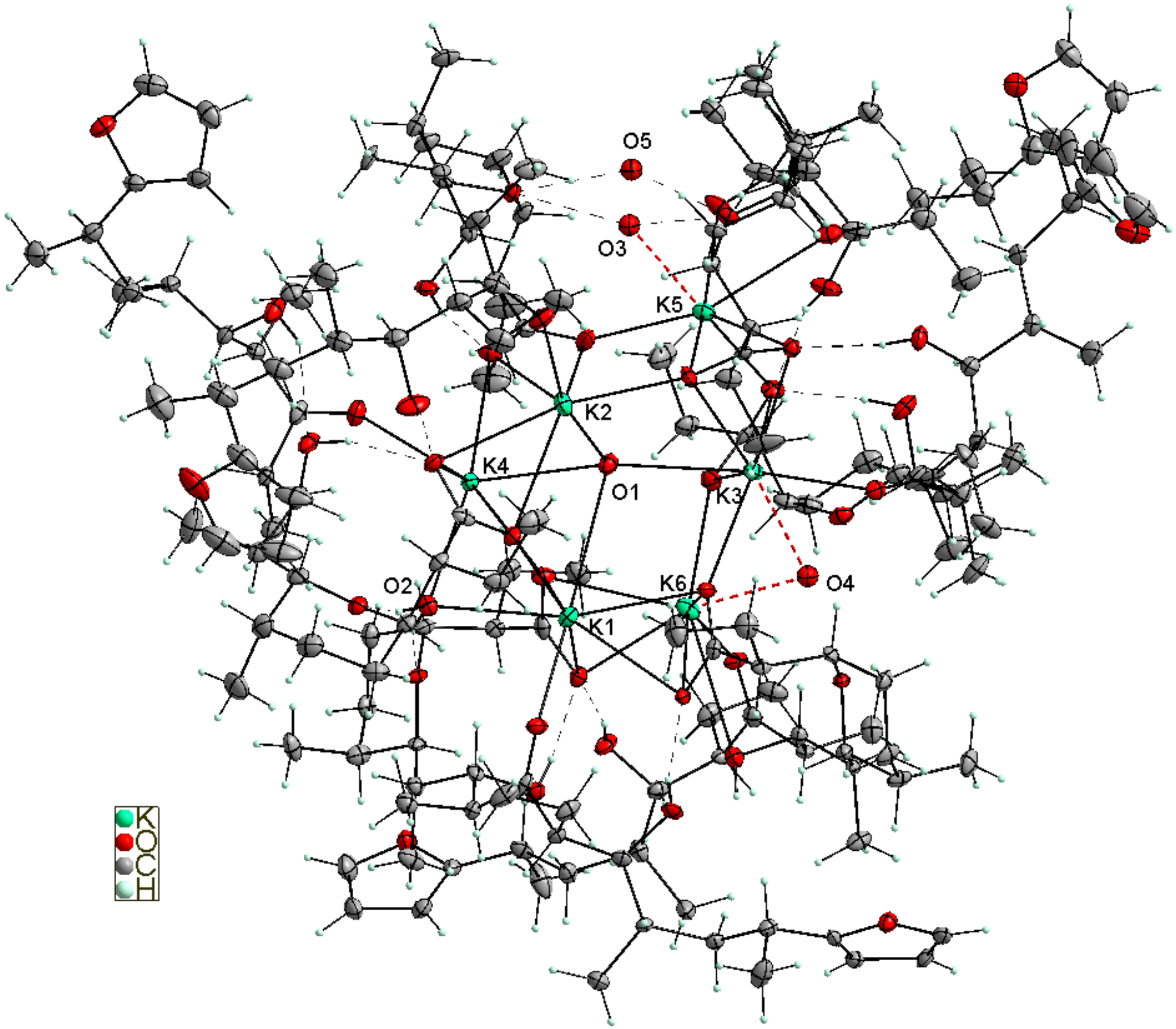

Fig. S12. View of the asymmetric unit of **2-K** with the labelling scheme. Displacement ellipsoids are shown at the 50% probability level.

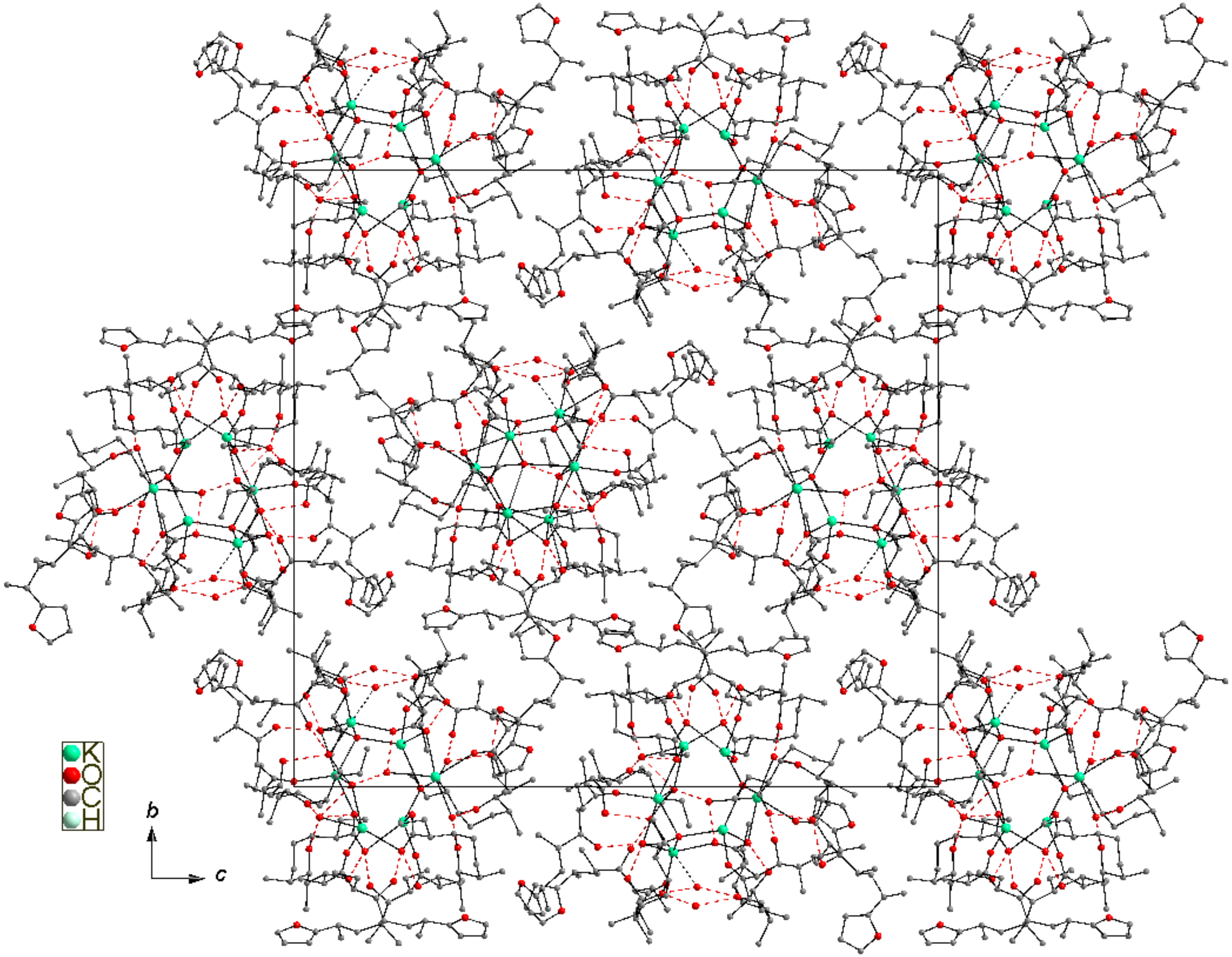

Fig. S13. Arrangement of supramolecular K$_6$-complex aggregates in the crystal. Broken lines represent the O-H…O intramolecular interactions in the supramolecular K$_6$-complex aggregates.

PUBLIKACJA II
wraz z suplementem

Yuri N. Antonenko, Marta Jędrzejczyk, Tatyana I. Rokitskaya, Ljudmila S. Khailova, Elena A. Kotova, Adam Huczyński

„Rate of translocation across lipid bilayer of triphenylphosphonium-linked salinomycin derivatives contributes significantly to their K^+/H^+ exchange activity on membranes”

Bioelectrochemistry 145 (2022) 108089

Bioelectrochemistry 145 (2022) 108089

Contents lists available at ScienceDirect

Bioelectrochemistry

journal homepage: www.journals.elsevier.com/bioelectrochemistry

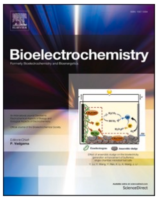

Rate of translocation across lipid bilayer of triphenylphosphonium-linked salinomycin derivatives contributes significantly to their K^+/H^+ exchange activity on membranes

Yuri N. Antonenko [a,*,1], Marta Jędrzejczyk [b,1], Tatyana I. Rokitskaya [a], Ljudmila S. Khailova [a], Elena A. Kotova [a], Adam Huczyński [b]

[a] *Belozersky Institute of Physico-Chemical Biology, Lomonosov Moscow State University, Leninskie Gory 1, Moscow 119991, Russia*

[b] *Department of Medical Chemistry, Faculty of Chemistry, Adam Mickiewicz University, Uniwersytetu Poznańskiego 8, 61-614 Poznań, Poland*

ARTICLE INFO

Keywords:
Bilayer lipid membrane
Liposome
Mitochondria
Ionophore
K^+/H^+-exchange
Salinomycin

ABSTRACT

Salinomycin (**SAL**), a polyether antibiotic exerting K^+/H^+-exchange on cellular membranes, effectively kills cancer stem cells. A series of cationic triphenylphosphonium (TPP^+)-linked **SAL** derivatives were synthesized aiming to render them mitochondria-targeted. Remarkably, attaching a TPP^+ moiety *via* a triazole linker at the C-20 position of **SAL** (compound **5**) preserved the ion carrier potency of the antibiotic, while analogs with TPP^+ linked at the C-1 position of **SAL** (**6**, **8**) were ineffective. On planar bilayer lipid membranes (BLM), the **SAL** analogs **6** and **8** exhibited slow electrical current relaxation upon a voltage jump, similar to previously studied alkyl-TPP compounds. However, **5** demonstrated much faster current relaxation, which suggested its high permeability through BLM resulting in its pronounced potency to transport potassium and hydrogen ions across both artificial (liposomal) and mitochondrial membranes. **SAL** and **5** did not induce a steady-state electrical current through the planar lipid bilayer, thereby confirming that the transport mechanism is the electrically silent K^+/H^+ exchange. The ion exchange mediated by **5** in energized mitochondria was more active than that caused by **SAL**, which was apparently due to accumulation of **5** in mitochondria. Thus, compound **5** can be regarded as a promising lead compound for testing anticancer and antimicrobial activity.

1. Introduction

Salinomycin (**SAL**) is an ionophore polyether antibiotic discovered at the end of the last century. **SAL** and its derivatives show high antibacterial activity against *Staphylococcus aureus* and *Mycobacterium tuberculosis*. **SAL** kills breast cancer stem cells (CSCs) in mice at least 100 times more effectively than paclitaxel, the most widely used anticancer drug [1]. The mechanism of **SAL** antitumor activity is not fully understood. Bearing in mind that **SAL**, like other polyether antibiotics, such as nigericin and monensin, is an ionophore capable of exchanging monovalent cations for hydrogen ions in an electrically neutral manner, its anticancer activity is believed to originate from the disturbance of intracellular cation homeostasis. At the same time, according to [1], the effect of the classical K^+/H^+-exchanger nigericin on CSCs was noticeably weaker than that of **SAL**, despite much higher toxicity of nigericin for animals [2]. According to [3], **SAL** induces apoptosis in a variety of human cancer cells. The ability of **SAL** to kill CSCs and overcome MDR of cancer cells makes **it** a promising component of novel, more potent anticancer drugs [4]. As shown in [5], **SAL** can cause death of cells resistant to various chemotherapeutic drugs such as doxorubicin, cisplatin, gemcitabine, temozolomide and verapamil, and sensitize radioresistant cells.

SAL is able to transport potassium and sodium cations across cell plasma membranes, which reduces gradients of these cations and augments the sodium cation concentration in the cytoplasm [6,7]. Another effect of **SAL** is a decrease in the pH gradient on the inner mitochondrial

---

Abbreviations: **SAL**, salinomycin; TPP^+, triphenylphosphonium; P-TPP^+, tetraphenylphosphonium; C_{12}TPP, dodecyltriphenylphosphonium; CuAAC, copper-catalyzed azide-alkyne cycloaddition; DPhytanylPC, 1,2-di-*O*-phytanyl-*sn*-glycero-3-phosphocholine; POPC, 1-palmitoyl-2-oleoyl-*sn*-glycero-3-phosphocholine; POPG, 1-palmitoyl-2-oleoyl-*sn*-glycero-3-phosphoglycerol; BLM, bilayer lipid membrane; RLM, rat liver mitochondria; CSCs, cancer stem cells.

[*] Corresponding author.

E-mail address: antonen@belozersky.msu.ru (Y.N. Antonenko).

[1] Antonenko and Jędrzejczyk contributed equally to this work.

https://doi.org/10.1016/j.bioelechem.2022.108089
Received 25 January 2022; Received in revised form 19 February 2022; Accepted 21 February 2022

membrane (acidification of the mitochondrial matrix) and a short-term increase in the mitochondrial membrane potential, followed by its decrease due to inhibition of mitochondrial respiration [8], which enabled the authors to conclude that mitochondrial dysfunction underlies the **SAL** anticancer effects. **SAL** reduces pH gradients on endosomal membranes [9], which apparently leads to the development of stress in the endoplasmic reticulum, called the unfolded protein response [10]. Similar to nigericin, it can be assumed that **SAL** lowers the pH in the cytosol [11] and can induce autophagy and mitophagy [12,13].

Like other polyether ionophores, **SAL** possesses unique structural features, such as an exterior alkyl backbone and an oxygen-rich internal cavity, that are crucial for the ability to transport metal ions. The terminal carboxyl at C1 is also important for exerting the cation-carrying activity: its modification can switch the transport mechanism from electroneutral to electrogenic [14]. Several series of **SAL** derivatives were synthesized and characterized [4,15,16]. Importantly, the anticancer activity of some of them exceeded that of unmodified **SAL** and commonly used cytostatic drugs in the MDR cell lines [17,18]. According to [19], “the phenotype selectivity of salinomycin appears to originate from a capacity for efficient ion transport”. With a functionally competent fluorescent derivative of **SAL**, the accumulation in the endoplasmic reticulum of cells was demonstrated [20]. On the other hand, the cytotoxicity of **SAL** was attributed to its direct effects on mitochondria [8,21].

A triphenylphosphonium (TPP$^+$) cationic group is commonly used as a vector for targeting to mitochondria various cargos [22,23], enabling them to readily penetrate through mitochondrial membranes and accumulate in mitochondria in response to membrane potential generation. To obtain mitochondria-targeted **SAL** analogs, here we synthesized TPP$^+$-linked **SAL** derivatives using C-1 and C-20 positions in the molecule and various linkers (Fig. 1). The new analog with TPP$^+$ attached to the C-20 position of **SAL** *via* a triazole linker (compound **5**) exhibited high ionophoric activity on both artificial (planar bilayers and liposomes) and natural membranes (mitochondria), while **SAL** derivatives with TPP$^+$ attached at the position C-1 (**6**, **8**, Fig. 1) were inactive.

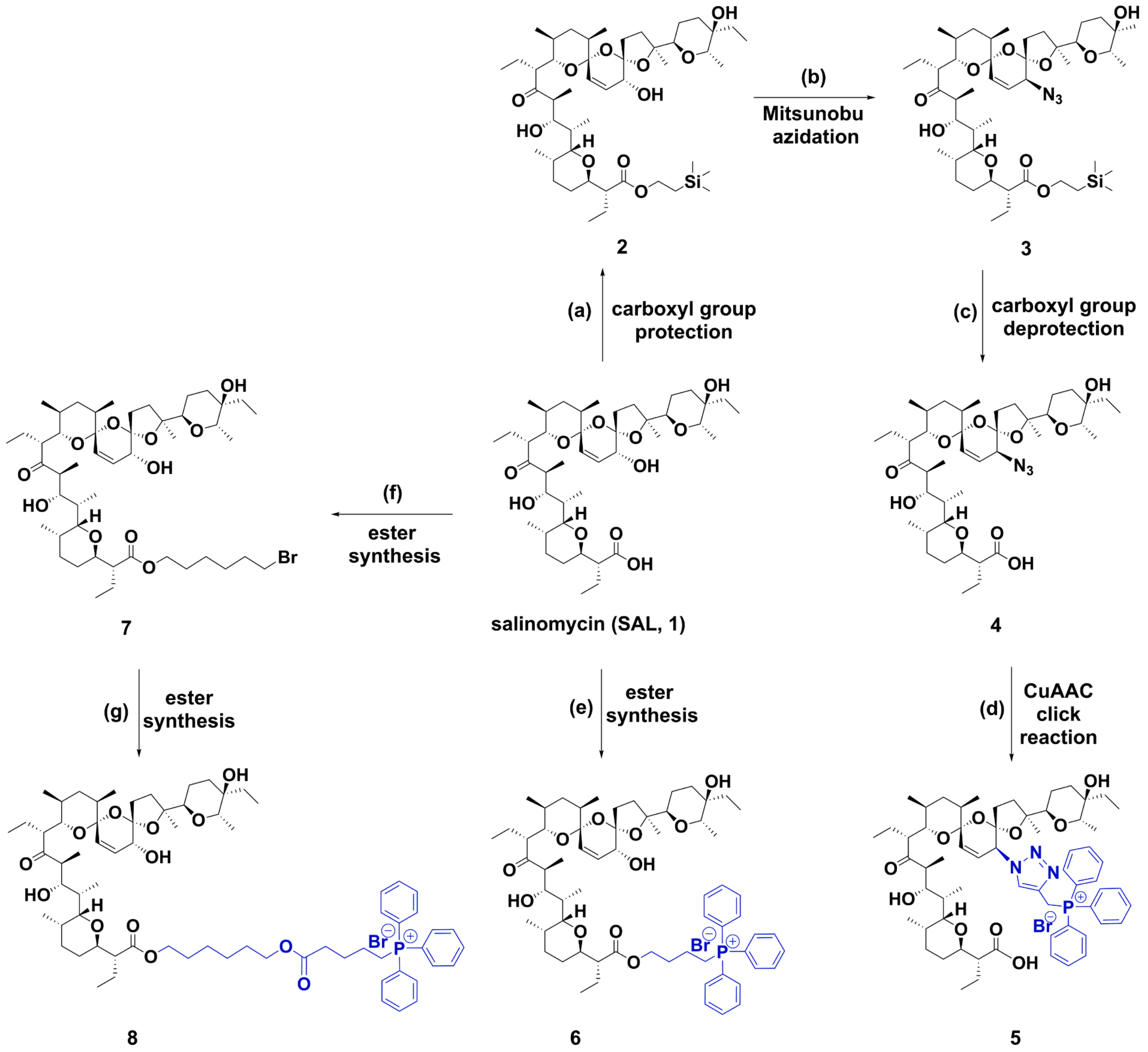

Fig. 1. A synthetic approach to a new class of salinomycin-TPP$^+$ conjugates. Reagents and reaction conditions: (a) TMS(CH2)2OH, *N,N,N′,N′*-tetramethylchloroformamidinium hexafluoro-phosphate (TCFH), 4-(dimethylamino)pyridine (DMAP), CH_2Cl_2, 0°→RT; (b) triphenylphosphine (PPh3), diisopropyl azodicarboxylate (DIAD), diphenylphosphoryl azide (DPPA), anhydrous THF, RT; (c) tetrabutylammonium fluoride (TBAF), THF; (d) triphenylpropargylphosphonium bromide, CuI, acetonitrile, RT; (e) (4-bromobutyl)triphenylphosphonium bromide, 1,8-diazabicyclo[5.4.0]undec-7-ene (DBU), DMF, 100 °C; (f) 1,6-dibromohexane, DBU, toluene, 100 °C; (g) 4-(carboxybutyl)triphenylphosphonium bromide, DBU, DMF, 100 °C.

2. Materials and methods

Details on the synthesis and characterizations of TPP$^+$-linked derivatives of **SAL** (SAL-TPP$^+$) and any associated references are given in the **Supporting Information** (**SI**).

K$^+$/H$^+$-exchange activity of **SAL** and its derivatives was studied: i) in artificial lipid membranes with the pH-sensitive fluorescent dye pyranine, using pyranine-loaded liposomes, and ii) in isolated rat liver mitochondria (RLM), via monitoring mitochondria swelling in the potassium acetate medium under nonenergized conditions by measuring changes in absorbance at 540 nm due to a decrease in light scattering with a SPECORD® 50 Analytik Jena spectrophotometer, and via recording mitochondrial membrane potential with a tetraphenylphosphonium (P-TPP$^+$)-sensitive electrode (NIKO-ANALIT, Moscow, Russia) under energized conditions (**SI**).

Translocation of compounds across planar bilayer lipid membranes (BLM) was studied by recording time courses of voltage jump-induced relaxation of electrical current across BLM in the presence of the compounds (**SI**).

3. Results

3.1. *Synthesis of SAL-TPP$^+$ derivatives*

Here, a series of **SAL** conjugates were synthesized *via* regioselective modifications of either the C1 carboxyl or the C20 hydroxyl group of **SAL** (Fig. 1). Modifications of **SAL** with the inversion of configuration at the C20 position were performed to obtain C20-epi-azide (**3**), an excellent starting compound to be conjugated with other, biologically active components using copper-catalyzed azide-alkyne cycloaddition (CuAAC click reaction) [24].

The first step to obtain the compound **5** was protection of the C1 carboxylic group of **SAL** by its esterification with 2-(trimethylsilyl) ethanol (TMS(CH$_2$)$_2$OH) in the presence of *N,N,N′,N′*-tetramethylchloroformamidinium hexafluorophosphate (TCFH) and 4-dimethylamino-pyridine (DMAP). This reversible strategy of the carboxylic group protection was proposed previously by Strand and colleagues [25] (Fig. 1). The obtained TMSEt-ester (**2**) was converted to the C-20-*epi*-azidosalinomycin derivative **3** using the Mitsunobu reaction with diphenylphosphoryl azide (DPPA) as a nucleophile, following the procedure reported by Shi *at al.* [26]. In the compound **3,** the inversion of the C20 hydroxyl group by the respective azido group occurred, which enabled us to obtain a 1,2,3-triazole conjugate, using the CuAAC click reaction in acetonitrile in the presence of copper(I) iodide (compound **5**). Deprotection of TMSEt-ester **(3)** was performed with tetrabutylammonium fluoride (TBAF), giving a **SAL** derivative that contained an unprotected carboxylic acid group (compound **4**) [27].

C1 **SAL** esters with a TPP$^+$ cation (compounds **6** and **8**) were prepared by one-step or two-step esterification of **SAL**, based on direct alkylation of a carboxylate ion. In this method, the appropriate alkyl bromides with 1,8-diazabicyclo[5.4.0]undec-7-ene (DBU) were used [28].

Structures and purity of all final products were examined using the ESI-MS, HRMS, ^{1}H NMR and ^{13}C NMR methods (**SI**).

3.2. *Ion transport activity of SAL-TPP$^+$ derivatives in pyranine-loaded liposomes*

The ion-carrying activity of **SAL** can be measured in liposomes loaded with the fluorescent pH-probe pyranine [19,29]. In the absence of an ion carrier, the pH shift in the bulk buffer solution does not lead to pH changes inside liposomes, while the addition of **SAL**, inducing an exchange of potassium for hydrogen ions, should produce pH equilibration upon shifting the outside pH.

Fig. 2**A** shows the kinetics of the pH gradient dissipation on membranes of liposomes (pH = 6 inside, pH = 8 outside) after the addition of an aliquot of KOH to the medium having 100 mM KCl in the presence of **SAL** or its TPP$^+$-conjugates. The effect of the compound **5** (40 nM) on the liposomal pH developed within minutes and was similar to that of **SAL** (Fig. 2A, red and black curves). Other compounds (**6**, **8**) were ineffective at this concentration (Fig. 2A, blue and green curves). Fig. 2**B** shows the statistics of the transport activity for the analogues studied. The activity decreased in the series: **5** ≥ **SAL** ≫ **8** ≥ **6.**

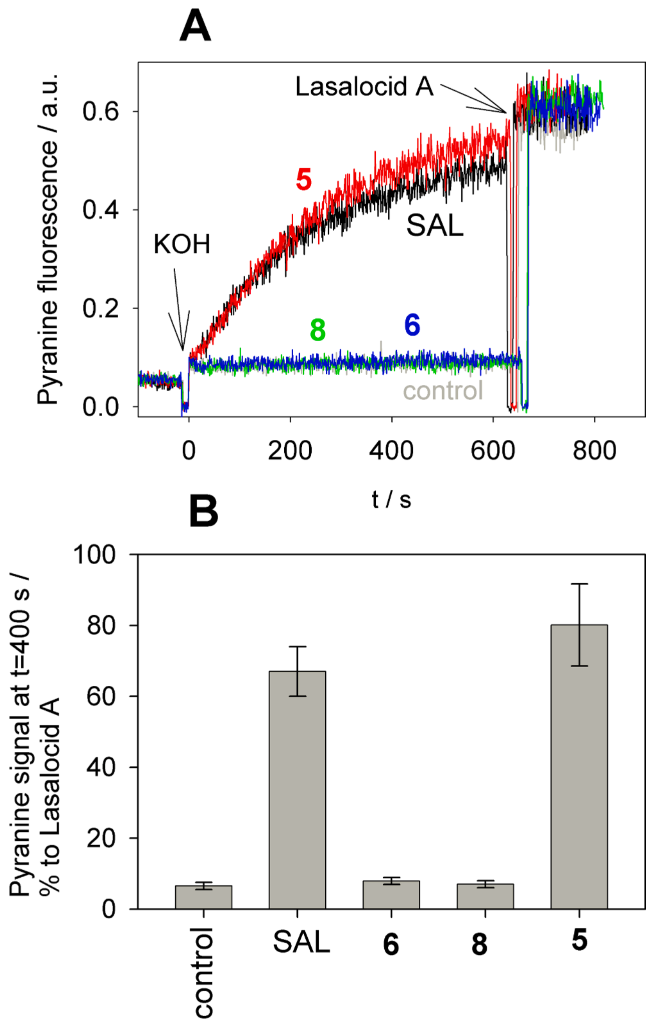

Fig. 2. **A.** Effects of salinomycin (**SAL**, black curve) and its TPP$^+$-conjugates on the induction of proton fluxes through liposomes loaded with the pH probe pyranine in the presence of 100 mM KCl. The inner liposomal pH was estimated from the pyranine fluorescence intensities measured at 505 nm upon excitation at 455 nm. 1 μM lasalocid A was added at about 650 s to equilibrate the pH. **SAL** and its derivatives concentration was 40 nM. Lipid concentration was 20 μg/ml, T = 15 °C. The proton flux was initiated by the alkaline pH shift from pH 6 to pH 8 resulting from the addition of the previously determined aliquot of KOH. In the presence of the compounds, the pyranine fluorescence gradually increased, indicating equilibration of the pH inside and outside liposomes due to proton transfer mediated by the K$^+$/H$^+$-exchangers. **B.** Statistics of the effect of 40 nM of **SAL**, **5**, **6**, and **8** at 400 s after their additions. Results are expressed as mean ± SD (n = 3).

3.3. *K$^+$/H$^+$-exchange induced by SAL-TPP$^+$ derivatives in nonenergized mitochondria*

One of the conventional assays for studying the ionophoric activity of nigericin and similar ionophores on mitochondrial membranes consists in recording the swelling kinetics of isolated non-respiring mitochondria in the potassium acetate medium [30]. The swelling of RLM was monitored as a decrease in the absorbance at 540 nm.

Fig. 3**A** shows the **SAL**-mediated swelling (black curve) of RLM compared to the swelling mediated by the compound **5** (red curve). Other compounds (**6**, **8**) were of no effect at this concentration (200 nM). Statistical analysis of several experiments comparing effects of **5** and **SAL** under these conditions showed that the compound **5** caused the K^+/H^+ exchange on the inner mitochondrial membrane at a rate close to that of **SAL** (the difference was statistically insignificant, Fig. 3**B**).

3.4. K^+/H^+-exchange Induced by SAL-TPP$^+$ derivatives in energized mitochondria

The swelling experiments (Fig. 3) refer to nonenergized mitochondria lacking both electrical potential and pH gradient on their membranes. It is known that the K^+/H^+-exchanger nigericin decreases the pH gradient on the inner mitochondrial membrane, while the K^+-carrier valinomycin increases it, at least immediately after the addition [31]. The mitochondrial membrane potential is about 180 mV (negative inside), while the pH gradient is about 1 unit (matrix is alkaline). In contrast to the electrogenic potassium carrier valinomycin, nigericin induces the efflux of potassium ions in exchange for protons, leading to a decrease in the pH gradient and a subsequent increase in the membrane potential. The total electrochemical potential difference of protons, which is the sum of an electrical potential difference (membrane potential) and a pH gradient, is preserved in the presence of nigericin and other Me^+/H^+-exchangers, due to pumping of protons across the inner mitochondrial membrane by the enzymes of the electron transport chain,. To study the effect of **SAL** and the compound **5** on the proton fluxes in energized mitochondria, we used a P-TPP$^+$-selective electrode to monitor the mitochondrial uptake of P-TPP$^+$ cations, driven by the mitochondrial membrane potential. The measurements were conducted without phosphate which is known to diminish the pH gradient on the

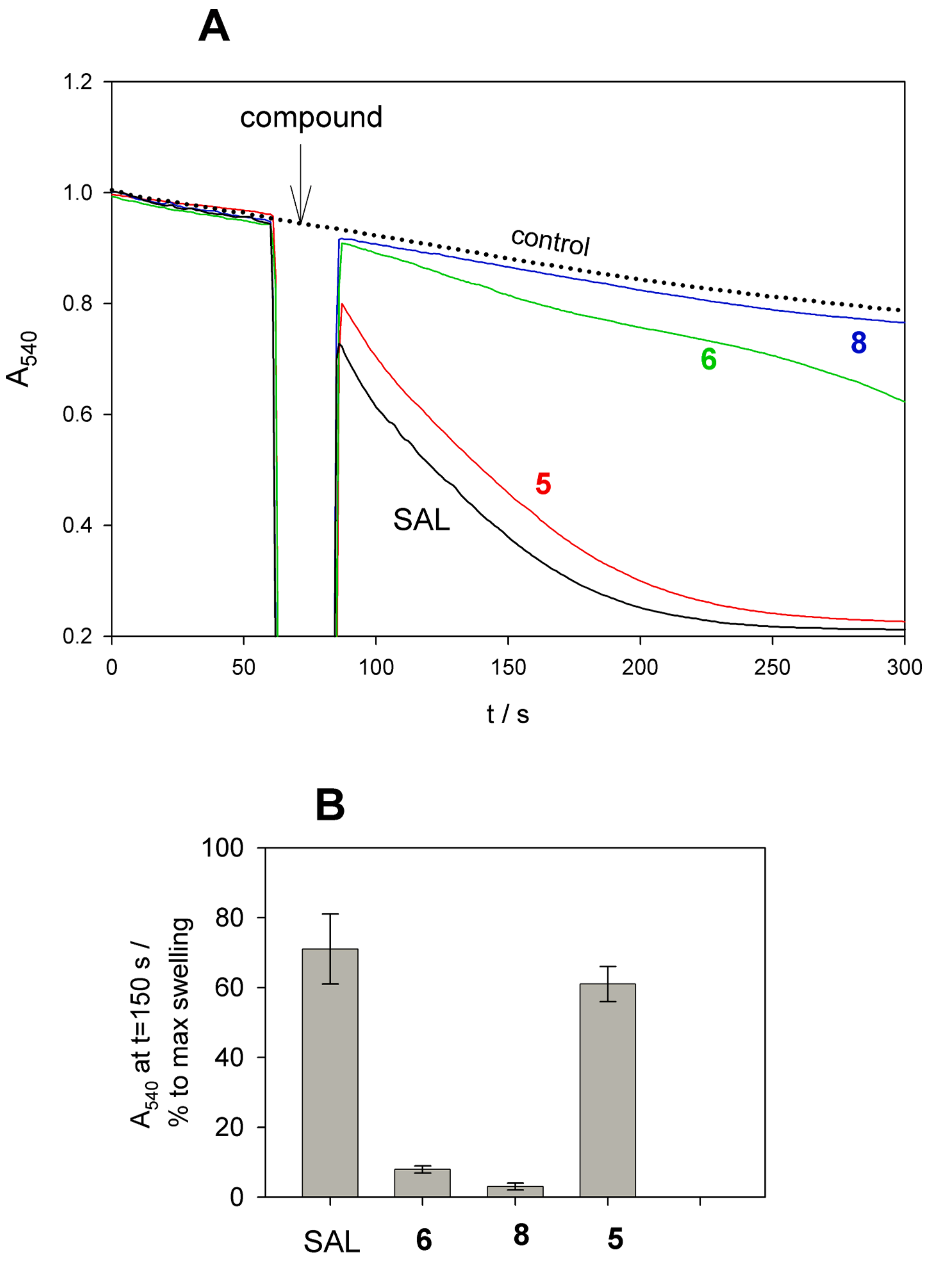

Fig. 3. Induction of K^+/H^+-exchange on the inner mitochondrial membrane by **SAL** and its TPP$^+$ conjugates, as estimated from the swelling of RLM by measuring changes in absorbance at 540 nm. Incubation mixture: 145 mM potassium acetate, 5 mM Tris, 0.2 mM EDTA, pH 7.4, and 1 μM rotenone. Mitochondrial protein 0.2 mg/ml. **B**. Statistics of the effect of 200 nM of **SAL**, **5**, **6**, and **8** on A540 at 90 s after their additions. Results are expressed as mean ± SD (n = 4).

inner mitochondrial membrane. The addition of succinate after rotenone led to influx of P-TPP$^+$ into mitochondria due to generation of membrane potential (Fig. 4**A**). Subsequent additions of 20 and 40 nM **SAL** (black curve) or **5** (red curve) increased the membrane potential, i.e. **SAL** and **5** behaved like nigericin in this system (blue curve). The classical electrogenic protonophore CCCP decreased the membrane potential, as expected. Statistical analysis of several experiments, comparing effects of **5** and **SAL** under these conditions, showed that **5** was more effective than **SAL** in the induction of K^+/H^+-exchange in energized mitochondria (Fig. 4**B**). Of note, the compound **5** carries a TPP$^+$ moiety and may interfere with the P-TPP$^+$-sensitive electrode. However, control experiments showed that nanomolar concentrations of **5** did not affect the readout of the P-TPP$^+$-electrode (data not shown). The present data on the **SAL**-caused mitochondrial membrane hyperpolarization are in agreement with earlier observations [8]. Therefore, both **SAL** and **5** exert nonelectrogenic K^+/H^+-exchange in energized mitochondria, similar to nigericin. Other SAL-TPP$^+$ conjugates (**6**, **8**) were inactive in this system (green and pink curves).

Thus, the experiments on both liposomal and mitochondrial membranes revealed an enormous difference between the K^+/H^+-exchange activity of the compound **5** and those of the compounds **6** and **8**, which could be associated with a difference in the translocation rate constants for these compounds.

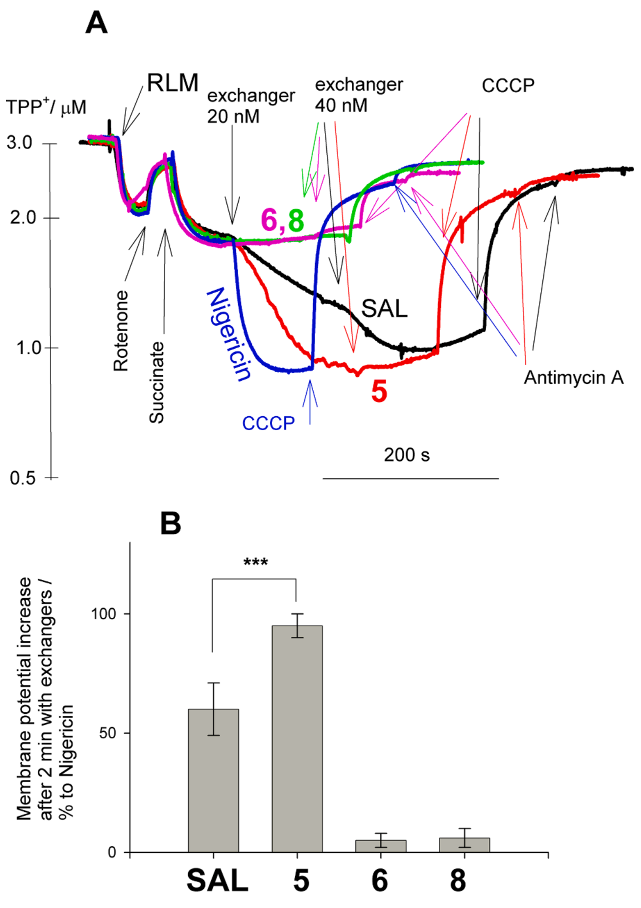

Fig. 4. **A.** Effect of **SAL** (black curve), nigericin (blue curve), compounds **5** (red curve), **6** (pink), and **8** (green) on the membrane potential of RLM estimated by tetraphenylphosphonium (P-TPP$^+$)-concentration in RLM suspension. Concentration of succinate was 1.5 mM, rotenone; 3 μM, CCCP; 200 nM, antimycin A; 1 μM. 20 nM **SAL** and other exchangers were added at t = 180 s (first addition marked by black arrow) and 40 nM (second addition) at the moments marked by arrows of corresponding color. Reaction mixture contained 250 mM sucrose, 10 mM Tris, 10 mM KCl, 0.2 mM EDTA, pH 7.4. The mitochondrial protein concentration was 0.6 mg/ml. For other conditions, see Materials and methods. **B**. Statistics of the effect of 20 nM of **SAL**, **5**, **6**, and **8** at 2 min after the addition on the membrane potential of RLM in % to that of nigericin. Results are expressed as mean ± SD (n = 4), *** $p < 0.001$, Student's *t*-test.

3.5. Electrical current relaxation induced by by SAL-TPP$^+$ derivatives on planar lipid bilayers

To test the above assumption, we performed experiments on planar lipid bilayers. According to [32,33], dodecyltriphenylphosphonium (C_{12}TPP) cations can bind readily to the surface of BLM and an application of a voltage jump to the BLM leads to redistribution of the surface concentrations of C_{12}TPP between the lipid monolayers (flip-flop), manifesting itself as electrical current relaxation. To measure the translocation of the synthesized SAL-TPP$^+$ derivatives across BLM, we recorded the current relaxation kinetics after a voltage jump in the presence of these compounds. BLMs were formed from *n*-decane solution of 1,2-di-*O*-phytanyl-*sn*-glycero-3-phosphocholine (DPhytanylPC), containing ether linkages. Due to the absence of carbonyl groups in this lipid, the magnitude of the dipole potential of such a membrane is lower by more than 100 mV, compared to the membrane formed from the ester bond-containing lipid [34,35]. This leads to an about 70-fold increase in translocation rate constants of lipophylic cations, thereby facilitating the measurements [36].

Fig. 5 shows time courses of electrical current through BLM in the presence of 0.1 μM C_{12}TPP or one of the three SAL-TPP$^+$ conjugates, measured upon switching on the 100-mV voltage at t = 0 s. Each positive current curve is followed by a negative one observed upon switching off the potential ($V = 0$ mV), which corresponded to backward redistribution of the cations leading to equal surface concentrations at both sides of the membrane. We shifted the negative current curves on the plots of Fig. 5, so that the moment of switching off the voltage was set at t = 0 s for simplicity. With C_{12}TPP, the experimental curves are fitted well by monoexponential curves with characteristic times $\tau_{on} = 3.5$ s (after application of $V = 100$ mV) and $\tau_{off} = 8.05$ s (after switching off, red curves in Fig. 5**A**), in good agreement with our previous measurements [37]. In the case of the compound **6,** the kinetics of the current relaxation was moderately faster than that of C_{12}TPP (Fig. 5**B**) with $\tau_{on} = 2.05$ s and $\tau_{off} = 3.55$ s, while with the compound **8** it was somewhat slower ($\tau_{on} = 21$ s and $\tau_{off} = 46$ s, Fig. 5**C**). **SAL** did not exhibit the current relaxation or induction of any BLM current (data not shown). In the case of the compound **5,** the current relaxation was extremely fast and completed in less than 1 s (Fig. 5**D**). Both on and off curves were poorly fitted by a single-exponential function, but can be well fitted by a double- exponential function with $\tau_{on(1)} = 0.10$ s and $\tau_{on(2)} = 0.60$ s; $\tau_{off(1)} = 0.20$ s and $\tau_{off(2)} = 0.72$ s (Fig. 5**D**). Remarkably, the amplitude of the relaxation for the compound **5** exceeded considerably those for other TPP$^+$-containing compounds, reaching 800 pA at $V = 100$ mV (Fig. 5**D**). The high amplitude of the relaxation actually resulted from the acceleration of the kinetics, because the area under the relaxation curve corresponds to the total charge of the cations adsorbed to one side of the membrane-water interface, which is similar for all the cations.

Panel **E** of Fig. 5 shows the statistics of the current relaxation at $V = 100$ mV. Patterned columns in the case of compound **5** corresponded to measurements made at 100 mM KCl (other measurements were carried out at 10 mM KCl). Both $\tau_{on(1)}$ and $\tau_{on\ (2)}$ did not depend on the concentration of KCl.

4. Discussion

The high rate of the compound **5** translocation can be a result of i) a decrease in the barrier for translocation of the TPP$^+$ fragment, owing to the complex structure of the whole molecule of **5**, or ii) the contribution of the interaction of the compound **5** with potassium and hydrogen ions to the kinetics of the total ion transport process. The latter possibility is similar to acceleration of translocation of the anionic form of a protonophore at the appropriate pH due to the high rate of translocation of its protonated form [38,39]. If so, the compound **5** translocation kinetics

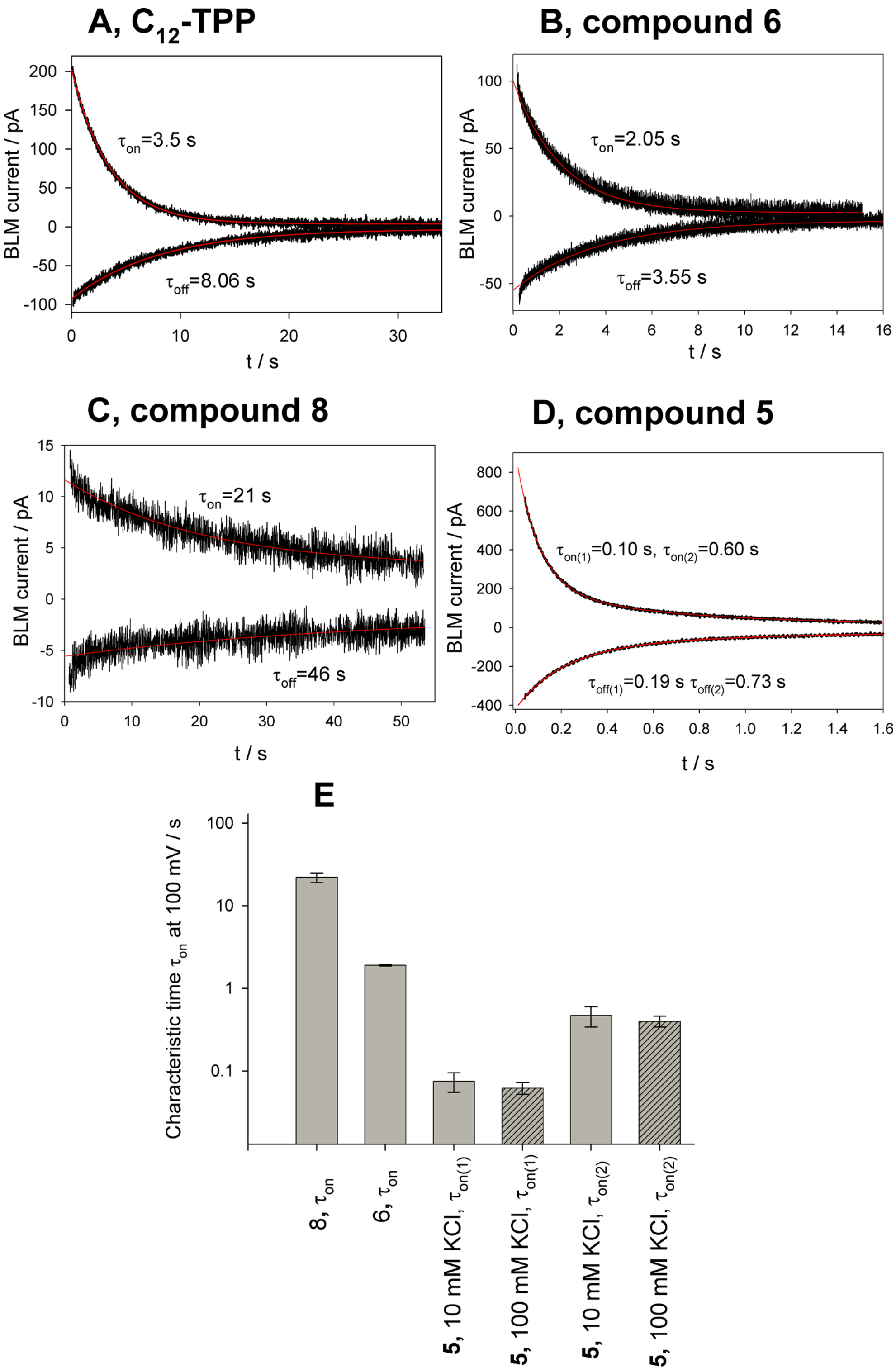

Fig. 5. Time courses of electrical current through planar BLM after application of a voltage jump from 0 mV to 100 mV (positive curve, i.e. "on" response) and from 100 mV to 0 mV (negative curve, i.e. "off" response) in the presence of 0.1 μM of C_{12}TPP (panel **A**), **6** (**B**), **5** (**C**), and **8** (**D**) and their best fits by a monoexponential (panels 1, B, and D) or double-exponential functions (panel C). Fitting curves are shown in red. All compounds' concentration was 0.1 μM. BLM was made from DPhytanylPC. The BLM bathing solution was 10 mM Mes, 10 mM Tris, 10 mM β-Alanine, 10 mM KCl, pH = 6.8. Shown fitting curves have the following parameters: A, τ = 6.3 s (V = 100 mV) and τ = 8.15 s (V = 0 mV); B, τ = 2.03 s (V = 100 mV) and τ = 3.55 s (V = 0 mV); C, τ = 20.8 s (V = 100 mV) and τ = 46 s (V = 0 mV); D, $\tau_{on(1)}$ = 0.10 s and $\tau_{on(2)}$ = 0.60 s (V = 100 mV) and $\tau_{off(1)}$ = 0.20 s and $\tau_{off(2)}$ = 0.72 s (V = 0 mV). **E.** Statistics of the current relaxations kinetics at 100 mV for **5**, **6**, and **8**. In case of **5** the measurements were carried out in 100 mM KCl also. Results are expressed as mean ± SD (n = 3).

should depend on pH and/or potassium ion concentration. Our experiments showed, however, that the relaxation kinetics of **5** did not depend on the potassium concentration (Fig. 5**E**) or pH (data not shown).

As seen in Fig. 5**A-D,** the addition of **SAL** or its analogs did not induce any steady-state current across BLM. These data suggest that **SAL** and the compound **5** carry cations in an electrically silent form. Of note, nigericin is able to induce an electrical current on BLM at micromolar concentrations [40,41], demonstrating both electrically silent and electrogenic ion transport. Therefore, **SAL** and nigericin exhibit different modes of action in this respect. Overall, it can be concluded that linking TPP$^+$ *via* triazole at C-20 of **SAL** (**5**) does not reduce its translocation efficacy, which is much higher than those of the compounds **6** and **8**. Therefore, the pronounced K$^+$/H$^+$ exchange activity of the compound **5** could be linked to its high translocation rate constant.

Fig. 6 shows a scheme of K$^+$/H$^+$-exchange mediated by **SAL** (panel **A**) and the compound **5** (panel **B**). We assume that the mechanism of action of both ionophores is similar, differing in the charge of the permeant species only. Namely, the complexes of **SAL** with K$^+$ and H$^+$ are

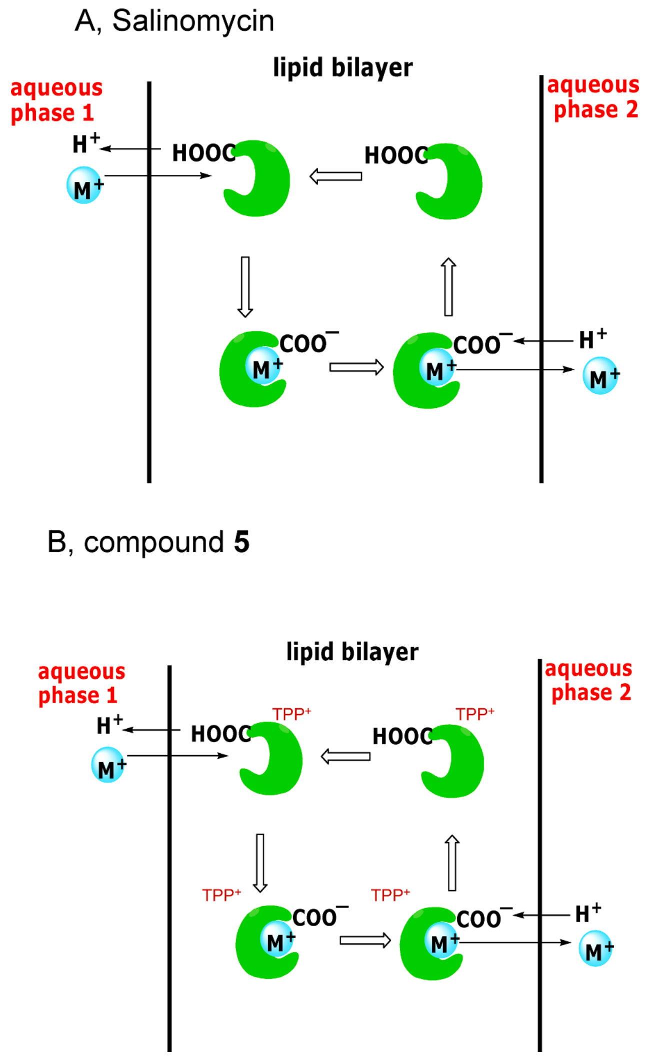

Fig. 6. Scheme of **SAL**- and **5**-mediated K^+/H^+-exchange on membrane. **SAL** forms electrically neutral complex with H^+ or metal cation M^+, while the complexes of **5** are cationic owing to the TPP^+ moiety.

neutral, while in the case of **5** the complexes are positively charged due to the TPP^+ moiety. Generally speaking, the translocation of cations is much slower compared to structurally similar neutral compounds or even anions, owing to the existence of a dipole potential on lipid-water interface [42]. Accordingly, the rates of translocation of **6** and **8** are low. However, the translocation rate of **5** is surprisingly high (Fig. 5). We think that the high membrane permeability of **5** determines the ability of the compound to exchange K^+ and H^+ on lipid membranes. The reason for this high permeability of the cationic compound **5** is not clear now. According to our recent findings [37], the introduction of methyl groups in the phenyl rings of the TPP^+ cation increases considerably the rate of TPP^+ translocation, while the introduction of halogens decreases it. It has been concluded that the translocation rate is not determined by hydrophobicity of the compounds but rather by the free energy of solvation of the cations, i.e. the interaction of the cations with water molecules. Similarly, it can be proposed that the structure of the compound **5** provides the formation of a reduced hydration shell in the membrane for the TPP^+ moiety compared to those of **6** and **8**. Further work would shed light on the detailed mechanism of this phenomenon. Nevertheless, there is accumulating evidence that integration of quaternary phosphonium and 1,2,3-triazole moieties can result in excellent biological activity [43].

It can be proposed that the cationic compound **5** is able to accumulate in mitochondria having high (about 180 mV) inside-negative membrane potential, similar to other TPP^+ conjugates. Actually, the ionophoric activity of **5** exceeded that of **SAL** in energized mitochondria (Fig. 4) and was close to that of **SAL** in nonenergized mitochondria (Fig. 3), which was apparently associated with the accumulation of **5** in mitochondria upon their energization.

5. Conclusion

In this study, we report the first synthesis of TPP^+-linked derivatives of **SAL**, an antibiotic isolated from *Streptomyces albus*. Since anticancer impact of **SAL** is associated with disturbance of mitochondrial metabolism, synthesis of such mitochondria-targeted **SAL** analogs seems to be an urgent task. Of the SAL-TPP^+ derivatives obtained here, only the compound **5**, synthesized via the CuAAC reaction, had similar to that of the pristine **SAL** or even increased ability to facilitate K^+/H^+-exchange across artificial and natural membranes. In view of the predominant contribution of the **SAL** ionophoric activity to its anticancer potency, **5** can be proposed as a lead compound for the design of new anticancer drugs. Electrophysiological experiments with artificial planar lipid bilayers enabled us to reveal the key role of the translocation across membranes in the ionophoric efficacy of the SAL-TPP^+ derivatives.

Thus, appending TPP^+ via CuAAC click chemistry to **SAL** renders this anticancer ionophore mitochondria-targeted and supports its K^+/H^+-exchange activity on artificial and natural membranes.

Declaration of Competing Interest

The authors declare that they have no known competing financial interests or personal relationships that could have appeared to influence the work reported in this paper.

Acknowledgements

The studies on the planar BLM, liposomes and mitochondria were financially supported by the Russian Science Foundation grant № 21-14-00062 to Y.N.A.; the syntheses of SAL-TPP^+ derivatives were financially supported from the project OPUS (grant 2021/41/B/ST4/00088) funded by the National Science Centre, Poland (NCN) to A.H. For the purpose of Open Access, the author (A.H.) has applied public copyright license to any Author Accepted Manuscript (AAM) version arising from this submission.

Appendix A. Supplementary material

Supplementary data to this article can be found online at https://doi.org/10.1016/j.bioelechem.2022.108089.

References

[1] P.B. Gupta, T.T. Onder, G. Jiang, K. Tao, C. Kuperwasser, R.A. Weinberg, E. S. Lander, Identification of selective inhibitors of cancer stem cells by high-throughput screening, Cell 138 (4) (2009) 645–659.
[2] F.W. Oehme, J.A. Pickrell, An analysis of the chronic oral toxicity of polyether ionophore antibiotics in animals, Vet. Hum. Toxicol. 41 (1999) 251–257.
[3] D. Lu, M.Y. Choi, J. Yu, J.E. Castro, T.J. Kipps, D.A. Carson, Salinomycin inhibits Wnt signaling and selectively induces apoptosis in chronic lymphocytic leukemia cells, Proc. Natl. Acad. Sci. U.S.A. 108 (32) (2011) 13253–13257.
[4] M. Antoszczak, A. Huczynski, Anticancer activity of polyether ionophore-salinomycin, Antimicrob. Agents Chemother. 15 (2015) 575–591.
[5] J.M. Garcia-Heredia, A. Carnero, Role of mitochondria in cancer stem cell resistance, Cells 9 (2020) 1693.
[6] D. Steberding, D.W. Sexton, Trypanocidal activity of salinomycin is due to sodium influx followed by cell swelling, Parasit. Vectors 6 (2013) 78.
[7] M. Yamasaki, K. Nakamura, N. Tamura, S.-J. Hwang, M. Yoshikawa, N. Sasaki, H. Ohta, O. Yamato, Y. Maede, M. Takiguchi, Effects and mechanisms of action of ionophorous antibiotics valinomycin and salinomycin-Na on Babesia gibsoni in vitro, J. Parasitol. 95 (6) (2009) 1532–1538.
[8] A. Managò, L. Leanza, L. Carraretto, N. Sassi, S. Grancara, R. Quintana-Cabrera, V. Trimarco, A. Toninello, L. Scorrano, L. Trentin, G. Semenzato, E. Gulbins,

M. Zoratti, I. Szabò, Early effects of the antineoplastic agent salinomycin on mitochondrial function, Cell Death. Dis. 6 (10) (2015) e1930.

[9] Y. Jang, J.S. Shin, Y.-S. Yoon, Y.Y. Go, H.W. Lee, O.S. Kwon, S. Park, M.-S. Park, M. Kim, J.U. Jung, Salinomycin inhibits influenza virus infection by disrupting endosomal acidification and viral matrix protein 2 function, J. Virol. 92 (24) (2018).

[10] T. Li, L. Su, N. Zhong, X. Hao, D. Zhong, S. Singhal, X. Liu, Salinomycin induces cell death with autophagy through activation of endoplasmic reticulum stress in human cancer cells, Autophagy 9 (7) (2013) 1057–1068.

[11] A.V. Berezhnov, M.P.M. Soutar, E.I. Fedotova, M.S. Frolova, H. Plun-Favreau, V. P. Zinchenko, A.Y. Abramov, Intracellular pH modulates autophagy and mitophagy, J. Biol. Chem. 291 (16) (2016) 8701–8708.

[12] J.R. Jangamreddy, S. Ghavami, J. Grabarek, G. Kratz, E. Wiechek, B. Fredriksson, R.K. Pariti, A. Cieslar-Pobuda, S. Panigrahi, M.J. Los, Salinomycin induces activation of autophagy, mitophagy and affects mitochondrial polarity: differences between primary and cancer cells, Biochim. Biophys. Acta 1833 (2013) 2057–2069.

[13] J.R. Jangamreddy, S. Panigrahi, M.J. Łos, Monitoring of autophagy is complicated - salinomycin as an example, Biochim. Biophys. Acta 1853 (3) (2015) 604–610.

[14] Y.N. Antonenko, T.I. Rokitskaya, A. Huczyński, Electrogenic and nonelectrogenic ion fluxes across lipid and mitochondrial membranes mediated by monensin and monensin ethyl ester, Biochim. Biophys. Acta-Biomembr. 1848 (4) (2015) 995–1004.

[15] X. Huang, B. Borgstrom, S. Kempengren, L. Persson, C. Hegardt, D. Strand, S. Oredsson, Breast cancer stem cell selectivity of synthetic nanomolar-active salinomycin analogs, BMC Cancer 16 (2016) 145.

[16] D. Czerwonka, M. Mielczarek-Puta, M. Antoszczak, A. Cioch, M. Struga, A. Huczynski, Evaluation of the anticancer activity of singly and doubly modified analogues of C20-epi-salinomycin, Eur. J. Pharmacol. 908 (2021), 174347.

[17] M. Antoszczak, A comprehensive review of salinomycin derivatives as potent anticancer and anti-CSCs agents, Eur. J. Med. Chem. 166 (2019) 48–64.

[18] A. Versini, L. Saier, F. Sindikubwabo, S. Müller, T. Cañeque, R. Rodriguez, Chemical biology of salinomycin, Tetrahedron Lett. 74 (39) (2018) 5585–5614.

[19] B. Borgstrom, X. Huang, E. Chygorin, S. Oredsson, D. Strand, Salinomycin hydroxamic acids: synthesis, structure, and biological activity of polyether ionophore hybrids, ACS Med. Chem. Lett. 7 (2016) 635–640.

[20] X. Huang, B. Borgström, J. Stegmayr, Y. Abassi, M. Kruszyk, H. Leffler, L. o. Persson, S. Albinsson, R. Massoumi, I.G. Scheblykin, C. Hegardt, S. Oredsson, D. Strand, The molecular basis for inhibition of stemlike cancer cells by salinomycin, ACS Cent. Sci. 4 (6) (2018) 760–767.

[21] J. Li, Y. Min, Pre-clinical evidence that salinomycin is active against retinoblastoma via inducing mitochondrial dysfunction, oxidative damage and AMPK activation, J. Bioenerg. Biomembr. 53 (5) (2021) 513–523.

[22] M.P. Murphy, R.A.J. Smith, Targeting antioxidants to mitochondria by conjugation to lipophilic cations, Annu. Rev. Pharmacol. Toxicol. 47 (1) (2007) 629–656.

[23] V.P. Skulachev, Cationic antioxidants as a powerful tool against mitochondrial oxidative stress, Biochem. Biophys. Res. Commun. 441 (2) (2013) 275–279.

[24] M. Meldal, C.W. Tornøe, Cu-catalyzed azide-alkyne cycloaddition, Chem. Rev. 108 (8) (2008) 2952–3015.

[25] B. Borgstrom, X. Huang, M. Posta, C. Hegardt, S. Oredsson, D. Strand, Synthetic modification of salinomycin: selective O-acylation and biological evaluation, Chem. Commun. 49 (2013) 9944–9946.

[26] Q. Shi, Y.u. Li, S. Bo, X. Li, P. Zhao, Q.i. Liu, Z. Yang, H. Cong, H. Deng, M. Chen, S. Chen, X. Zhou, H. Ding, Z.-X. Jiang, Discovery of a (19)F MRI sensitive salinomycin derivative with high cytotoxicity towards cancer cells, Chem. Commun. 52 (29) (2016) 5136–5139.

[27] Y. Li, Q. Shi, J. Shao, Y. Yuan, Z. Yang, S. Chen, X. Zhou, S. Wen, Z. Jiang, Synthesis and biological evaluation of 20-epi-amino-20-deoxysalinomycin derivatives, Eur. J. Med. Chem. 148 (2018) 279–290.

[28] M. Antoszczak, K. Popiel, J. Stefanska, J. Wietrzyk, E. Maj, J. Janczak, G. Michalska, B. Brzezinski, A. Huczynski, Synthesis, cytotoxicity and antibacterial activity of new esters of polyether antibiotic - salinomycin, Eur. J. Med. Chem. 76 (2014) 435–444.

[29] N. Sakai, S. Matile, The determination of the ion selectivity of synthetic ion channels and pores in vesicles, J. Phys. Org. Chem. 19 (8-9) (2006) 452–460.

[30] G.P. Brierley, Passive permeability and energy-linked ion movements in isolated heart mitochondria, Ann. N. Y. Acad. Sci. 227 (1974) 398–411.

[31] D.W. Jung, M.H. Davis, G.P. Brierley, Estimation of matrix pH in isolated heart mitochondria using a fluorescent probe, Anal. Biochem. 178 (2) (1989) 348–354.

[32] T.I. Rokitskaya, S.S. Klishin, I.I. Severina, V.P. Skulachev, Y.N. Antonenko, Kinetic analysis of permeation of mitochondria-targeted antioxidants across bilayer lipid membranes, J. Membr. Biol. 224 (1-3) (2008) 9–19.

[33] T.M. Il'yasova, T.I. Rokitskaya, I.I. Severina, Y.N. Antonenko, V.P. Skulachev, Substitution of ether linkage for ester bond in phospholipids increases permeability of bilayer lipid membrane for SkQ1-type penetrating cations, Biochemistry (Moscow) 77 (9) (2012) 1038–1043.

[34] K. Gawrisch, D. Ruston, J. Zimmerberg, V.A. Parsegian, R.P. Rand, N. Fuller, Membrane dipole potentials, hydration forces, and the ordering of water at membrane surfaces, Biophys. J. 61 (5) (1992) 1213–1223.

[35] U. Peterson, D.A. Mannock, R.N. Lewis, P. Pohl, R.N. McElhaney, E.E. Pohl, Origin of membrane dipole potential: contribution of the phospholipid fatty acid chains, Chem. Phys. Lipids 117 (2002) 19–27.

[36] T.I. Rokitskaya, G.A. Korshunova, Y.N. Antonenko, Effect of alkyl chain length on translocation of rhodamine B n-alkyl esters across lipid membranes, Biophys. J. 115 (3) (2018) 514–521.

[37] T.I. Rokitskaya, V.B. Luzhkov, G.A. Korshunova, V.N. Tashlitsky, Y.N. Antonenko, Effect of methyl and halogen substituents on the transmembrane movement of lipophilic ions, Phys. Chem. Chem. Phys. 21 (42) (2019) 23355–23363.

[38] R. Benz, S. McLaughlin, The molecular mechanism of action of the proton ionophore FCCP (carbonylcyanide p-trifluoromethoxyphenylhydrazone), Biophys. J. 41 (3) (1983) 381–398.

[39] K. O'Shaughnessy, S.B. Hladky, Transient currents carried by the uncoupler, carbonyl cyanide m-chlorophenylhydrazone, Biochim. Biophys. Acta 724 (3) (1983) 381–387.

[40] M. Toro, E. Arzt, J. Cerbòn, G. Alegría, R. Alva, Y. Meas, S. Estrada-O, Formation of ion-translocating oligomers by nigericin, J. Membr. Biol. 95 (1) (1987) 1–8.

[41] V.S. Markin, V.S. Sokolov, L.I. Boguslavsky, L.S. Jaguzhinsky, Nigericin-induced charge transfer across membranes, J. Membr. Biol. 25 (1) (1975) 23–45.

[42] E.A. Liberman, V.P. Topaly, Permeability of biomolecular phospholipid membranes for fat-soluble ions, Biophysics (Moscow) 14 (1969) 477–487.

[43] W. Tan, J. Zhang, Y. Mi, F. Dong, Q. Li, Z. Guo, Enhanced antifungal activity of novel cationic chitosan derivative bearing triphenylphosphonium salt via azide-alkyne click reaction, Int. J. Biol. Macromol. 165 (2020) 1765–1772.

The rate of translocation across a lipid bilayer of triphenylphosphonium-linked salinomycin analogs contributes significantly to their K^+/H^+ exchange activity on artificial and mitochondrial membranes

Yuri N. Antonenko[1#], Marta Jędrzejczyk[2#], Tatyana I. Rokitskaya[1], Ljudmila S. Khailova[1], Elena A. Kotova[1], and Adam Huczyński[2]

[1]*Belozersky Institute of Physico-Chemical Biology, Lomonosov Moscow State University, Leninskie Gory 1, Moscow 119991, Russia*
[2]*Department of Medical Chemistry, Faculty of Chemistry, Adam Mickiewicz University, Uniwersytetu Poznańskiego 8, 61-614 Poznań, Poland*

Supporting information

Materials

Reagents were purchased from Sigma-Aldrich unless specified otherwise. Sucrose was from ICN, 1,2-di-*O*-phytanyl-sn-glycero-3-phosphocholine (DPhytanylPC), 1-palmitoyl-2-oleoyl-glycero-3-phosphocholine (POPC), 1-palmitoyl-2-oleoyl-sn-glycero-3-phospho-(1'-rac-glycerol) (POPG) and cholesterol were purchased from Avanti Polar Lipids. Dodecyltriphenylphosphonium bromide (C_{12}-TPP) was prepared in our laboratory, as described in [1].

Synthesis of triphenylphosphonium (TPP^+)-linked derivatives of salinomycin (SAL-TPP^+)

General procedure

All reagents and all solvents were obtained from Merck or Trimen Chemicals S.A. (Poland), and were used as received without further purification. CD_2Cl2 and CD_3CN spectral grade solvents were stored over 3Å molecular sieves for several days. Reaction mixtures were stirred using teflon-coated magnetic stir bars and were monitored by thin layer chromatography (TLC) using aluminum-backed plates (Merck 60F254). TLC plates were visualized by UV-light (254 nm), followed by treatment with phosphomolybdic acid (PMA, 5% in absolute EtOH) and gentle heating. Products of the reactions were purified using CombiFlash® Rf^+ Lumen Flash Chromatography System (Teledyne Isco) with integrated ELS and UV detectors. All solvents used in flash chromatography were of HPLC grade (Merck) and were used as received. Solvents were removed using a rotary evaporator.

NMR spectra were recorded on a Varian 400 (^1H NMR at 403 MHz, ^{13}C NMR at 101 MHz) magnetic resonance spectrometer. 1H NMR spectra are reported in chemical shifts downfield from TMS using the respective residual solvent peak as internal standard (CD_2Cl_2 δ 5.32 ppm and CD_3CN δ 2.04 ppm). Significant peaks are reported within the overlapping ~2.00–0.50 ppm region of the ^1H NMR spectra. The ^{13}C NMR spectra are reported in chemical shifts downfield from TMS using the respective residual solvent peak as internal standard (CD_2Cl_2 δ 53.84 ppm and CD_3CN δ 118.69 ppm and 1.39 ppm). Line broadening parameters were 0.5 or 1.0 Hz, while the error of chemical shift value was 0.1 ppm.

The electrospray ionization (ESI) mass spectra were recorded on a Waters/Micromass ZQ mass spectrometer (Waters Alliance) equipped with a Harvard syringe pump. The samples were prepared in dry acetonitrile, and were infused into the ESI source using a Harvard pump at a flow rate of 20 ml min–1. The ESI source potentials were: capillary 3 kV, lens 0.5 kV, and extractor 4 V. The standard ESI mass spectra were recorded at the cone voltages of 10 and 30 V. The source temperature was 120 °C and the desolvation temperature was 300 °C. Nitrogen was used as the nebulizing and desolvation gas at flow-rates of 100 dm^3 h^{-1}. Mass spectra were acquired in the positive ion detection mode with unit mass resolution at a step of 1 m/z unit. The mass range for ESI experiments was from m/z = 300 to m/z = 1500.

The HRMS spectra were recorded using high resolution hybrid quadrupole-time-of-flight (TOF) mass spectrometer (Impact HD, Bruker Daltonics) in the positive ion mode.

SAL (**1**) was isolated as sodium salt from commercially available veterinary premix SACOX®, using the procedure described previously [2,3]. Thereafter, isolated sodium salt of **SAL** was dissolved in CH_2Cl_2 and vigorously stirred with a layer of aqueous sulphuric acid (pH 1.0). Then organic layer containing **SAL** was washed with distilled water, and CH_2Cl_2 was evaporated under reduced pressure to dryness giving **SAL** as clear oil. After the 3-times repeated evaporation with n-pentane, this oil was transformed to white amorphous solid. The spectral properties of **SAL** were in agreement with the previously published data.

Synthesis of compound ***2***

To a solution of **SAL** (1 eq.) in dichloromethane, DMAP (5 eq.), TMSEtOH (6 eq.) and TCFH (1.2 eq.) were added successively. The reaction mixture was cooled in an ice bath for the first 2 hours, then the reaction was conducted for 22 hours under room temperature. The mixture was concentrated under reduced pressure with silica gel and the residue was purified by column flash chromatography using CombiFlash®Rf+ (hexane/ethyl acetate, increasing concentration gradientt) with an integrated Evaporative Light Scattering Detector (ELSD) and UV detector.
Yield: 58.00 %
ESI-MS for $C_{47}H_{82}O_{11}Si$ (*m/z*): $[M+Na]^+$ 874.

Synthesis of compound ***3***

To a solution of **2** in anhydrous tetrahydrofuran, triphenylphosphine (1.5 eq.) was added. After 15 minutes of stirring, DIAD (1.2 eq.) was added. After the next 15 minutes, DPPA (1.1 eq.) was introduced. The reaction mixture was cooled in an ice bath during the addition of reagents. The mixture was stirred for 3 days and then was concentrated under reduced pressure to dryness. The residue was purified by column flash chromatography using CombiFlash®Rf+ (hexane/ethyl acetate, increasing concentration gradient) with an integrated Evaporative Light Scattering Detector (ELSD) and UV detector.
Yield: 53.10 %
ESI-MS for $C_{47}H_{8}1N_3O_{10}Si$ (*m/z*): $[M+Na]^+$ 899, $[M+K]^+$ 915

Synthesis of compound ***4***

To a solution of **3** in tetrahydrofuran, TBAF (3 eq.) was added. The mixture was stirred for 24 hours. Then the organic solvent was removed by evaporation under reduced pressure to dryness. The residue was purified chromatographically by CombiFlash®Rf+ system (hexane/ethyl acetate, increasing concentration gradient) with an integrated Evaporative Light Scattering Detector (ELSD) and UV detector.
Yield: 68.20 %

Synthesis of compound ***5***

Under a nitrogen atmosphere, to a solution of **4** (1.0 eq.) in anhydrous CH_3CN, triphenylpropargylphosphonium bromide (2.5 eq.) and DIPEA (2.0 eq.) were added, followed by the addition of catalytic CuI (0.2 eq.) in one portion. The reaction mixture was stirred at room temperature for 24 h, then the organic solvent was evaporated under reduced pressure to dryness and purified by column flash chromatography using CombiFlash®Rf+ (chloroform/ethyl acetate/acetone, increasing concentration gradient) with an integrated Evaporative Light Scattering Detector (ELSD).
Yield: 37.60 %
ESI-MS for $C_{63}H_{87}N_3O_{10}P^+$ (*m/z*): $[M]^+$ 1077

HR-MS (*m/z*) calculated for $C_{63}H_{87}N_3O_{10}P^+$ 1076.6124; found 1076.6088
^{13}C NMR (101 MHz, CD_3CN) δ 214.8, 170.9, 136.1, 136.0, 134.9, 134.8, 134.6, 134.5, 131.7, 131.6, 131.5, 131.3, 108.3, 99.8, 89.7, 79.9, 77.9, 74.5, 74.2, 73.3, 71.5, 70.3, 58.9, 55.7, 49.8, 48.1, 40.7, 39.2, 37.3, 36.9, 33.7, 32.9, 31.9, 30.4, 29.5, 26.8, 25.3, 24.0, 23.9, 22.4, 22.3, 21.6, 20.9, 18.5, 17.6, 16.7, 15.2, 14.8, 13.9, 12.5, 12.1, 8.5, 6.9 (signals overlapped)
^{1}H NMR (400 MHz, CD_3CN) δ 7.93 – 7.54 (m, 11H), 6.58 – 6.39 (m, *J* = 14.5, 14.0, 10.9, 1.0 Hz, 2H), 6.08 – 5.91 (m, 2H), 4.01 – 3.93 (m, 1H), 3.86 (dd, *J* = 5.1, 0.8 Hz, 1H), 3.78 – 3.71 (m, 1H), 3.69 – 3.58 (m, 3H), 3.49 (dd, *J* = 9.7, 2.4 Hz, 1H), 3.45 – 3.32 (m, 2H), 3.12 (ddd, *J* = 14.8, 7.4, 4.2 Hz, 2H), 3.04 – 2.91 (m, 2H), 2.68 – 2.54 (m, 2H), 2.47 – 2.42 (m, 1H), 2.40 (d, *J* = 2.4 Hz, 1H), 2.16 – 2.06 (m, 2H), 2.02 – 0.06 (m, 53H).

*Synthesis of compound **6***

To a solution of **SAL** (1 eq.) in *N,N*-dimethylformamide, DBU (1.75 eq.) was added. The reaction mixture was stirred and heated in temperature 100–110°C. After 15 minutes (4-bromobutyl)triphenylphosphonium bromide (2.2 eq.) was added and the mixture was stirred and heated for another 5 h. Then the reaction was conducted for next 19 h in a room temperature. The organic solvent was removed by evaporation under reduced pressure to dryness by using three portions of toluene and three portions of acetonitrile. Then the residue was purified chromatographically by CombiFlashR+ system (chloroform/acetone, increasing concentration gradient) with an integrated Evaporative Light Scattering Detector (ELSD).
Yield: 31.5 %
ESI-MS for $C_{64}H_{92}O_{11}P^+$ (*m/z*): $[M]^+$ 1068
HR-MS (*m/z*) calculated for $C_{64}H_{92}O_{11}P^+$ 1067.6372; found 1067.6343
^{13}C NMR (101 MHz, CD_3CN) δ 215.9, 176.5, 1362, 136.2, 134.7, 134.6, 131.4, 131.3, 107.3, 100.0, 88.7, 79.8, 77.9, 75.8, 75.0, 72.6, 71.3, 70.4, 68.3, 64.5, 57.7, 49.6, 47.9, 41.5, 39.4, 37.4, 37.3, 34.3, 32.1, 31.3, 30.2, 30.0, 29.9, 28.9, 26.7, 26.3, 23.4, 22.8, 22.5, 22.0, 19.9, 19.9, 19.8, 17.9, 16.0, 15.4, 14.8, 13.5, 12.3, 11.6, 7.9, 6.8. (signals overlapped)
^{1}H NMR (401 MHz, CD_2Cl_2) δ 7.86 – 7.68 (m, 10H), 5.97 (dd, *J* = 31.0, 10.7 Hz, 2H), 4.41 – 4.32 (m, 1H), 4.16 – 4.08 (m, 1H), 3.95 – 3.83 (m, *J* = 19.2, 9.5 Hz, 4H), 3.82 – 3.67 (m, *J* = 23.1, 15.8, 9.9 Hz, 4H), 3.60 – 3.50 (m, *J* = 20.8, 10.7, 5.4 Hz, 5H), 3.06 – 2.94 (m, 2H), 2.79 (t, *J* = 5.3 Hz, 1H), 2.63 – 2.57 (m, 1H), 2.48 (s, 1H), 2.37 – 0.47 (m, 60H).

*Synthesis of compound **7***

To a solution of **SAL** (1 eq.) in toluene, DBU (1.75 eq.) was added. The reaction mixture was stirred and heated in temperature 90–100°C. After 15 minutes 1,6-dibromohexane (2.2 eq.) was added and the mixture was stirred and heated for another 5 h. Then the reaction was conducted for next 19 h in a room temperature. The organic solvent was removed by evaporation under reduced pressure to dryness by using three portions of acetonitrile. Then the residue was evaporated under reduced pressure with silica gel and purified chromatographically by CombiFlashR+ system (hexane/ethyl acetate, increasing concentration gradient) with an integrated Evaporative Light Scattering Detector (ELSD) and UV detector.
Yield: 73.00 %

*Synthesis of compound **8***

To a solution of (4-carboxybutyl)triphenylphosphonium bromide (1 eq.) in *N,N*-dimethylformamide, DBU (1.5 eq.) was added. The reaction mixture was stirred and heated in temperature 100–110°C. After 15 minutes compound **7** (0.5 eq.) was added and the mixture was stirred and heated for another 5 h. Then the reaction was conducted for next 19 h in a room temperature. The organic solvent was removed by evaporation under reduced pressure to dryness by using three portions of toluene and three portions of acetonitrile. Then the residue was purified chromatographically by CombiFlashR+ system (chloroform/acetone, increasing concentration gradient) with an integrated Evaporative Light Scattering Detector (ELSD).

Yield: 88.15%
ESI-MS for $C_{71}H_{104}O_{13}P^+$ (*m/z*): $[M]^+$ 1196
HR-MS (*m/z*) calculated for $C_{71}H_{104}O_{13}P^+$ 1195.7209; found 1195.7193
^{13}C NMR (101 MHz, cd_3cn) δ 214.9, 176.5, 173.7, 136.2, 136.1, 134.8, 134.7, 133.9, 131.4, 131.3, 121.9, 119.8, 107.3, 100.0, 88.7, 80.2, 77.9, 75.7, 75.0, 72.7, 71.3, 70.3, 68.4, 65.6, 65.10, 57.5, 49.6, 48.0, 41.5, 39.4, 37.3, 37.3, 34.2, 33.8, 32.1, 31.3, 30.2, 29.4, 29.3, 29.1, 26.9, 26.5, 26.4, 26.4, 26.3, 23.5, 22.9, 22., 22.54, 22.5, 22.3, 20.5, 20.1, 17.9, 16.0, 15.4, 14.7, 13.5, 12.3, 11.5, 8.0, 6.8 (signals overlapped)
^{1}H NMR (401 MHz, CD_3CN) δ 7.91 – 7.63 (m, 10H), 5.93 (dd, 2H), 4.32 (dt, *J* = 10.9, 6.7 Hz, 1H), 4.11 (dt, *J* = 10.9, 6.5 Hz, 3H), 3.96 (t, *J* = 6.7 Hz, 4H), 3.69 (q, *J* = 6.9 Hz, 1H), 3.59 (ddd, *J* = 19.5, 10.1, 4.0 Hz, 4H), 3.51 – 3.41 (m, 1H), 3.35 – 3.26 (m, 3H), 3.14 – 3.05 (m, 1H), 3.00 (td, *J* = 10.6, 4.7 Hz, 1H), 2.89 – 2.82 (m, 1H), 2.64 (d, *J* = 5.6 Hz, 1H), 2.63 – 2.57 (m, 1H), 2.38 – 0.58 (m, 70H).

Assessment of K^+/H^+-exchange activity using pyranine-loaded liposomes

The lumenal pH of the liposomes was assayed with by a slightly modified procedure of [4]. To prepare pyranine-loaded liposomes, lipid (5.5 mg POPC, 1.5 mg POPG and 3 mg cholesterol) in a chloroform suspension was dried in a round-bottom flask under a stream of nitrogen. The lipid was then resuspended in 1 ml of buffer (100 mM KCl, 20 mM MES, 20 mM MOPS, 20 mM Tricine titrated with KOH to pH 6.0) containing 0.5 mM pyranine. The suspension was vortexed and then freeze-thawed three times. Unilamellar liposomes were prepared by extrusion through 0.1-µm-pore size Nucleopore polycarbonate membranes using an Avanti Mini-Extruder. The unbound pyranine was then removed by passage through a Sephadex G-50 coarse column equilibrated with the same buffer solution and stored at 4°C. To measure the rate of pH dissipation in liposomes with lumenal pH 6.0, the liposomes were diluted in solution with the same pH and supplemented with 2 mM *p*-xylene-bis-pyridinium bromide to suppress the fluorescence of leaked pyranine. The inner liposomal pH was estimated from the pyranine fluorescence intensity measured at 505 nm upon excitation at 455 nm with the Panorama Fluorat 02 spectrofluorimeter [5]. At the end of each recording, 1 µM lasalocid A was added to dissipate the remaining pH gradient. All experiments with liposomes were carried out at 15°C.

Electrical current across planar lipid bilayers

Planar bilayer lipid membranes (BLM) were formed from a solution of 1,2-di-*O*-phytanyl-sn-glycero-3-phosphocholine (DPhytanylPC) in n-decane (Avanti Polar Lipids). The membranes [6] were spread from a lipid solution in n-decane across a circular aperture (0.8 mm in diameter) in a polytetrafluorethylene septum, which separated two aqueous phases of a PTFE chamber. Membrane thinning was observed optically and electrically, via the determination of membrane capacitance. The electric currents (*I*) were recorded under voltage-clamp conditions. Voltages were applied to BLMs with Ag-AgCl electrodes connected via agar bridges. The currents measured by means of a patch-clamp amplifier (OES-2, OPUS, Moscow) were digitized using an NI-DAQmx (National Instruments) and analyzed with a personal computer with the use of WinWCP Strathclyde Electrophysiology Software designed by J. Dempster (University of Strathclyde). In the current relaxation experiments the voltage was switched from zero to some particular value of V at $t = 0$ and the current across the membrane ($I(t)$) started to decrease from the initial level I_0 to steady-state level I_∞. At the beginning of each experiment we recorded capacitance response of the unmodified membrane (control record of the current after voltage-jump). Cationic compounds **5**, **6**, **8** and C_{12}-TPP were added from stock solutions in ethanol to the bathing solutions at both sides of the BLM and incubated for at least 10 min with constant stirring. The record in the presence of a hydrophobic cation was analyzed after subtraction of the control record. In most of the experiments, the solution contained 10 mM KCl, 10 mM Tris, 10 mM Mes, 10 mM β-Ala pH=6.8. All experiments were carried out at room temperature (23-25°C).

Isolation of rat liver mitochondria

Rat liver mitochondria (RLM) were isolated by differential centrifugation [7] in a medium containing 250 mM sucrose, 5 mM MOPS, 1 mM EGTA, pH 7.4. The final washing was performed in the medium additionally containing bovine serum albumin (0.1 mg/ml). Protein concentration was determined using the Biuret method. Handling of animals and experimental procedures were conducted in accordance with the international guidelines for animal care and use and were approved by the Institutional Ethics Committee of A.N. Belozersky Institute of Physico-Chemical Biology at the Moscow State University (protocol #3 on February 12, 2018).

Swelling of mitochondria

The K^+/H^+-exchange activity of **SAL** and its analogs was tested by induction of swelling of non-respiring rat liver mitochondria incubated in buffered isotonic potassium acetate. Under these conditions, mitochondria do not swell, because acetate can cross the membrane only as undissociated acetic acid [8]. Swelling of mitochondria was recorded as a decrease in absorbance of the mitochondrial suspension at 550 nm. In short, an aliquot of mitochondria was added to 1 ml of the `swelling medium' containing 145 mM potassium acetate, 5 mM Tris, 0.2 mM EDTA, 1 µM rotenone at pH 7.4. Kinetic experiments were carried out at room temperature (23-25°C).

Mitochondrial membrane potential measurements

Membrane potential was measured with the help of a tetraphenylphosphonium (TPP)-sensitive electrode (NIKO-ANALIT, Moscow, Russia). The incubation medium contained 250 mM sucrose, 5 mM MOPS, 1 mM EGTA, pH 7.4. Mitochondrial protein concentration was 0.4 mg/ml. Kinetic experiments were carried out at room temperature (23-25°C).

References

1. T.I.Rokitskaya, N.V.Sumbatyan, V.N.Tashlitsky, G.A.Korshunova, Y.N.Antonenko, V.P.Skulachev, Mitochondria-targeted penetrating cations as carriers of hydrophobic anions through lipid membranes, Biochim.Biophys. Acta 1798 (2010) 1698-1706.

2. M.Antoszczak, K.Popiel, J.Stefanska, J.Wietrzyk, E.Maj, J.Janczak, G.Michalska, B.Brzezinski, A.Huczynski, Synthesis, cytotoxicity and antibacterial activity of new esters of polyether antibiotic - salinomycin, Eur. J. Med. Chem. 76 (2014) 435-444.

3. M.Antoszczak, E.Maj, J.Stefanska, J.Wietrzyk, J.Janczak, B.Brzezinski, A.Huczynski, Synthesis, antiproliferative and antibacterial activity of new amides of salinomycin, Bioorg. Med. Chem. Lett. 24 (2014) 1724-1729.

4. Y.Chen, M.Schindler, S.M.Simon, A mechanism for tamoxifen-mediated inhibition of acidification, J. Biol. Chem. 274 (1999) 18364-18373.

5. S.S.Denisov, E.A.Kotova, L.S.Khailova, G.A.Korshunova, Y.N.Antonenko, Tuning the hydrophobicity overcomes unfavorable deprotonation making octylamino-substituted 7-nitrobenz-2-oxa-1,3-diazole (n-octylamino-NBD) a protonophore and uncoupler of oxidative phosphorylation in mitochondria, Bioelectrochemistry 98 (2014) 30-38.

6. P.Mueller, D.O.Rudin, H.T.Tien, W.C.Wescott, Methods for the formation of single bimolecular lipid membranes in aqueous solution, J. Phys. Chem. 67 (1963) 534-535.

7. D.Johnson, H.Lardy, Isolation of liver or kidney mitochondria, Methods Enzymol. 10 (1967) 94-96.

8. G.P.Brierley, Passive permeability and energy-linked ion movements in isolated heart mitochondria, Ann. N. Y. Acad. Sci. 227 (1974) 398-411.

PUBLIKACJA III
wraz z suplementem

Marta Jędrzejczyk, Michał Sulik, Magdalena Mielczarek-Puta, Gwan Yong Lim, Małgorzata Podsiad, Jakub Hoser, Piotr Bednarczyk, Marta Struga, Adam Huczyński

„Anticancer activity of salinomycin quaternary phosphonium salts"

European Journal of Medicinal Chemistry 282 (2025) 117055

European Journal of Medicinal Chemistry 282 (2025) 117055

Contents lists available at ScienceDirect

European Journal of Medicinal Chemistry

journal homepage: www.elsevier.com/locate/ejmech

Research paper

Anticancer activity of salinomycin quaternary phosphonium salts

Marta Jędrzejczyk [a], Michał Sulik [a], Magdalena Mielczarek-Puta [b], Gwan Yong Lim [b], Małgorzata Podsiad [b], Jakub Hoser [c], Piotr Bednarczyk [c], Marta Struga [b], Adam Huczyński [a,*]

[a] Department of Medical Chemistry, Faculty of Chemistry, Adam Mickiewicz University, Uniwersytetu Poznańskiego 8, 61–614, Poznań, Poland
[b] Chair and Department of Biochemistry, Faculty of Medicine, Medical University of Warsaw, Banacha 1, 02–097, Warsaw, Poland
[c] Department of Physics and Biophysics, Institute of Biology, Warsaw University of Life Sciences SGGW, Nowoursynowska 159, 02-776, Warsaw, Poland

ARTICLE INFO

Keywords:
Ionophores
Mitochondria-targeting
Triphenylphosphine
TPP cation
Anticancer

ABSTRACT

In recent years salinomycin has emerged as a promising anticancer drug. Many literature reports have proved its remarkable antiproliferative activity. Moreover, chemical modifications of salinomycin lead to analogues with even higher cytotoxicity against cancer cell lines and a better selectivity index for malignant cells than those of the unmodified compound or a standard anticancer drug such as doxorubicin. In this paper we report the synthesis of a series of twelve novel salinomycin conjugates and their characterization by spectroscopic and spectrometric methods. Salinomycin was conjugated with different triphenylphosphonium cations in order to find out whether the conjugation with mitochondrial targeting vectors would have a beneficial impact on biological properties. Salinomycin and its novel conjugates were tested to determine their *in vitro* antiproliferative and antimicrobial activity. Taking into account the presence of triphenylphosphonium moiety, the impact of the obtained analogues on mitochondria activity was evaluated by MitoTrackers dyes, furthermore their apoptosis effect and cell cycle arrest were assessed. In addition, the changes in the mitochondrial membrane potential were measured and the ability to generate reactive oxygen species was assessed. Finally, we conducted biophysical studies to investigate the impact of the obtained salinomycin analogues on mitochondrial respiration rates and their electrophysiological properties. Results of this study have proved that conjugation of salinomycin with phosphonium cations leads to promising results in the search for promising anticancer agents.

1. Introduction

Mitochondria are one of the most significant organelles in the intracellular environment. Because of their crucial role in energy metabolism and the regulation of the apoptosis process, they are generally known as a “powerhouse of the cell” [1]. It has been proven for decades that improper functioning of mitochondria is associated with human diseases such as cancer, diabetes, and neurodegenerative disorders [2]. Furthermore, mitochondrial dysfunctions contribute to carcinogenesis and cancer progression. These effects result from the fact that metabolism in malignant mitochondria differs from that in their normal cell counterparts and the proliferation process progresses more rapidly, which is followed by much higher rates of glycolysis than in non-malignant organelles [3]. Nowadays, discovering effective cancer treatment is still an enormous challenge for scientific world. It is a widely known fact that the methods of cancer treatment such as chemotherapy and radiotherapy are insufficient strategies because of their low selectivity and developed multi-drug resistance of cancer cells. It proves that looking for a new approach to cancer therapy is an urgent problem and mitochondria-targeting therapeutic strategies can be promising for this purpose [4] (see Scheme 1).

It has been shown that the membrane of malignant mitochondria is hyperpolarized (−220 mV) in comparison to their healthy counterparts (−160 mV), which facilitates the penetration of positively charged molecules to the cancer cells mitochondria [5]. An excellent example of this kind of molecule is triphenylphosphonium cation (TPP), which plays the pivotal role as a mitochondrial targeting vector. TPP ion bears a positive charge delocalized over three phenyl rings and stabilized by resonance, besides, the lipophilic character of the cation increases its ability to penetrate the hydrophobic inner mitochondrial membrane [6]. Over the last decade the interest in mitochondria targeting strategy has increased and numerous examples of using TPP as a ligand have been reported [6,7]. In 2013, the conjugation of chlorambucil molecule with TPP was studied. Chlorambucil belongs to the class of nitrogen mustards

---

* Corresponding author.
E-mail address: adhucz@amu.edu.pl (A. Huczyński).

https://doi.org/10.1016/j.ejmech.2024.117055
Received 4 October 2024; Received in revised form 31 October 2024; Accepted 11 November 2024

and has been widely used in chemotherapy as a DNA damaging anticancer agent. The conjugate TPP-chlorambucil was examined using breast and pancreatic cancer cell lines, which were insensitive to the parent drug. The cytotoxicity results revealed that TPP derivative exhibited even 12-fold higher activity against breast cancer cells in comparison to unmodified chlorambucil, and reversed drug resistance in both panels of breast and pancreatic cancer cell lines [7]. As follows from the reports, the conjugation of this compound with TPP ion can lead to promising results for cancer therapy and should be considered as a new approach. Furthermore, it is worth mentioning that conjugation with TPP moiety positively impacts antimicrobial activity. The study conducted by Pavlova et al. has evidenced that TPP derivatives of chloramphenicol show the ability to be dual-acting compounds by targeting the ribosomes and cellular membranes of bacteria at the same time [8]. Additionally, three years later, subsequent derivatives of chloramphenicol obtained by Li et al., showed promising therapeutic effects against methicillin-resistant *Staphylococcus aureus* (MRSA) both *in vitro* and *in vivo* [9]. In 2024 the antibacterial activity of TPP analogues of naturally occurring thymol was proved to be nearly 100 times higher than that of unmodified monoterpene phenol [10].

Bearing that in mind, salinomycin (**SAL**) as a one of the most active compounds from among ionophore antibiotics would be also a good candidate for conjugation with TPP. It is a well-known polyether compound with natural origin which exhibits a vast spectrum of biological properties, such as antimicrobial, antiparasitic, antifungal, and antiproliferative activity [11]. For the first time **SAL** was isolated from *Streptomyces albus* during screening tests devoted to seeking new antibiotics in 1974. Currently, **SAL** is commonly used in veterinary medicine as a coccidiostatic agent for poultry and cattle [12]. Its wide spectrum of biological activity is related to the ability of transporting metal cations (especially Na^+ and K^+) through bilayer lipid membranes into a cell. It leads to the disturbance of intracellular pH, mitochondrial injuries, increase in the osmotic pressure, formation of vacuoles in a cell, and finally programmed cell death called apoptosis [13].

Since 2009, the perception of **SAL** as a potential anticancer drug has changed fundamentally. In that year an insightful screening of about 16,000 compounds was conducted to identify agents with specific toxicity towards epithelial cancer stem cells (CSCs) in breast cancer. **SAL** was shown as the most active agent among tested compounds and exhibited nearly 100-fold higher activity than commercially available paclitaxel (Taxol®) used in chemotherapy [14]. It is worth noting that CSCs play a significant role in disease progression, hence, by directly targeting CSCs it is possible to prevent the spreading of cancer cells and even cancer relapses [15]. Moreover, there are many literature reports which have proved that chemical modifications of **SAL** can lead to analogues exhibiting higher cytotoxicity and better selectivity [16]. By combining all presented facts, the conclusion is simple to put: the search for novel **SAL** derivatives can be a promising direction for future scientific medicine. Furthermore, in 2022 we have already proved that rational conjugation of **SAL** with TPP resulted in biologically attractive analogues. In the test with natural membranes from rat liver mitochondria, we were able to induce the mitochondrial swelling using one of the SAL-TPP salts which indicated its accumulation inside the organelle [17]. That is precisely why in this study we have attempted to design and synthesize a series of **SAL** conjugates combined with the phosphonium cation. Our overriding goal was to modify the carboxyl group at the C-1 position and examine the antiproliferative and antimicrobial activities of the obtained derivatives. Additionally, by conducting biophysical studies it was possible to investigate the impact of the synthesized compounds on cellular respiration and find out whether there is a difference between classic benzyl ester and TPP esters bearing positive charge.

2. Results and discussion

2.1. Design and synthesis of SAL-TPP$^+$ hybrid compounds

Twelve ester salts of **SAL** were obtained in a two-step synthesis via a rational and chemical modification of carboxyl group at C-1 position. The **SAL** analogues differed in the length of carbon chain and the type of phosphonium cation. Conjugation of molecules with TPP cation was not a totally new concept. In 2017 Zielonka et al. described how beneficial

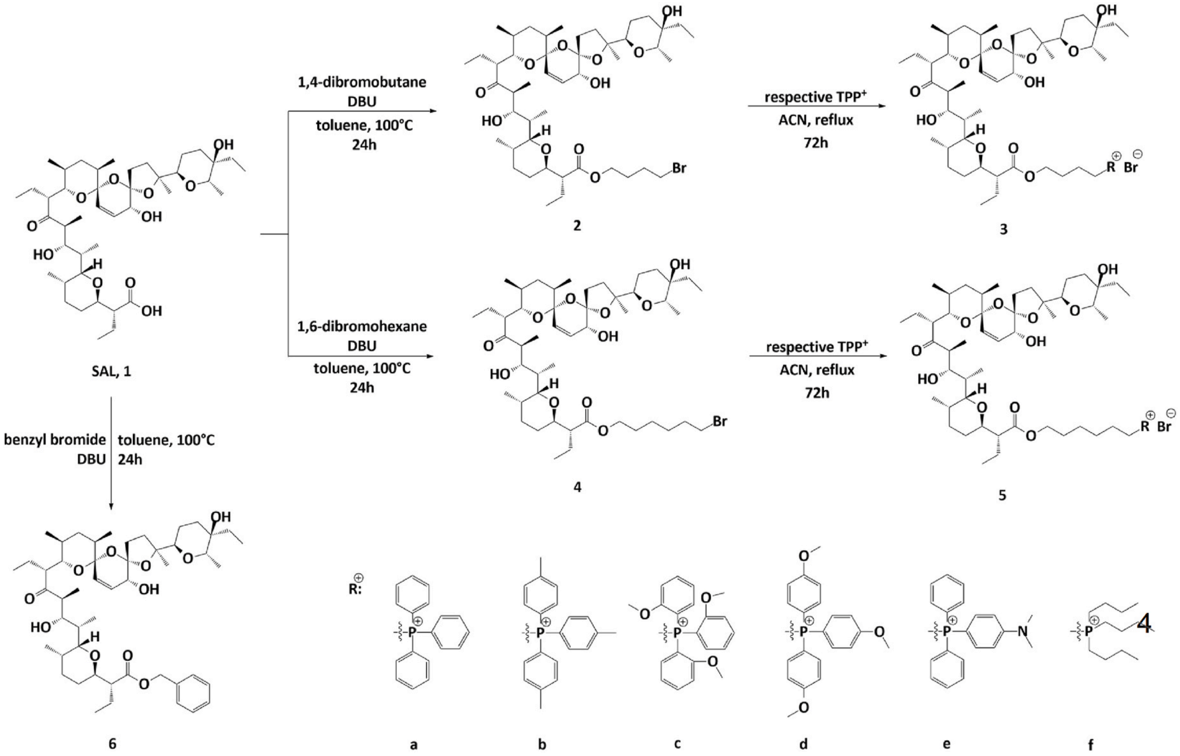

Scheme 1. Synthesis of **SAL** conjugates.

can be the linking of biologically active compounds with mitochondria-targeting moiety such as TPP, using different types of linkers [6]. Additionally, in 2019 Rokitskaya et al. performed a series of tests to measure TPP penetration through the lipid membrane depending on the substituents introduced into the aromatic rings [18]. Considering the results of the above-mentioned literature reports, we designed a series of esters that differ in carbon chain length and bear various substituents. By implementing five different cations with substituted aromatic rings and one alkyl cation, it was possible to determine the structure and activity relationship (SAR) of the derivatives and to investigate how the implementation may impact the ability of the obtained compounds to penetrate through biological membranes. It is worth mentioning that during the project implementation, Tsyganov et al. confirmed that the length of a linker chain may affect the activity of TPP-conjugated molecules [19]. Likewise in the beginning of 2024, Rokitskaya et al. proved that methylation of aromatic rings in TPP moiety can enhance the protonophoric activity, increasing proton transport across lipid membranes and uncoupling of mitochondria [20]. Therefore, using different substituents we also were able to investigate whether the electron density on the aromatic rings affects the analogues' properties. Additionally, benzyl ester **6** was synthesized to check its biological activity and the effect on the cellular respiration in comparison to those of the TPP analogues, which also permitted to establish if the appearance of phosphonium cation in the structure was crucial.

Salinomycin sodium salt (**SAL-Na**) was isolated from commercially available veterinary premix - SACOX®, according to the procedures presented previously [18]. To obtain the acidic form (**SAL**, **1**), SAL-Na was dissolved in CH$_2$Cl$_2$ and the extraction with sulphuric acid solution (pH = 1) was conducted [21].

Compounds **2**, **4**, and **6** were obtained by one of the esterification methods. It is worth pointing to the fact that **SAL** is sensitive to harsh acidic conditions and rapid heating, hence the reaction conditions have to be selected with caution. From among the available esterification methods, we chose a well-known procedure to be run in mild conditions and with a satisfying yield, for example compound **2** was obtained with 87.6 % yield. The appropriate bromides with 1,8-diazabicyclo[5.4.0]undec-7-ene (DBU) were used as non-nucleophilic bases, following the procedure described previously [22]. The next synthesis step was a substitution reaction (S$_N$1) between esters (**2** or **4**) and the appropriate phosphonium cation to obtain the final products **3a**-**3f**, and **5a**-**5f**. The reaction was conducted by heating at 70 °C for 72 h in acetonitrile.

All **SAL** derivatives were easily purified by CombiFlash®Rf+ (chloroform/acetone, increasing concentration gradient) combined with Evaporative Light Scattering Detector (ELSD) and Electrospray Ionization (ESI) mass spectroscopy.

The structures of the newly synthesized derivatives of **SAL** (**3a–3f** and **5a–5f**) were determined using spectroscopic (^{1}H NMR, ^{13}C NMR, ^{31}P NMR) and spectrometric (HRMS) methods. In the ^{13}C NMR spectra of **SAL** derivatives, the signals of the highest analytical significance were assigned to the carbonyl group of the ester moiety at C1 position. Depending on the type of substituent and linker used, the signal from the ester group appeared in the narrow range of 176.5–176.2 ppm. In the ^{31}P NMR spectra, the signal from the phosphonium salt appeared in the range of -22.53–35.03 ppm depending on the type of substituent used. The HRMS analysis confirmed the formation of the desired products, with [M]$^+$ as the main peak (intensity 100 %). The relative error associated with the analysis was small and ranged from 0.1 ppm to 2.6 ppm depending on the compound tested.

2.2. Biological activity

2.2.1. Antiproliferative activity

The cytotoxic activity of **SAL** and its derivatives **3a-6** was assessed against seven selected cell lines to evaluate their therapeutic potential. The cell lines included five cancer cell lines (SW480, SW620, PC3, MDA-MB-231, A549) and two non-cancerous cell lines (HaCaT and V79). Cytotoxic activity was determined using the 3-[4,5-dimethylthiazole-2-yl]-2,5-diphenyltetrazolium bromide (MTT) colorimetric assay and expressed as inhibitory concentrations (IC$_{50}$). Additionally, the selectivity index (SI) was used to evaluate the compounds' specificity toward neoplastic cell lines. As a well-established anticancer regimen, doxorubicin was used as a reference drug in this biological study.

In the MTT assay, the derivatives conjugated with TPP cation (**3a-f**, **5a-f**) exhibited high cytotoxic activity towards cancer cells with IC$_{50}$ below 1 μM, except for PC3 cell line. Additionally, **3a-5f** compounds showed more potent anticancer effects compared to that of **SAL**, except for compound **5a**, which showed higher IC$_{50}$ values towards SW620 and MDA-MB-231 cells. On the other hand, compound **6** exhibited weaker cytotoxic effects on all cell lines chosen for the study. The antiproliferative ability of **SAL** derivatives towards SW480 and PC3 cells was 2–3 times higher than that of **SAL**, while their activity towards SW620 and A549 cells was even 4–5 times higher compared to that of the unmodified antibiotic (Table 1). Table 2 shows the selectivity index (SI) values of each compound measured for all of the human cancer and normal cell lines used in the study. SI was calculated as the ratio of

Table 1

Cytotoxicity (IC$_{50}$, μM) of studied compounds estimated by the MTT assay [23].

	Cancer cell lines					Non-tumor cell lines	
	SW480	SW620	PC3	MDA-MB-231	A549	HaCaT	V79
SAL, 1	1.36 ± 0.01	1.81 ± 0.08	3.00 ± 0.34	1.22 ± 0.19	1.86 ± 0.04	0.80 ± 0.19	1.44 ± 0.33
3a	0.39 ± 0.15	0.14 ± 0.01	1.35 ± 0.19	0.74 ± 0.01	0.67 ± 0.07	1.23 ± 0.02	0.13 ± 0.03
3b	0.44 ± 0.09	0.50 ± 0.04	2.21 ± 1.77	0.83 ± 0.17	0.81 ± 0.05	1.02 ± 0.33	3.77 ± 0.24
3c	0.56 ± 0.37	1.25 ± 0.34	0.88 ± 0.06	0.74 ± 0.08	0.70 ± 0.05	0.94 ± 0.19	0.64 ± 0.13
3d	0.73 ± 0.10	1.28 ± 0.46	2.24 ± 0.31	1.42 ± 0.23	0.66 ± 0.12	1.12 ± 0.19	0.67 ± 0.08
3e	0.57 ± 0.13	0.11 ± 0.05	2.52 ± 1.27	0.78 ± 0.17	0.75 ± 0.11	1.28 ± 0.08	0.37 ± 0.10
3f	0.49 ± 0.09	0.52 ± 0.05	1.45 ± 0.31	0.90 ± 0.09	0.86 ± 0.05	0.70 ± 0.12	0.59 ± 0.01
5a	0.71 ± 0.07	2.57 ± 0.45	1.85 ± 0.11	2.65 ± 1.15	0.72 ± 0.17	0.78 ± 0.17	0.63 ± 0.06
5b	0.61 ± 0.04	0.72 ± 0.08	1.58 ± 0.19	0.83 ± 0.27	0.98 ± 0.01	1.05 ± 0.27	0.67 ± 0.09
5c	0.71 ± 0.16	0.74 ± 0.18	1.23 ± 0.06	1.15 ± 0.07	0.88 ± 0.08	0.62 ± 0.05	0.56 ± 0.05
5d	0.53 ± 0.12	0.81 ± 0.18	1.40 ± 0.13	0.60 ± 0.03	0.92 ± 0.02	0.63 ± 0.05	0.60 ± 0.07
5e	0.58 ± 0.09	0.71 ± 0.01	1.47 ± 0.26	0.88 ± 0.01	0.85 ± 0.05	0.71 ± 0.05	0.60 ± 0.11
5f	0.50 ± 0.09	0.67 ± 0.14	2.89 ± 0.17	1.02 ± 0.04	1.05 ± 0.21	0.62 ± 0.06	0.65 ± 0.07
6	3.48 ± 0.20	7.77 ± 0.45	8.79 ± 0.20	16.54 ± 2.82	7.52 ± 1.52	8.00 ± 1.36	5.83 ± 1.46
DOX	0.29 ± 0.08	0.31 ± 0.08	0.59 ± 0.02	0.83 ± 0.03	0.63 ± 0.2	0.29 ± 0.01	2.01 ± 0.03

Table 2
The selectivity index of studied compounds [23].

	HaCaT					V79				
	SW480	SW620	PC3	MDA-MB-231	A549	SW480	SW620	PC3	MDA-MB-231	A549
SAL, 1	0.6	0.4	0.3	0.66	0.4	1.1	0.8	0.5	1.2	0.8
3a	3.2	8.8	0.9	1.7	1.8	0.3	0.9	0.1	0.2	0.2
3b	2.3	2.0	0.5	1.2	1.3	8.6	7.5	1.7	4.5	4.7
3c	1.7	0.8	1.1	1.3	1.3	1.1	0.5	0.7	0.9	0.9
3d	1.5	0.9	0.5	0.8	1.7	0.9	0.5	0.3	0.5	1.0
3e	2.2	11.6	0.5	1.6	1.7	0.6	3.4	0.1	0.5	0.5
3f	1.4	1.3	0.5	0.8	0.8	1.2	1.1	0.4	0.7	0.7
5a	1.1	0.3	0.4	0.3	1.1	0.9	0.2	0.3	0.2	0.9
5b	1.7	1.5	0.7	1.3	1.1	1.1	0.9	0.4	0.8	0.7
5c	0.9	0.8	0.5	0.5	0.7	0.8	0.8	0.5	0.5	0.6
5d	1.2	0.8	0.5	1.1	0.7	1.1	0.7	0.4	1.0	0.7
5e	1.2	1.0	0.5	0.8	0.8	1.0	0.8	0.4	0.7	0.7
5f	1.2	0.9	0.2	0.6	0.6	1.3	1.0	0.2	0.6	0.6
6	2.3	1.0	0.9	0.5	1.1	1.7	0.8	0.7	0.3	0.8
DOX	1.0	0.9	0.5	0.3	0.46	6.9	6.5	3.4	2.4	3.2

inhibitory concentration (IC_{50}) of non-cancerous cells (immortal keratinocyte cells (HaCaT) and Chinese hamster lung fibroblasts (V79)) to IC_{50} of the respective cancer cell lines. In the case of HaCaT cells, compound **3a** was categorized as highly selective towards both SW480 and SW620 cells (SI = 3.2 and 8.8 respectively) as well in MDA-MB-231 and A549 cells, with SI values close to 2.0. In addition, compound **3e** with high SI value (11.6 and 2.2 for SW620 and SW480 cells, respectively), indicates its promising therapeutic use. On the contrary, compound **5a**, **5c**, **5f** showed lower selectivity towards SW620, PC3, MDA-MB-231, and A549 cells. Compound **3b** showed low toxic effects on both tested non-tumour cell lines as compared to that shown towards cancer cells (SI values ranged from 1.2 to 8.6). In contrast to HaCaT cells, compound **3a** exhibited low SI values towards V79 cells, similar to the other studied compounds. No significant differences in IC_{50} values for cancer and non-cancer V79 cells may be attributed to the fact that V79 is a non-human cell line.

Data are expressed as mean ± SD (n = 3), IC_{50} (μM) - the concentration of the compound that corresponds to a 50 % growth inhibition of cell line (as compared to the control) after culturing the cells for 72 h with the studied compound. Human primary colon cancer cells (SW480); human metastatic colon cancer cells (SW620); human metastatic prostate cancers (PC3); human breast cancer cells (MDA-MB-231); human lung cancer cells (A549); human immortal keratinocyte cells (HaCaT); Chinese hamster lung fibroblasts (V79). Doxorubicin - the selected reference compound commonly used in cancer treatment (DOX).

The SI (selectivity index) was calculated using the formula: $SI = IC_{50}$ for normal cell line/IC_{50} for cancer cell line. Human primary colon cancer cells (SW480); human metastatic colon cancer cells (SW620); human metastatic prostate cancers (PC3); human breast cancer cells (MDA-MB-231); human lung cancer cells (A549); human immortal keratinocyte cells (HaCaT); Chinese hamster lung fibroblasts (V79). Doxorubicin - the selected reference compound commonly used in cancer treatment (DOX). $SI < 1$ high toxicity, $SI \geq 1$ low toxicity, $SI > 3$ highly selective agents.

To sum up, the obtained **SAL** derivatives exhibited higher anticancer activity against cancer cells compared to that of unmodified **SAL**. Additionally, the cytotoxicity of these derivatives was independent of cell type, highlighting their potential as universal anti-cancer agents. While most of the compounds did not demonstrate exceptionally high selectivity, their low cytotoxic concentrations suggest the possibility of using smaller doses in future clinical applications, potentially reducing side effects. Additionally, the selectivity of most tested compounds surpasses that of **SAL**, indicating a potential therapeutic advantage.

2.2.2. *Mitochondria activity*

MitoTracker Green FM dye binds covalently to mitochondrial proteins and accumulates in the mitochondrial matrix independently of mitochondrial membrane potential (MMP), representing mitochondrial mass.

MitoTracker Red CMXRos dye is attracted to the electronegative interior of mitochondria in living cells, and the intensity of fluorescence represents the condition of mitochondria [24,25].

The results from MTGreen staining cancer cells treated with **SAL** and its derivatives demonstrated the highest, 6-fold increase in the mean fluorescence intensity (MFI) for compounds **3a** and **3f** in A459 cells and almost 8-fold in MDA-MB-231 cells, relative to the control. Above 70 % of MTGreen positive cells were observed in the response to **3a** and **3f** compounds in A549 cells, while this percentage increased to 90 % in MDA-MB-231 cells. A slight increase in MFI was found for compound **6** and **SAL** applied towards both cancer cell lines (Figs. 1 and 2).

The flow cytometry analysis of MTRed CMXRos staining revealed that MFI of A549 cells were about threefold elevated after treatment with **3a** and **3f** derivatives with 50 % of MTRed CMXRos positive cells as compared to the control. Similar results for **3a** compound were obtained for MDA-MB-231 cells, while the use of **3f** derivative caused a fivefold increase in MFI in comparison to the control, resulting in 90 % of MTRed CMXRos positive cells. No significant changes were noted for **SAL** and compound **6**-treated cancer cells (Figs. 1 and 2).

Mitochondria are not only fundamental structures in cellular energy production but they also carry out critical functions in calcium homeostasis, innate immunity, metabolic reprogramming to maintain physiological demands, and the regulation of both cell and organelle death. Mitochondrial activity is intricately regulated through the processes of fusion and fission, which drive changes in mitochondrial morphology and metabolism, enabling the cells to adapt to fluctuating environmental conditions [26]. Maintaining a balance between mitochondrial fusion and fission is crucial for optimal cell metabolism and stress adaptation. Mitochondrial fusion facilitates the transfer of gene products between mitochondria for optimal functioning, especially under metabolic and environmental stress, which improves mitochondrial membrane potential, respiration, and ATP production. On the other hand, mitochondrial fission is essential for regulating apoptosis and mitophagy and crucial for mitochondrial division [26].

In this study, derivatives **3a** and **3f** were observed to significantly elevate MTGreen fluorescence of A549 and MDA-MB-231 cells, a finding that indicates an increase in mitochondrial mass associated with the mitochondrial fission process. Moreover, the simultaneous rise in MTRed CMX Ros fluorescence following the treatment with **3a** and **3f** suggests an enhancement of mitochondrial function. However, it is noteworthy that the increase in MTRed CMX Ros fluorescence is not

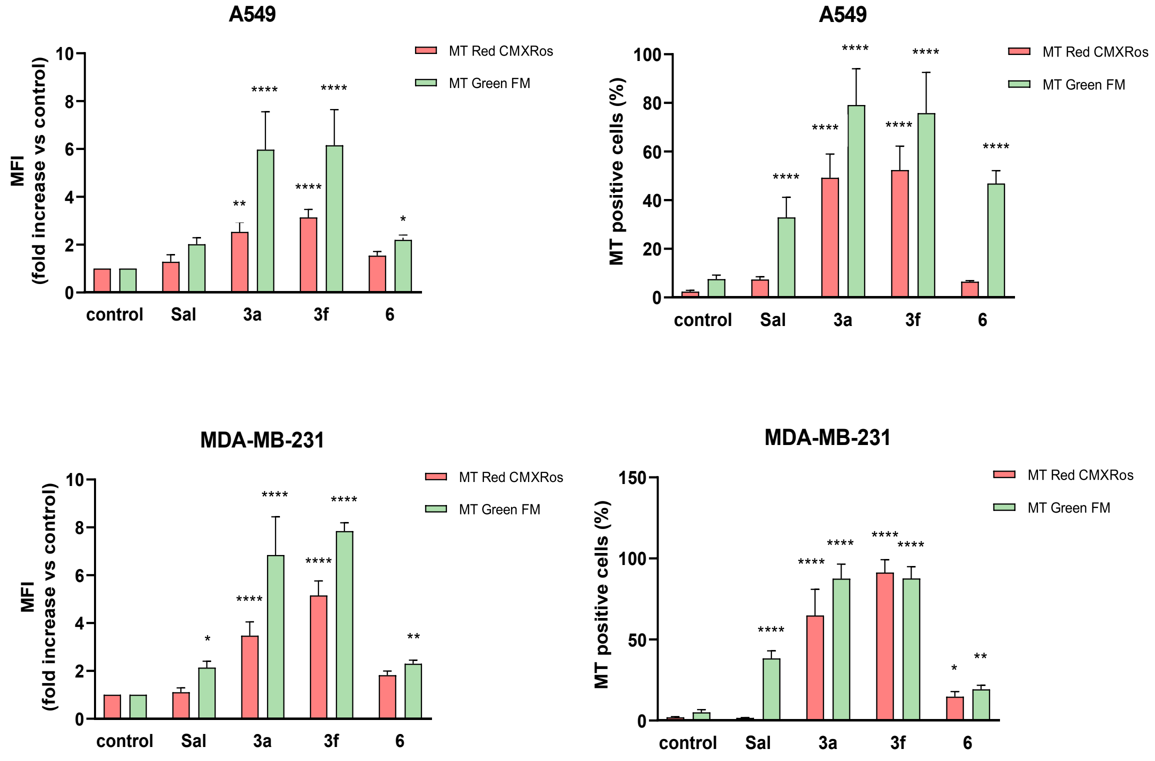

Fig. 1. Flow cytometry analysis of MitoTracker Red CMXRos and MitoTracker Green FM mitochondrial staining in A549 and MDA-MB-231 cells after treatment with **SAL** and its derivatives **3a**, **3f**, **6** for 48 h at their IC_{50} concentrations. Untreated cells were used as the control. The bars represent the fold change in mean fluorescent intensity (left panel) and % of MitoTrackers positive cells as compared to the control (right panel). The results are presented by means ± SD, n = 4. Statistical significance was determined at $p < 0.05$ (*); $p < 0.01$ (**); $p < 0.001$ (***) and $p < 0.0001$ (****) by 2-way ANOVA.

directly proportional to the MTGreen fluorescence, implying that the mitochondria generated during fission may exhibit reduced activity. This observed effect is stronger for TPP conjugates than for **SAL**. This phenomenon could be interpreted as a cellular defence mechanism in response to the mitotoxic treatment, that seems to be only partially effective since new mitochondria are formed but remain functionally inactive. Therefore, both compounds (**3a** and **3f**) may have a considerable potential as therapeutic strategies targeting the regulation of mitochondrial dynamics and function in cancer cells.

2.2.3. Induction of cell cycle arrest and apoptosis

To assess the anticancer properties and associated cell cycle alterations, PI-metric cell cycle analysis was performed using flow cytometry. The cells A549 and MDA-MB-231 were incubated for 24 h after the addition of **SAL** and its derivative compounds (**3a**, **3f**, and **6**) in their IC_{50} concentration. In this test untreated cancer cells were used as the control (A549 and MDA-MD-231 respectively).

The **SAL**-treated A549 cells showed a cell cycle phase distribution similar to that of the control. In contrast, after treatment with compound **3a** an increase in the percentage of cells in G0/G1 phase was noted (from 54.3 % in the control to 68.5 %) and in SubG1 phase (from 0.71 % to 6.0 %), while the cell populations in the phases S and G2 were reduced from 21.6 % to 13.2 % and from 20.8 % to 12 %, respectively. A similar phase pattern was observed after treatment with compound **3f**, while **6**-treated A549 cells demonstrated no significant differences in cell population distribution compared to the control (Figs. 3A and 4A).

In MDA-MD-231 cells, **SAL** and all its derivatives elevated the population of the cells in G0/G1 phase with a reduction of those in the phases S and G2. The most significant changes were observed after exposure to **3a** and **3f** compounds. The percentage of the cells in G0/G1 phase increased from 50.9 % in the control to 77.7 % and 76.2 % in the cells treated with **3a** and **3f**, respectively. Similarly, the highest decrease in the number of cells in S and G2 phases as compared to those in the control was found after treatment with **3a** and **3f** compounds.

To sum up, **SAL** derivatives **3a**, **3f**, **6** induced G0/G1 phase arrest in both studied cancer cell lines, whereas **SAL** inhibited division only in MDA-MB-231 cells. It should be noted that compounds **3a** and **3f** were the inducers of the G0/G1 phase arrest and also slightly increased the subG1 population of the cells (Figs. 3A and 4B).

Among the four compounds, exposure to **3a** and **3f** had the highest effect, followed by compound **6**, with **SAL** being the last.

The selected compounds (**3a**, **3f**, and **6**) and **SAL** were analysed by flow cytometry to determine the apoptotic effect. The experiment was carried out for 72 h on two cell lines (A549 and MDA-MB-231) using the Annexin V-FITC/PI binding assay.

The **SAL**-treated A549 cells showed a higher percentage of early apoptosis (9.72 %) and necrosis (3.67 %) compared to those of the control (1.68 % and 0.97 %, respectively). A 35-fold increase in early apoptosis (59.17 %) was observed for the derivative **3a**-treated cells, a similar observation was made for compound **3f** treated cells (52.57 %) but more necrotic and late apoptotic cells were found (12.94 % and 14.59 %, respectively) in response to the treatment. Additionally, these derivatives induced the highest percentage of necrosis from all four compounds and showed the highest cytotoxic effect. In contrast, the data for compound **6** are similar to those for the **SAL**-treated cells, with a lower necrosis level (2.02 %) (Figs. 3B and 5A).

For MDA-MB-231, the overall trend was similar to that observed for A549 cell line. However, **SAL** and its derivatives were found to induce a higher ratio of late apoptosis to necrosis. After treatment with compound **3a**, 27.96 % of the cells were shown to be in the early apoptosis, whereas late apoptotic effect increased 5-fold compared to the control (15.32 %). In the case of compound **3f**-treated cells, more than half of them were in early apoptosis (39.5 %) or late apoptosis/necrosis (21.8 %) after 72 h. Compared to its effect on A549 cells, the compound **3f**-

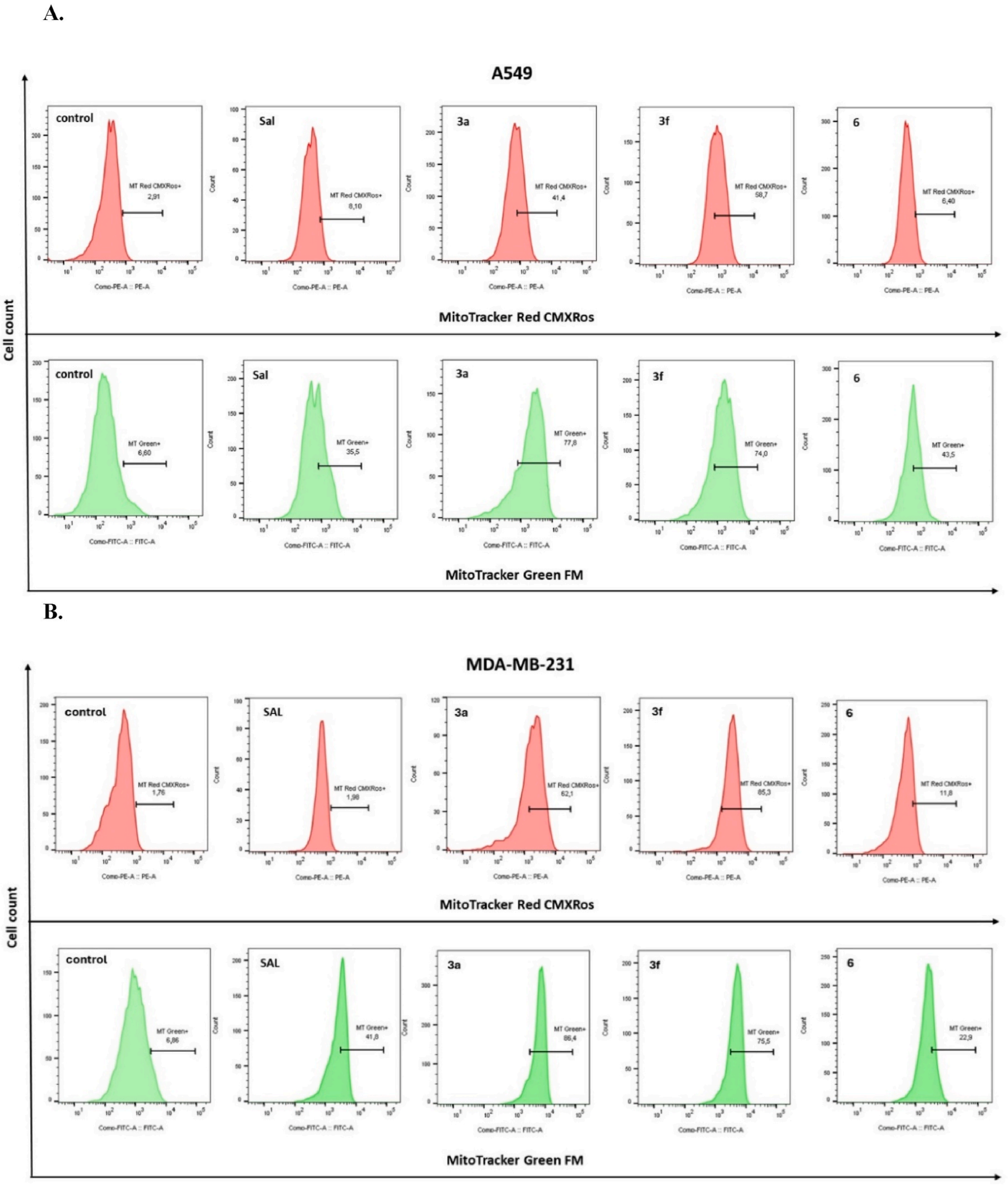

Fig. 2. Results of a representative experiment by MitoTracker Red CMXRos and MitoTracker Green FM fluorescence assays of A549 (**A**) and MDA-MB-231 (**B**) cells after treatment with **SAL** and its derivatives **3a**, **3f**, **6,** analysed by flow cytometry.

treated MDA-MB-231 cell line was characterized by a higher rate of late apoptosis/necrosis. Besides, compound **6** revealed weaker anti-cancer properties when compared to those of **SAL** towards the MDA-MB-231 cell line (Figs. 3B and 5B).

Overall, the cytotoxic effect of **3a** and **3f** towards MDA-MB-231 decreased when compared to that towards A549 cells, while the strongest necrotic activity was found for **3f** towards A549 cell lines (12.94 %).

Many antitumour compounds currently under investigation exert their cytostatic or cytotoxic effects at different stages of the cell cycle. The control of cell cycle progression in cancer cells is widely regarded as a potentially effective strategy for managing tumour growth. By precisely targeting the regulatory mechanisms that govern the cell cycle, we may be able to disrupt the unchecked proliferation characteristic of malignant cells, thereby offering a promising avenue for therapeutic intervention [27].

The data indicate that the synthesized derivatives **3a** and **3f** exhibited stronger inhibition of cell cycle in the G0/G1 phase compared to that of naturally occurring **SAL,** for A549 and MDA-MB-231 cells. Additionally, the proportion of cells in the sub-G1 phase (indicative of apoptosis) increased after 24 h of treatment with these derivatives, suggesting the induction of cell death. This observation was further confirmed by apoptosis analysis after 72 h, which showed the highest percentages of cells in early and late apoptosis for the cells treated with compounds **3a** and **3f**. In conclusion, these derivatives inhibit tumour

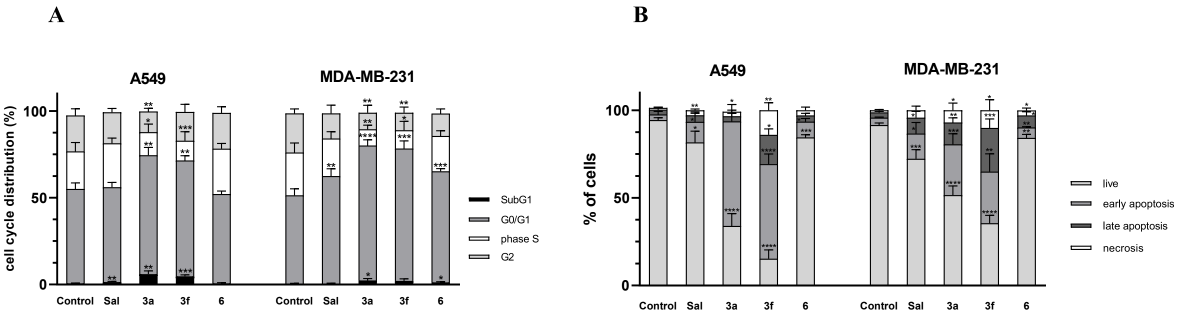

Fig. 3. The effect of a **SAL** and derivatives on the cell cycle (**A**) and apoptosis (**B**) of A549 and MDA-MB-231 cells. The bars represent the effect of **SAL**, **3a**, **3f** and **6** derivatives on the number of cells in particular cell cycle phases. The cells were incubated for 24 h with the compounds at their IC_{50} concentrations, stained with PI and analysed by flow cytometry (**A**). The bars represent % of live cells, the cells at the early and late stage of apoptosis and necrosis. The cells were incubated for 72 h with the compounds at their IC_{50} concentrations, stained with Annexin V-FITC and PI and analysed by flow cytometry (**B**). Untreated cells were used as the control. The results are presented by means ± SD, n = 4. Statistical significance was determined at $p < 0.05$ (*); $p < 0.01$ (**); $p < 0.001$ (***) and $p < 0.0001$ (****) by 2-way ANOVA.

growth by disrupting cell cycle regulation and promoting apoptosis.

2.2.4. Mitochondrial membrane potential

The detection of mitochondrial membrane potential was determined by JC-10 assay that is based on changes in cationic and lipophilic JC-10 dye fluorescence of the cells. In the cells with active mitochondria, JC-10 concentrates in the mitochondrial matrix where it forms red fluorescent aggregates, whereas in apoptotic and necrotic cells, JC-10 diffuses out of mitochondria, changes to a monomeric form and stains cells with green fluorescence.

The treatment with **SAL** and its derivatives resulted in the loss of MMP evidenced by a loss of red fluorescence and increase in green emission from the induced cells. The percentage of the cells showing green fluorescence was the highest for MDA-MB-231 cells in the presence of compounds **3a** and **3f** (60.8 % and 70.7 %, respectively) in comparison to the control (8.89 %). In turn, in A549 cells these compounds elevated the percent of JC-10 monomers from 8.33 % in the control to 41.7 % for **3a**, and 32.5 % for **3f** derivative. The results obtained for **SAL** and compound **6** revealed lower percent of cells (range from 18.8 % to 25.0 %) showing green fluorescence in A549 cells as well MDA-MB-231 cells (Figs. 6 and 7).

The mitochondrial membrane potential (MMP) is a critical indicator of mitochondrial function, directly reflecting the organelle's capacity to generate ATP through oxidative phosphorylation. MMP represents the electrical potential difference across the inner mitochondrial membrane and, in conjunction with the proton gradient, it forms the proton motive force essential for ATP production via oxidative phosphorylation [28].

Our findings indicate that derivatives **3a** and **3f** induce a more pronounced loss of MMP relative to that of **SAL** in the studied cancer cell lines. This significant reduction in mitochondrial membrane potential is strongly correlated with the induction of apoptosis, particularly in MDA-MB-231 cells. These results suggest that targeting MMP could be a key mechanism by which these derivatives exert their pro-apoptotic effects, offering potential therapeutic benefits in the treatment of cancer.

2.2.5. ROS generation

CellROX Green Reagent used in present study measures the number of reactive oxygen species (ROS) in live cells. Upon oxidation, this dye is bound to DNA, thus, its signal is localized primarily in the nucleus and mitochondria.

The results obtained in the present study showed that the ROS level was around 2-fold elevated after treatment with compounds **3a** and **3f** of both cancer cell lines as compared to the control. Only a slight insignificant increase in the ROS level was observed in response to the treatment with **SAL** and compound **6** (Fig. 8).

Cancer cells generally exhibit elevated basal levels of reactive oxygen species (ROS) compared to those in normal cells. This characteristic is exploited in cancer therapy, as high ROS levels can inflict substantial damage on proteins, nucleic acids, lipids, membranes, and organelles, ultimately leading to cancer cell death [29]. Consequently, the augmentation of ROS through prooxidant agents, such as **SAL**, presents a promising therapeutic strategy [30]. Our results demonstrate that the newly synthesized phosphonium salts **3a** and **3f**, exhibit a greater potential for ROS generation, especially **3a** in MDA-MB-231 compared to that of the parent compound, suggesting enhanced efficacy in inducing oxidative stress and promoting cancer cell death.

2.2.6. Antimicrobial activity

To assess the antibacterial properties of **SAL** and its obtained conjugates, eight bacterial strains were used: five standard Gram-positive bacteria (*S. aureus* NCTC 4163, ATCC 25923, ATCC 6538, and ATCC 29213; *S. epidermidis* ATCC 12228 and ATCC 35984) and two Gram-negative rods (*P. aeruginosa* ATCC 15442 and *E. coli* ATCC 25922). As presented in Table 3, all synthesized TPP analogues (**3a**-**5f**) exhibited high antimicrobial activity against Gram-positive bacteria. Similarly to unmodified **SAL**, each of its derivatives was inactive against Gram-negative bacterial strains. Furthermore, most novel analogues were more active than benzyl ester **6**. The conjugates with four-carbon chains revealed higher activity than their counterparts with six-carbon chains. Analogue **3a** exhibited the highest biological activity from among all **SAL** derivatives. However, none of the obtained conjugates exhibited higher antibacterial activity than unmodified **SAL** and ciprofloxacin, commonly used in bacterial disease treatment, which was significantly more active against *E. coli* and *P. aeruginosa* bacteria than any of **SAL** analogues studied.

2.3. Biophysical studies

2.3.1. Mitochondrial respiration rate

The effects of **SAL** and its derivatives on cell respiration rate were examined using Oxygraph-2K system. To determine the respiration rate of A549 cells, high-resolution respirometry was applied to measure changes in the oxygen consumption. The measurement was conducted in live non-permeabilized cells to analyse the effect of **SAL** and its analogues (**3a**, **3b**, **3e**, **3f**, and **6**) on mitochondria and their ability to cause changes in the A549 cells respiration rate. The maximum respiration rate was observed as a result of the application of carbonyl cyanide 4-(trifluoromethoxy) phenylhydrazone, which is commonly used as a potent mitochondrial uncoupler. As shown in Fig. 9, **SAL** did not change the oxygen respiration rate at any concentration, while the FCCP application confirmed mitochondria's proper functioning via full uncoupling. A similar observation was made for inactive benzyl ester derivative **6**. A small increase in oxygen consumption rate was observed for analogue **3f**, while no full uncoupling was performed by FCCP.

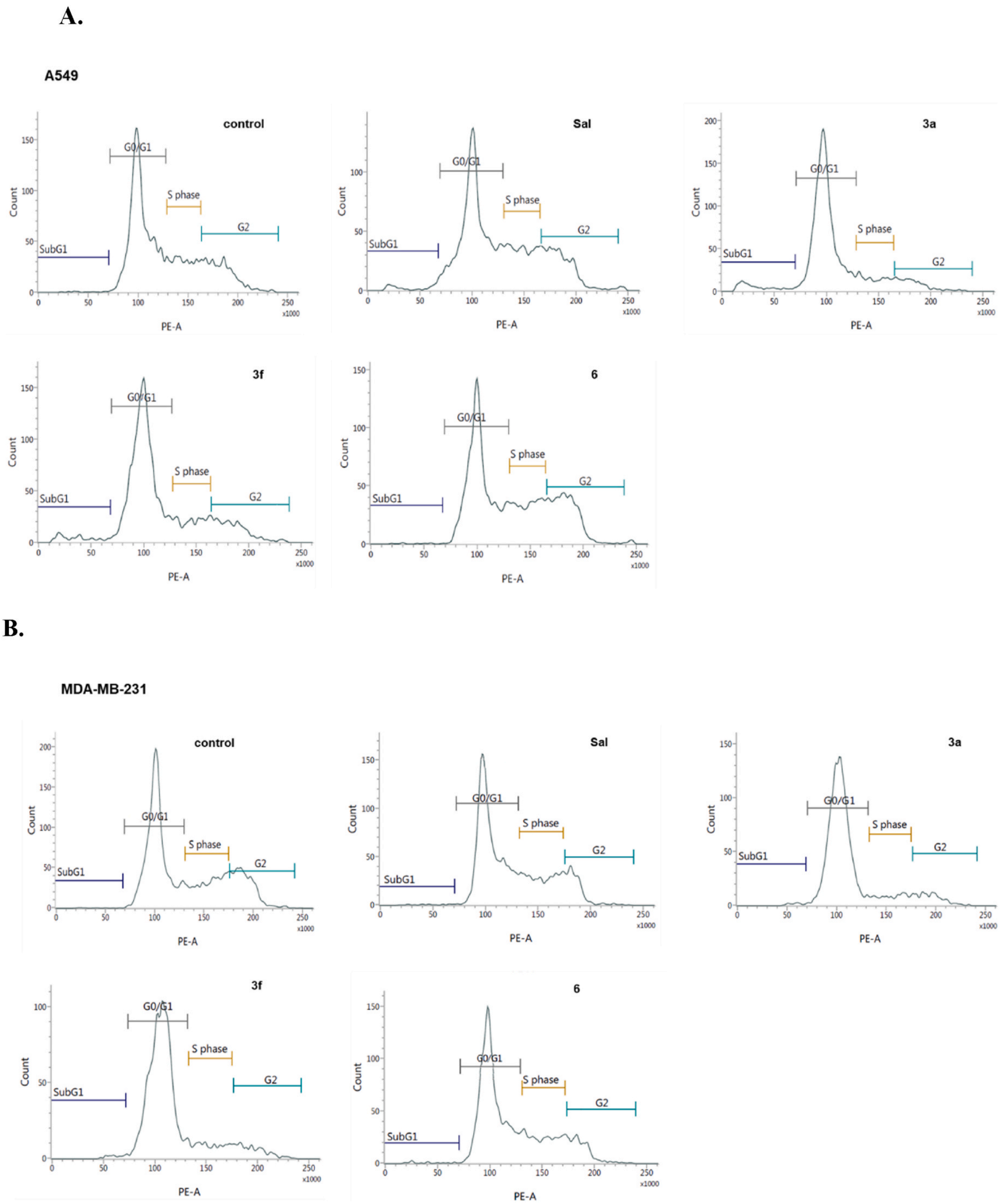

Fig. 4. Results of a representative experiment of cell cycle analysis of A549 (**A**) and MDA-MB-231 (**B**) cells after treatment with **SAL** and its derivatives **3a**, **3f**, and **6**, obtained by flow cytometry.

Compound **3a** caused an increase in oxygen consumption upon its concentration increasing to 10 μM, which destabilised mitochondria by a decrease in the respiration rate. A similar effect of decreasing oxygen consumption after achieving the top level was observed in the presence of analogues **3e** and **3b** in concentration of 3 μM. Both these compounds were responsible for a 2.5 times increase in the mitochondria respiration rate when applied in a concentration of 1 μM.

2.3.2. Interaction of salinomycin and its derivatives with black lipid membranes

To prove the electrophysiological activity of **SAL** and its derivatives, we performed black lipid membrane (BLM) technique experiments in gradient solutions 50/150 mM KCl (*cis/trans*) (Fig. 10). After assessment of the activity of the compounds on oxygraph examination, we chose **SAL** and its three conjugates **3a**, **3b**, and **3e** to check their capability of ionic transport. Using this approach, we did not observe the formation of specific channel-like structures, irregular disturbances in membrane permeability and membrane rapture events.

Unmodified **SAL** did not change the ionic current flow through the azolectin bilayer membrane at any concentration up to 10 μM concentration. At the same time, its analogues were capable of current generation in a dose-dependent manner. Similarly to the experiments with an

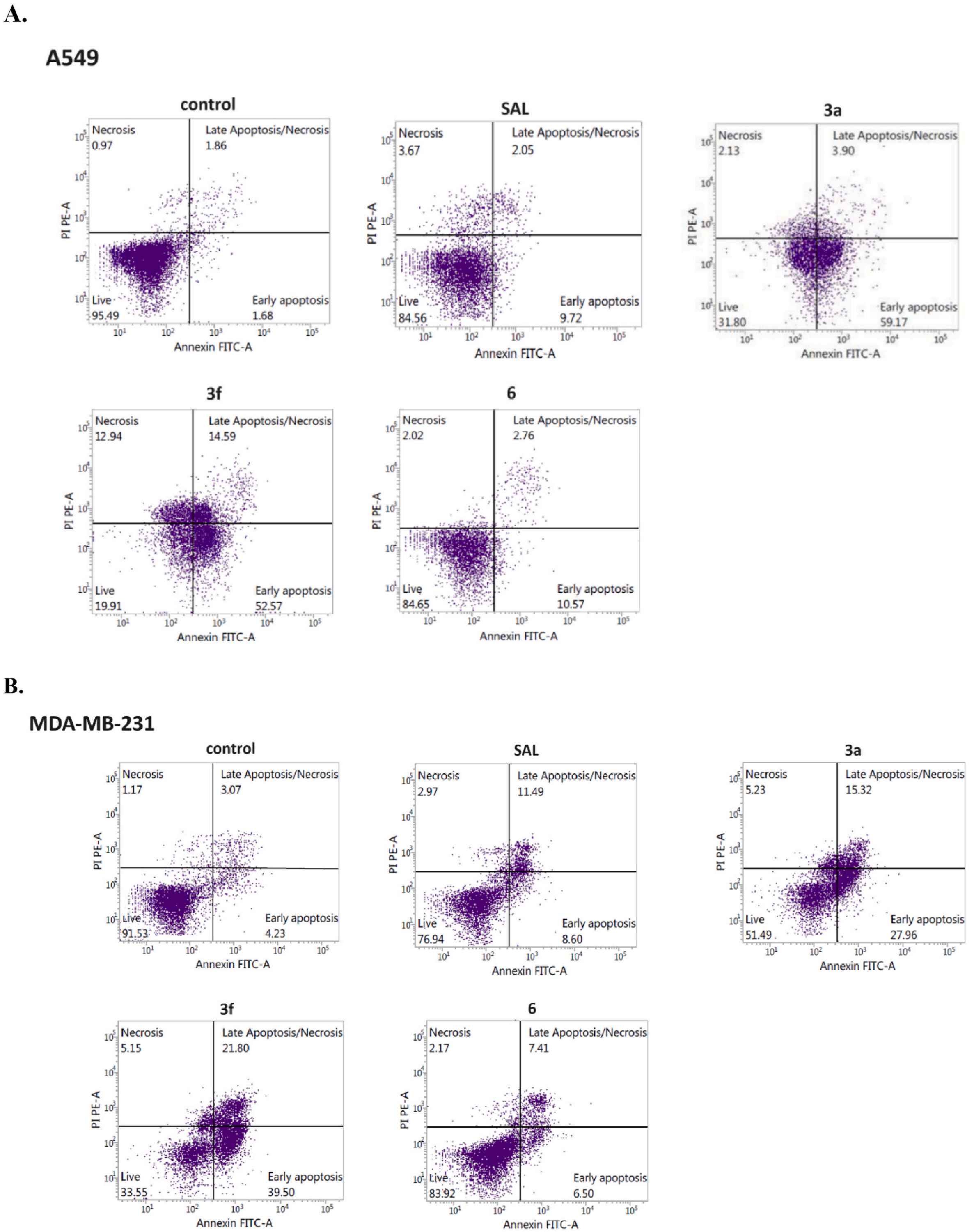

Fig. 5. Representative results (%) as dot plots showing apoptosis of A549 (**A**) and MDA-MB-231 (**B**) cells after treatment with **SAL** and its derivatives **3a**, **3f**, **6**, analysed by flow cytometry.

oxygraph, the effects were observed from the concentration of 1 μM. It seems that compound **3b** at −60 mV induced 2.5 times higher current than **3a** at 10 mM. Additionally, examples of current recordings of the measured signals are shown in Fig. 10 (left panel). Basal ionic current was observed in the presence of conjugates; however, no open and close states, like in typical channel behaviour, were observed. The current flow was smooth without any irregular activity traces. It is worth adding that the conjugates in some experiments caused membrane disruption, probably from a too close incorporation of two compounds.

3. Conclusions

In this study, twelve novel derivatives of **SAL** with TPP moiety at the C-1 position (**3a-f**, **5a-f**) were obtained. Additionally, benzyl ester **6** was synthesized and included in biological and biophysical studies to check if the properties of **SAL** would differ depending on the type of molecule

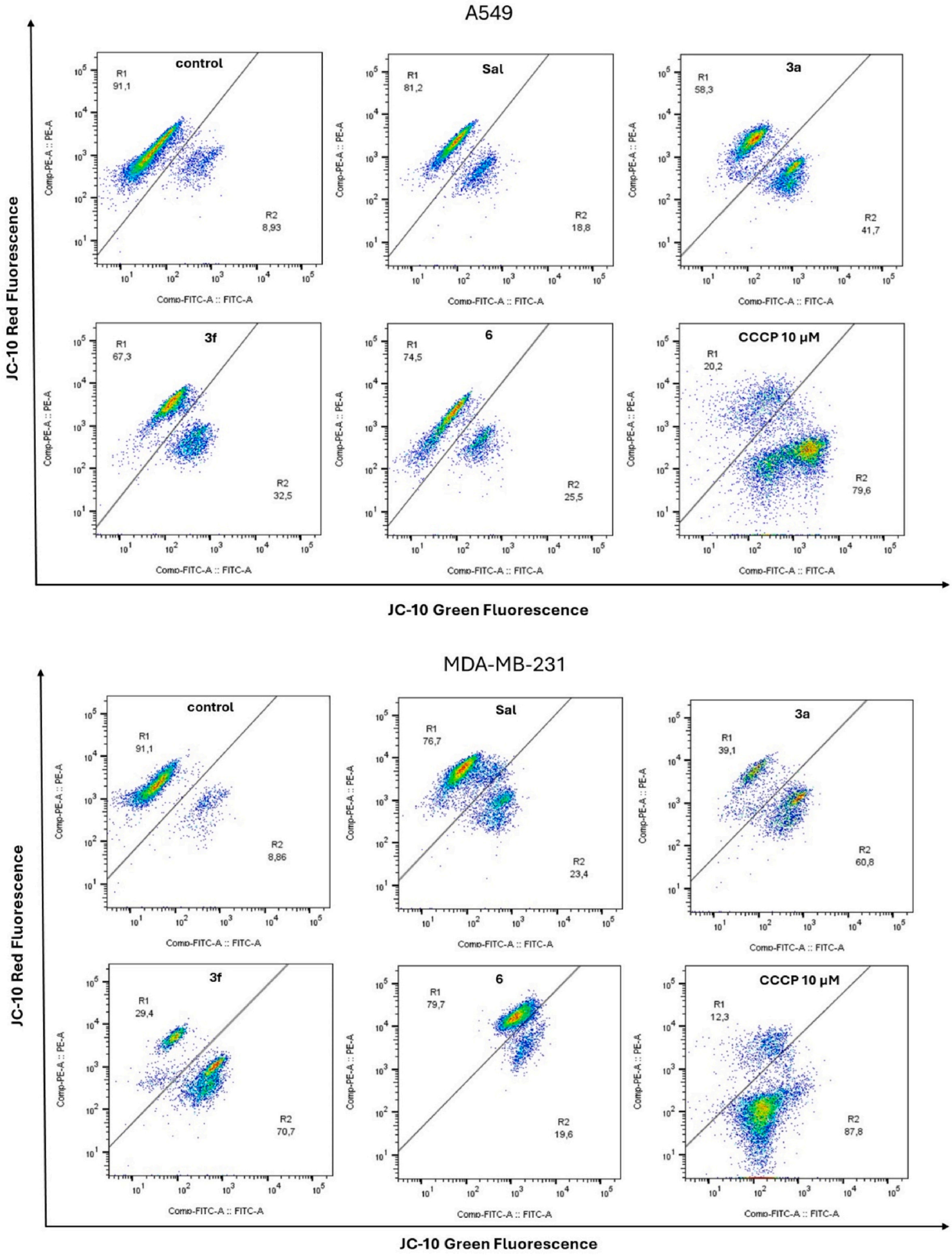

Fig. 6. Results of a representative experiment of JC-10 fluorescence assays in A549 and MDA-MB-231 cells after treatment with **SAL** and **3a**, **3f**, **6** derivatives, analysed by flow cytometry.

used to block the carboxylic group. Each of the quaternary phosphonium salts was obtained in a two-step synthesis with a mean yield of 29.6 %. Biological tests of antiproliferative activity showed that all of the **SAL** derivatives were more active than unmodified **SAL** and its benzyl ester. However, of the newly synthesized derivatives two analogues **3a** and **3e** exhibited higher antiproliferative activity than commonly used doxorubicin, against human metastatic colon cancer cells (SW620) and human breast cancer cells (MDA-MG-231). Furthermore, all obtained analogues showed a tendency to higher activity against breast cancer cells and were less toxic towards human immortal keratinocyte cells (HaCaT) than widely used doxorubicin. Assessment of selectivity indices (SI) towards each cancer cell line revealed that compound **3a** was highly

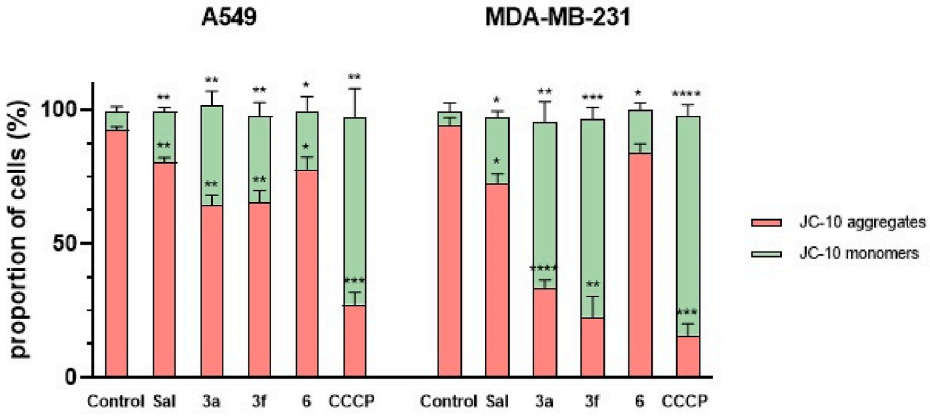

Fig. 7. Flow cytometry analysis of changes in the mitochondrial membrane potential (MMP) in A549 and MDA-MB-231 cells after treatment with **SAL,** its derivatives **3a**, **3f**, **6** and carbonylcyanide-*m*-chlorophenylhydrazone (CCCP) for 48 h at their IC_{50} concentrations. Untreated cells were used as the control. The bars represent the proportion of cells (%) showing green and red fluorescence. The results are presented by means ± SD, n = 4. Statistical significance was determined at $p < 0.05$ (*); $p < 0.01$ (**); $p < 0.001$ (***) and $p < 0.0001$ (****) by 2-way ANOVA.

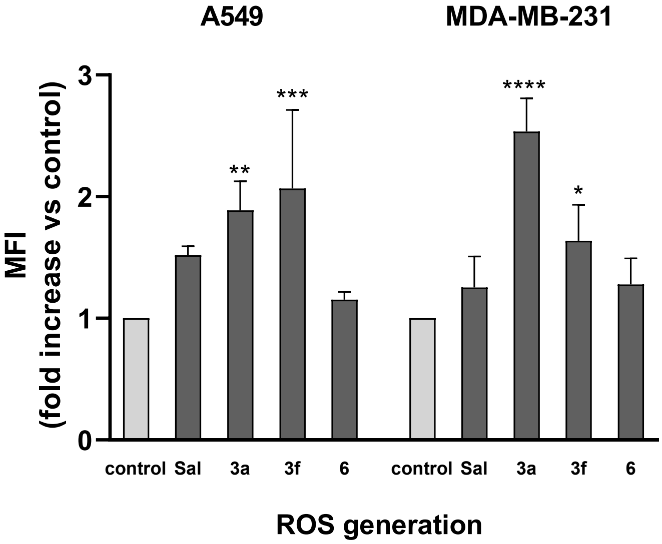

Fig. 8. The effect of **SAL** and its derivatives **3a**, **3f**, **6** on ROS production in A549 and MDA-MB-231 cells. The bars show the fold change in mean fluorescent intensity as compared to the control. The cells were incubated for 6 h with the compounds at their IC_{50} concentrations, labelled with CellROX Geen Reagent and analysed by microplate-based fluorimetry. Untreated cells were used as the control. The results are presented by means ± SD, n = 4. Statistical significance was determined at $p < 0.05$ (*); $p < 0.01$ (**); $p < 0.001$ (***) and $p < 0.0001$ (****),by 2-way ANOVA.

selective towards both SW480 and SW620 cell lines, in the standard of HaCaT. Furthermore, compound **3e** with high SI = 11.6 towards SW620 cell line, revealed its promising therapeutic potential. In the study of mitochondria activity using two types of MitoTrackers dyes, two derivatives **3a** and **3f** showed the ability to control mitochondrial dynamics and functions in cancer cells. The elevation of dye fluorescence in A549 and MDA-MB-231 cells suggests the increase in mitochondrial mass and improvement of mitochondrial functions. Moreover, the effects of TPP analogues on mitochondria were stronger than that of **SAL**. Results of the cell cycle arrest study proved that esters **3a**, **3f**, and **6** induced G0/G1 phase arrest in both studied cancer cell lines (A549 and MDA-MB-231), while **SAL** inhibited division only in MDA-MB-231 cells. More importantly, conjugates **3a** and **3f** were the strongest inducers of G0/G1 phase arrest. The results of the flow cytometry analysis of the apoptotic effect showed that the highest percentages of cells in early and late apoptosis were observed after treatment with compounds **3a** and **3f**. For A549 cell line as high as a 35-fold increase in early apoptosis was observed, 59.17 % for derivative **3a**-treated cells and 52.57 % for those exposed to compound **3f**, and very similar effects were noted for MDA-MB-231 cell line. To sum up, these two derivatives inhibited tumour growth by promoting apoptosis and disrupting cell cycle regulation, while unmodified **SAL** and benzyl ester **6** exhibited significantly lower anticancer activity. Additionally, both previously mentioned TPP conjugates, **3a** and **3f**, were capable of causing a significant reduction in mitochondrial membrane potential which was correlated with the induction of apoptosis. The percentage of the cells that were affected by the loss of MMP was the highest for MDA-MB-231 cells in the presence of **3a** and **3f** compounds (60.8 % and 70.7 %, respectively). The results of ROS generation demonstrated that the newly synthesized phosphonium esters **3a** and **3f** exhibit considerable potential for ROS generation (especially **3a** in MDA-MB-231 cell line) in contrast to **SAL** and compound **6**, suggesting enhanced efficacy in inducing oxidative stress and promoting cancer cell death. The antimicrobial tests revealed that unlike the parent compound and widely used ciprofloxacin, the synthesized analogues exhibit lower activity against bacterial strains. However, compound **3a** was the most effective and all of TPP conjugates appeared to be far more active than benzyl ester **6**. By measuring changes in the mitochondrial respiration rates we provided a proof that **SAL** conjugated with TPP moiety may cause an increase in oxygen consumption by A549 cells. On the basis of electrophysiological activity results, we proved that unmodified **SAL** did not change ionic current flow through the azolectin bilayer membrane at any concentration up to that of 10 μM, while its analogues were capable of the current generation in a dose-dependent manner. For comparison, compound **3b** induced 2.5 times higher current than **3a** in a similar concentration range. To conclude, in this study, we proved that conjugation of **SAL** with phosphonium cations leads to obtaining of highly promising, effective, and potent agents with considerable therapeutic potential. Furthermore, this study revealed that the shortening of the carbon chain has a beneficial effect on antiproliferative activity and from among all obtained TPP analogues, compound **3a** without any substituents in the aromatic rings appeared to be the most active one. Additionally, the conjugation improved the biological properties of a parent compound and proved that it is a good direction in the search for novel and more potent anticancer agents.

Table 3
Antimicrobial activities of SAL and its conjugates against Gram-positive and Gram-negative bacteria – minimal inhibitory concentrations (MIC, μg/mL).

	Strains of Gram-positive and Gram-negative bacteria							
	S. aureus NCTC 4163	*S. aureus* ATCC 25923	*S. aureus* ATCC 6538	*S. aureus* ATCC 29213	*S. epidermidis* ATCC 12228	*S. epidermidis* ATCC 35984	*E. coli* ATCC 25922	*P. aeruginosa* ATCC 15442
SAL	0.5	0.5	0.5	0.5	0.5	1	>256	>256
3a	2	2	1	1	2	1	256	256
3b	2	4	2	4	4	4	>256	>256
3c	2	2	2	2	2	2	256	256
3d	4	4	4	64	16	8	>256	>256
3e	2	4	2	2	4	4	>256	>256
3f	2	2	2	2	2	2	>256	>256
5a	2	2	2	2	2	2	256	256
5b	8	16	8	8	16	16	>256	>256
5c	8	8	8	8	8	8	>256	>256
5d	4	8	4	8	8	8	>256	>256
5e	8	8	8	8	8	8	>256	>256
5f	2	2	2	2	2	2	>256	>256
6	64	64	32	64	64	>256	>256	>256
ciprofloxacin	0.125	0.25	0.125	0.25	0.125	0.125	0.0075	0.125

4. Material and methods

4.1. Chemistry

4.1.1. General procedures

All reagents and all solvents were obtained from Merck or Trimen Chemicals S.A. (Poland), and were used as received without further purification. $CDCl_3$ spectral grade solvent was stored over 3 Å molecular sieves for several days. Reaction mixtures were stirred using teflon-coated magnetic stir bars and were monitored by thin layer chromatography (TLC) using aluminium-backed plates (Merck $60F_{254}$). TLC plates were visualized by UV-light (254 nm), followed by treatment with phosphomolybdic acid (PMA, 5 % in absolute EtOH) and gentle heating. Products of the reactions were purified using CombiFlash®Rf$^+$ Lumen Flash Chromatography System (Teledyne Isco) with integrated ELS and UV detectors and Electrospray Ionization (ESI) mass spectroscopy. All solvents used in flash chromatography were of HPLC grade (Merck) and were used as received. Solvents were removed using a rotary evaporator.

NMR spectra were recorded on a Varian 400 (^1H NMR at 403 MHz, ^{13}C NMR at 101 MHz, ^{31}P NMR at 122 MHz) magnetic resonance spectrometer, Bruker AvanceNEO 600 (^1H NMR at 600 MHz and ^{13}C NMR at 151 MHz) magnetic resonance spectrometer or Mercury 300 (^{31}P NMR at 162 MHz) magnetic resonance spectrometer. ^1H NMR spectra are reported in chemical shifts downfield from TMS using the respective residual solvent peak as internal standard (CD_3CN δ 1.96 ppm). ^1H NMR spectra are reported as follows: chemical shift (δ, ppm), multiplicity (s = singlet, d = doublet, q = quartet, dd = doublet of doublets, dt = doublet of triplets, dq = doublet of quartets, ddd = doublet of doublet of doublets, ddt = doublet of doublet of triplets, dddd = doublet of doublet of doublet of doublets, m = multiplet), coupling constant(s) in Hz, and integration. Significant peaks are reported within the overlapping ~2.00–0.50 ppm region of the ^1H NMR spectra. The ^{13}C NMR spectra are reported in chemical shifts downfield from TMS using the respective residual solvent peak as internal standard (CD_3CN δ 1.39 ppm, 118.69 ppm). Line broadening parameters were 0.5 or 1.0 Hz, while the error of chemical shift value was 0.1 ppm. The ^{31}P NMR spectra are reported in chemical shifts.

The electrospray ionization (ESI) high-resolution mass spectra were recorded on a QTOF (Impact HD, Bruker Daltonics) mass spectrometer in the positive ion detection mode. Samples were prepared in dry acetonitrile. The mass range for ESI experiments was from $m/z = 400$ to $m/z = 1300$.

SAL (**1**) was isolated as sodium salt from commercially available veterinary premix SACOX®, using the procedure described previously [21]. Thereafter, isolated sodium salt of **SAL** was dissolved in CH_2Cl_2 and vigorously extracted with a layer of aqueous sulphuric acid (pH 1.0). Then organic layer containing **SAL** was washed with distilled water, and CH_2Cl_2 was evaporated under reduced pressure to dryness, giving **SAL** as clear oil. After the 3-times repeated evaporation with n-pentane, this oil was transformed to white amorphous solid. The spectral properties of **SAL** were in agreement with the previously published data.

4.1.2. Synthesis of **2**, **4**, and **6**

SAL (**1**, 1.0 eq) was dissolved in toluene (25 ml), and DBU (1.7 eq) was added. Then, the mixture was stirred and heated to 100 °C, and after 30 min the respective halide (3.0 eq) was added. The reaction was stirred and heated to 100 °C and kept at this temperature for 6 h and then stirred at room temperature for 18 h. The mixture was evaporated to dryness using acetonitrile to remove toluene. The residue was purified by column flash chromatography on silica gel using CombiFlash®Rf$^+$ (hexane/ethyl acetate, increasing concentration gradient) with an integrated Evaporative Light Scattering Detector (ELSD), UV detector, and Electrospray Ionization (ESI) mass spectroscopy. **Compound 2:** Yield: 87.6 % ESI-MS for $C_{46}H_{77}BrO_{11}$ (m/z): $[M+Na]^+$ 909. **Compound 4:** Yield: 68.2 % ESI-MS for $C_{48}H_{81}BrO_{11}$ (m/z): $[M+Na]^+$ 925. **Compound 6:** Yield: 85.3 % HRMS (ESI+) m/z: $[M+Na]^+$ Calcd for $C_{49}H_{76}O_{11}$: 863.5285; Found: 863.5286. ^1H NMR (401 MHz, CD_3CN) δ 7.47–7.44 (m, 2H), 7.40–7.33 (m, 3H), 6.06 (dd, $J = 10.8$, 2.3 Hz, 1H), 5.84 (dd, $J = 10.7$, 1.4 Hz, 1H), 5.46 (d, $J = 12.5$ Hz, 1H), 5.18 (d, 1H), 4.08–4.02 (m, 1H), 3.96–3.89 (m, 2H), 3.69 (q, $J = 6.8$ Hz, 1H), 3.62 (ddd, $J = 10.5$, 7.1, 2.2 Hz, 3H), 3.18–3.03 (m, 2H), 2.76 (s, 1H), 2.65 (dt, $J = 9.8$, 2.8 Hz, 1H), 2.61 (d, $J = 5.6$ Hz, 1H), 2.34–2.22 (m, 2H), 2.20 (s, 1H), 1.99–0.58 (m, 52H) ppm; ^{13}C NMR (101 MHz, CD_3CN) δ 215.02, 176.14, 137.68, 133.87, 129.65, 129.50, 129.37, 129.13, 121.93, 107.32, 100.04, 88.82, 80.29, 77.98, 75.61, 75.09, 72.81, 71.33, 70.31, 68.41, 67.40, 57.32, 49.74, 48.15, 41.54, 39.44, 37.40, 37.35, 34.12, 32.05, 31.20, 30.21, 29.09, 26.94, 26.34, 23.63, 22.89, 20.52, 20.00, 17.91, 16.06, 15.46, 14.75, 13.61, 12.27, 11.52, 8.06, 6.83 ppm.

4.1.3. Synthesis of **3a-f** and **5a-f**

A respective compound **2** or **4** (1.0 eq.) was dissolved in acetonitrile (25 ml). Then, the mixture was stirred and the respective phosphonium cation was added (3 eq.). The reaction was stirred and heated under reflux for 72 h. The mixture was evaporated to dryness in the presence of silica gel and the residue was purified by column flash chromatography using CombiFlash®Rf$^+$ (chloroform/acetone, increasing concentration gradient) with an integrated Evaporative Light Scattering Detector (ELSD) and Electrospray Ionization (ESI) mass spectroscopy.

Compound 3a: Yield: 27.4 %. HRMS (ESI+) m/z: $[M]^+$ Calcd for $C_{64}H_{92}O_{11}P^+$ 1067.6372; Found: 1067.6377. ^1H NMR (400 MHz, CD_3CN) δ 7.89–7.83 (m, 2H), 7.77–7.68 (m, 8H), 6.02 (dd, $J = 10.8$, 2.3

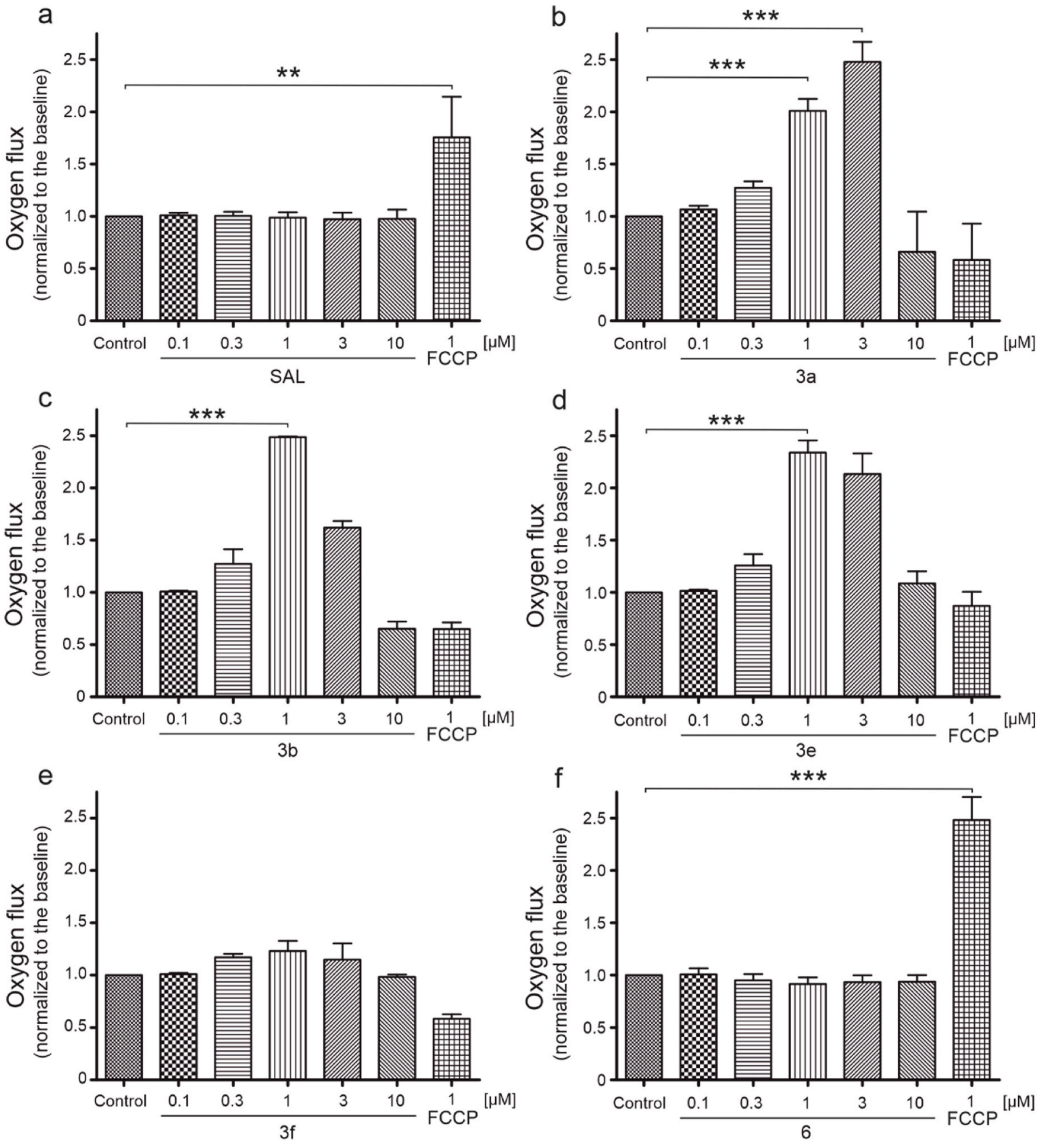

Fig. 9. The effect of **SAL** and its derivatives on oxygen consumption rate in the whole A549 cell model in starving DMEM. The bars represent the effect of **SAL** and its conjugates at different concentrations: 0.1, 0.3, 1, 3 and 10 μM on A549 cell oxygen consumption rate, measured with a high-resolution respirometer. The effects of the tested compounds: a) salinomycin (**SAL**), b) **3a**, c) **3b**, d) **3e**, e) **3f**, and f) **6** were compared to the oxygen consumption rate measured after stabilization before addition of any compounds. Full uncoupling was induced by 1 μM FCCP. The results are represented by means ± SD, n = 4. Statistical significance was determined at $p < 0.01$ (**) and $p < 0.001$ (***) by one-way ANOVA.

Hz, 1H), 5.88 (d, $J = 11.7$ Hz, 1H), 4.36 (dt, $J = 11.3$, 6.3 Hz, 1H), 4.13–4.06 (m, 1H), 3.94–3.90 (m, 1H), 3.89–3.84 (m, 1H), 3.77–3.67 (m, 2H), 3.63–3.58 (m, 1H), 3.56 (t, $J = 3.3$ Hz, 1H), 3.52–3.38 (m, 2H), 3.06–2.98 (m, 2H), 2.71 (d, $J = 4.6$ Hz, 1H), 2.57 (td, $J = 5.6$, 2.8 Hz, 1H), 2.31–2.14 (m, 2H), 2.00–0.57 (m, 64H) ppm. ^{13}C NMR (101 MHz, CD$_3$CN) δ 215.89, 176.27, 135.98, 135.95, 134.54, 134.44, 133.52, 131.22, 131.09, 121.85, 119.50, 118.64, 107.18, 99.83, 88.35, 79.34, 77.67, 75.62, 74.90, 72.35, 71.19, 70.36, 67.86, 64.28, 57.12, 55.25, 49.44, 47.74, 41.33, 39.11, 37.12, 36.90, 33.97, 31.88, 30.02, 29.62, 28.73, 26.51, 26.31, 23.20, 22.28, 21.77, 20.26, 19.76, 19.72, 17.72, 15.84, 15.21, 14.53, 13.28, 12.15, 11.34, 7.76, 6.70 ppm; ^{31}P NMR (122 MHz, CD$_3$CN) δ 25.12 ppm.

Compound 3b: Yield: 30.6 %. HRMS (ESI+) *m/z*: [M]$^+$ Calcd for $C_{67}H_{98}O_{11}P^+$ 1109.6841; Found: 1109.6818. ^{1}H NMR (400 MHz, CD$_3$CN) δ 7.61–7.50 (m, 8H), 6.01 (dd, $J = 10.8$, 2.3 Hz, 1H), 5.88 (d, $J = 11.7$ Hz, 1H), 4.39–4.32 (m, 1H), 4.13–4.06 (m, 1H), 3.93 (d, $J = 8.6$ Hz, 1H), 3.88 (dd, $J = 10.5$, 4.9 Hz, 1H), 3.74 (dd, $J = 11.0$, 4.1 Hz, 1H), 3.72–3.67 (m, 1H), 3.62–3.54 (m, 2H), 3.51 (dd, $J = 11.2$, 5.5 Hz, 1H), 3.40–3.23 (m, 2H), 3.07–2.98 (m, 2H), 2.72 (dd, $J = 10.4$, 4.8 Hz, 1H), 2.57 (d, $J = 4.3$ Hz, 1H), 2.46 (s, 6H), 2.34 (s, 2H), 2.12 (s, 1H), 1.96–0.53 (m, 69H) ppm. ^{13}C NMR (101 MHz, CD$_3$CN) δ 215.85, 176.32, 147.32, 147.29, 134.38, 134.27, 133.57, 131.82, 131.70, 121.85, 116.45, 115.57, 107.22, 99.85, 88.39, 79.33, 77.75, 75.68, 74.93, 72.43, 71.19, 70.37, 67.91, 64.32, 57.17, 55.21, 49.47, 47.78, 41.37, 39.16, 37.17, 36.97, 34.04, 32.12, 31.88, 30.02, 29.80, 28.78, 26.55, 26.31, 23.88, 23.21, 22.54, 21.73, 21.71, 20.32, 19.73, 19.70, 17.74,

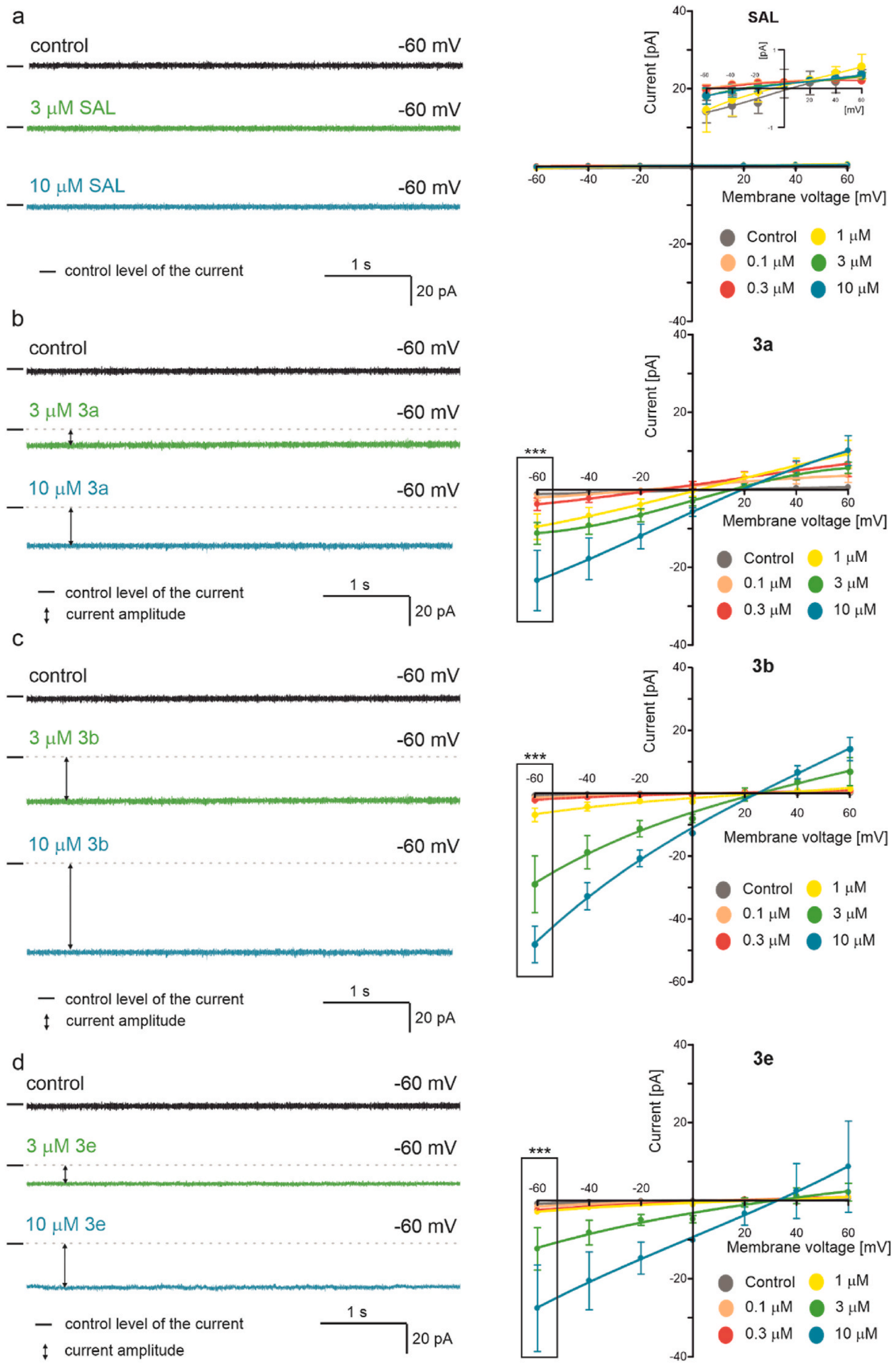

Fig. 10. Current–time recordings of ionic current flow through the lipid bilayer membranes and current-voltage (i–v) relationship measured in gradient of 50/150 mM KCl (*cis*/*trans*). Left panel shows representative recordings for the control and in the presence of 3 or 10 μM (a) salinomycin (**SAL**), (b) **3a,** (c) **3b**, (d) **3e** at a potential of −60 mV. Right panel presents current-voltage characteristics in the presence of (a) salinomycin (**SAL**), (b) **3a**, (c) **3b** and (d) **3e** at concentrations of 0.1, 0.3, 1, 3 and 10 μM at potentials from −60 to 60 mV. The average current values of the measurement points and their standard deviations (SD) are marked in the chart (n = 4). The experiment was performed in four repetitions. Dashes indicate the control level of the current in the absence of the studied substance, while the symbol ↕ indicates a representative amplitude of measured current in the presence of the conjugate. Statistical significance was determined at $p < 0.001$ (***) by one-way ANOVA.

15.85, 15.21, 14.50, 13.22, 12.14, 11.36, 7.77, 6.69 ppm; ^{31}P NMR (122 MHz, CD_3CN) δ 24.08 ppm.

Compound 3c: Yield: 17.0 %. HRMS (ESI+) *m/z*: $[M]^+$ Calcd for $C_{67}H_{98}O_{14}P^+$ 1157.6689; Found: 1157.6703. ^{1}H NMR (400 MHz, CD_3CN) δ 7.79 (m, *J* = 8.3, 3.1, 1.1 Hz, 2H), 7.26 (dd, *J* = 8.4, 5.9 Hz, 2H), 7.20–7.13 (m, 4H), 6.02 (dd, *J* = 10.8, 2.2 Hz, 1H), 5.85 (d, *J* = 10.8 Hz, 1H), 4.34–4.27 (m, 1H), 4.09–4.03 (m, 1H), 3.93–3.89 (m, 1H), 3.85 (dd, *J* = 10.1, 5.2 Hz, 1H), 3.77 (dd, *J* = 10.3, 5.4 Hz, 1H), 3.72 (s, 6H), 3.69 (dd, *J* = 8.9, 4.4 Hz, 1H), 3.60–3.55 (m, *J* = 10.3, 2.0 Hz, 2H), 3.16 (ddd, *J* = 14.6, 10.5, 6.0 Hz, 2H), 3.08–3.01 (m, 1H), 3.01–2.94 (m, 1H), 2.62–2.55 (m, 2H), 2.44 (s, 2H), 2.30–2.18 (m, 2H), 2.12–2.11 (m, 1H), 1.94 (dt, *J* = 4.9, 2.5 Hz, 1H), 1.92–0.62 (m, 62H) ppm. ^{13}C NMR

(101 MHz, CD_3CN) δ 215.11, 176.15, 162.48, 162.46, 137.69, 137.67, 135.62, 135.54, 133.55, 122.81, 122.69, 121.70, 113.65, 113.58, 107.32, 107.09, 106.40, 99.78, 88.42, 79.69, 77.62, 75.52, 74.86, 72.33, 71.12, 70.13, 69.85, 68.00, 64.84, 57.23, 56.80, 55.28, 49.38, 47.66, 41.30, 39.15, 37.04, 36.95, 33.93, 32.14, 31.88, 31.21, 30.36, 30.17, 30.00, 28.71, 26.56, 26.16, 24.83, 24.28, 23.26, 22.47, 21.50, 21.46, 20.21, 17.72, 15.82, 15.23, 14.56, 13.30, 12.05, 11.24, 7.73, 6.66 ppm; ^{31}P NMR (122 MHz, CD_3CN) δ 26.78 ppm.

Compound 3d: Yield: 43.2 %. HRMS (ESI+) *m/z*: $[M]^+$ Calcd for $C_{67}H_{98}O_{14}P^+$ 1157.6689; Found: 1157.6679. ^{1}H NMR (400 MHz, CD_3CN) δ 7.64–7.58 (m, 4H), 7.22–7.17 (m, 4H), 6.01 (dd, $J = 10.8$, 2.2 Hz, 1H), 5.85 (dd, 1H), 4.39–4.33 (m, 1H), 4.13–4.06 (m, 1H), 3.89 (s, 6H), 3.76 (dd, $J = 11.0$, 4.3 Hz, 1H), 3.71–3.65 (m, 1H), 3.57 (dd, $J = 10.3$, 2.4 Hz, 2H), 3.27 (m, $J = 21.1$, 16.2, 8.2 Hz, 2H), 3.08–2.96 (m, 2H), 2.66 (d, $J = 5.1$ Hz, 1H), 2.59–2.54 (m, 1H), 2.31–2.18 (m, 2H), 1.97–0.58 (m, 66H) ppm (2 signals overlapped). ^{13}C NMR (101 MHz, CD_3CN) δ 215.66, 176.30, 165.49, 165.46, 136.41, 136.30, 133.65, 121.81, 116.76, 116.63, 110.53, 109.60, 107.16, 99.82, 88.41, 79.44, 77.66, 75.60, 74.83, 72.35, 71.12, 70.22, 68.04, 64.36, 57.34, 56.64, 49.41, 47.76, 41.29, 39.17, 37.19, 37.02, 34.09, 31.87, 31.25, 30.00, 29.78, 29.61, 28.73, 26.48, 26.12, 23.23, 23.16, 22.61, 22.49, 20.30, 19.66, 19.63, 17.77, 15.82, 15.22, 14.57, 13.20, 12.10, 11.34, 7.73, 6.67 ppm; ^{31}P NMR (122 MHz, CD_3CN) δ 22.75 ppm.

Compound 3e: Yield: 38.0 %. HRMS (ESI+) *m/z*: $[M]^+$ Calcd for $C_{66}H_{97}NO_{11}P^+$ 1110.6794; Found: 1110.6810. ^{1}H NMR (400 MHz, CD_3CN) δ 7.76–7.57 (m, 10H), 7.39–7.32 (m, 2H), 6.82–6.77 (m, 2H), 5.93 (dd, $J = 10.8$, 2.3 Hz, 1H), 5.78 (d, $J = 11.6$ Hz, 1H), 4.32–4.26 (m, 1H), 4.05–3.99 (m, 1H), 3.85–3.81 (m, $J = 9.2$ Hz, 1H), 3.81–3.77 (m, 1H), 3.70–3.65 (m, 1H), 3.61 (dd, $J = 13.8$, 6.8 Hz, 1H), 3.50 (dd, $J = 10.2$, 1.8 Hz, 2H), 3.30–3.12 (m, 3H), 2.96 (s, 6H), 2.59 (d, $J = 4.8$ Hz, 1H), 2.49 (dt, $J = 5.4$, 3.0 Hz, 1H), 2.21–2.09 (m, 2H), 1.90–0.50 (m, 60H) ppm.^{13}C NMR (101 MHz, CD_3CN) δ 215.64, 176.27, 155.00, 154.97, 135.65, 135.54, 135.46, 135.43, 134.23, 134.14, 133.60, 130.99, 130.86, 121.78, 121.37, 120.50, 113.32, 113.18, 107.15, 99.81, 99.23, 98.24, 88.40, 79.44, 77.69, 75.60, 74.88, 72.37, 71.12, 70.27, 67.97, 64.37, 57.25, 49.44, 47.73, 41.33, 40.08, 39.16, 37.17, 36.99, 34.02, 31.88, 31.34, 30.01, 29.83, 29.66, 28.75, 26.53, 26.20, 23.23, 22.86, 22.44, 22.32, 20.30, 19.75, 19.71, 17.76, 15.84, 15.23, 14.58, 13.27, 12.13, 11.36, 7.75, 6.69 ppm; ^{31}P NMR (122 MHz, CD_3CN) δ 23.49 ppm.

Compound 3f: Yield: 33.9 %. HRMS (ESI+) *m/z*: $[M]^+$ Calcd for $C_{58}H_{104}O_{11}P^+$ 1007.7311; Found: 1007.7337. ^{1}H NMR (401 MHz, CD_3CN) δ 6.05 (dd, $J = 10.7$, 2.1 Hz, 1H), 5.86 (d, $J = 11.7$ Hz, 1H), 4.35 (dd, $J = 11.7$, 5.5 Hz, 1H), 4.10 (q, $J = 11.3$, 5.9 Hz, 1H), 3.97–3.89 (m, 4H), 3.71 (q, $J = 7.1$ Hz, 1H), 3.64–3.57 (m, $J = 17.6$, 7.1 Hz, 3H), 3.07 (ddd, $J = 15.5$, 10.3, 5.9 Hz, 2H), 2.93 (s, 1H), 2.66 (d, $J = 5.3$ Hz, 1H), 2.65–2.61 (m, $J = 9.2$ Hz, 1H), 2.35 (s, 1H), 2.33–2.20 (m, 5H), 2.20–2.11 (m, 8H), 1.98–0.62 (m, 73H) ppm. ^{13}C NMR (101 MHz, CD_3CN) δ 215.64, 176.41, 133.74, 121.72, 107.15, 99.85, 88.47, 79.64, 77.76, 75.70, 74.86, 72.46, 71.13, 70.33, 68.18, 64.43, 57.60, 49.44, 47.84, 41.35, 39.31, 37.23, 37.13, 34.24, 31.90, 31.23, 30.23, 30.06, 29.66, 28.83, 28.57, 27.92, 26.59, 26.07, 24.73, 24.54, 24.49, 24.38, 23.88, 23.83, 23.29, 22.60, 20.34, 19.19, 18.90, 18.86, 18.71, 17.85, 15.85, 15.25, 14.75, 13.83, 13.53, 13.23, 12.18, 11.36, 7.84, 6.68 ppm; ^{31}P NMR (122 MHz, CD_3CN) δ 35.03 ppm.

Compound 5a: Yield: 17.3 %. HRMS (ESI+) *m/z*: $[M]^+$ Calcd for $C_{66}H_{96}O_{11}P^+$ 1095.6685; Found: 1095.6690.^{1}H NMR (400 MHz, CD_3CN) δ 7.89–7.83 (m, 3H), 7.77–7.70 (m, 12H), 6.05–6.02 (m, 1H), 5.88 (d, $J = 10.8$ Hz, 1H), 4.31–4.25 (m, 1H), 4.13–4.04 (m, 2H), 3.96–3.87 (m, 4H), 3.85–3.81 (m, 1H), 3.73 (dd, $J = 13.8$, 6.9 Hz, 1H), 3.68–3.64 (m, 1H), 3.64–3.50 (m, 4H), 3.35–3.28 (m, 2H), 3.04 (td, $J = 11.4$, 4.6 Hz, 2H), 2.69 (d, $J = 4.7$ Hz, 1H), 2.63–2.59 (m, 1H), 2.49 (s, 1H), 2.29–2.21 (m, 2H), 2.12–2.11 (m, 2H), 1.96–0.64 (m, 54H) ppm; ^{13}C NMR (101 MHz, CD_3CN) δ 215.08, 176.27, 135.93, 135.90, 134.54, 134.44, 133.46, 131.16, 131.04, 121.80, 119.63, 118.77, 107.18, 99.77, 88.37, 77.75, 75.60, 74.93, 72.47, 71.17, 67.79, 65.21, 55.26, 49.42, 47.70, 41.35, 39.11, 37.05, 36.87, 33.84, 32.14, 31.88, 30.47, 30.30, 30.02, 29.63, 28.82, 28.71, 26.70, 26.36, 25.68, 23.28, 22.81, 22.68, 22.17, 20.29, 17.65, 15.85, 15.21, 14.45, 13.32, 12.17, 11.30, 7.85, 6.72 ppm; ^{31}P NMR (162 MHz, CD_3CN) δ 24.92 ppm.

Compound 5b: Yield: 25.6 %. HRMS (ESI+) *m/z*: $[M]^+$ Calcd for $C_{69}H_{102}O_{11}P^+$ 1137.7154; Found: 1137.7163. ^{1}H NMR (401 MHz, CD_3CN) δ 7.59–7.51 (m, 12H), 6.05–6.00 (m, 1H), 5.83 (d, $J = 10.9$ Hz, 1H), 4.29 (dt, $J = 11.0$, 6.8 Hz, 1H), 4.11–4.03 (m, 1H), 3.92 (dd, $J = 9.6$, 6.3 Hz, 4H), 3.70 (q, $J = 6.7$ Hz, 1H), 3.60–3.55 (m, 3H), 3.21–3.12 (m, 2H), 3.07 (dd, $J = 10.1$, 7.1 Hz, 1H), 3.00 (td, $J = 10.6$, 4.3 Hz, 1H), 2.88 (s, 1H), 2.63 (d, $J = 5.4$ Hz, 1H), 2.59 (d, $J = 11.5$ Hz, 1H), 2.46 (s, 6H), 2.32–2.29 (m, 4H), 2.28–2.19 (m, 2H), 1.96 (s, 1H), 1.94 (dt, $J = 5.0$, 2.5 Hz, 3H), 1.90–0.63 (m, 55H) ppm; ^{13}C NMR (101 MHz, CD_3CN) δ 215.08, 176.46, 147.45, 147.42, 134.53, 134.43, 133.85, 131.95, 131.82, 121.90, 118.31, 116.75, 115.87, 107.32, 99.98, 88.68, 80.06, 77.92, 75.73, 75.03, 72.65, 71.31, 70.31, 68.28, 65.44, 57.38, 49.61, 47.96, 41.49, 39.42, 37.32, 37.24, 34.15, 32.05, 31.38, 30.61, 30.45, 30.20, 29.82, 29.02, 28.87, 26.86, 26.28, 25.83, 23.48, 23.15, 23.00, 22.95, 22.77, 22.62, 21.88, 20.53, 17.91, 16.01, 15.42, 14.68, 13.49, 12.26, 11.53, 7.99, 6.84 ppm; ^{31}P NMR (122 MHz, CD_3CN) δ 23.96 ppm.

Compound 5c: Yield: 15.0 %. HRMS (ESI+) *m/z*: $[M]^+$ Calcd for $C_{69}H_{102}O_{14}P^+$ 1185.7002; Found: 1185.7025. ^{1}H NMR (401 MHz, CD_3CN) δ 7.82–7.78 (m, 3H), 7.26 (dd, $J = 8.1$, 5.6 Hz, 3H), 7.18–7.14 (m, 6H), 6.06 (dd, $J = 10.8$, 2.4 Hz, 1H), 6.00 (d, $J = 11.9$ Hz, 1H), 4.31–4.25 (m, 1H), 4.13–4.07 (m, 1H), 4.01 (d, $J = 9.2$ Hz, 1H), 3.91 (dt, $J = 8.5$, 4.2 Hz, 3H), 3.81 (t, $J = 6.8$ Hz, 1H), 3.77–3.73 (m, 1H), 3.71 (s, 6H), 3.64 (dd, $J = 10.3$, 1.6 Hz, 1H), 3.62 (s, 1H), 3.52 (s, 4H), 3.51 (s, 1H), 3.47–3.43 (m, 2H), 3.21–0.63 (m, 66H) ppm; ^{13}C NMR (101 MHz, CD_3CN) δ 215.66, 176.42, 162.63, 162.61, 137.80, 137.78, 135.80, 135.71, 133.08, 122.96, 122.84, 122.22, 113.82, 113.75, 107.64, 107.55, 106.72, 99.92, 88.29, 79.16, 78.11, 75.98, 75.39, 72.81, 71.49, 71.10, 70.26, 70.00, 67.11, 65.33, 56.90, 56.60, 55.39, 49.67, 47.57, 41.73, 39.02, 37.00, 36.69, 33.66, 32.24, 32.05, 29.90, 29.03, 27.30, 27.05, 25.99, 24.52, 24.47, 24.41, 23.39, 20.43, 17.59, 16.02, 15.24, 14.45, 13.48, 12.52, 11.38, 8.10, 6.96 ppm; ^{31}P NMR (162 MHz, CD_3CN) δ 26.73 ppm.

Compound 5d: Yield: 40.1 %. HRMS (ESI+) *m/z*: $[M]^+$ Calcd for $C_{69}H_{102}O_{14}P^+$ 1185.7002; Found: 1185.7007. ^{1}H NMR (400 MHz, CD_3CN) δ 7.64–7.58 (m, 5H), 7.20 (dt, $J = 5.2$, 2.6 Hz, 5H), 6.03 (dd, $J = 10.8$, 2.2 Hz, 1H), 5.85 (d, $J = 11.2$ Hz, 1H), 4.29 (dt, $J = 10.9$, 6.8 Hz, 1H), 4.11–4.05 (m, 1H), 3.93 (dd, $J = 8.5$, 3.3 Hz, 2H), 3.90 (s, 6H), 3.74–3.68 (m, 1H), 3.59 (d, $J = 11.2$ Hz, 2H), 3.19–3.10 (m, 2H), 3.10–2.96 (m, 3H), 2.64 (d, $J = 9.3$ Hz, 1H), 2.63–2.58 (m, 1H), 2.45 (s, 1H), 2.32–2.25 (m, 1H), 2.25–2.19 (m, 1H), 1.98–0.65 (m, 65H) ppm (signals overlapped); ^{13}C NMR (101 MHz, CD_3CN) δ 214.93, 176.27, 165.46, 165.44, 136.39, 136.28, 133.59, 121.72, 116.73, 116.59, 110.66, 109.72, 107.14, 99.76, 88.44, 79.79, 77.72, 75.55, 74.86, 72.44, 71.10, 70.16, 67.97, 65.25, 57.07, 56.64, 56.63, 55.29, 49.39, 47.73, 41.30, 39.18, 37.10, 36.99, 33.91, 31.87, 31.30, 30.43, 30.27, 30.02, 29.64, 28.82, 28.70, 26.67, 26.16, 25.70, 23.61, 23.29, 23.07, 22.80, 22.76, 22.47, 20.30, 17.70, 15.84, 15.23, 14.49, 13.32, 12.12, 11.32, 7.81, 6.69 ppm; ^{31}P NMR (162 MHz, CD_3CN) δ −22.53 ppm.

Compound 5e: Yield: 35.4 %. HRMS (ESI+) *m/z*: $[M]^+$ Calcd for $C_{68}H_{101}NO_{11}P^+$ 1138.7107; Found: 1138.7129. ^{1}H NMR (401 MHz, CD_3CN) δ 7.72–7.65 (m, 10H), 7.45–7.39 (m, 2H), 6.90–6.87 (m, 2H), 6.03 (dd, $J = 10.8$, 2.2 Hz, 1H), 5.84 (d, $J = 10.2$ Hz, 1H), 4.29 (dt, $J = 10.9$, 6.8 Hz, 1H), 4.07 (dt, $J = 11.0$, 6.4 Hz, 1H), 3.92 (t, $J = 4.5$ Hz, 2H), 3.90 (s, 1H), 3.70 (q, $J = 6.9$ Hz, 1H), 3.61–3.56 (m, 3H), 3.17–3.08 (m, 2H), 3.05 (s, 6H), 2.64 (d, $J = 5.4$ Hz, 1H), 2.62–2.58 (m, 1H), 2.37 (s, 2H), 2.32–2.17 (m, 2H), 1.96–0.63 (m, 62H) ppm; ^{13}C NMR (101 MHz, CD_3CN) δ 215.05, 176.39, 155.16, 135.76, 135.65, 135.57, 135.54, 134.36, 134.26, 133.76, 131.10, 130.97, 121.88, 121.62, 120.76, 107.30, 99.93, 98.56, 88.62, 79.98, 77.89, 75.70, 75.00, 72.62, 71.28, 70.33, 68.18, 65.39, 57.25, 49.58, 47.89, 41.46, 40.21, 39.36, 37.26, 37.16, 34.07, 32.01, 31.42, 30.61, 30.45, 30.16, 29.78, 28.99, 28.86, 26.84, 26.29, 25.84, 23.43, 23.02, 22.97, 22.92, 22.66, 20.50, 17.86, 15.98, 15.37, 14.65, 13.48, 12.24, 11.50, 7.96 ppm; ^{31}P NMR (162 MHz, CD_3CN) δ 23.27 ppm.

Compound 5f: Yield: 31.5 %. HRMS (ESI+) *m/z*: $[M]^+$ Calcd for $C_{60}H_{108}O_{11}P^+$ 1035.7624; Found: 1035.7643. ^{1}H NMR (401 MHz, CD_3CN) δ 6.07–6.03 (m, 1H), 5.84 (d, *J* = 11.0 Hz, 1H), 4.32 (dt, *J* = 10.8, 6.7 Hz, 1H), 4.12 (dd, *J* = 10.9, 6.4 Hz, 1H), 3.93 (d, *J* = 8.6 Hz, 5H), 3.71 (t, *J* = 7.0 Hz, 1H), 3.59 (t, *J* = 10.3 Hz, 4H), 3.10 (dd, *J* = 10.2, 7.2 Hz, 1H), 3.02 (dt, *J* = 10.6, 5.2 Hz, 1H), 2.93 (s, 1H), 2.64 (d, *J* = 5.2 Hz, 2H), 2.61 (t, 1H), 2.37 (s, 1H), 2.31–2.22 (m, 2H), 2.19–2.08 (m, 13H), 1.96–0.61 (m, 72H) ppm; ^{13}C NMR (101 MHz, CD_3CN) δ 214.83, 176.29, 133.69, 121.73, 107.16, 99.82, 88.52, 79.99, 77.76, 75.57, 74.88, 72.50, 71.12, 70.17, 68.12, 65.34, 57.25, 49.45, 47.80, 41.33, 39.26, 37.17, 37.06, 33.97, 31.91, 31.21, 30.86, 30.70, 30.06, 28.89, 28.56, 27.92, 26.72, 26.12, 25.85, 24.86, 24.73, 24.52, 24.49, 24.34, 23.87, 23.82, 23.35, 22.62, 21.90, 21.85, 20.36, 19.39, 19.17, 18.91, 18.69, 17.75, 15.86, 15.26, 14.57, 13.83, 13.51, 13.38, 12.13, 11.37, 7.85, 6.69 ppm; ^{31}P NMR (122 MHz, CD_3CN) δ 34.86 ppm.

4.2. Biological studies

4.2.1. Culture cell lines

The studies were conducted on cell lines including, human primary (SW480) and metastatic (SW620) colon cancer, human metastatic prostate cancer (PC3), human breast cancer (MDA-MB-231), human lung cancer (A549), human immortal keratinocytes (HaCaT) and Chinese hamster lung fibroblasts (V79). All cell lines, obtained from the repository of the Medical University of Warsaw, were cultured in a recommended medium supplemented with 10 % foetal bovine serum, penicillin (100 U/mL) and streptomycin (100 μg/L) at 37 °C and 5 % CO_2. After 80 % of confluence, the cells were harvested (0.25 % trypsin, Gibco Life Technologies) and seeded on 96-, 12- and 6-well plates, incubated for 24 h at 37 °C with 5 % CO_2 for optimal attachment and used for further assays.

4.2.2. MTT assay

Cell lines (5×10^3 cells per well) were seeded on 96-well plates. **SAL** and its derivatives were added at concentrations ranged 1–40 μM and the plates were incubated for 72 h at 37 °C with 5 % CO_2. Subsequently, after removal of the culture medium, MTT solution (0.5 mg/mL) was applied to each well, followed by a 4 h incubation at 37 °C with 5 % CO_2. Formazan crystals that developed were then dissolved in DMSO and isopropanol mixture (1:1, v/v). The absorbance was measured at 570 nm using a Multiscan Go spectrophotometer (ThermoSci). Cell viability was expressed as the percentage of MTT reduction in cells treated with tested compounds compared to the control sample (untreated cells). The relative MTT level was calculated using the formula: [100 %] = A/B × 100 %, (A - test sample absorbance; B - the control sample absorbance). The IC_{50} values were estimated using GraphPad Prism 8.0.1 software (GraphPad Software).

4.2.3. Annexin V-FITC/PI binding assay

The cells (A549, MDA-MB-231) (5×10^4 cells per well) were seeded on 12-well plates and exposed for 72 h to **SAL** and its selected (**3a**, **3f**, **6**) derivatives at their IC_{50} concentration. Next, both adherent and detached cells were collected and centrifuged at 800×*g* for 5 min at 4 °C. The cells were then washed twice with cold PBS and labelled with Annexin V-FITC and propidium iodide (PI) according to the manufacturer's protocol (BD Biosciences Pharmingen). The stained cells were analysed by flow cytometry (Becton Dickinson FACS Verse) and identified as early apoptotic (Annexin V+/PI−) or late apoptotic/necrotic (Annexin V+/PI+).

4.2.4. Cell cycle analysis

The cells (1×10^5 per well) were seeded on 6-well plates and treated with the studied compounds at their IC_{50} concentration for 24 h. Next, both adherent and detached cells were collected and centrifuged at 450×*g* for 5 min at 4 °C. The cells were then washed twice with PBS and fixed in cold 70 % ethanol at 4 °C overnight. Prior to analysis, the fixed cells were centrifuged at 800×*g* for 5 min at 4 °C and washed again with PBS. They were then treated with RNase (100 μg/mL) and stained with PI (50 μg/mL) at 37 °C for 30 min in the dark. Finally, 200 μL of PBS was added to each sample. The identification of cells in various stages of the cell cycle (sub-G1, G0/G1, S, and G2/M phases) was performed by flow cytometry (Becton Dickinson FACS Verse).

4.2.5. Mitochondrial membrane potential (MMP) and mitochondrial activity assays

The cells (5×10^4 cells per well) were seeded on 12-well plates and treated with **SAL** and its selected derivatives at their IC_{50} concentration. After 48 h incubation at 37 °C with 5 % CO_2 both suspended and adherent cells were collected, centrifuged (800×*g* for 5 min at 4 °C) and washed twice with PBS. The mitochondrial activity was measured by staining with JC-10 (Abcam), MitoTracker Red CMXRos, MitoTracker Green FM dyes (Invitrogen) according to manufacturer's protocol. After 30 min incubation at 37 °C in the dark the samples were analysed by flow cytometry (Becton Dickinson FACS Verse). JC-10 aggregates (red fluorescence) are present in the mitochondria after potential-dependent aggregation, while JC-10 monomers (green fluorescence) increased in the cytosol after depolarization of the mitochondrial membrane. MitoTracker Green FM localized to mitochondrial membrane determine mitochondrial mass and MitoTracker Red CMXRos is localized to the matrix of the functional mitochondria and intact mitochondrial membrane potential.

4.2.6. ROS detection assay

The cells (5×10^4 cells per well) were seeded on dark 96-well plates, treated with **SAL** and its derivatives at their IC_{50} concentrations and incubated 6 h at 37 °C with 5 % CO_2. The ROS level was evaluated using the CellROX Green Reagent (Invitrogen) according to the manufacturer's instruction. The cell-permeant dye is weakly fluorescent, while in a reduced state, and exhibits bright green photostable fluorescence upon oxidation by reactive oxygen species (ROS) and subsequent binding to DNA. A sample with H_2O_2 (1.5 mM) was used as a positive control. The generation of ROS was measured by the Microplate Spectrofluorometer BioTek Synergy (BioTek Instruments).

4.2.7. Antibacterial studies

To characterize the antibacterial activity of triphenylphosphonium derivatives of **SAL**, reference bacterial strains from the international microbe collections, American Type Culture Collection (ATTC) and National Collection of Type Culture (NCTC), as well as a panel of clinical rods, were studied. The set contained six Gram-positive strains: *S. aureus* NCTC 4163; ATCC: 25923, 6538, and 29213; and *S. epidermidis* ATCC: 12228 and 35984, and additionally two Gram-negative organisms: *E. coli* ATCC 25922 and *P. aeruginosa* ATCC 15442. Antibiotic susceptibilities, including the resistance phenotypes of hospital strains, were tested using VITEK 2 Compact and VITEK 2 AES.

The MIC values were determined by the twofold microdilution method according to the CLSI reference procedure with some modifications [31]. The bacteria were cultured in brain heart infusion agar (BHI) and incubated at 37 °C for 24–48 h. Bacterial inoculum was prepared in a sterile saline solution and diluted in MH II liquid medium to a final concentration of 106 colony-forming units per mL (cfu/mL). The reference CP was tested in the range of 0.03–32 μg/mL, whereas the concentrations of the conjugates were varied from 0.025 to 25.6 μg/mL. The final concentration of DMSO in working solutions was less than 1 %. The bacteria were grown overnight in the presence of different concentrations of the tested compounds. After a 18 h period of incubation, the lowest concentration of the drugs that inhibited the visible growth of bacteria was considered as the MIC value. Tests were repeated independently three times.

The VITEK 2 Compact (BioMérieux) automated system for the antimicrobial susceptibility testing of microorganisms was used in accordance with the manufacturer's directions.

4.3. Biophysical studies

4.3.1. Chemicals

1,2-Diacyl-*sn*-glycero-3-phosphocholine (asolectin), n-decane were from MERCK, Darmstadt, Germany. All of the chemicals used were of analytical grade. **SAL** and its conjugates were obtained from the Department of Medicinal Chemistry of Adam Mickiewicz University in Poznań.

4.3.2. Cell culture

High resolution respirometry experiments were performed on the adenocarcinomic human alveolar basal epithelial cells (A549, MERCK, Darmstadt, Germany). Cells were cultured on T75 flasks (Googlab™ in Dulbecco Minimal Essential Medium (DMEM; MERCK, Darmstadt, Germany) supplemented with 10 % fetal bovine serum (FBS; Gibco, Thermo Fisher Scientific, Waltham, MA, USA) and antibiotics—100 U/mL penicillin and 100 mg/mL streptomycin (MERCK, Darmstadt, Germany). Cells were maintained within a humidified 5 % CO_2 atmosphere at 37 °C and reseeded when they reached 90 % confluence.

4.3.3. High resolution respirometry

High resolution respirometry was performed using Oxygraph-2K system (Oroboros Instruments, Innsbruck, Austria) according to a commonly used method [32]. Briefly, A549 cells were harvested, centrifuged, and resuspended in starving DMEM (1 % FBS) with 1×10^6 cells/cm^3. The cells were added to respiratory chambers to measure basal respiration. Next, **SAL** and its conjugates in concentrations of 0.1, 0.3, 1, 3 or 10 μM were added to chambers after stabilization of the respiration. The maximal uncoupled electron transfer system (ETS) was measured after application of carbonyl cyanide-*p*-trifluoromethoxyphenylhydrazone (FCCP; 1 μM). The data are reported as mean values ± SD (SD, standard deviation).

4.3.4. Black lipid membrane technique (BLM)

Asolectin dissolved in n-decane at a final concentration of 25 mg/mL was used as a model of the biological membrane and was applied using a polyethylene brush to the 250 μm diameter opening of the Teflon cup to separate two chambers (*cis/trans*) [33,34]. To improve the stability of the lipid bilayer, the outline of the aperture was coated with a lipid solution and N_2-dried prior to bilayer formation. Overall, 1 mL quantities of the solutions containing 50/150 mM KCl (*cis/trans*) and 10 mM HEPES at pH = 7.2 were added to measurement chambers and stirred via magnetic stirrers. Silver-chloride (Ag/AgCl) electrodes were introduced into the chambers and connected to the BLM-120 amplifier (Bio-Logic, Seyssinet-Pariset, France). The electric signal was processed by the PowerLab 2/25 (ADInstruments, Sydney, Australia) converter, recorded using LabChart5 software and analysed in the Clampfit 8 software. The experiments were performed in Faraday's cage to prevent external electromagnetic interferences. All measurements were carried out at room temperature (25 °C). In the actual experiment, **SAL** and its conjugates were added to *trans* side chamber in concentrations of 0.1, 0.3, 1, 3 or 10 μM.

Bilayer formation and thinning were monitored by the capacitance measurements and optical observations. The final accepted capacitance values ranged from 110 to 180 pF. Electrical connections were made by Ag/AgCl electrodes and agar salt bridges (3 M KCl) to minimize liquid junction potentials. Voltage was applied to the *cis* compartment and the *trans* compartment was grounded.

Single-channel data were filtered at 500 Hz. The current was digitized at a sampling rate of 100 kHz. Single-channel currents were recorded at different voltages in steps of 20 mV. The data are reported as mean value ± SD (SD, standard deviation).

CRediT authorship contribution statement

Marta Jędrzejczyk: Writing – review & editing, Writing – original draft, Validation, Resources, Project administration, Methodology, Investigation, Data curation, Conceptualization. **Michał Sulik:** Writing – original draft, Investigation, Data curation. **Magdalena Mielczarek-Puta:** Methodology, Investigation, Data curation. **Gwan Yong Lim:** Investigation. **Małgorzata Podsiad:** Investigation. **Jakub Hoser:** Writing – original draft, Methodology, Investigation, Data curation. **Piotr Bednarczyk:** Writing – original draft, Supervision, Methodology, Conceptualization. **Marta Struga:** Writing – original draft, Supervision, Methodology. **Adam Huczyński:** Writing – review & editing, Writing – original draft, Visualization, Validation, Supervision, Resources, Methodology, Investigation, Funding acquisition, Formal analysis, Data curation, Conceptualization.

Funding

This research was funded by the Polish National Science Centre (NCN), grant number 2021/41/B/ST4/00088. For the purpose of Open Access, the authors have applied public copyright license to any Author Accepted Manuscript (AAM) version arising from this submission.

Declaration of competing interest

The authors declare that they have no known competing financial interests or personal relationships that could have appeared to influence the work reported in this paper.

Acknowledgements

A.H. wishes to acknowledge the Polish National Science Centre (NCN) for financial support through an OPUS grant (2021/41/B/ST4/00088).

Appendix A. Supplementary data

Supplementary data to this article can be found online at https://doi.org/10.1016/j.ejmech.2024.117055.

Data availability

Data will be made available on request.

References

[1] Y. Liu, Y. Sun, Y. Guo, X. Shi, X. Chen, W. Feng, L.-L. Wu, J. Zhang, S. Yu, Y. Wang, Y. Shi, An overview: the diversified role of mitochondria in cancer metabolism, Int. J. Biol. Sci. 19 (2023) 897–915, https://doi.org/10.7150/ijbs.81609.

[2] J. Pourahmad, A. Salimi, E. Seydi, Mitochondrial targeting for drug development, in: Toxicology Studies - Cells, Drugs and Environment, InTech, 2015, https://doi.org/10.5772/59719.

[3] K. Klein, K. He, A.I. Younes, H.B. Barsoumian, D. Chen, T. Ozgen, S. Mosaffa, R. R. Patel, M. Gu, J. Novaes, A. Narayanan, M.A. Cortez, J.W. Welsh, Role of mitochondria in cancer immune evasion and potential therapeutic approaches, Front. Immunol. 11 (2020), https://doi.org/10.3389/fimmu.2020.573326.

[4] N. Badrinath, S.Y. Yoo, Mitochondria in cancer: in the aspects of tumorigenesis and targeted therapy, Carcinogenesis 39 (2018) 1419–1430, https://doi.org/10.1093/carcin/bgy148.

[5] M.T. Jeena, S. Kim, S. Jin, J.H. Ryu, Recent progress in mitochondria-targeted drug and drug-free agents for cancer therapy, Cancers 12 (2020), https://doi.org/10.3390/cancers12010004.

[6] J. Zielonka, J. Joseph, A. Sikora, M. Hardy, O. Ouari, J. Vasquez-Vivar, G. Cheng, M. Lopez, B. Kalyanaraman, Mitochondria-Targeted triphenylphosphonium-based compounds: syntheses, mechanisms of action, and therapeutic and diagnostic applications, Chem Rev 117 (2017) 10043–10120, https://doi.org/10.1021/acs.chemrev.7b00042.

[7] M. Millard, J.D. Gallagher, B.Z. Olenyuk, N. Neamati, A selective mitochondrial-targeted chlorambucil with remarkable cytotoxicity in breast and pancreatic cancers, J. Med. Chem. 56 (2013) 9170–9179, https://doi.org/10.1021/jm4012438.

[8] J.A. Pavlova, Z.Z. Khairullina, A.G. Tereshchenkov, P.A. Nazarov, D.A. Lukianov, I. A. Volynkina, D.A. Skvortsov, G.I. Makarov, E. Abad, S.Y. Murayama, S. Kajiwara, A. Paleskava, A.L. Konevega, Y.N. Antonenko, A. Lyakhovich, I.A. Osterman, A. A. Bogdanov, N.V. Sumbatyan, Triphenilphosphonium analogs of chloramphenicol as dual-acting antimicrobial and antiproliferating agents, Antibiotics 10 (2021) 489, https://doi.org/10.3390/antibiotics10050489.

[9] T. Li, X. He, W. Tao, R. Zhang, Q. He, H. Gong, Y. Liu, D. Luo, M. Zhang, C. Zou, S.-L. Zhang, Y. He, Development of membrane-targeting TPP+-chloramphenicol conjugates to combat methicillin-resistant staphylococcus aureus (MRSA) infections, Eur. J. Med. Chem. 264 (2024) 115973, https://doi.org/10.1016/j.ejmech.2023.115973.

[10] Z. Tang, J. Feng, M. Challa, S.R. Rowthu, S. Xiong, C. Zou, J. Li, C.S. Verma, H. Peng, X. He, C. Huang, Y. He, Discovery of novel Thymol-TPP antibiotics that eradicate MRSA persisters, Eur. J. Med. Chem. 270 (2024) 116381, https://doi.org/10.1016/j.ejmech.2024.116381.

[11] A. Huczynski, Salinomycin - a new cancer drug candidate, Chem. Biol. Drug Des. 79 (2012) 235–238, https://doi.org/10.1111/j.1747-0285.2011.01287.x.

[12] H.D. Chapman, Anticoccidial drugs and their effects upon the development of immunity to *Eimeria* infections in poultry, Avian Pathol. 28 (1999) 521–535, https://doi.org/10.1080/03079459994317.

[13] M. Antoszczak, J. Rutkowski, A. Huczyński, Structure and biological activity of polyether ionophores and their semisynthetic derivatives, in: Bioactive Natural Products, Wiley, 2014, pp. 107–170, https://doi.org/10.1002/9783527684403.ch6.

[14] P.B. Gupta, T.T. Onder, G. Jiang, K. Tao, C. Kuperwasser, R.A. Weinberg, E. S. Lander, Identification of selective inhibitors of cancer stem cells by high-throughput screening, Cell 138 (2009) 645–659, https://doi.org/10.1016/j.cell.2009.06.034.

[15] M. Antoszczak, A medicinal chemistry perspective on salinomycin as a potent anticancer and anti-CSCs agent, Eur. J. Med. Chem. 164 (2019) 366–377, https://doi.org/10.1016/j.ejmech.2018.12.057.

[16] M. Antoszczak, A comprehensive review of salinomycin derivatives as potent anticancer and anti-CSCs agents, Eur. J. Med. Chem. 166 (2019) 48–64, https://doi.org/10.1016/j.ejmech.2019.01.034.

[17] Y.N. Antonenko, M. Jędrzejczyk, T.I. Rokitskaya, L.S. Khailova, E.A. Kotova, A. Huczyński, Rate of translocation across lipid bilayer of triphenylphosphonium-linked salinomycin derivatives contributes significantly to their K+/H+ exchange activity on membranes, Bioelectrochemistry 145 (2022), https://doi.org/10.1016/J.BIOELECHEM.2022.108089.

[18] T.I. Rokitskaya, V.B. Luzhkov, G.A. Korshunova, V.N. Tashlitsky, Y.N. Antonenko, Effect of methyl and halogen substituents on the transmembrane movement of lipophilic ions, Phys. Chem. Chem. Phys. 21 (2019) 23355–23363, https://doi.org/10.1039/C9CP03460A.

[19] D.V. Tsyganov, A.V. Samet, E.A. Silyanova, V.I. Ushkarov, A.E. Varakutin, N. B. Chernysheva, R.N. Chuprov-Netochin, A.A. Khomutov, A.S. Volkova, S. V. Leonov, M.N. Semenova, V.V. Semenov, Synthesis and antiproliferative activity of triphenylphosphonium derivatives of natural allylpolyalkoxybenzenes, ACS Omega 7 (2022) 3369–3383, https://doi.org/10.1021/acsomega.1c05515.

[20] T.I. Rokitskaya, R.S. Kirsanov, L.S. Khailova, A.A. Panteleeva, K.G. Lyamzaev, G. A. Korshunova, E.A. Kotova, Y.N. Antonenko, Methylation of phenyl rings in ester-stabilized phosphorus ylides vastly enhances their protonophoric activity, Chembiochem 25 (2024) e202300848, https://doi.org/10.1002/cbic.202300848.

[21] A. Huczyński, J. Janczak, J. Stefańska, M. Antoszczak, B. Brzezinski, Synthesis and antimicrobial activity of amide derivatives of polyether antibiotic—salinomycin, Bioorg Med Chem Lett 22 (2012) 4697–4702, https://doi.org/10.1016/j.bmcl.2012.05.081.

[22] A. Huczyński, J. Stefańska, P. Przybylski, B. Brzezinski, F. Bartl, Synthesis and antimicrobial properties of Monensin A esters, Bioorg Med Chem Lett 18 (2008) 2585–2589, https://doi.org/10.1016/j.bmcl.2008.03.038.

[23] F. Denizot, R. Lang, Rapid colorimetric assay for cell growth and survival, J. Immunol. Methods 89 (1986) 271–277, https://doi.org/10.1016/0022-1759(86)90368-6.

[24] L. de B. Monteiro, G.G. Davanzo, C.F. de Aguiar, P.M.M. Moraes-Vieira, Using flow cytometry for mitochondrial assays, MethodsX 7 (2020) 100938, https://doi.org/10.1016/j.mex.2020.100938.

[25] K. Neikirk, A.G. Marshall, B. Kula, N. Smith, S. LeBlanc, A. Hinton, MitoTracker: a useful tool in need of better alternatives, Eur. J. Cell Biol. 102 (2023) 151371, https://doi.org/10.1016/j.ejcb.2023.151371.

[26] M. Adebayo, S. Singh, A.P. Singh, S. Dasgupta, Mitochondrial fusion and fission: the fine-tune balance for cellular homeostasis, Faseb. J. 35 (2021), https://doi.org/10.1096/fj.202100067R.

[27] X. Graña, E.P. Reddy, Cell cycle control in mammalian cells: role of cyclins, cyclin dependent kinases (CDKs), growth suppressor genes and cyclin-dependent kinase inhibitors (CKIs), Oncogene 11 (1995) 211–219.

[28] L.D. Zorova, V.A. Popkov, E.Y. Plotnikov, D.N. Silachev, I.B. Pevzner, S. S. Jankauskas, V.A. Babenko, S.D. Zorov, A.V. Balakireva, M. Juhaszova, S. J. Sollott, D.B. Zorov, Mitochondrial membrane potential, Anal. Biochem. 552 (2018) 50–59, https://doi.org/10.1016/j.ab.2017.07.009.

[29] H. Nakamura, K. Takada, Reactive oxygen species in cancer: current findings and future directions, Cancer Sci. 112 (2021) 3945–3952, https://doi.org/10.1111/cas.15068.

[30] K.Y. Kim, K.I. Park, S.H. Kim, S.N. Yu, D. Lee, Y.W. Kim, K.T. Noh, J.Y. Ma, Y. K. Seo, S.C. Ahn, Salinomycin induces reactive oxygen species and apoptosis in aggressive breast cancer cells as mediated with regulation of autophagy, Anticancer Res. 37 (2017) 1747–1758, https://doi.org/10.21873/anticanres.11507.

[31] CLSI, Performance Standards for Antimicrobial Susceptibility Testing, 29th ed., Clinical and Laboratory Standards Institute, Wayne, PA, 2019.

[32] A. Dabrowska, M. Zajac, P. Bednarczyk, A. Lukasiak, Effect of quercetin on mitoBKCa channel and mitochondrial function in human bronchial epithelial cells exposed to particulate matter, Int. J. Mol. Sci. 24 (2022) 638, https://doi.org/10.3390/ijms24010638.

[33] D. Kozon-Markiewicz, R.J. Kopiasz, M. Głusiec, A. Łukasiak, P. Bednarczyk, D. Jańczewski, Membrane lytic activity of antibacterial ionenes, critical role of phosphatidylcholine (PC) and cardiolipin (CL), Colloids Surf. B Biointerfaces 229 (2023) 113480, https://doi.org/10.1016/j.colsurfb.2023.113480.

[34] J. Hoser, A. Dabrowska, M. Zajac, P. Bednarczyk, Changes in ion transport across biological membranes exposed to particulate matter, Membranes 13 (2023) 763, https://doi.org/10.3390/membranes13090763.

European Journal of Medicinal Chemistry

Anticancer activity of salinomycin quaternary phosphonium salts

Marta Jędrzejczyk [a], Michał Sulik [a], Magdalena Mielczarek-Puta [b], Gwan Yong Lim [b], Małgorzata Podsiad [b], Jakub Hoser [c], Piotr Bednarczyk [c], Marta Struga [b], Adam Huczyński [a,*]

[a] *Department of Medical Chemistry, Faculty of Chemistry, Adam Mickiewicz University, Uniwersytetu Poznańskiego 8, 61–614 Poznań, Poland*

[b] *Chair and Department of Biochemistry, Faculty of Medicine, Medical University of Warsaw, Banacha 1, 02–097 Warsaw, Poland*

[c] *Department of Physics and Biophysics, Institute of Biology, Warsaw University of Life Sciences SGGW, Nowoursynowska 159, 02-776 Warsaw, Poland*

**corresponding author:* adhucz@amu.edu.pl

Supporting information

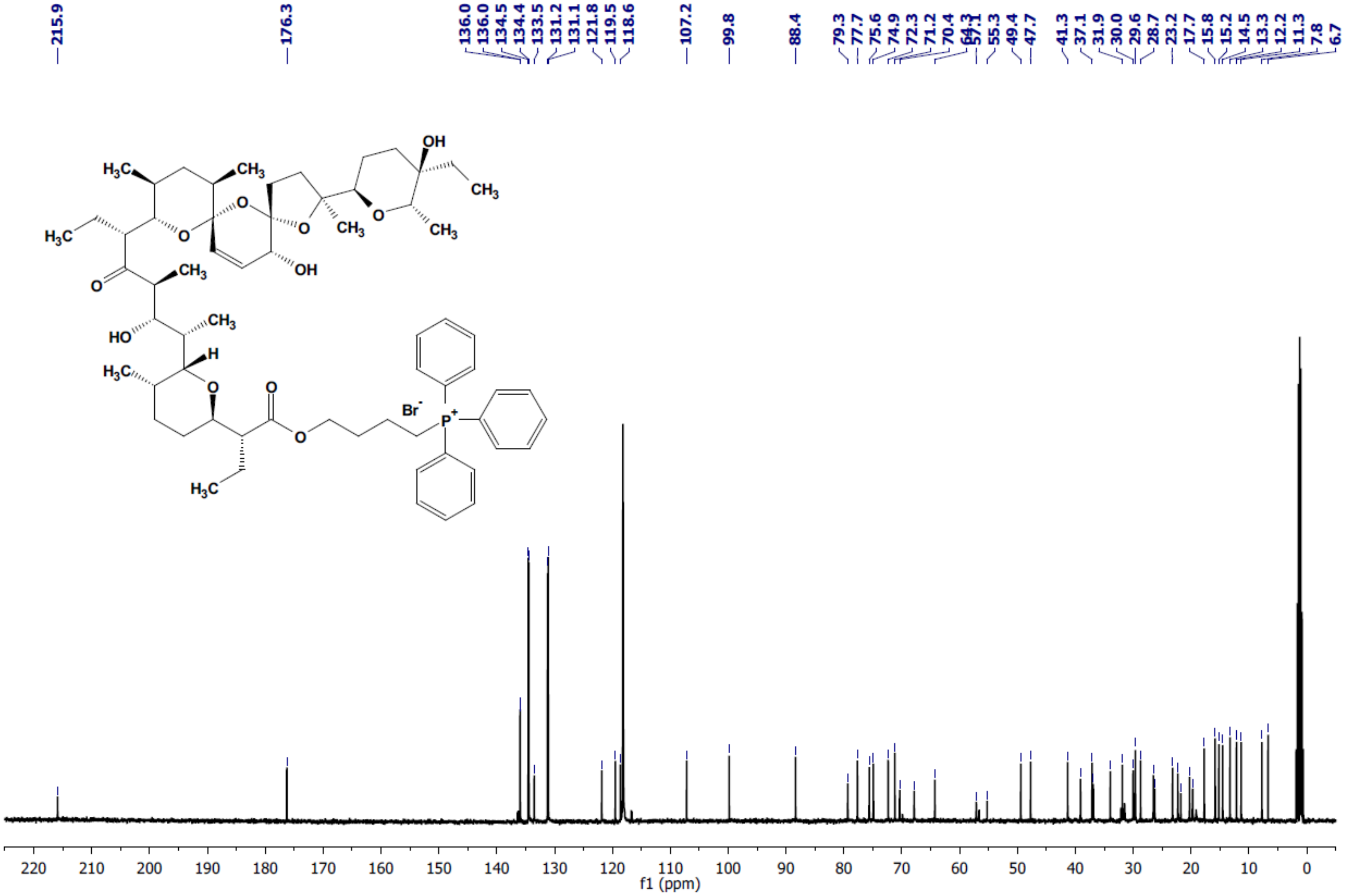

Fig. S1. The ^{13}C NMR spectrum of **3a** in CD_3CN.

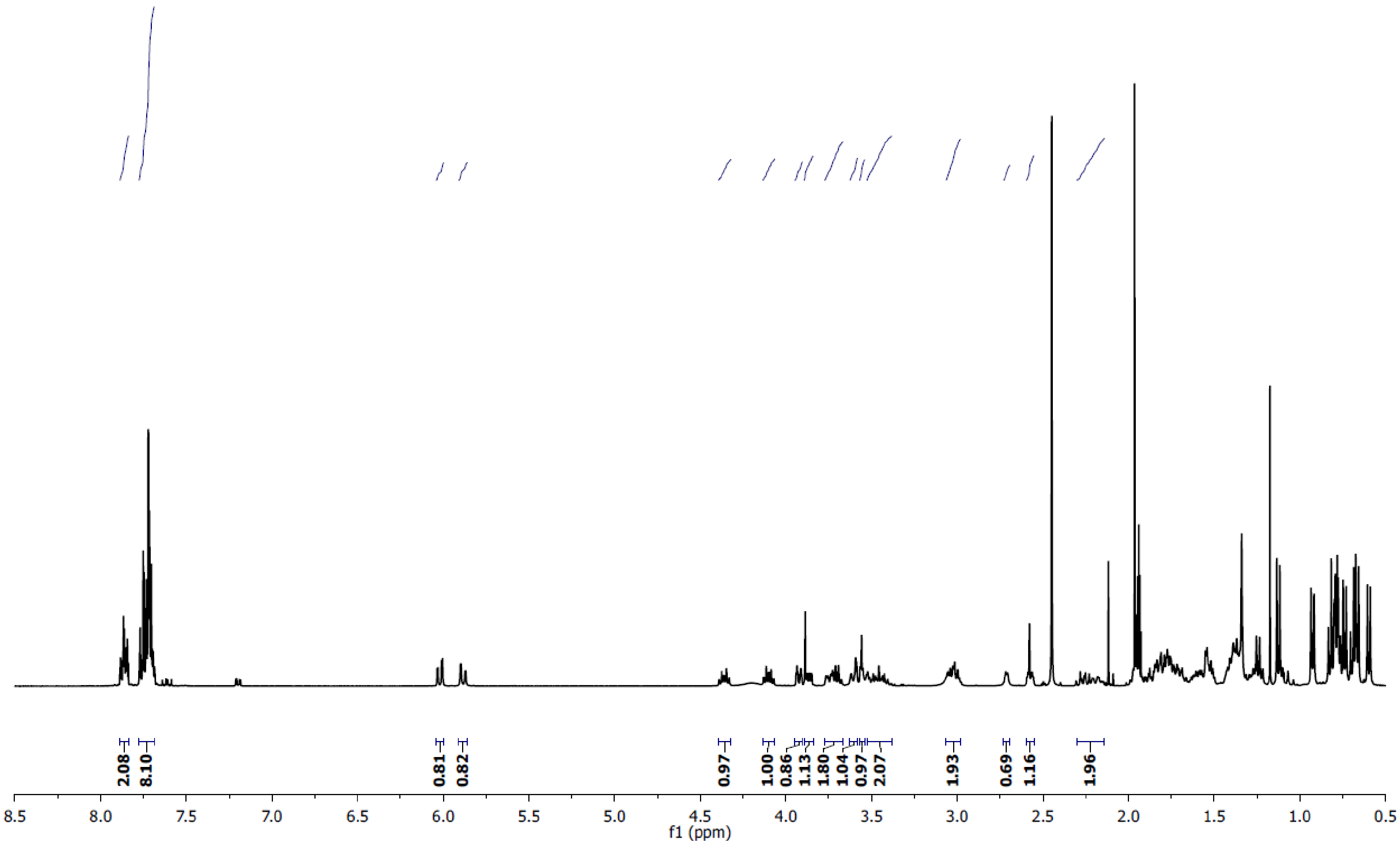

Fig. S2.The ^{1}H NMR spectrum of **3a** in CD_3CN.

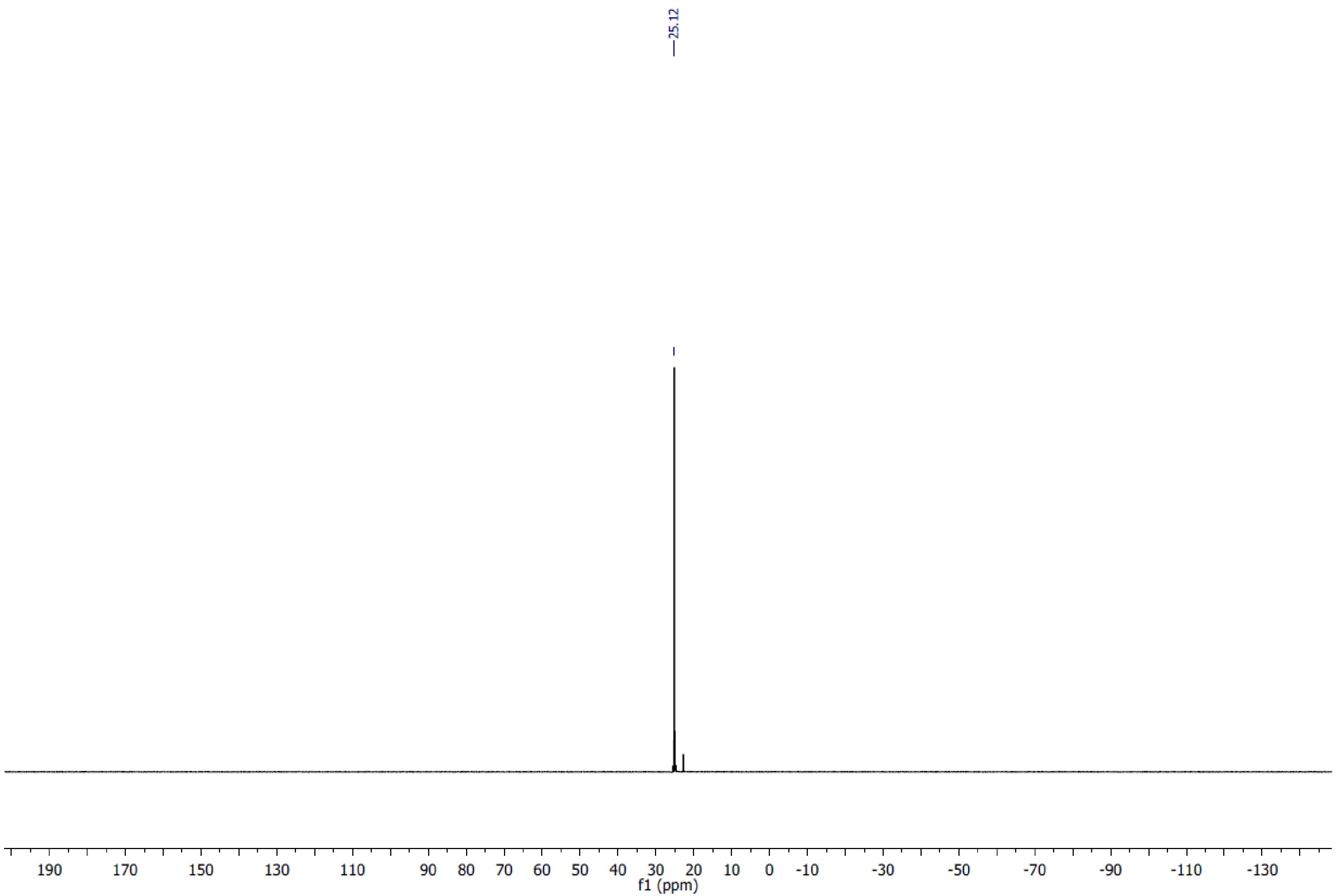

Fig. S3. The ^{31}P NMR spectrum of **3a** in CD_3CN.

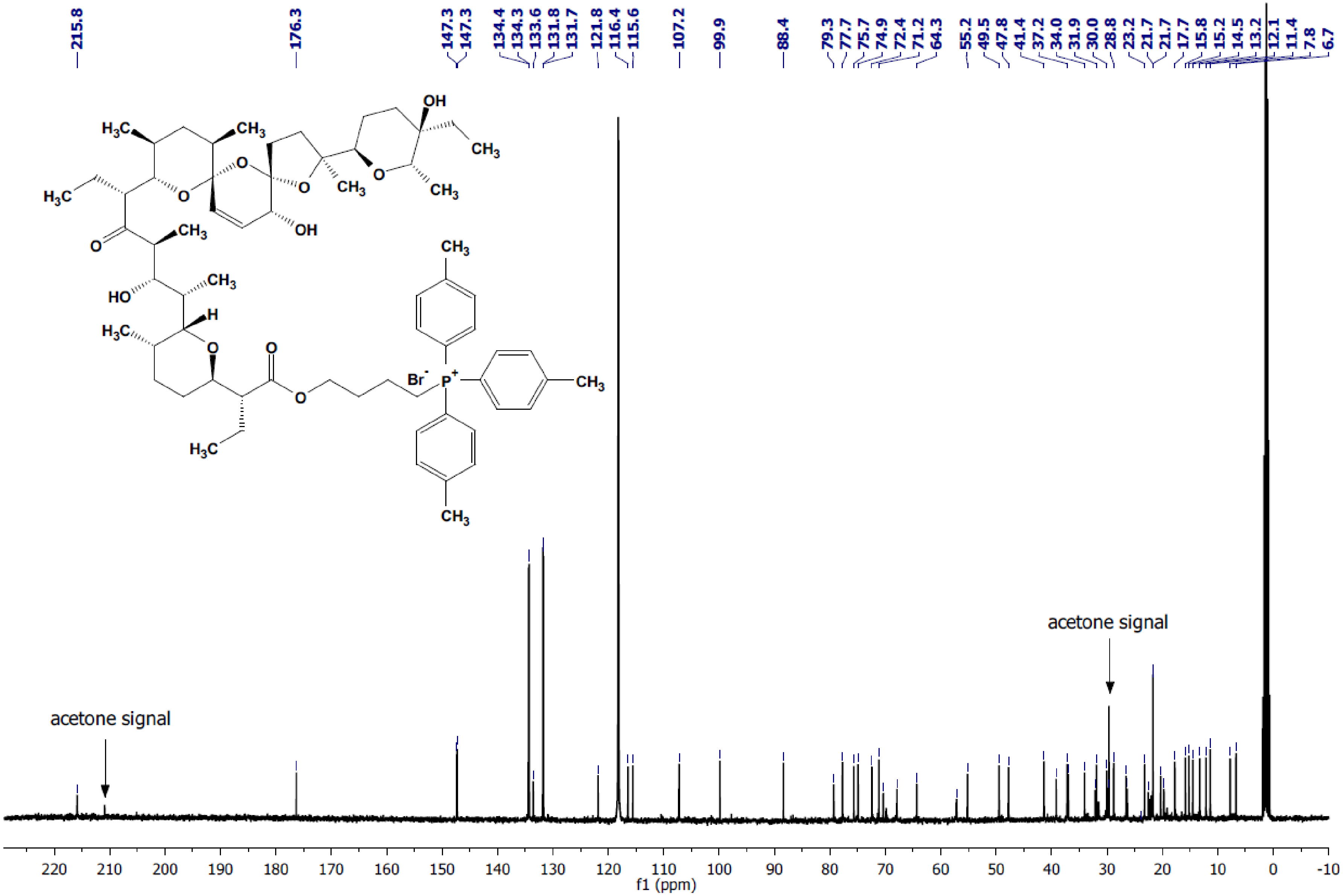

Fig. S4.The ^{13}C NMR spectrum of **3b** in CD_3CN.

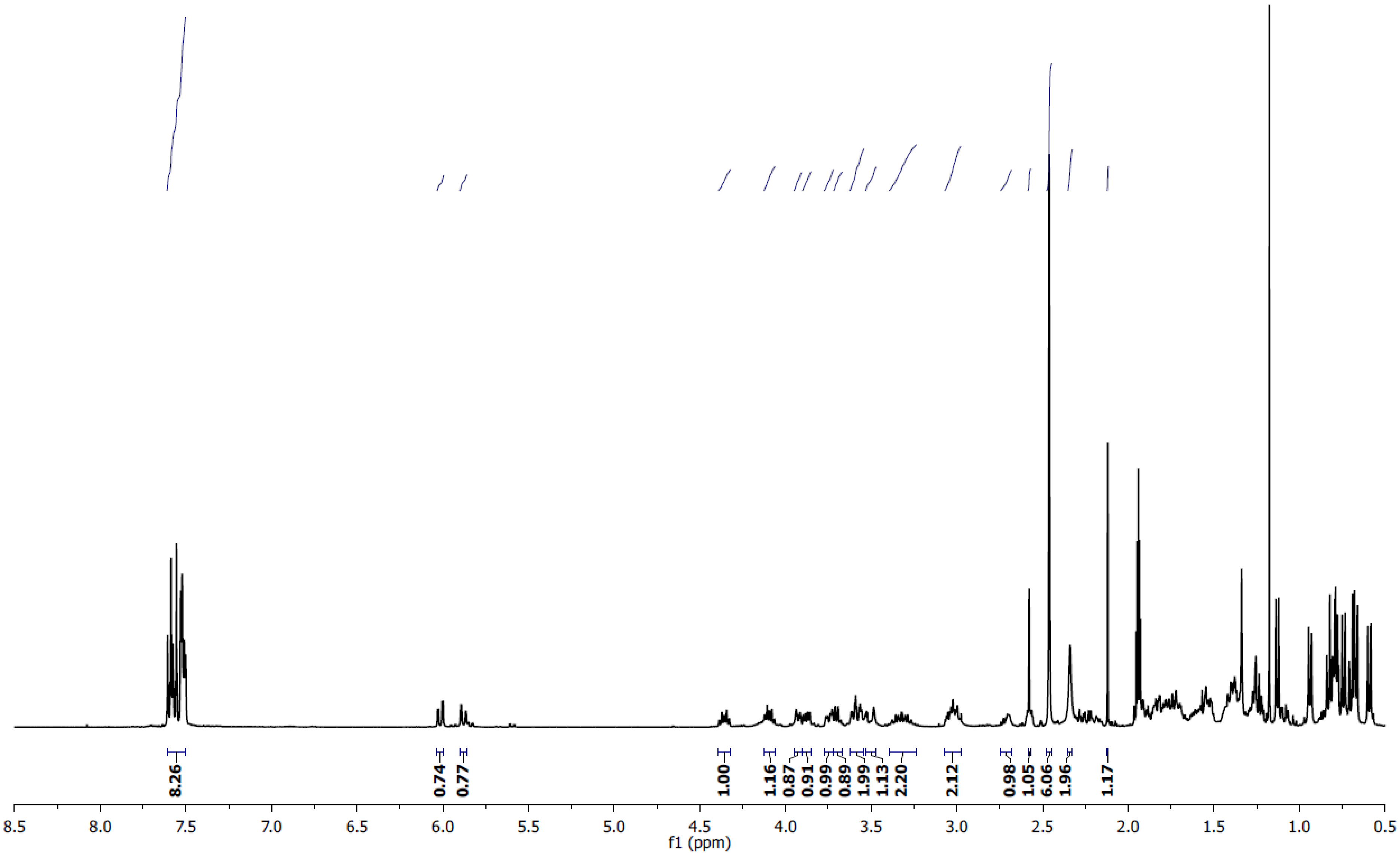

Fig. S5. The ^{1}H NMR spectrum of **3b** in CD$_3$CN.

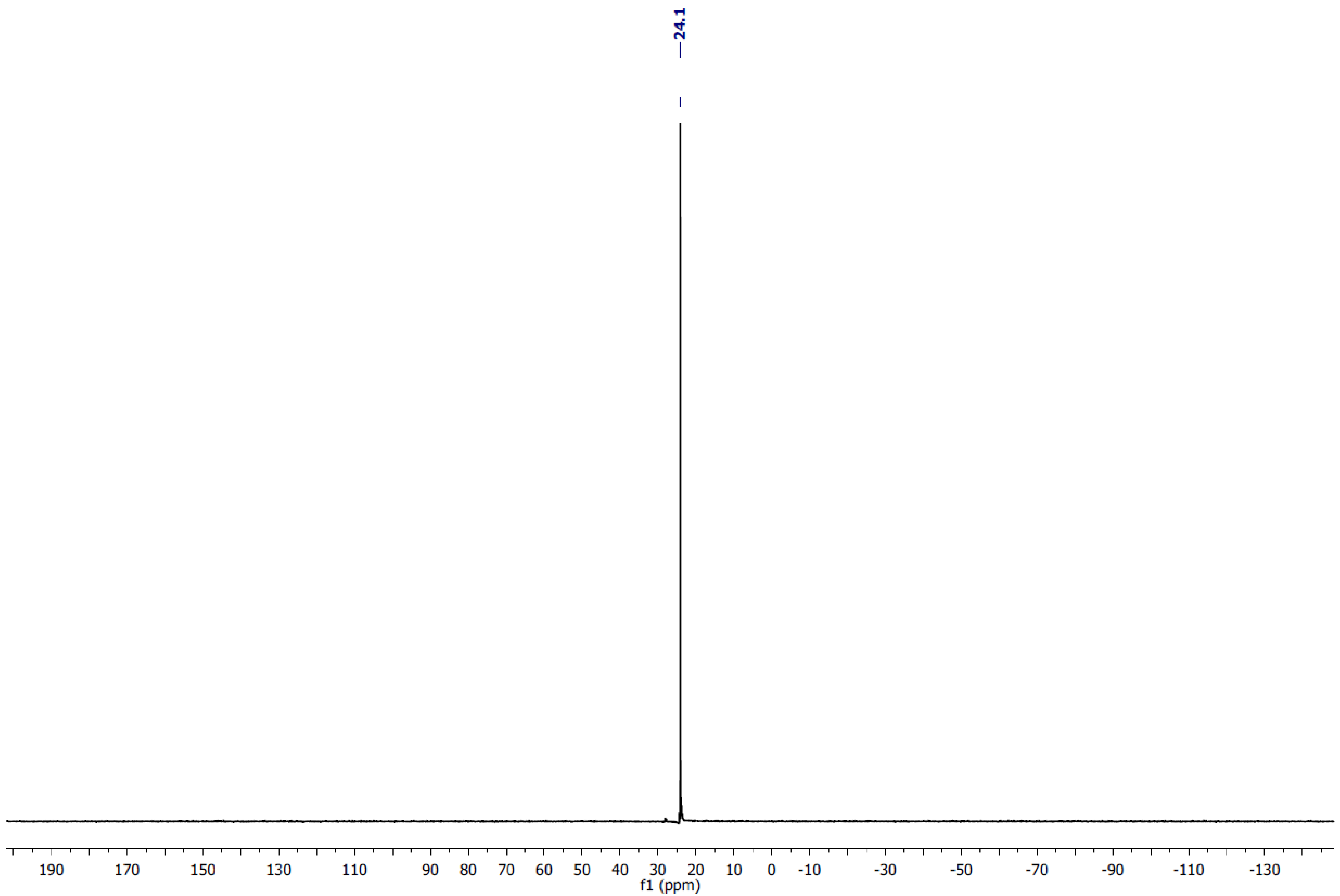

Fig. S6. The ^{31}P NMR spectrum of **3b** in CD_3CN.

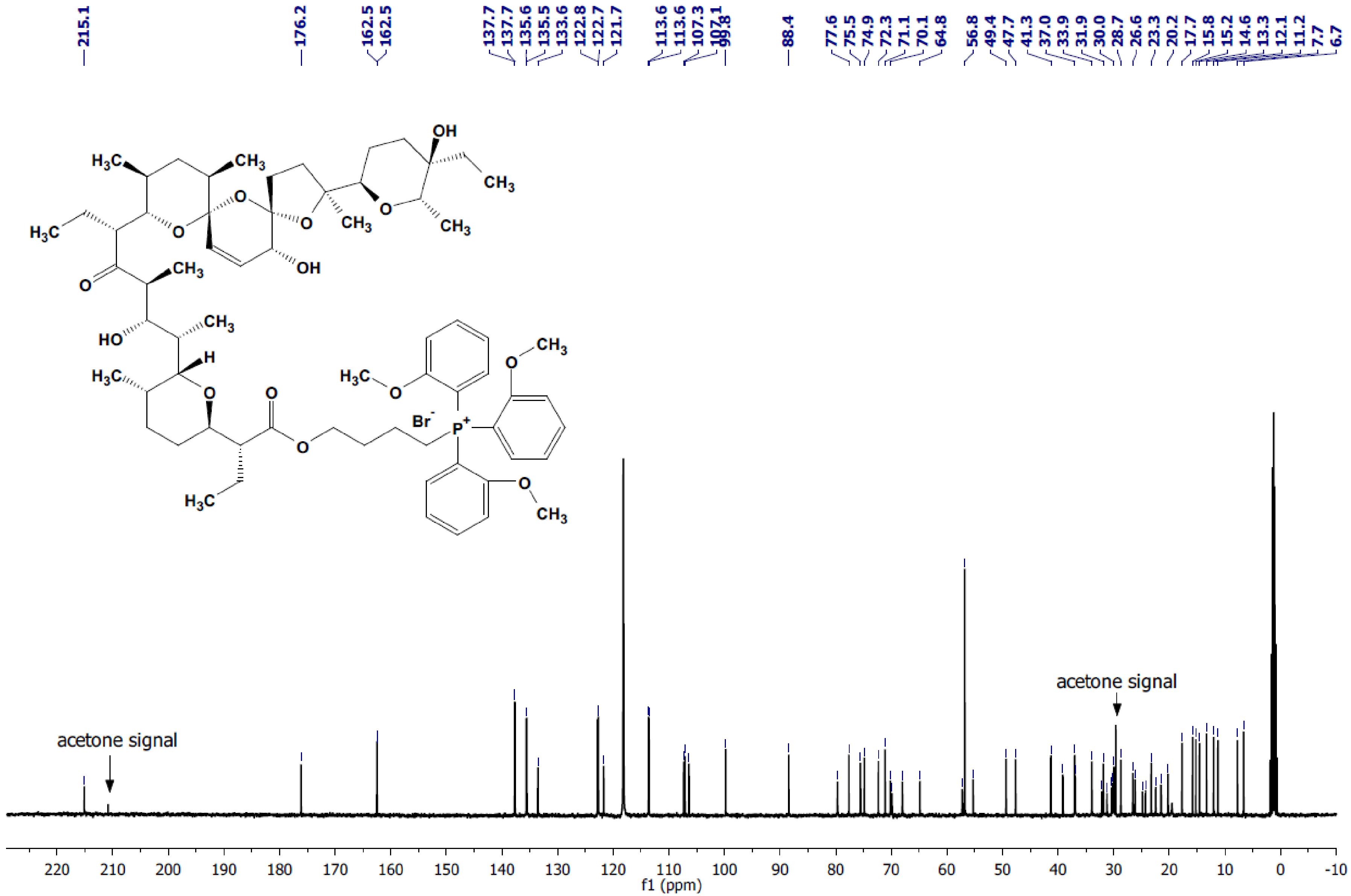

Fig. S7. The ^{13}C NMR spectrum of **3c** in CD$_3$CN.

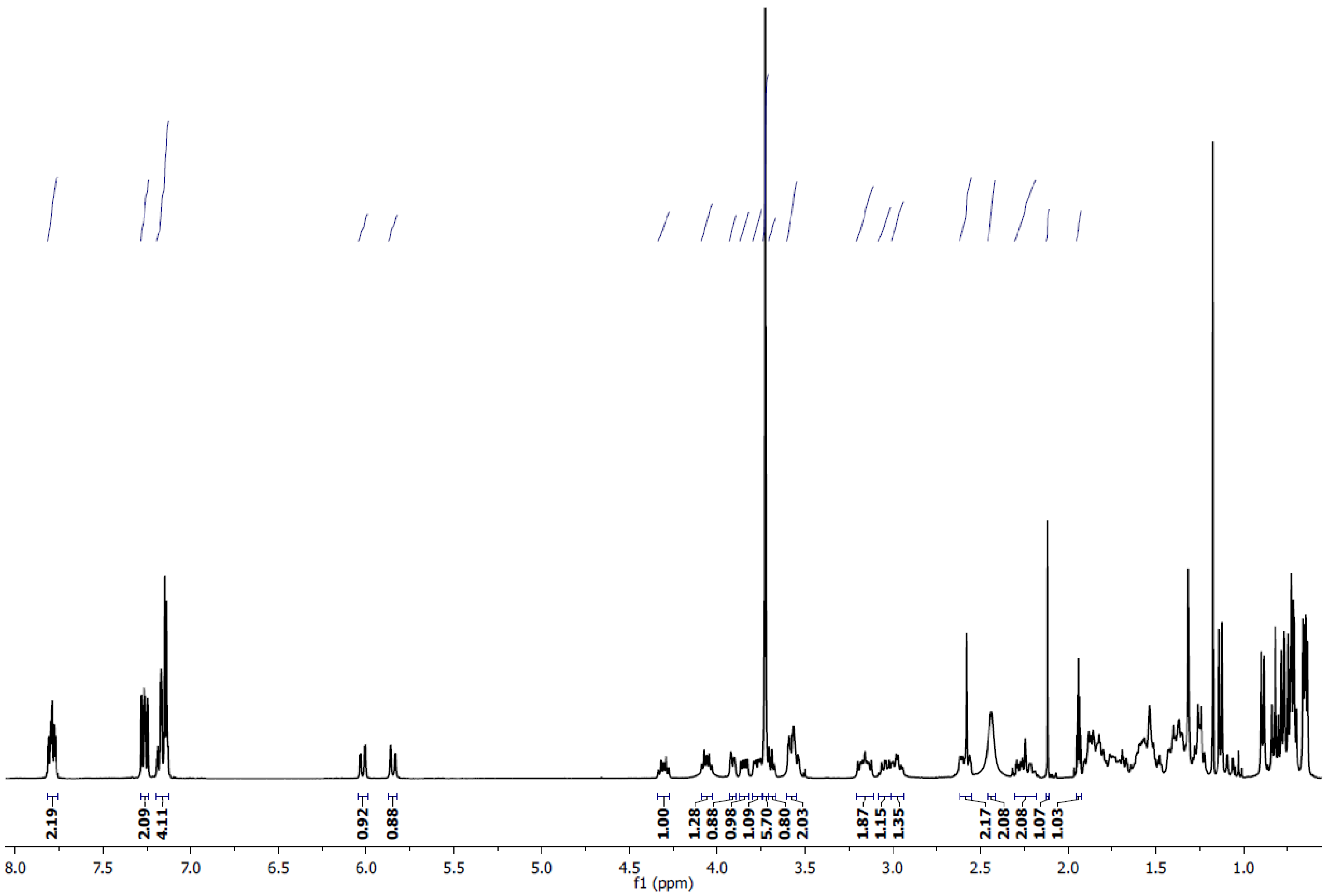

Fig. S8. The ^{1}H NMR spectrum of **3c** in CD_3CN.

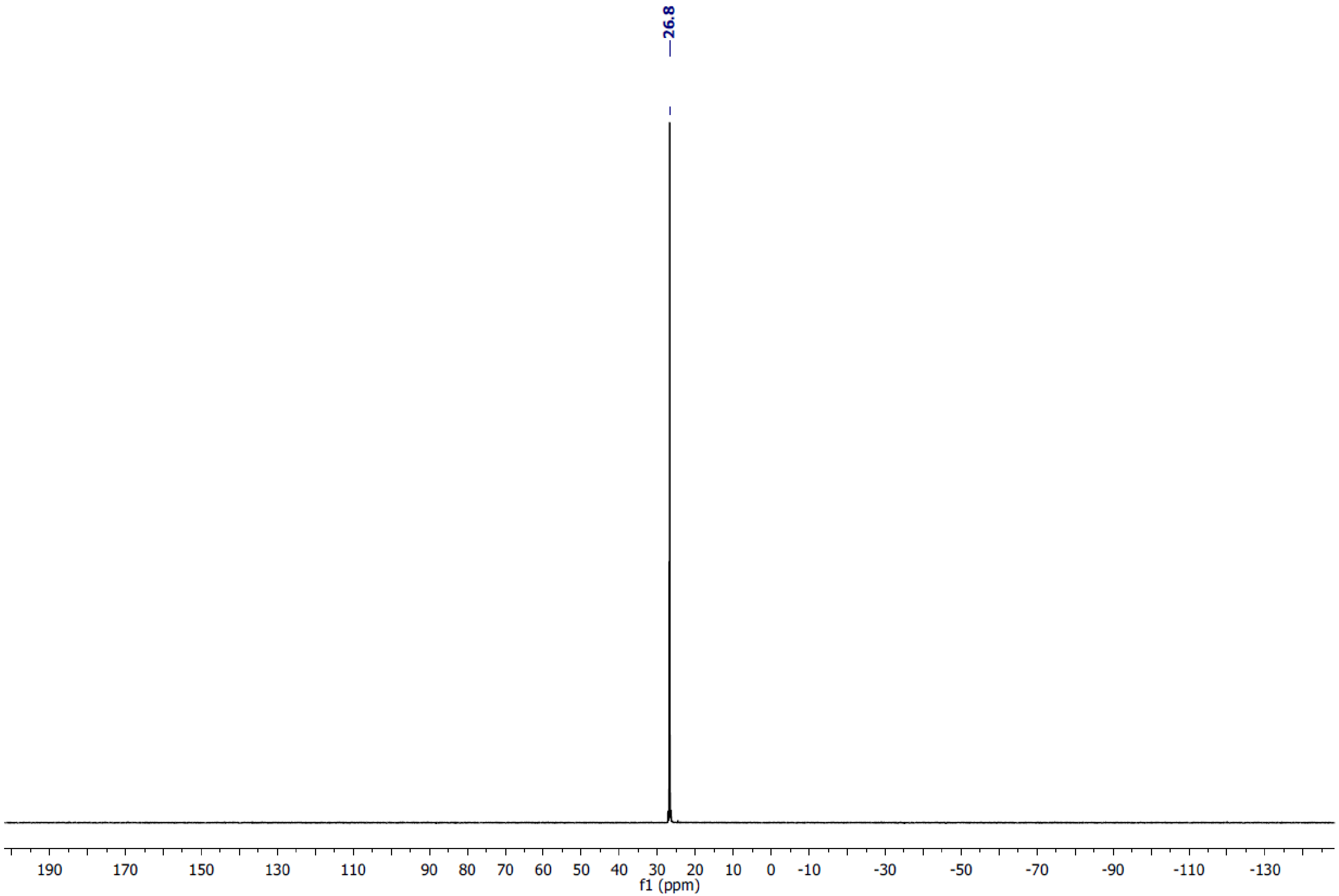

Fig. S9. The ^{31}P NMR spectrum of **3c** in CD_3CN.

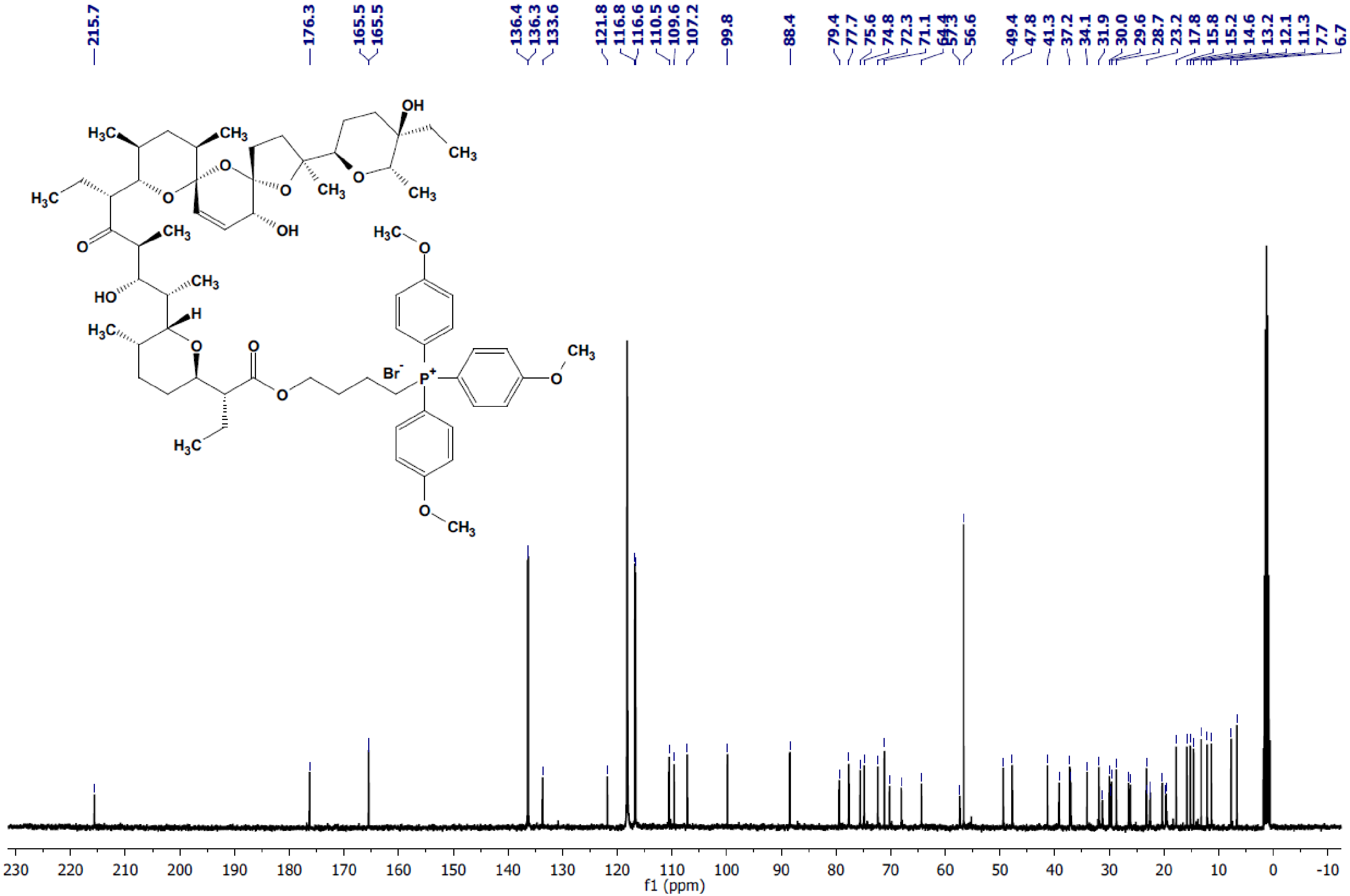

Fig. S10. The ^{13}C NMR spectrum of **3d** in CD_3CN.

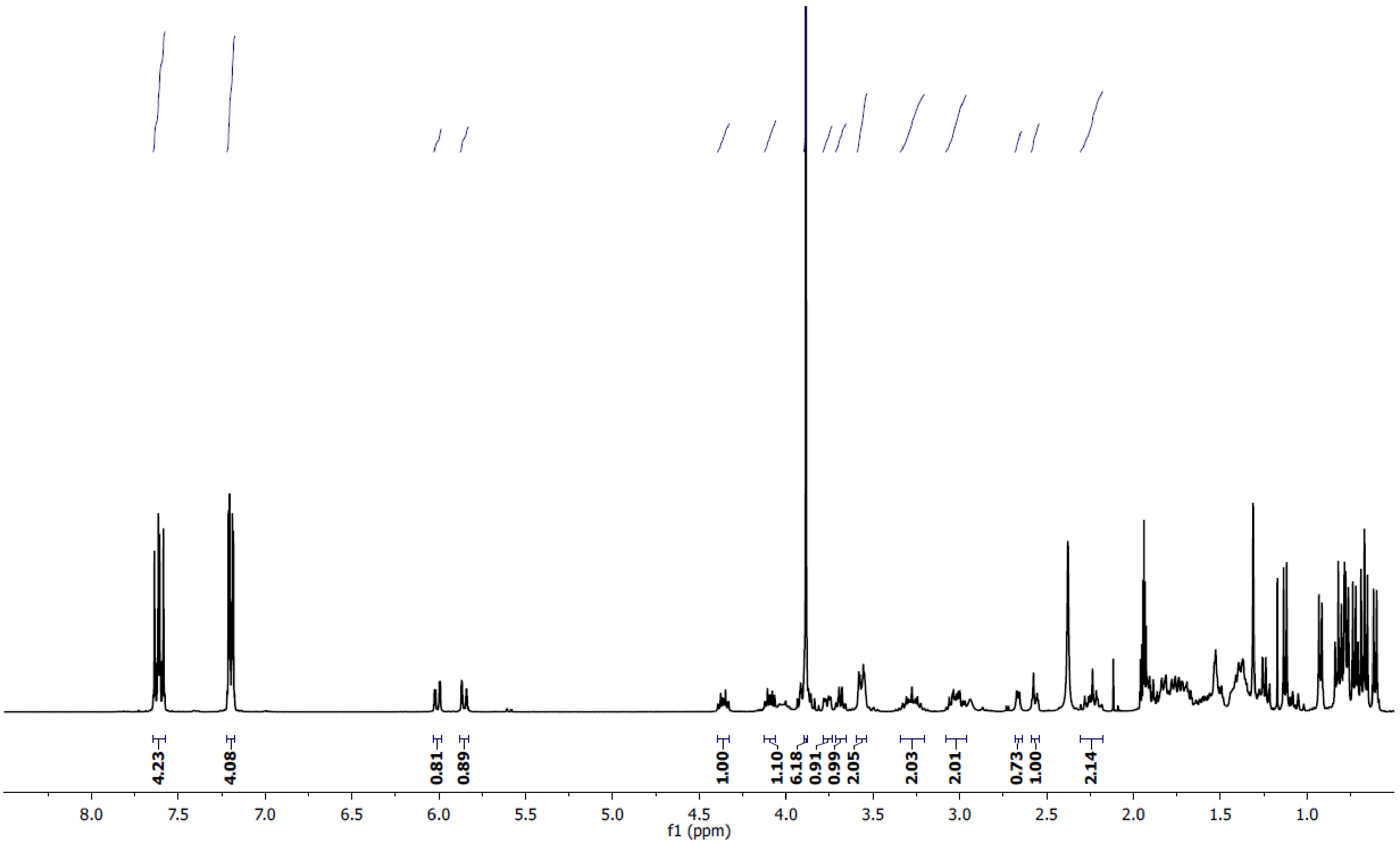

Fig. S11. The ^{1}H NMR spectrum of **3d** in CD_3CN.

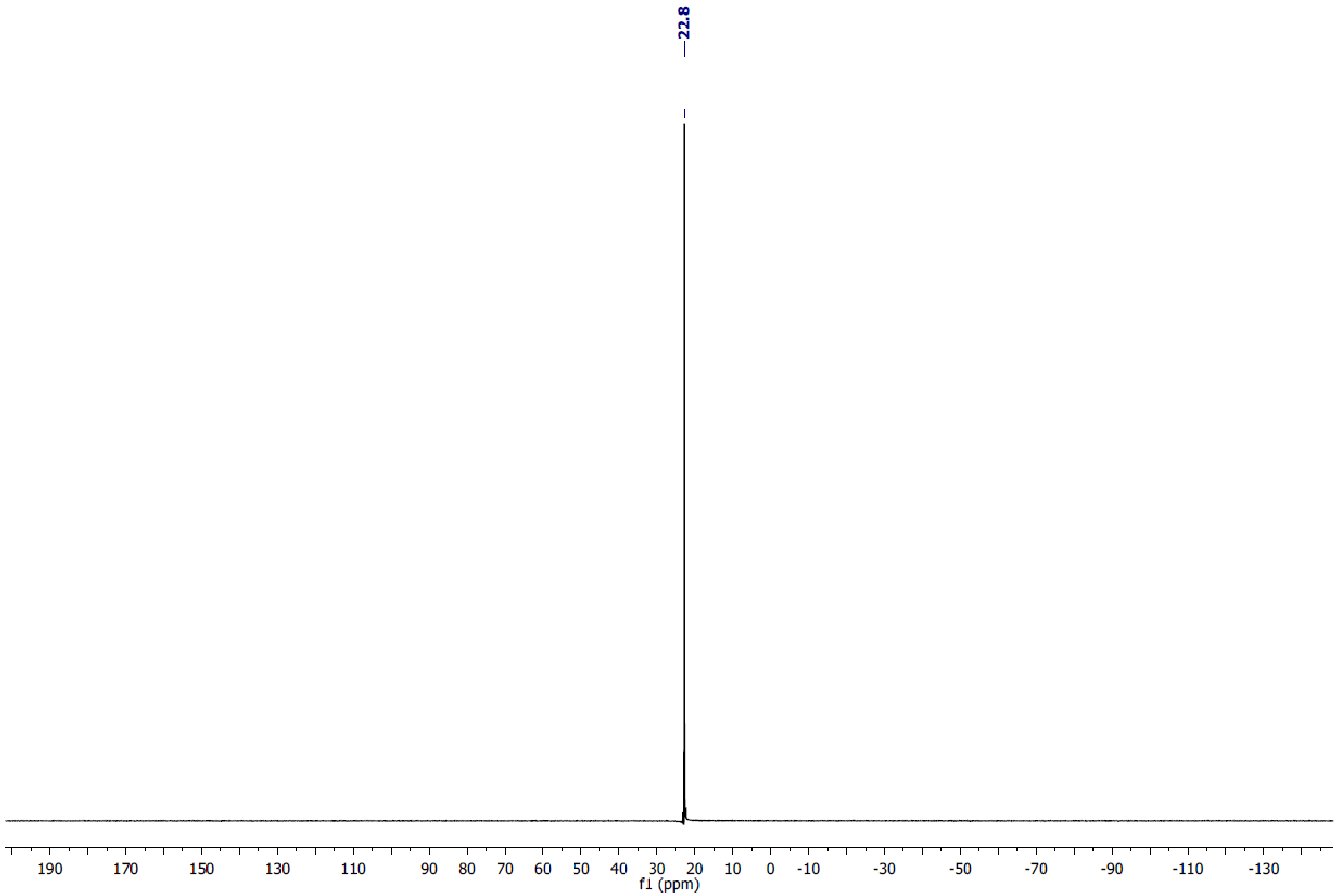

Fig. S12. The ^{31}P NMR spectrum of **3d** in CD_3CN.

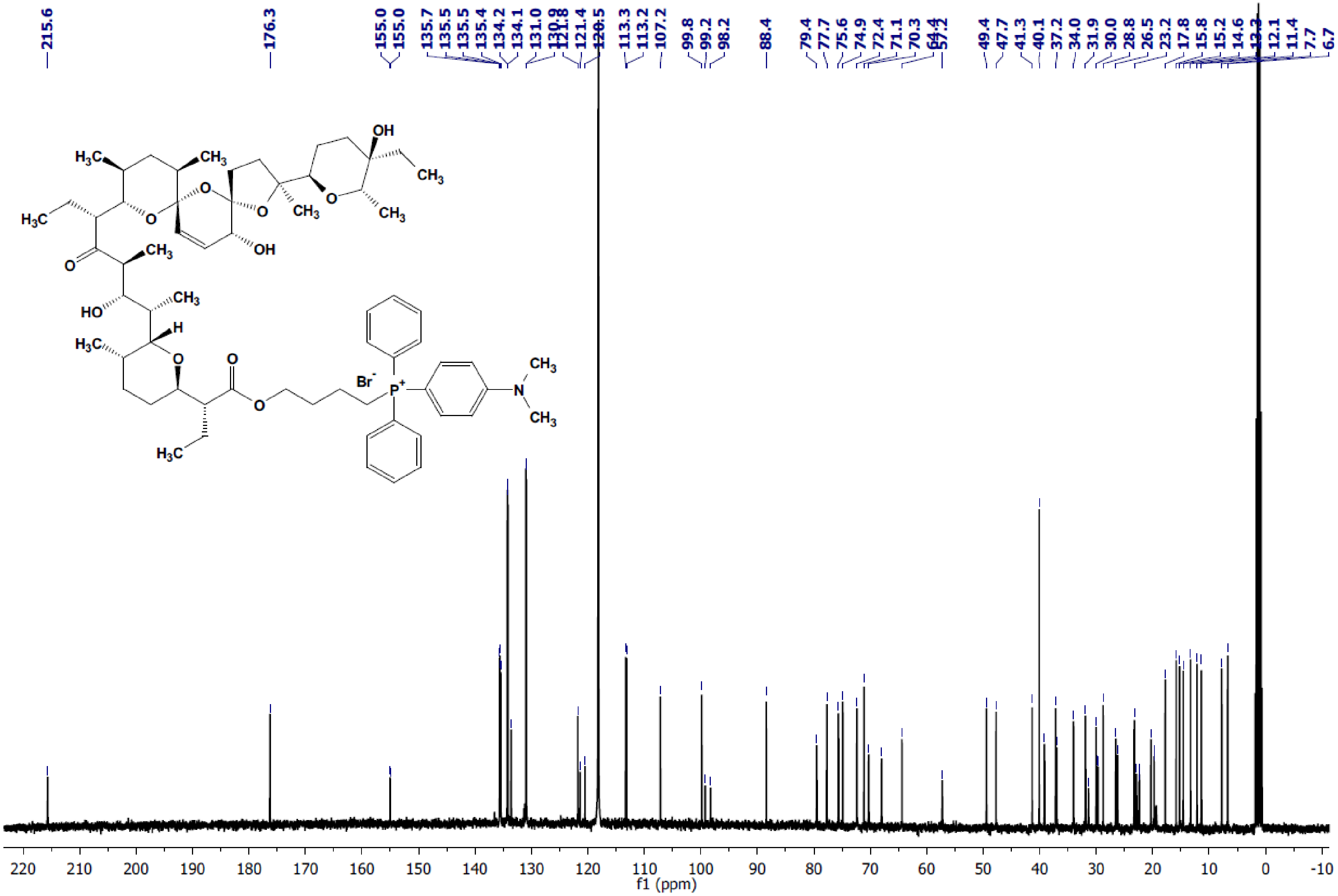

Fig. S13. The ^{13}C NMR spectrum of **3e** in CD_3CN.

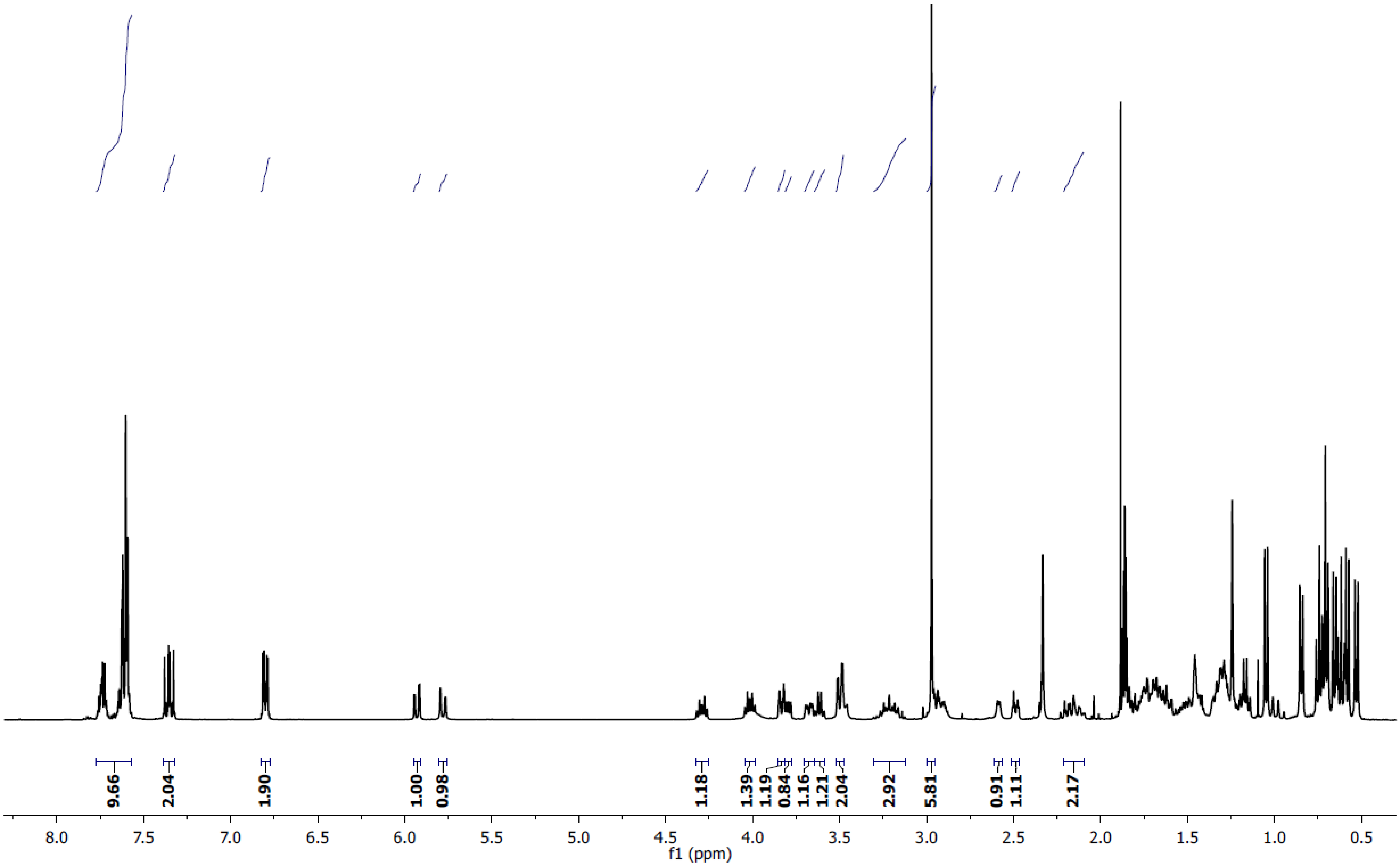

Fig. S14. The ^{1}H NMR spectrum of **3e** in CD_3CN.

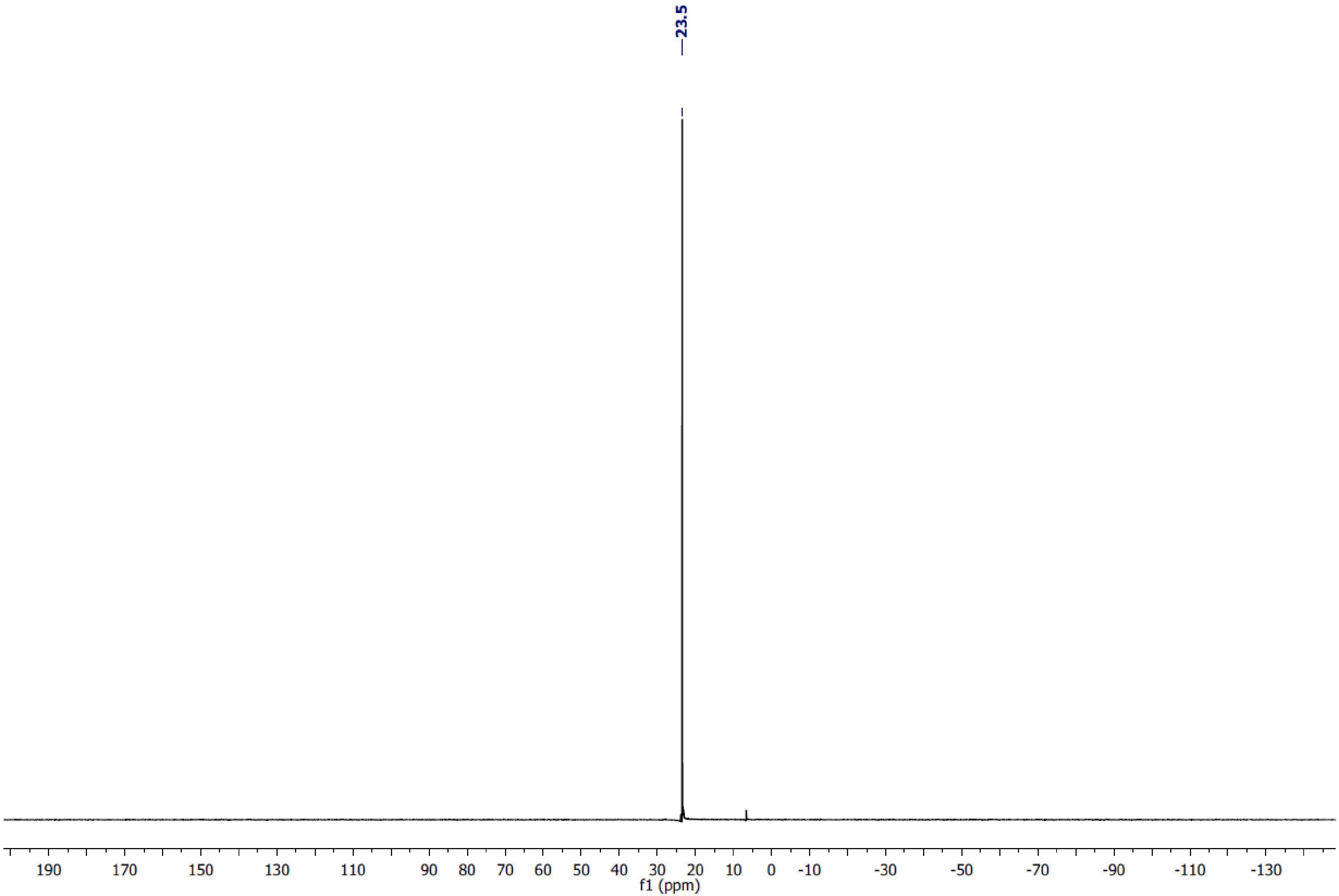

Fig. **S15**. The ^{31}P NMR spectrum of **3e** in CD_3CN.

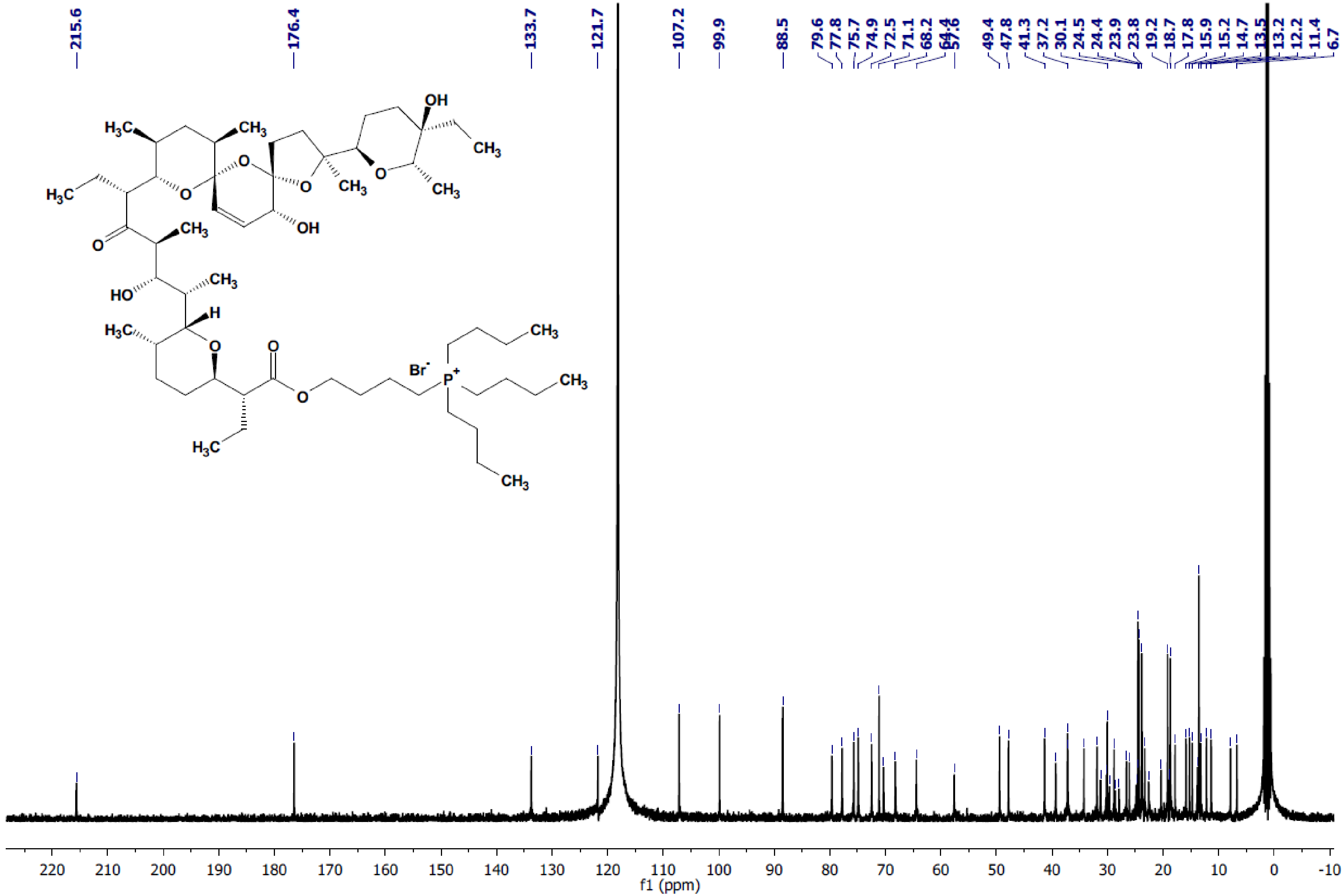

Fig. **S16.** The ^{13}C NMR spectrum of **3f** in CD_3CN.

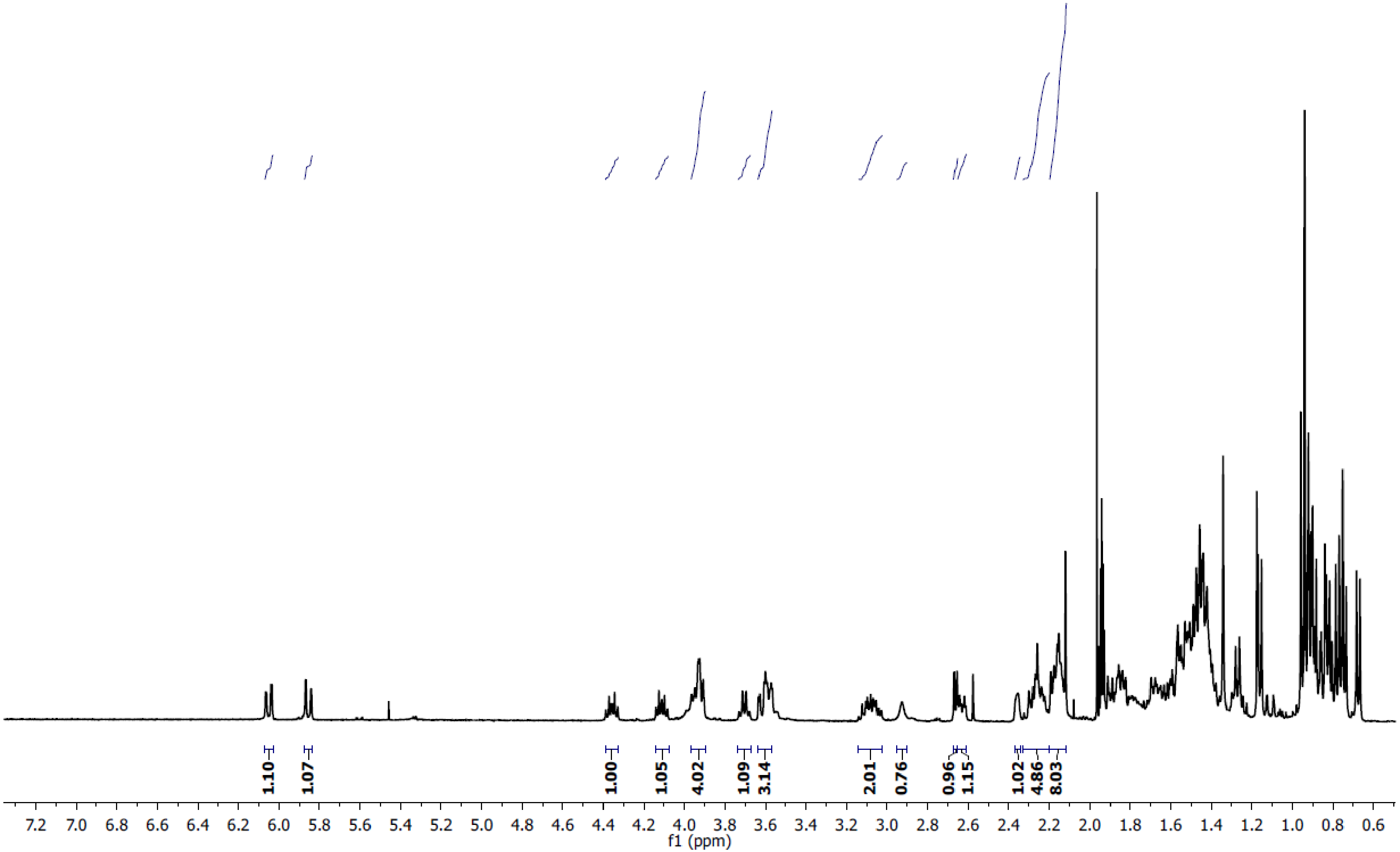

Fig. **S17.** The ^{1}H NMR spectrum of **3f** in CD_3CN.

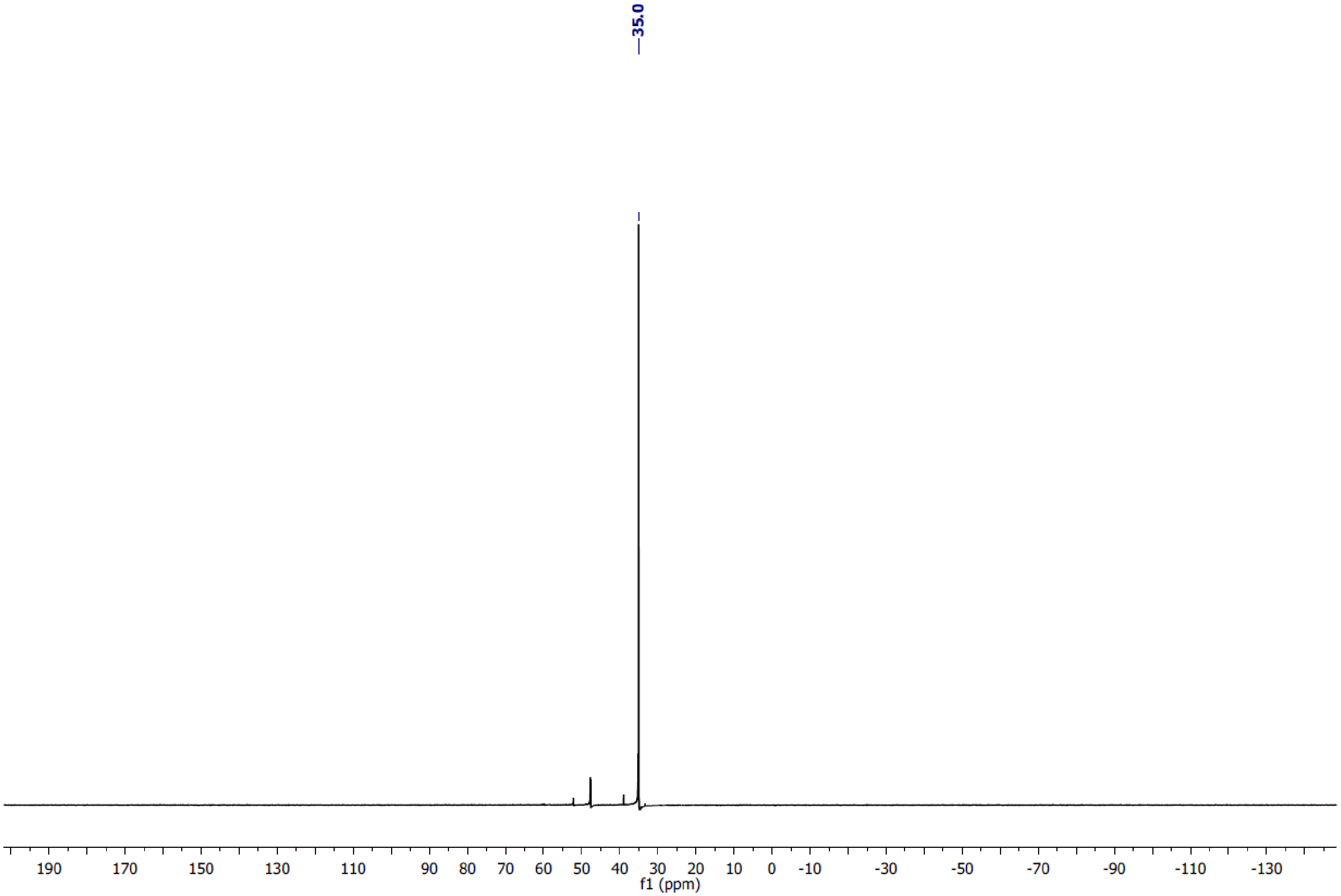

Fig. **S18.** The ^{31}P NMR spectrum of **3f** in CD_3CN.

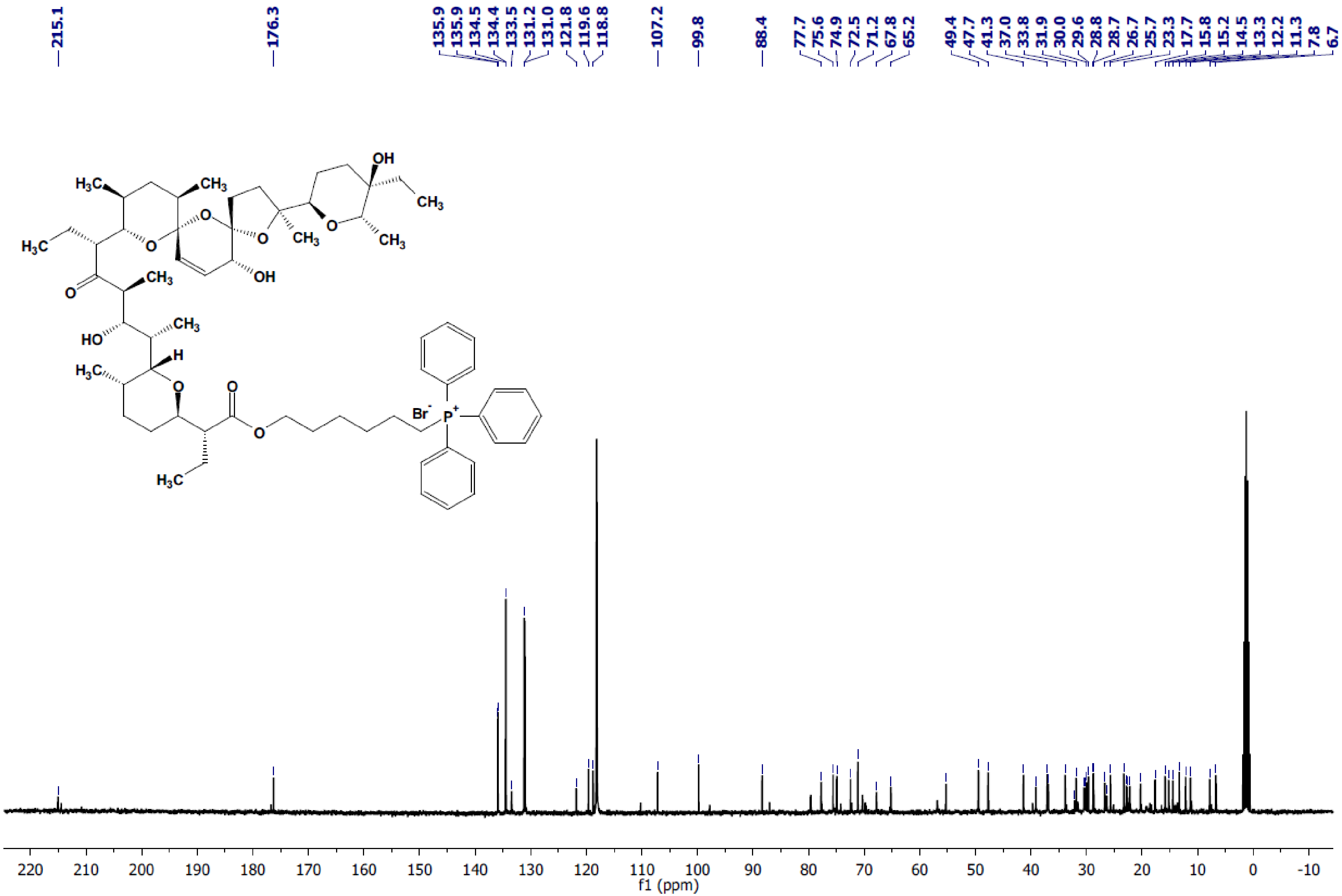

Fig. S19. The ^{13}C NMR spectrum of **5a** in CD_3CN.

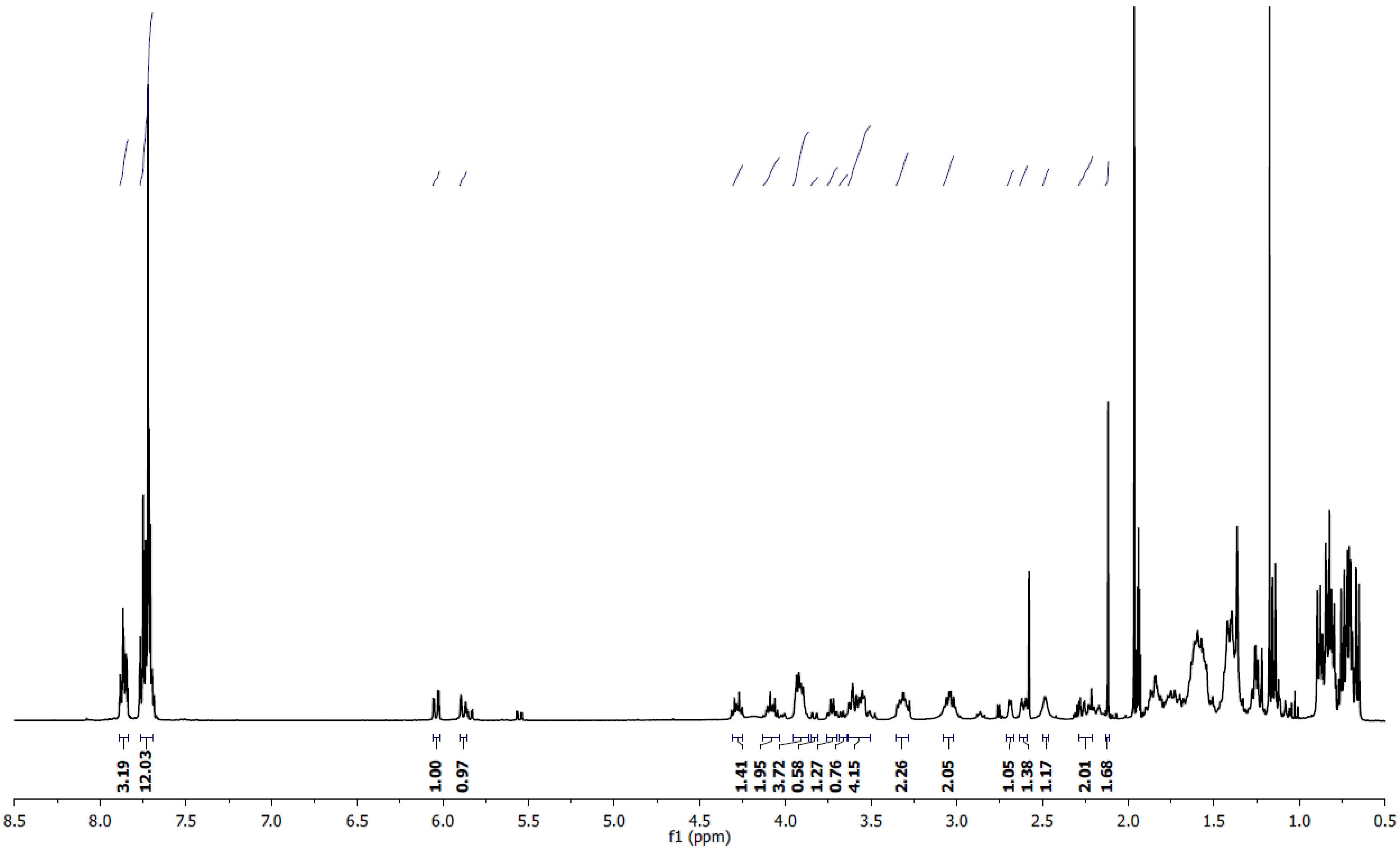

Fig. S20. The ^{1}H NMR spectrum of **5a** in CD_3CN.

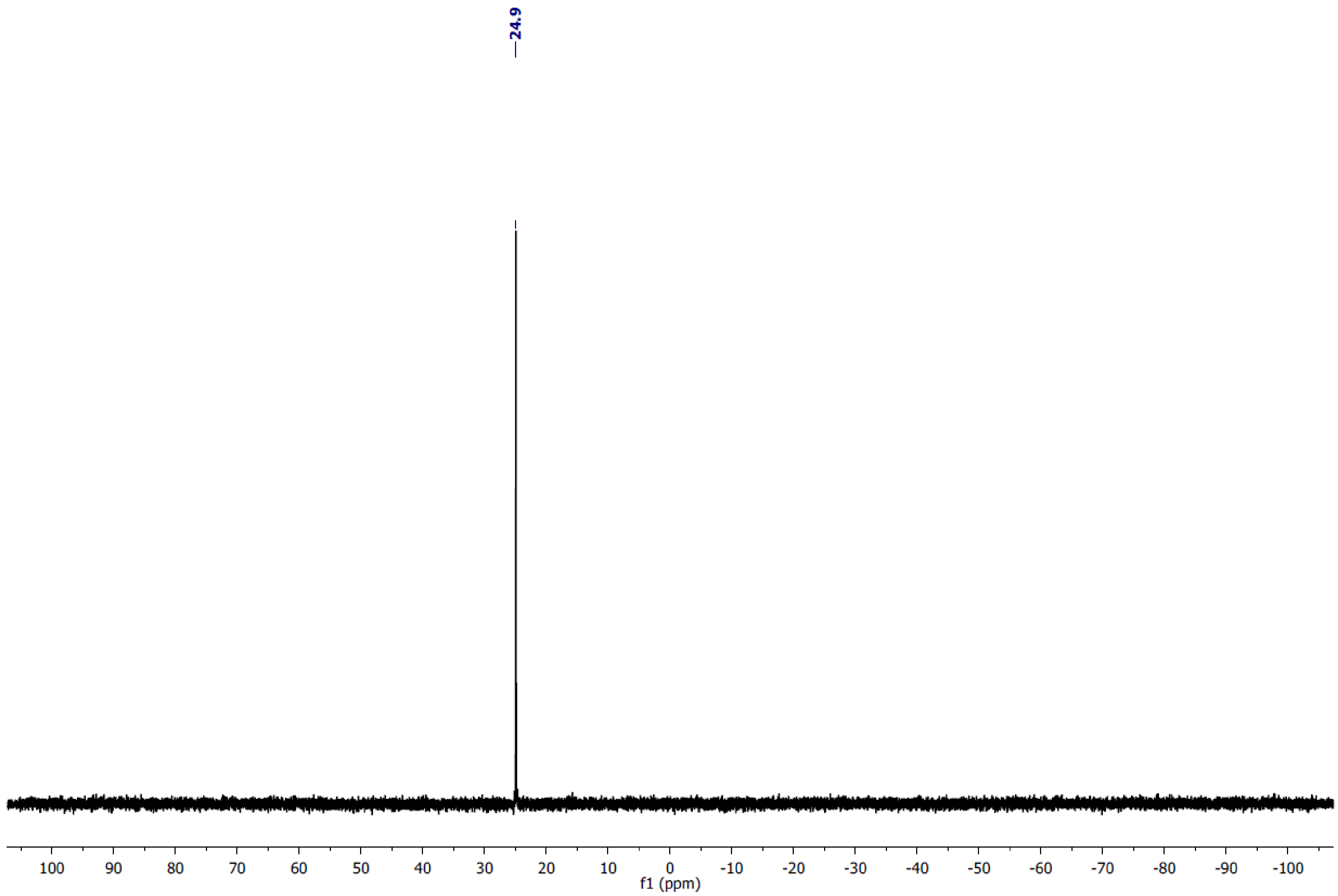

Fig. S21. The ^{31}P NMR spectrum of **5a** in CD_3CN.

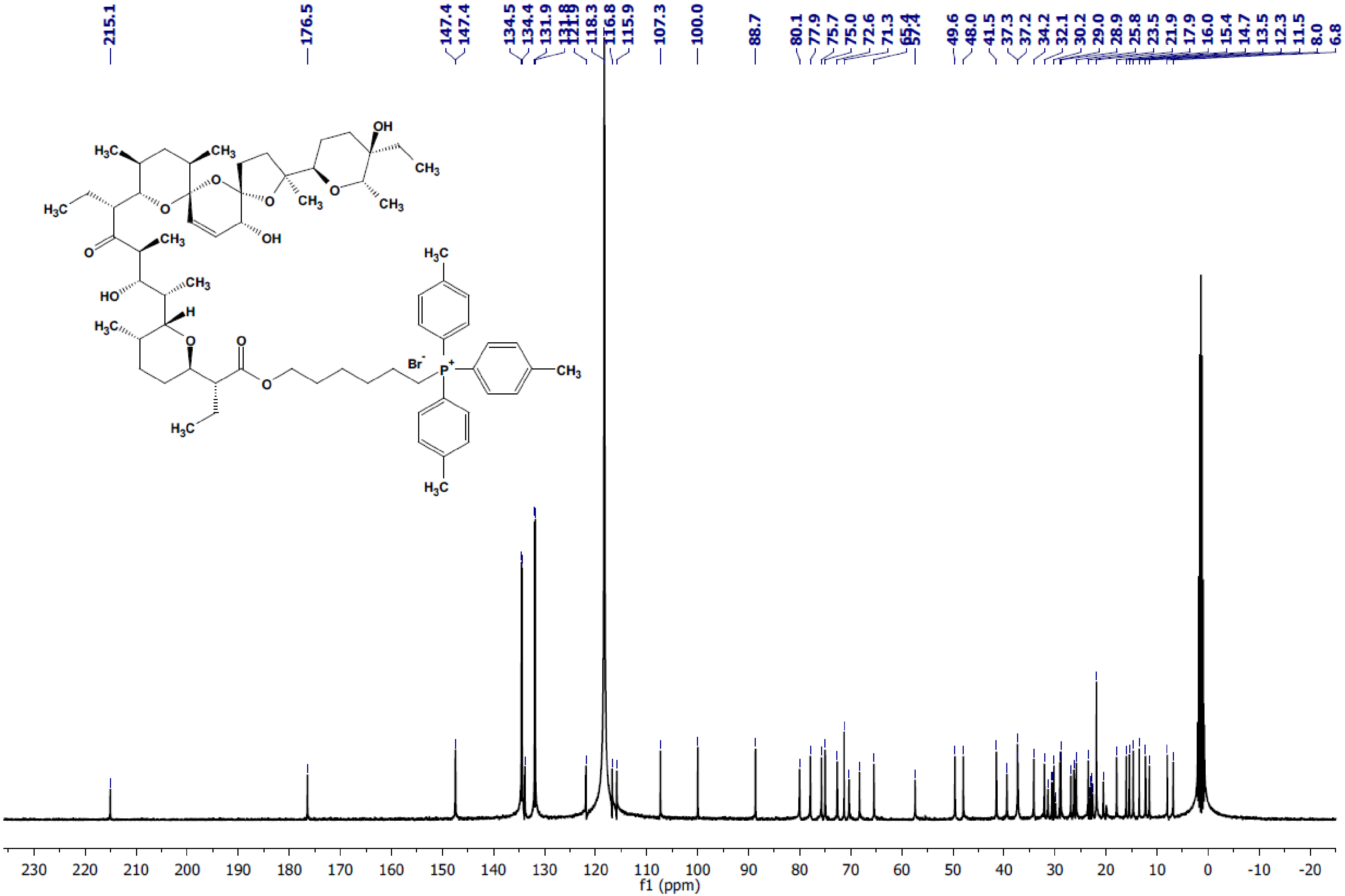

Fig. S22. The ^{13}C NMR spectrum of **5b** in CD$_3$CN.

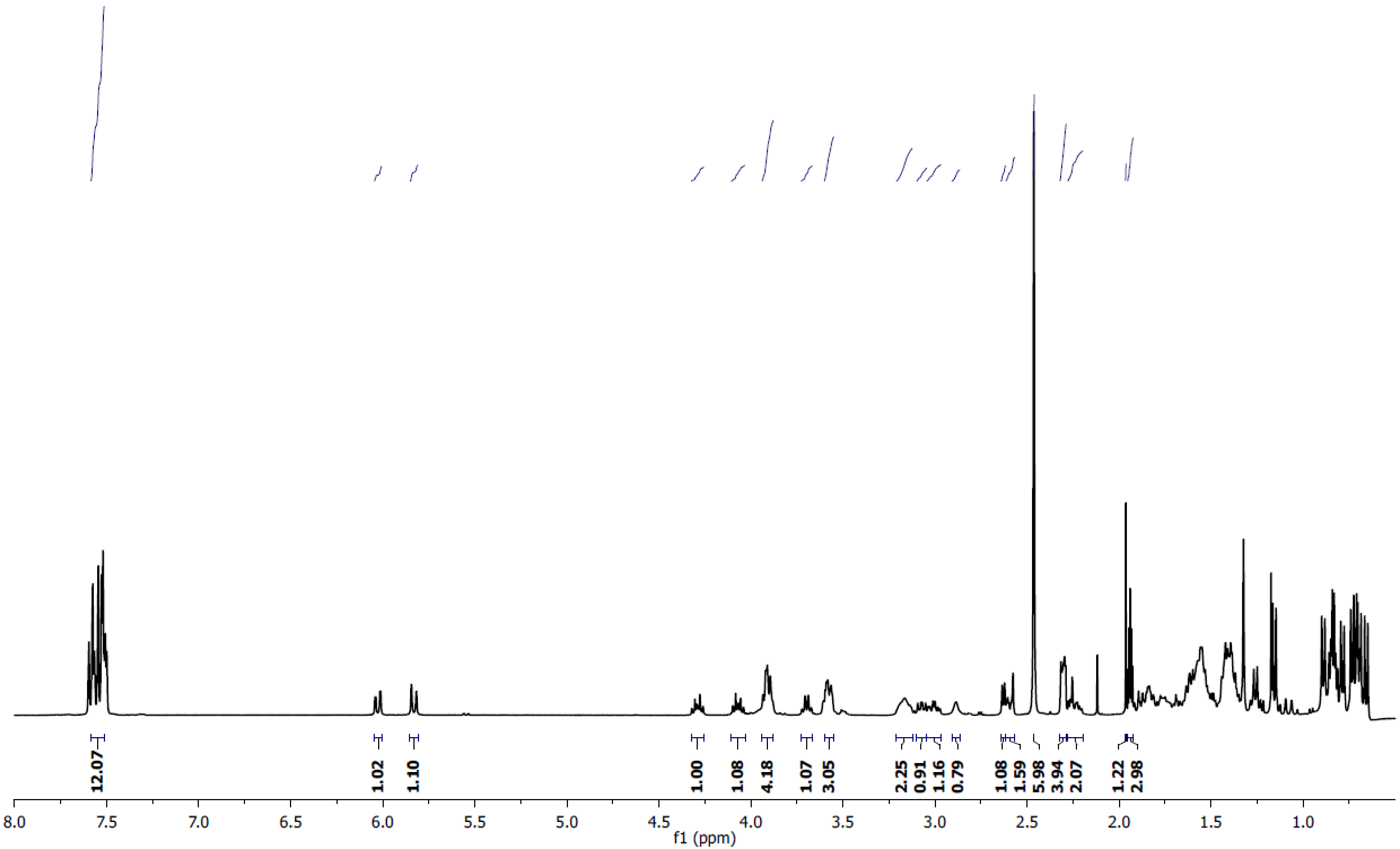

Fig. S23. The ^{1}H NMR spectrum of **5b** in CD_3CN.

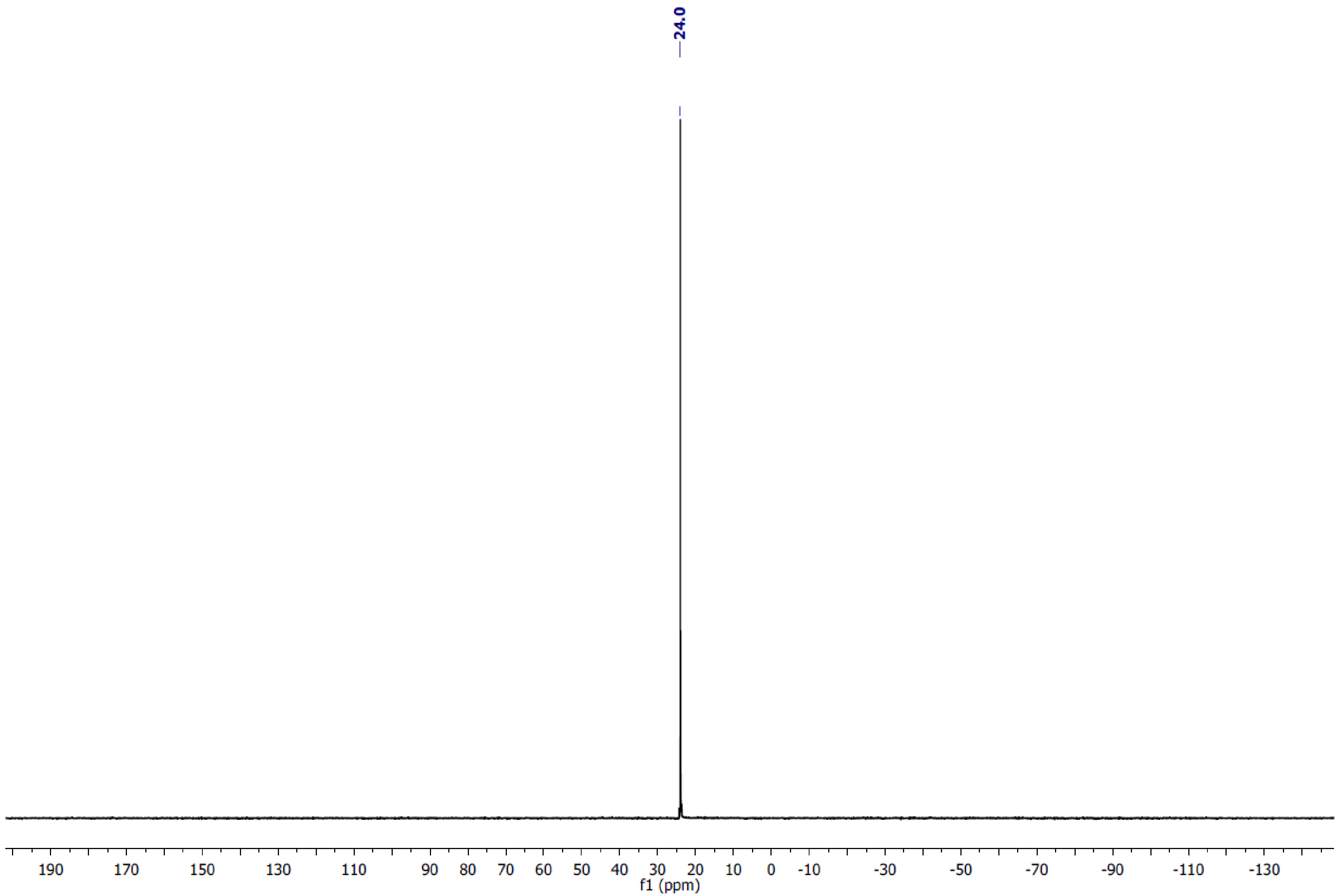

Fig. S24. The ^{31}P NMR spectrum of **5b** in CD_3CN.

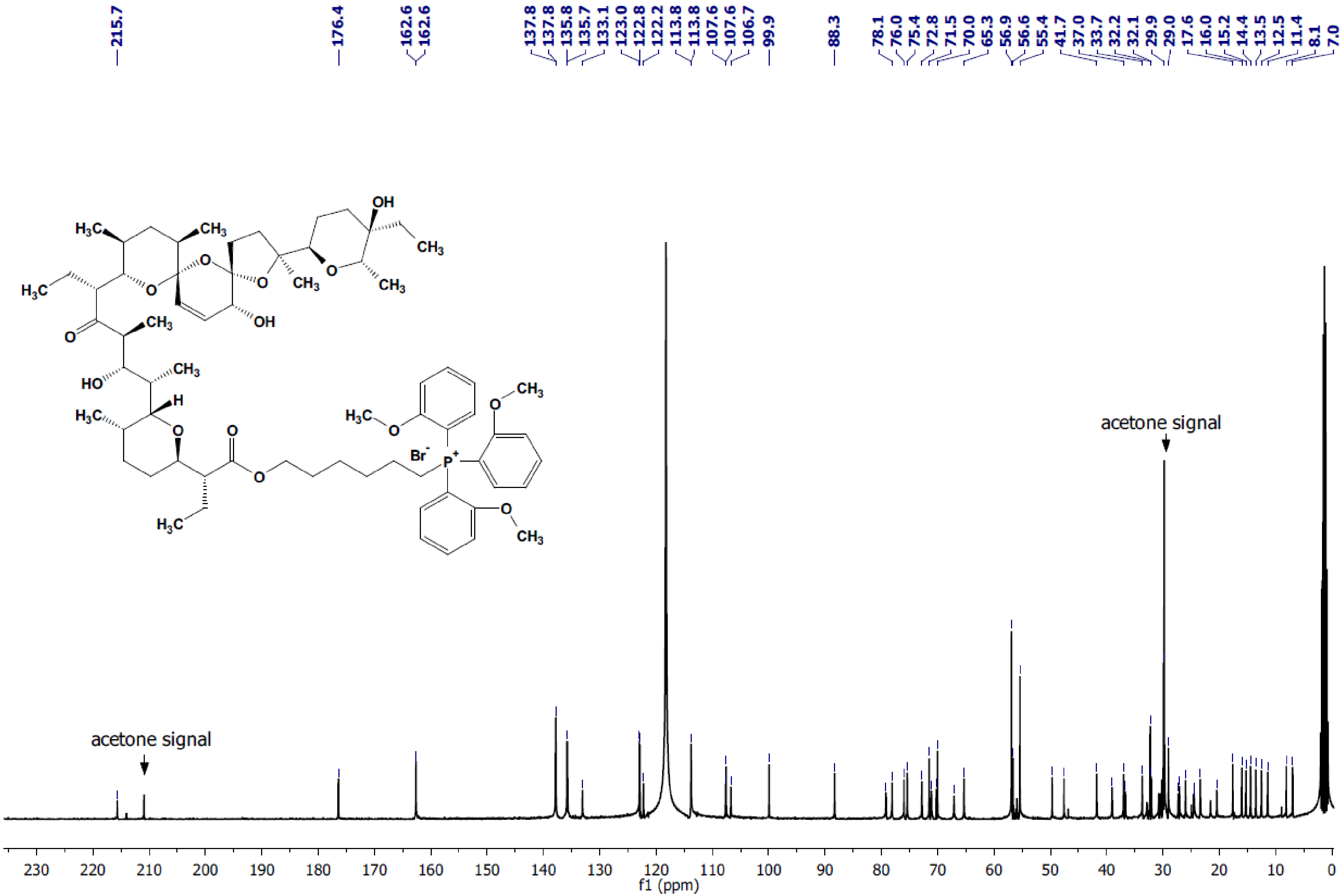

Fig. S25. The ^{13}C NMR spectrum of **5c** in CD$_3$CN.

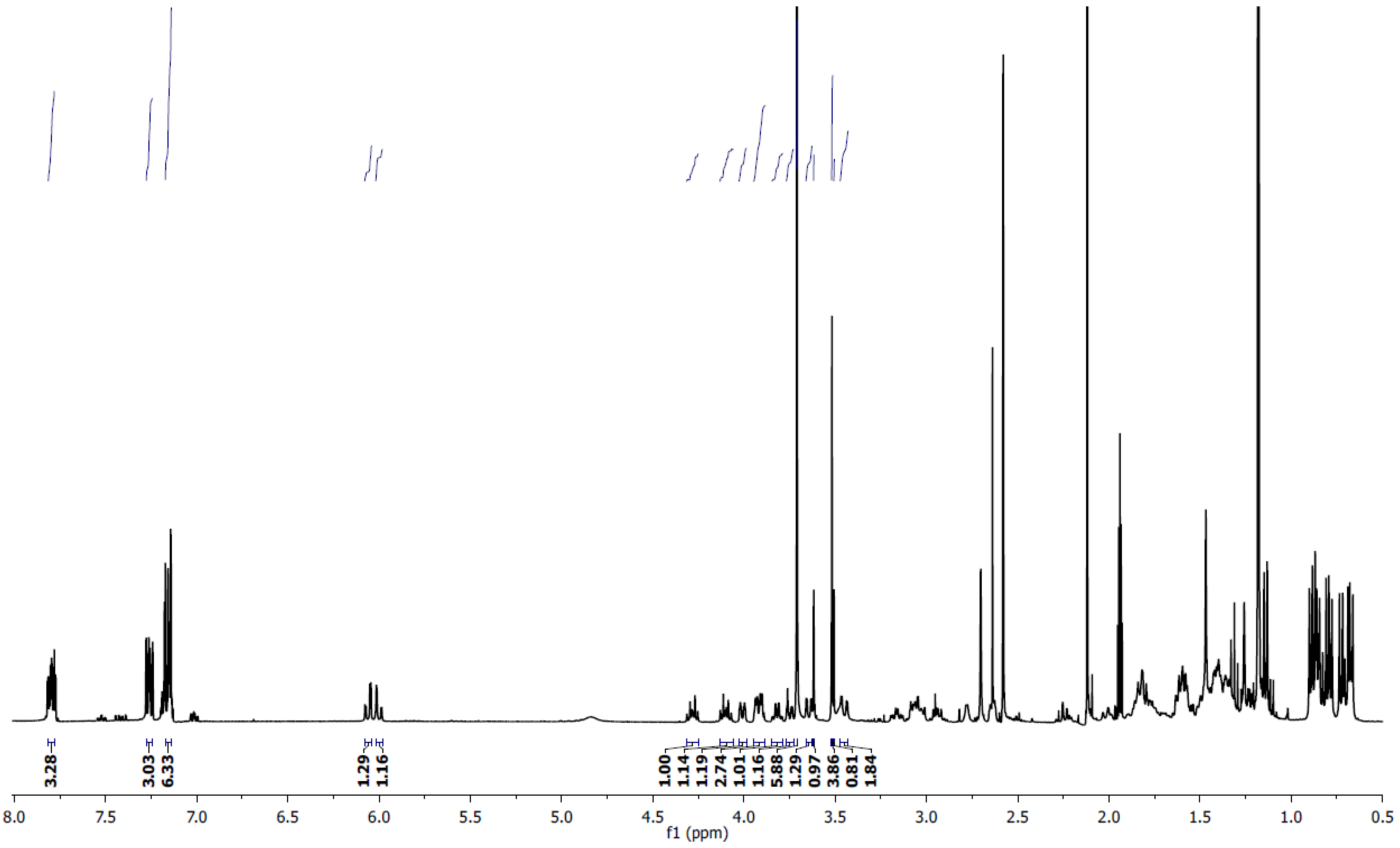

Fig. S26. The ^{1}H NMR spectrum of **5c** in CD_3CN.

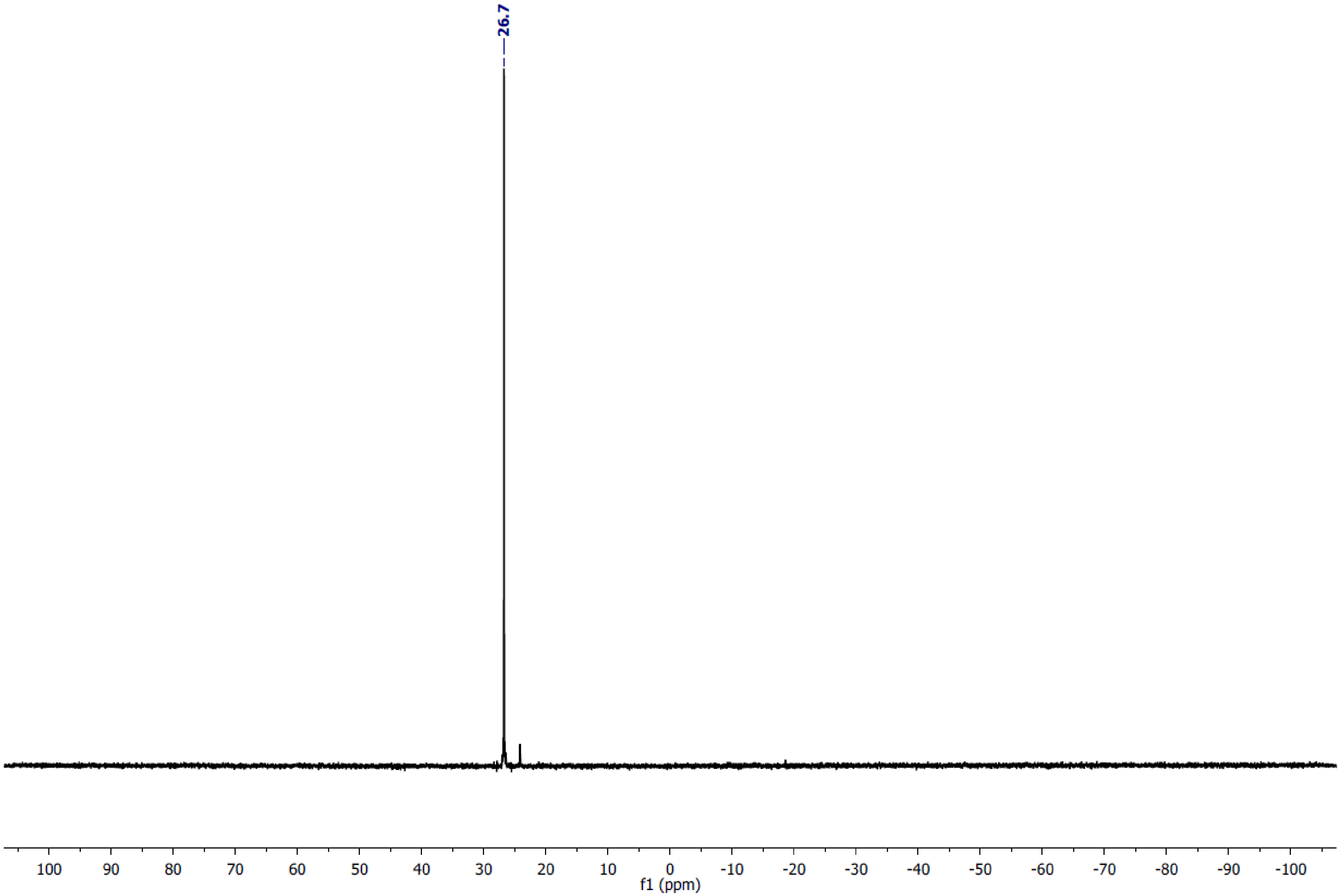

Fig. S27. The ^{31}P NMR spectrum of **5c** in CD_3CN.

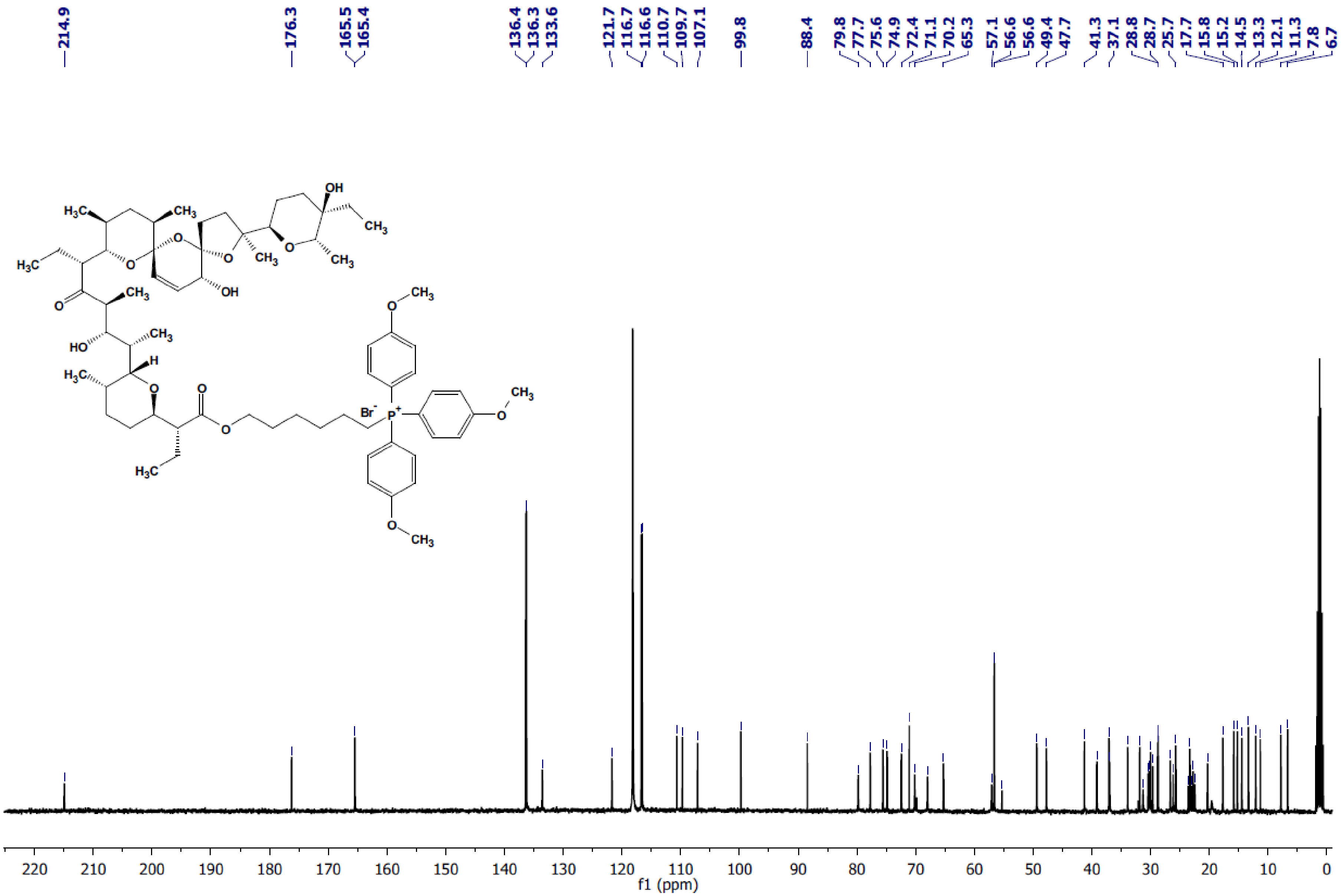

Fig. S28.The ^{13}C NMR spectrum of **5d** in CD_3CN.

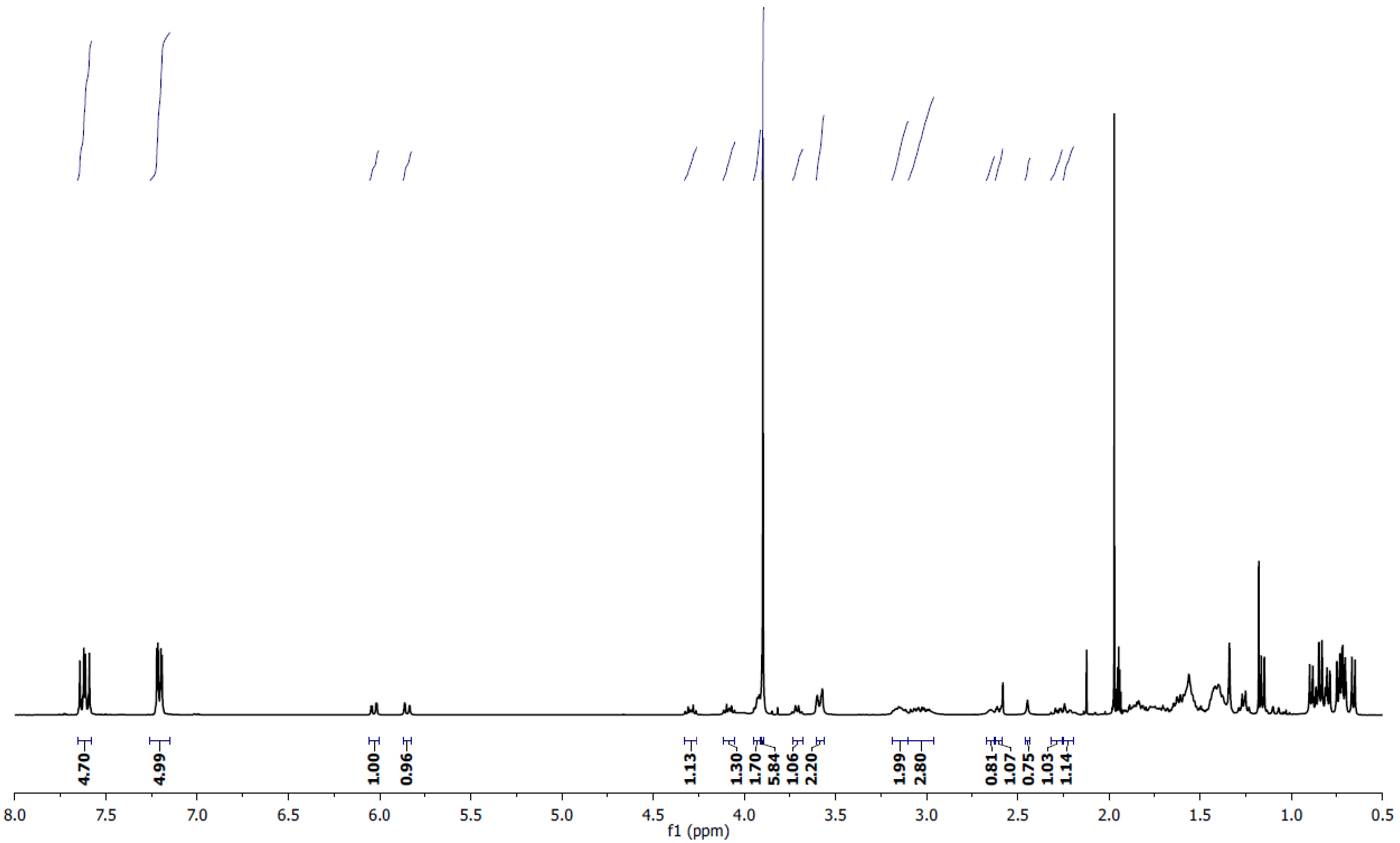

Fig. S29. The ^{1}H NMR spectrum of **5d** in CD_3CN.

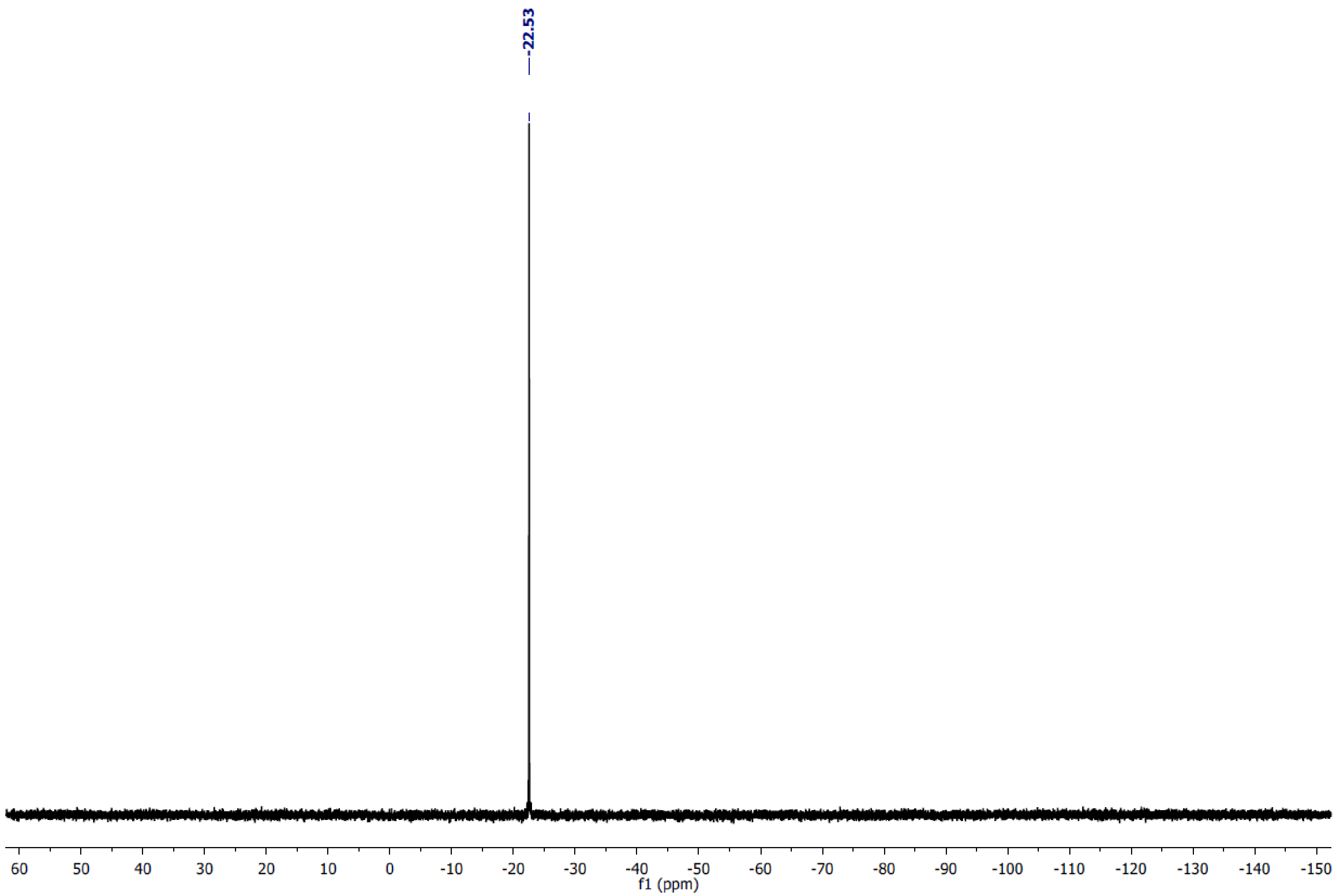

Fig. S30. The ^{31}P NMR spectrum of **5d** in CD_3CN.

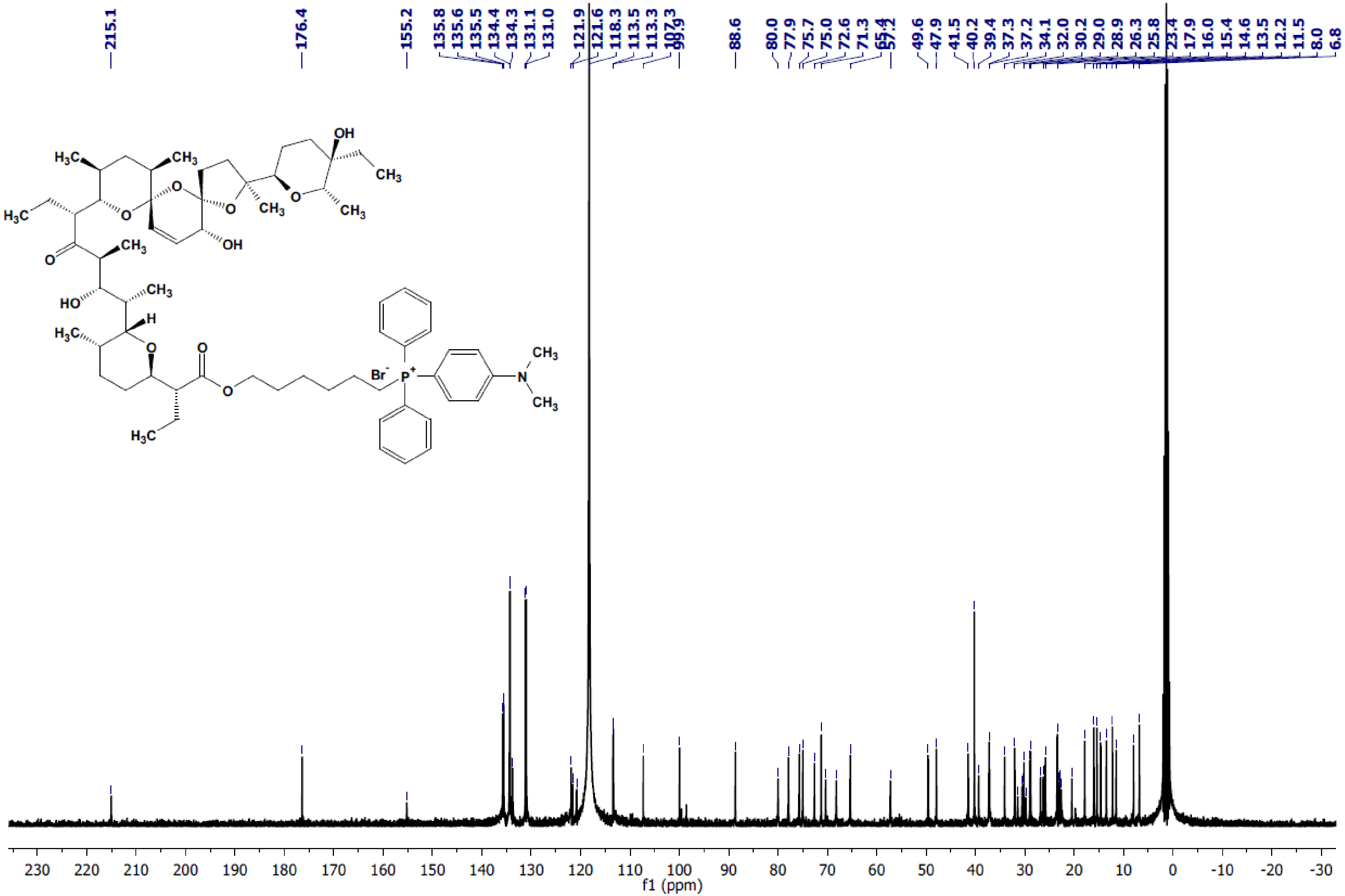

Fig. S31. The ^{13}C NMR spectrum of **5e** in CD_3CN.

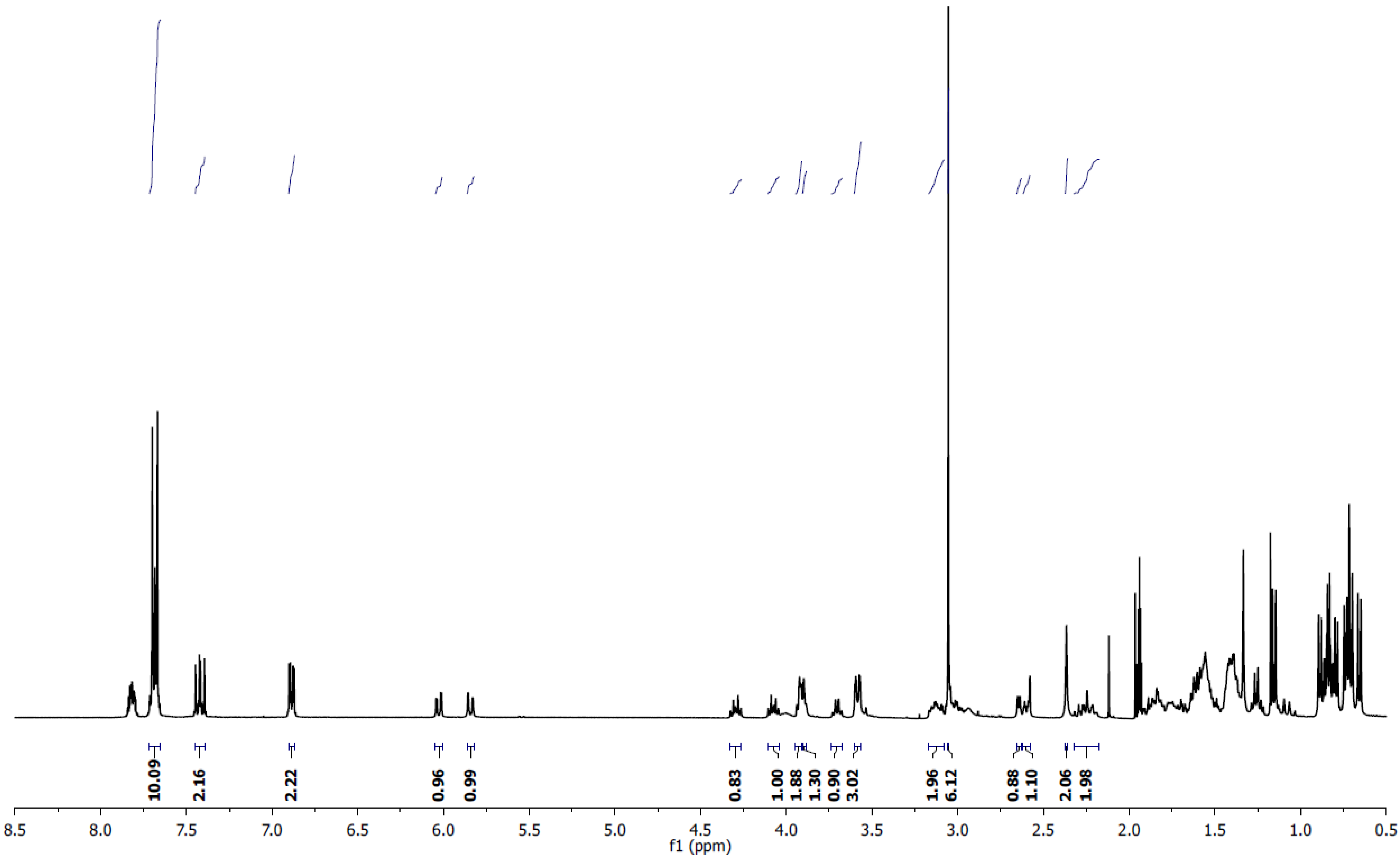

Fig. S32. The ^{1}H NMR spectrum of **5e** in CD_3CN.

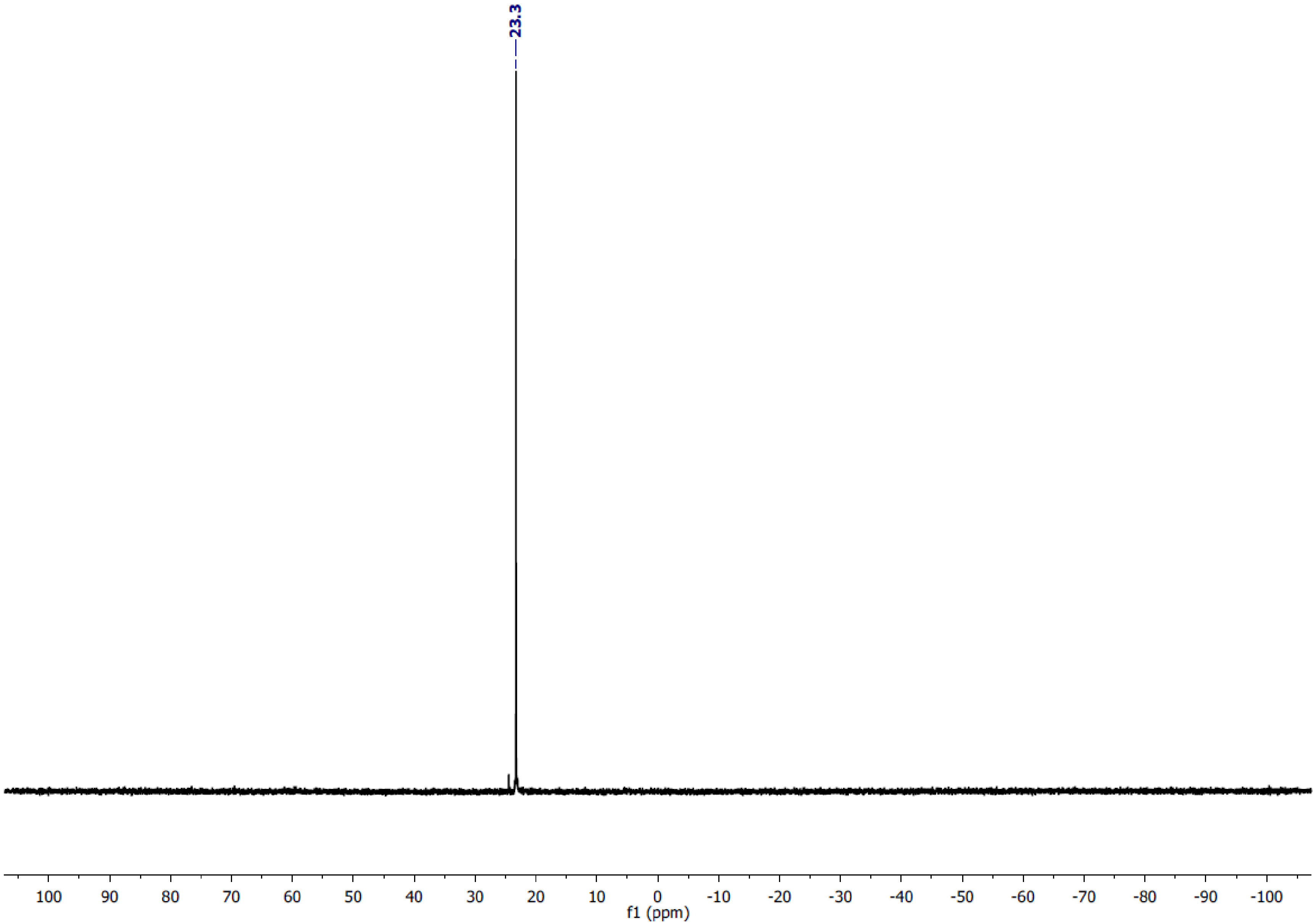

Fig. **S33**. The ^{31}P NMR spectrum of **5e** in CD_3CN.

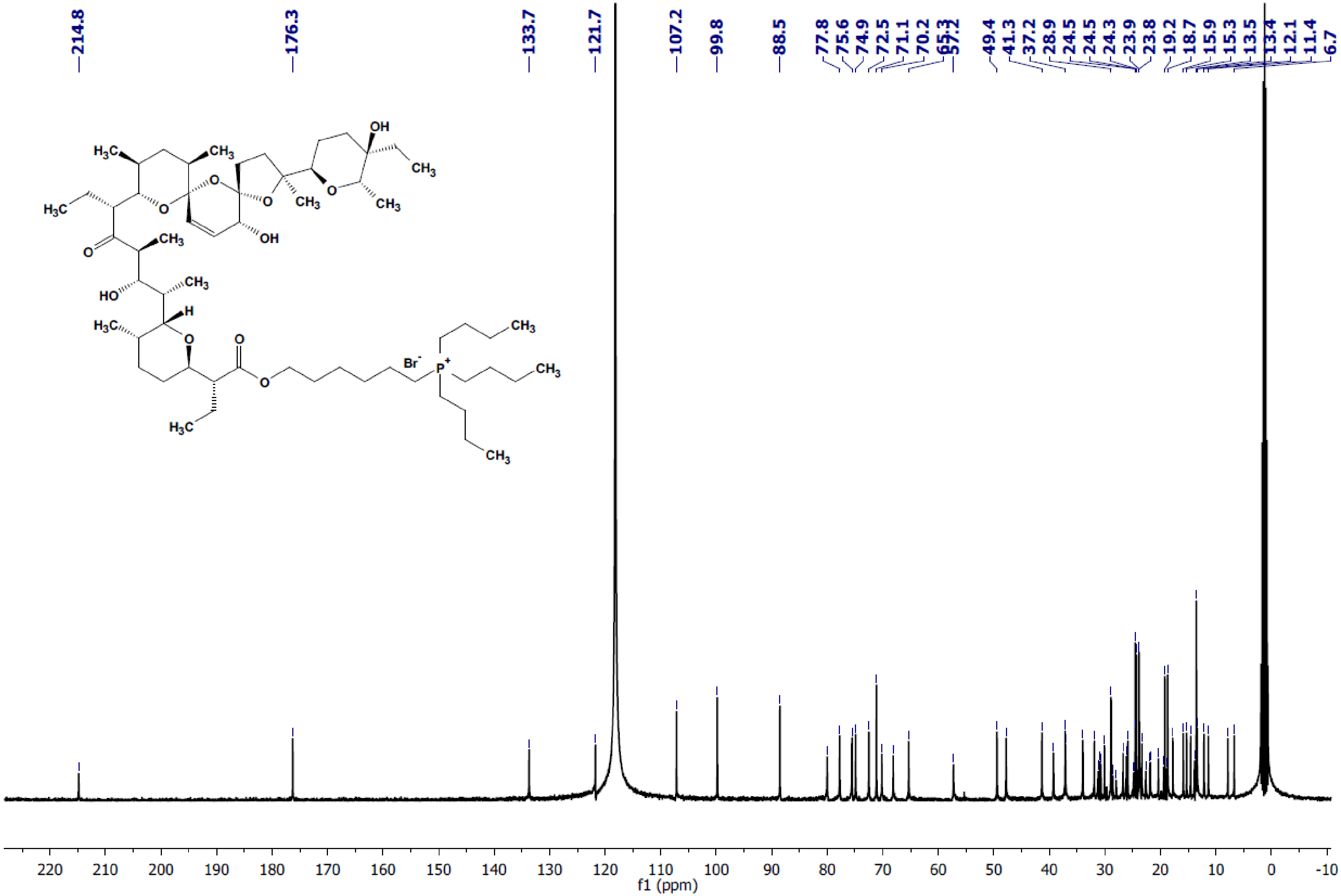

Fig. **S34.** The ^{13}C NMR spectrum of **5f** in CD_3CN.

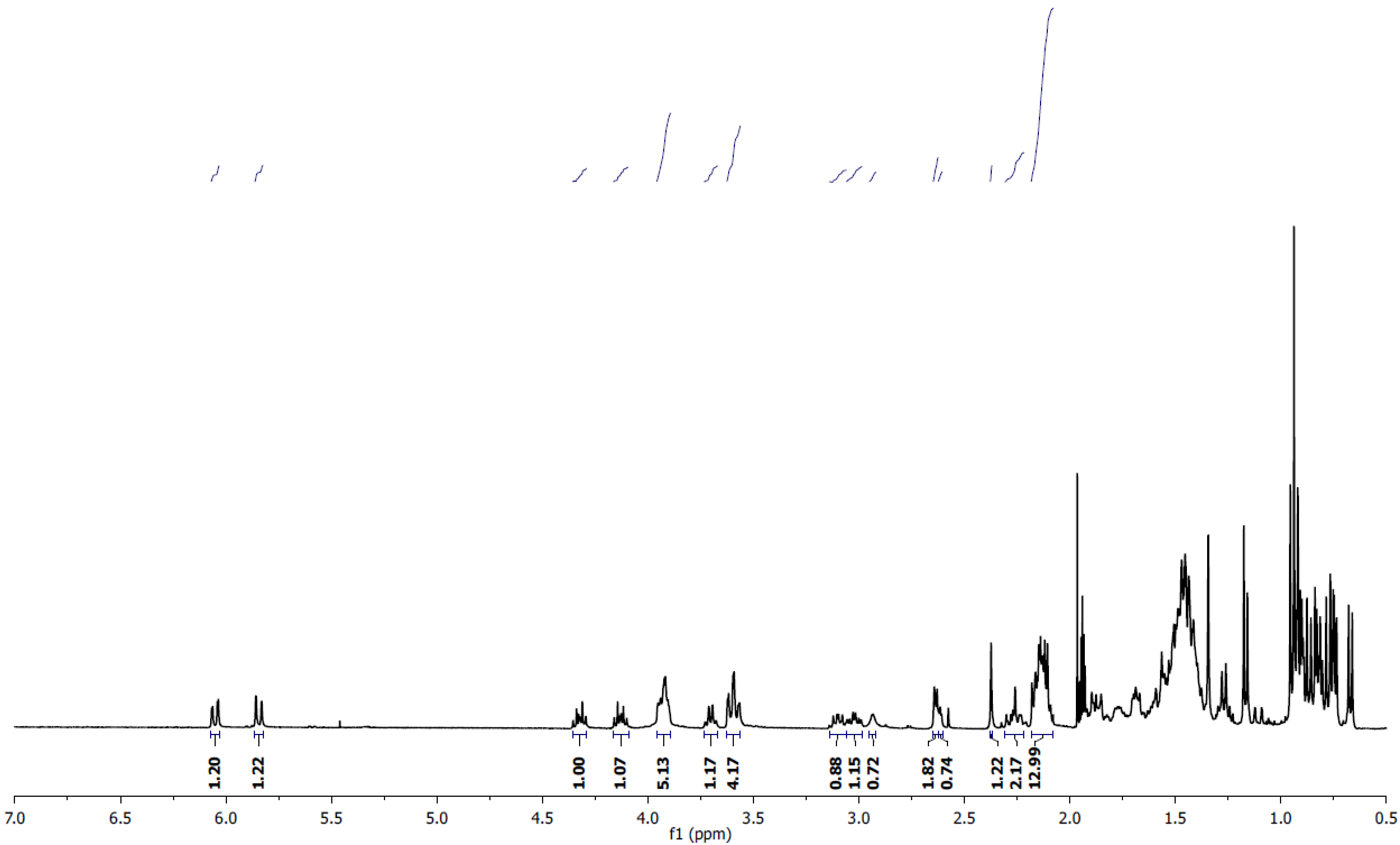

Fig. S35. The ^{1}H NMR spectrum of **5f** in CD_3CN.

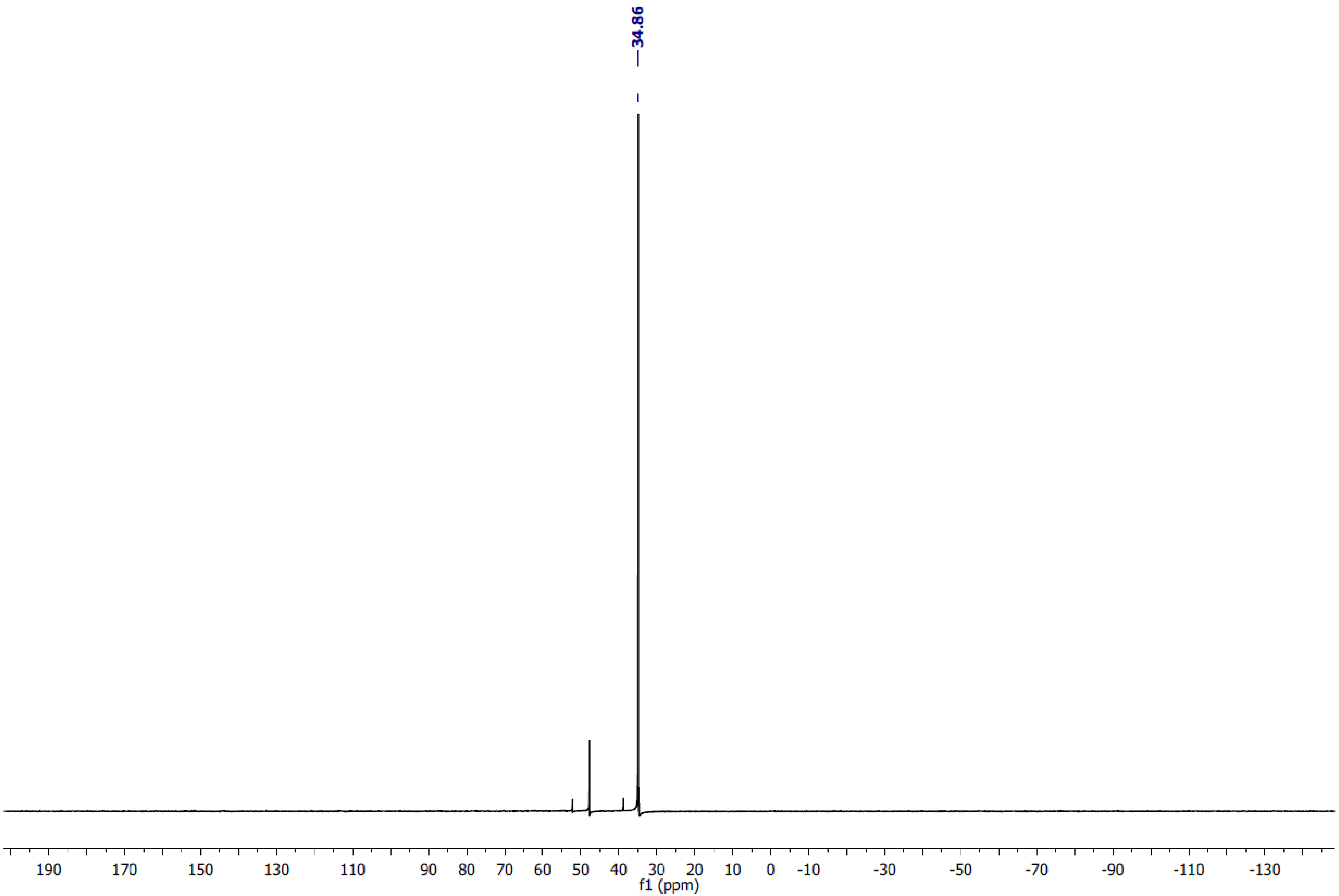

Fig. **S36.** The ^{31}P NMR spectrum of **5f** in CD_3CN.

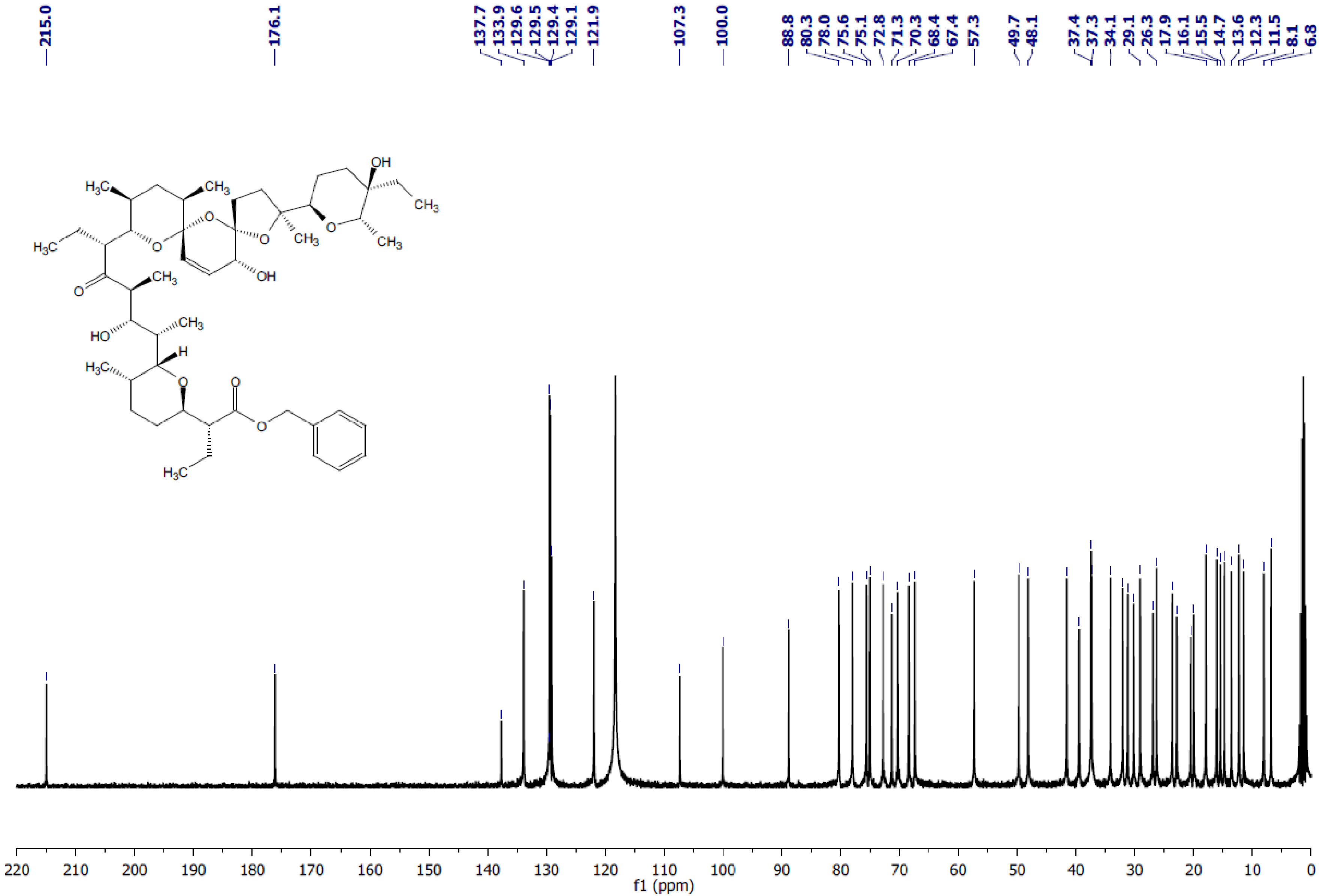

Fig. **S37.** The ^{13}C NMR spectrum of **6** in CD_3CN.

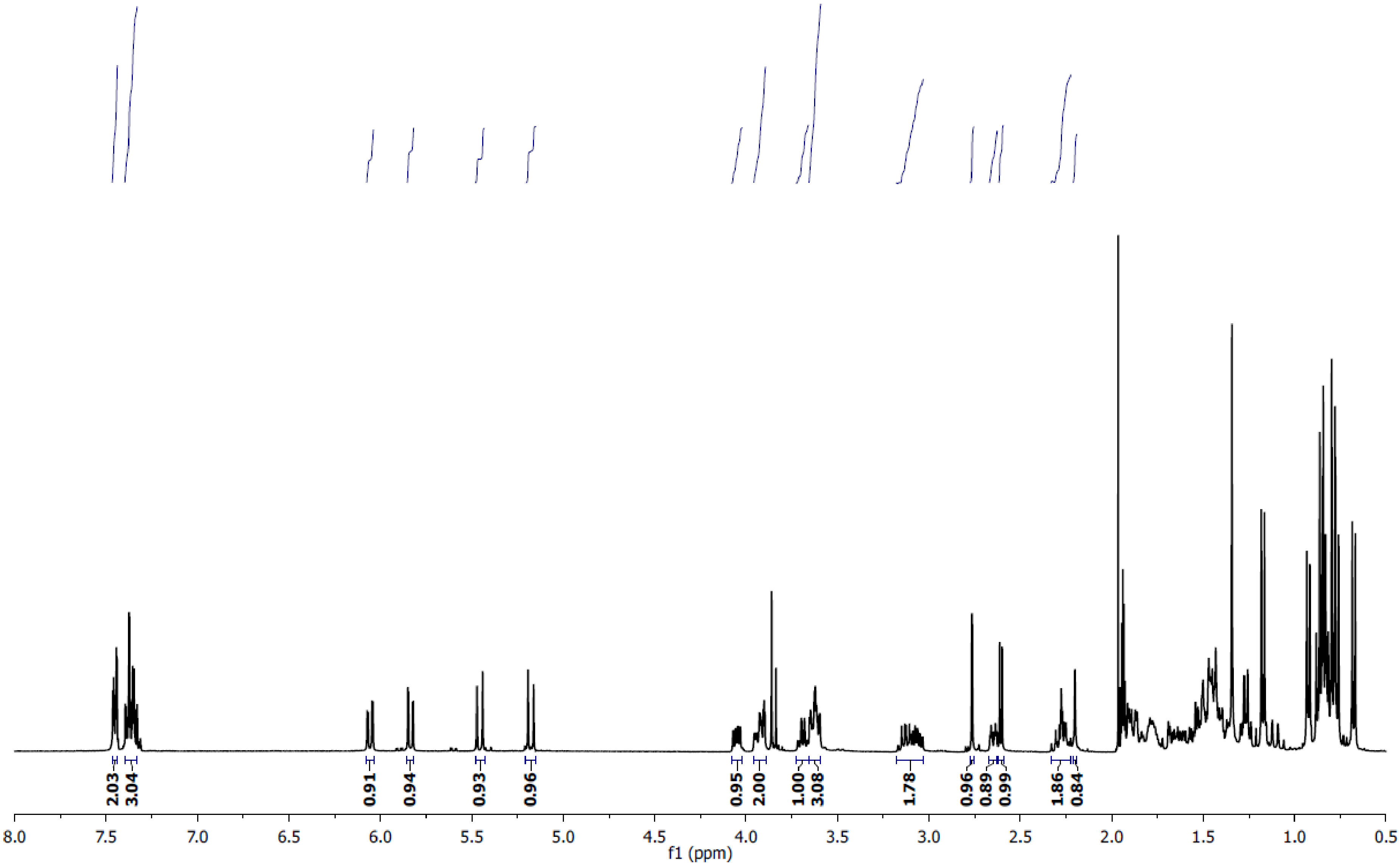

Fig. **S38.** The ^{1}H NMR spectrum of **6** in CD_3CN.

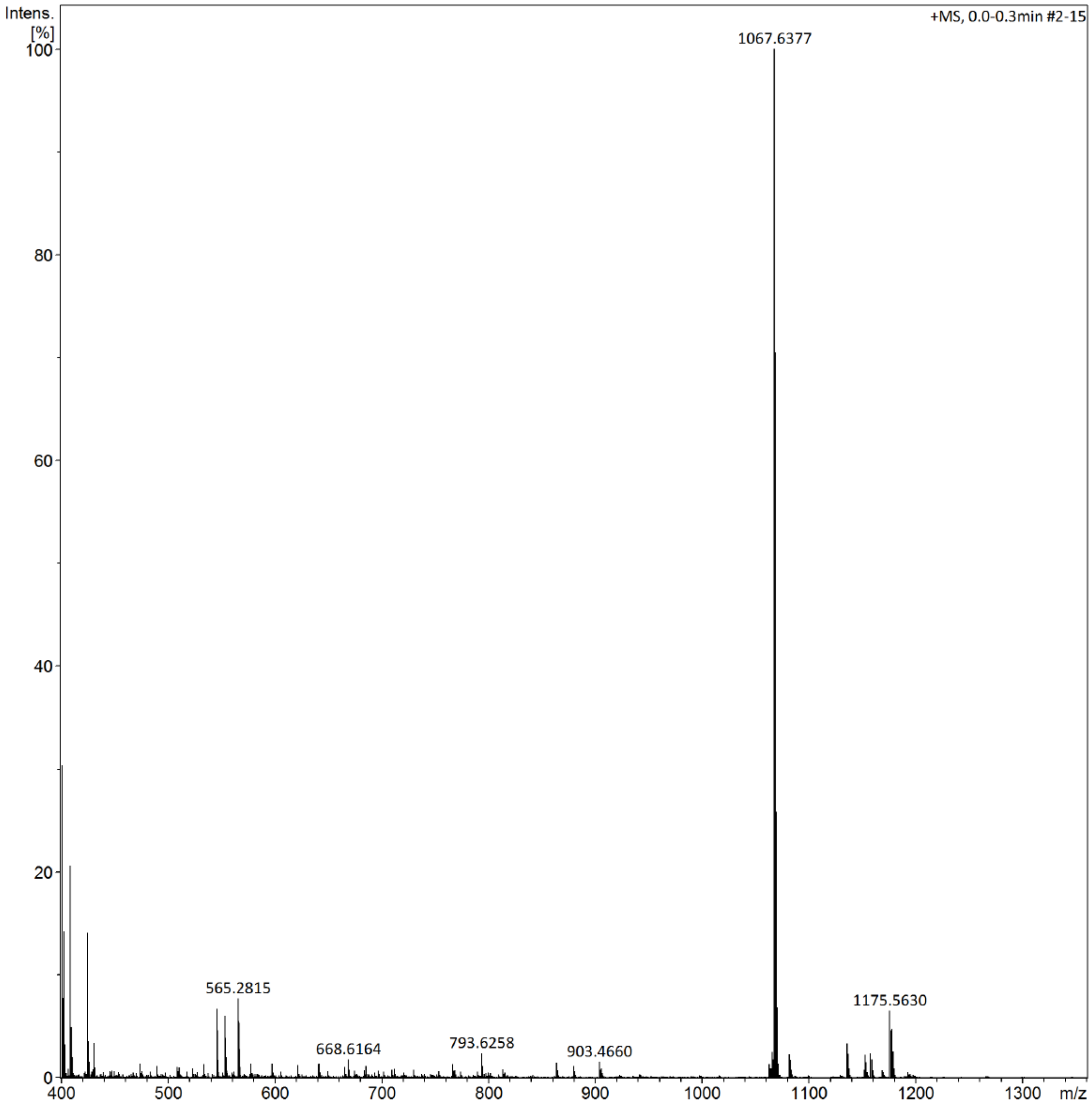

Fig. **S39.** The HR-MS spectra of **3a**.

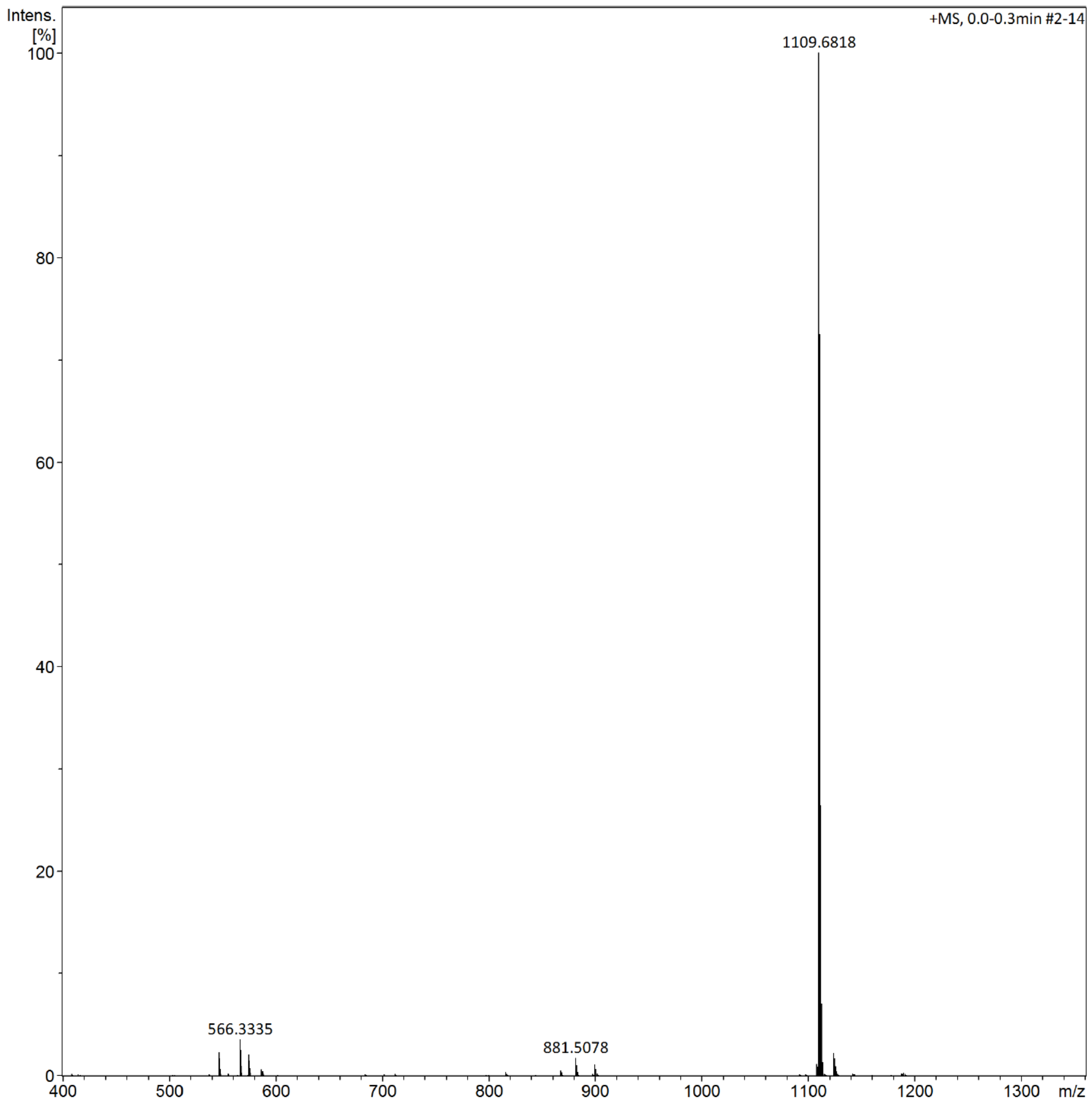

Fig. **S40.** The HR-MS spectra of **3b**.

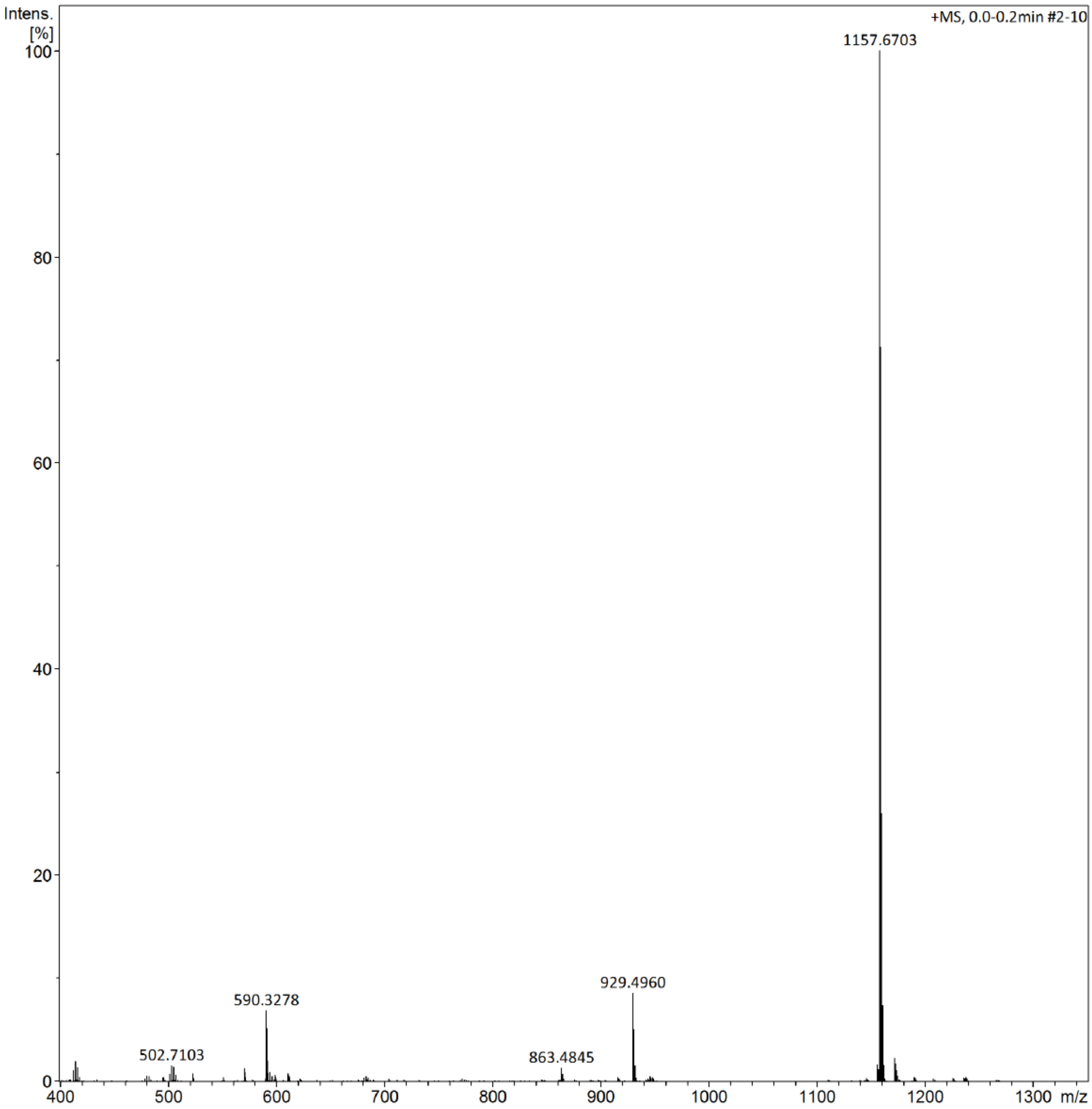

Fig. **S41.** The HR-MS spectra of **3c**.

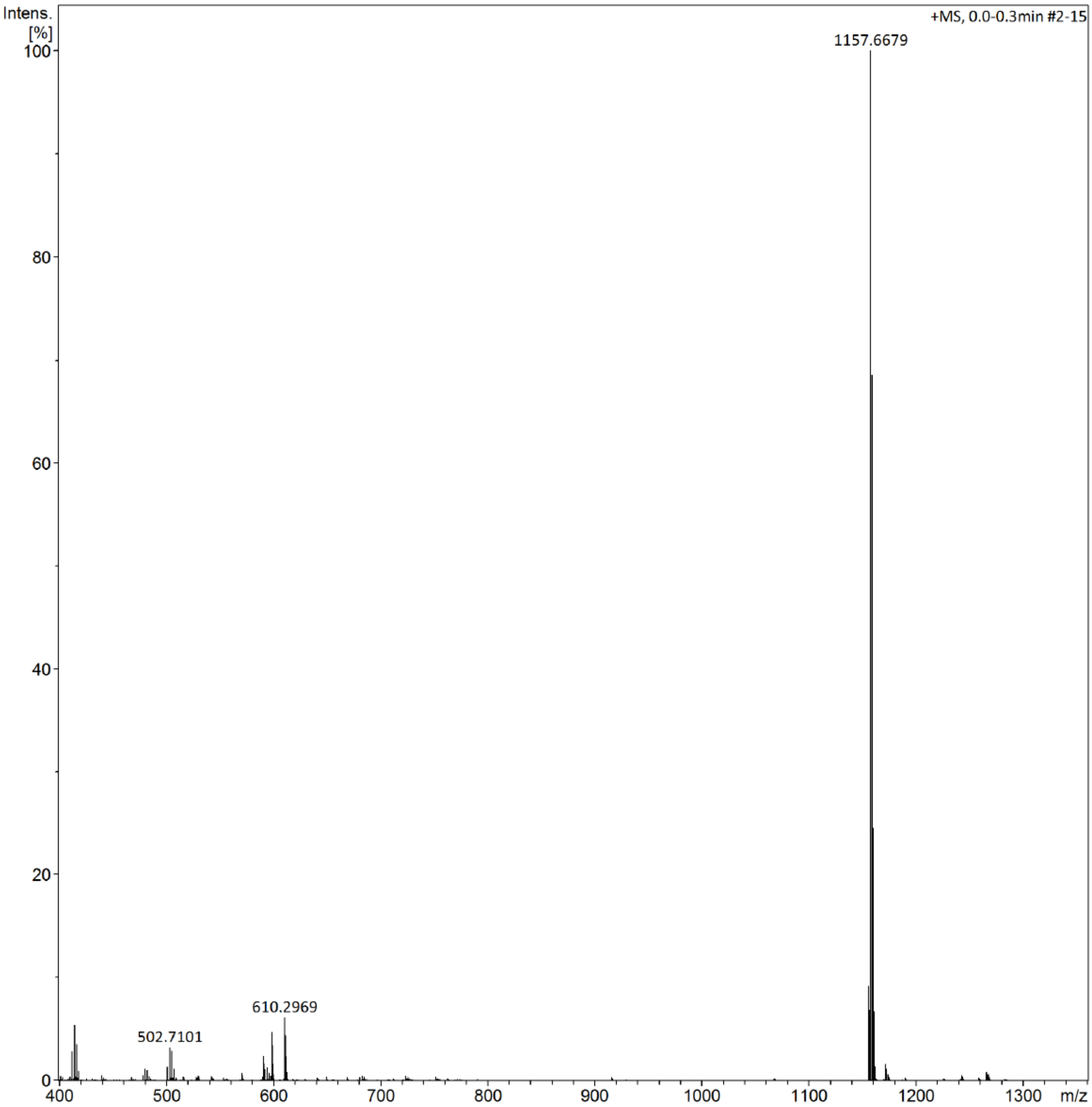

Fig. **S42.** The HR-MS spectra of **3d**.

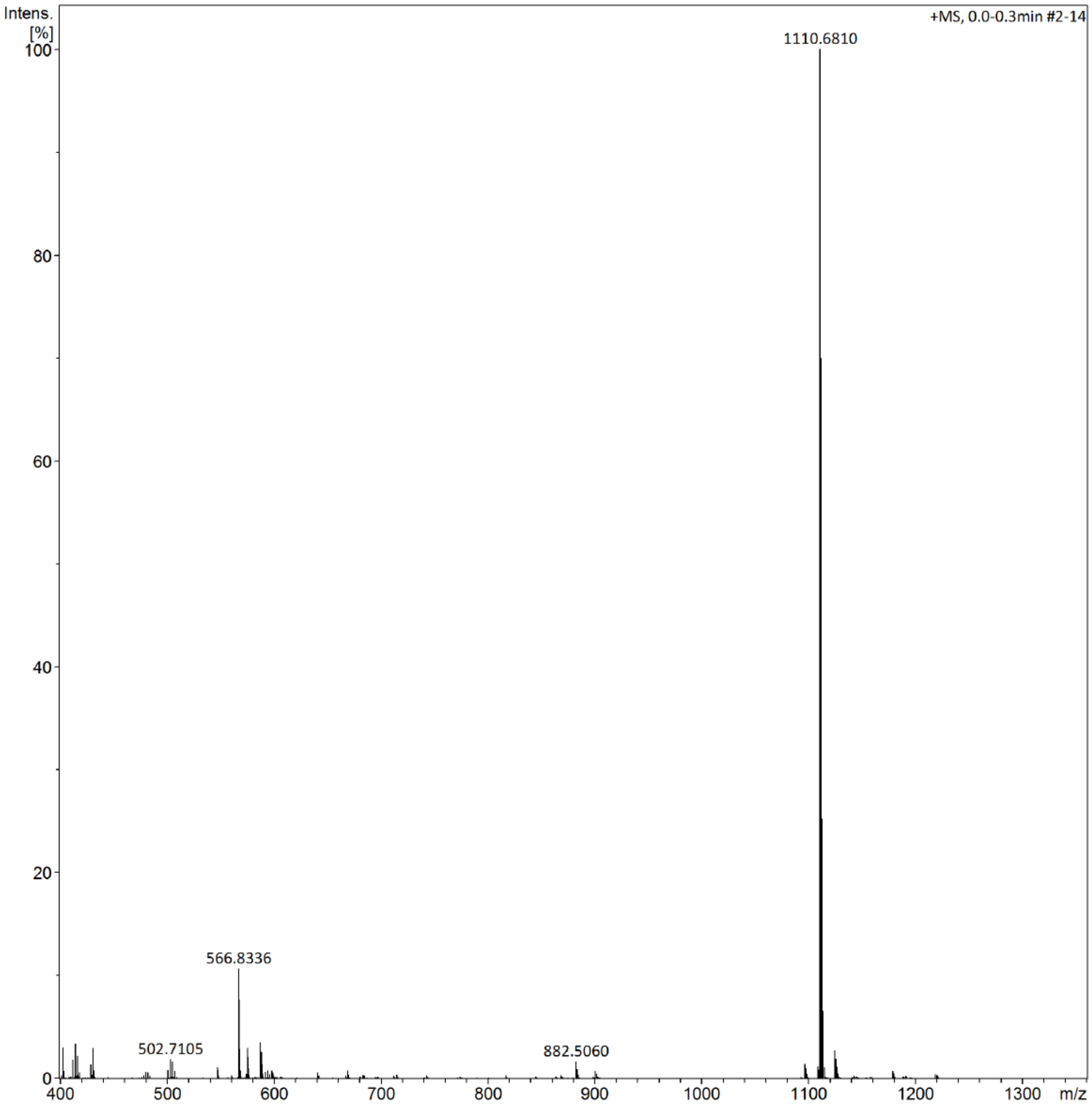

Fig. **S43.** The HR-MS spectra of **3e**.

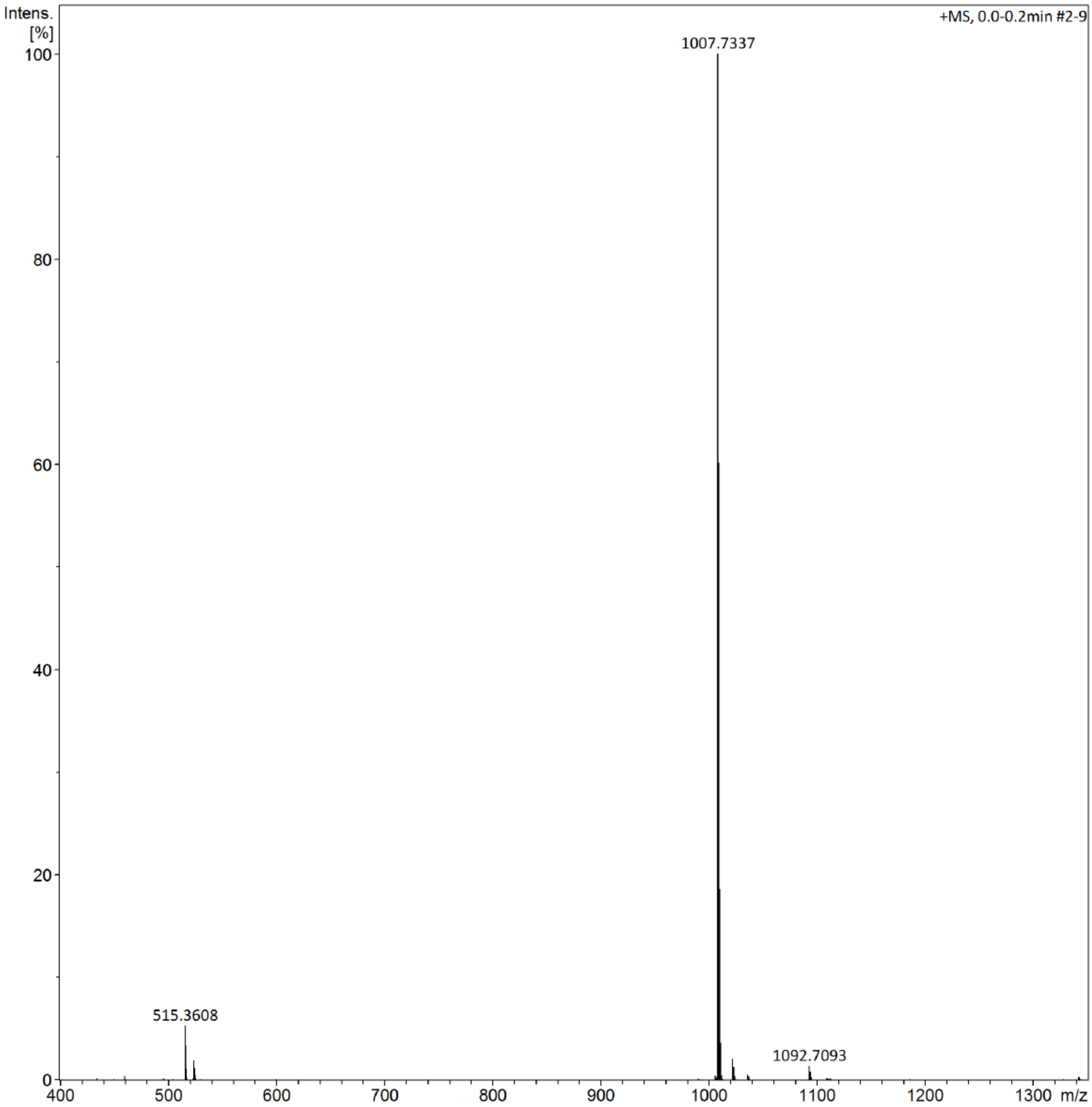

Fig. **S44.** The HR-MS spectra of **3f**.

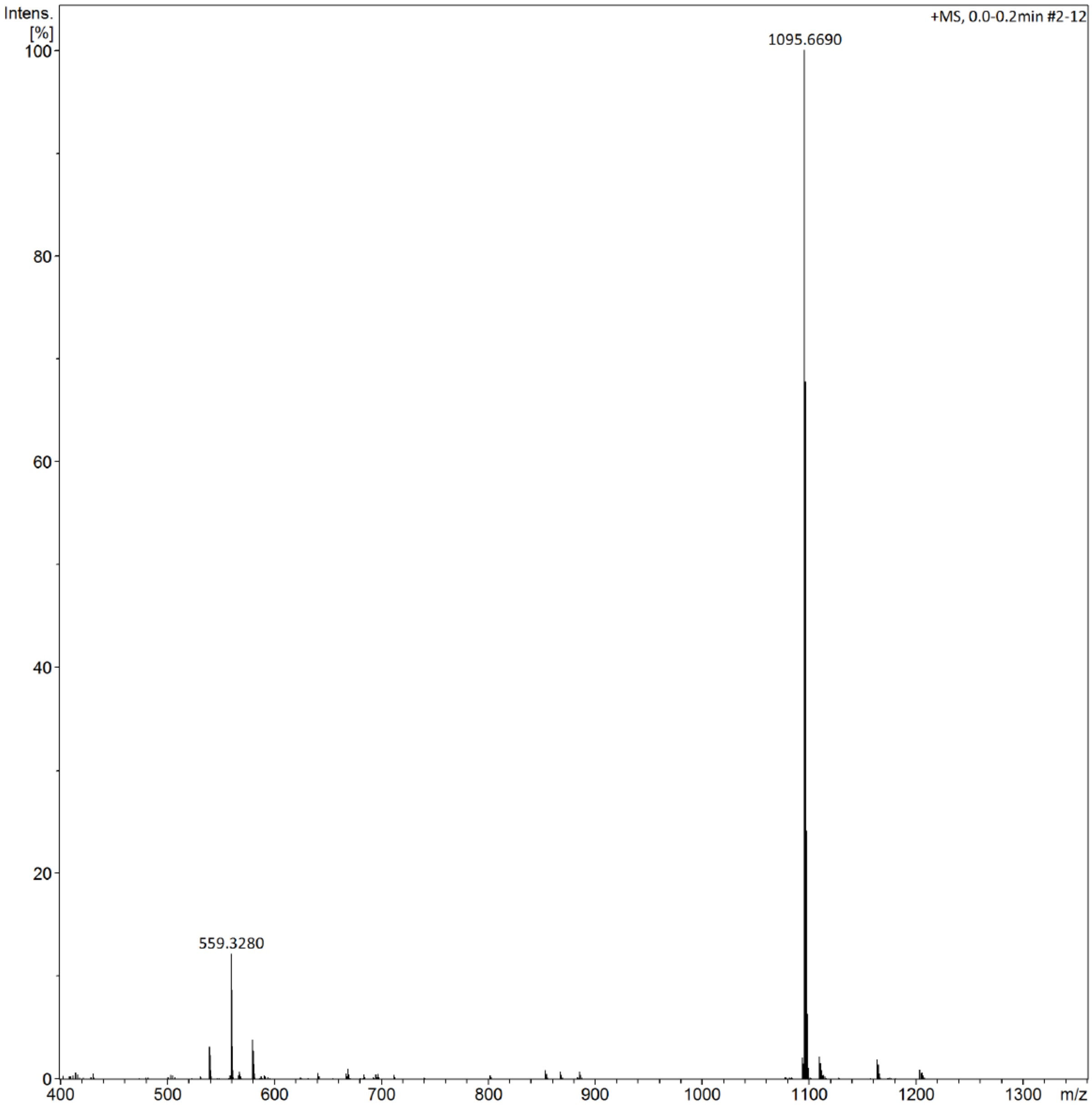

Fig. **S45.** The HR-MS spectra of **5a**.

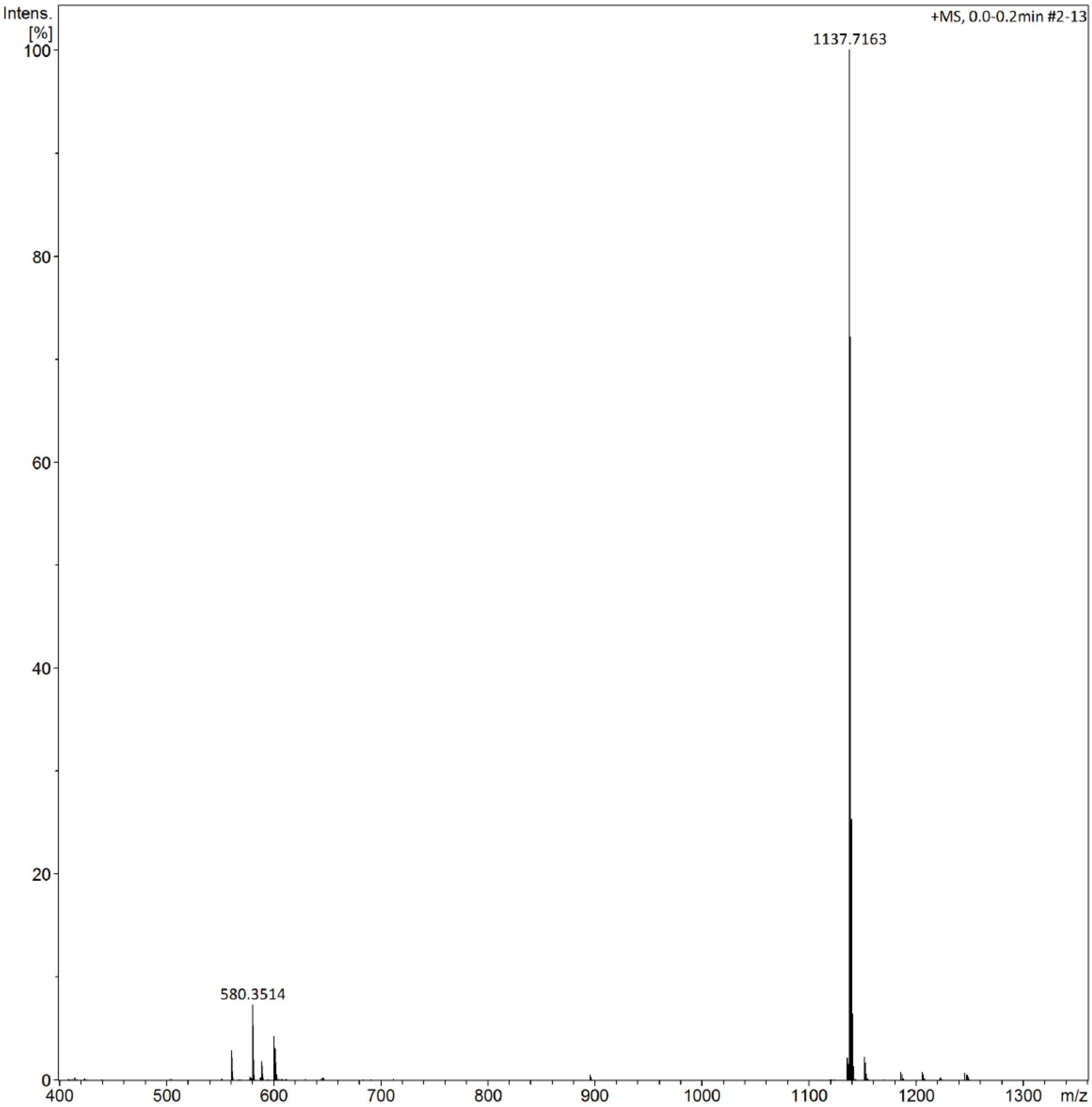

Fig. **S46.** The HR-MS spectra of **5b**.

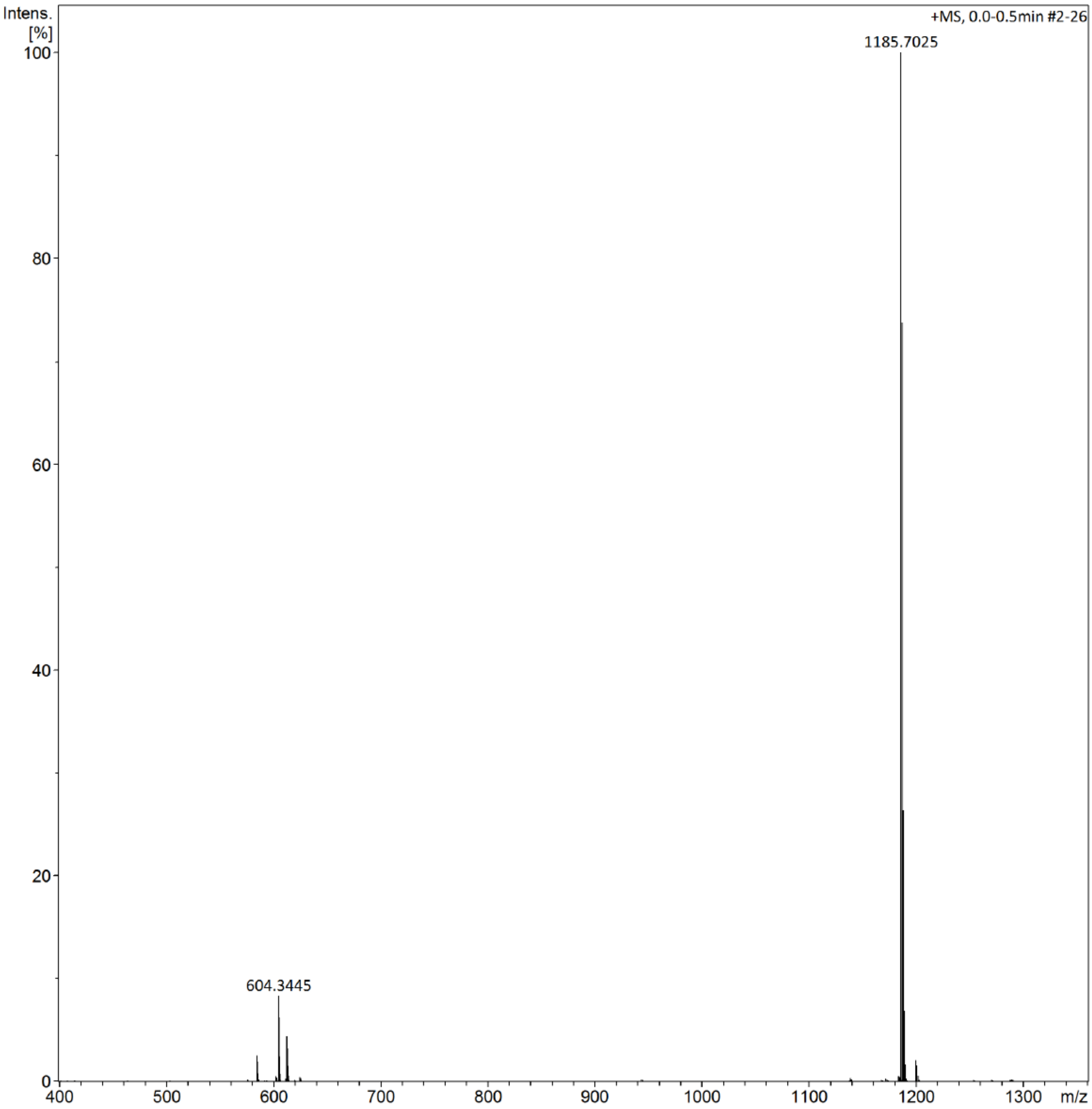

Fig. **S47.** The HR-MS spectra of **5c**.

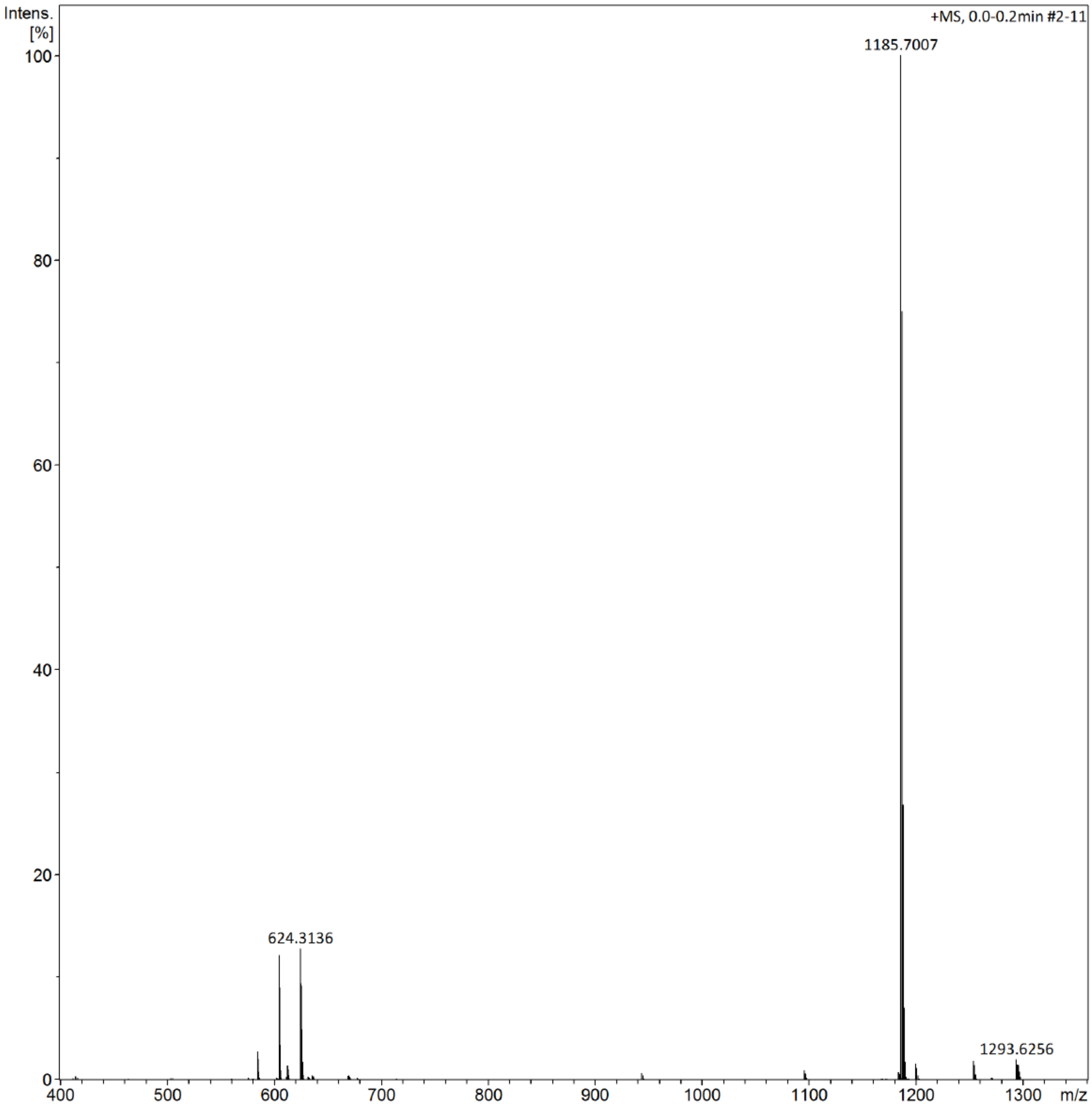

Fig. **S48.** The HR-MS spectra of **5d**.

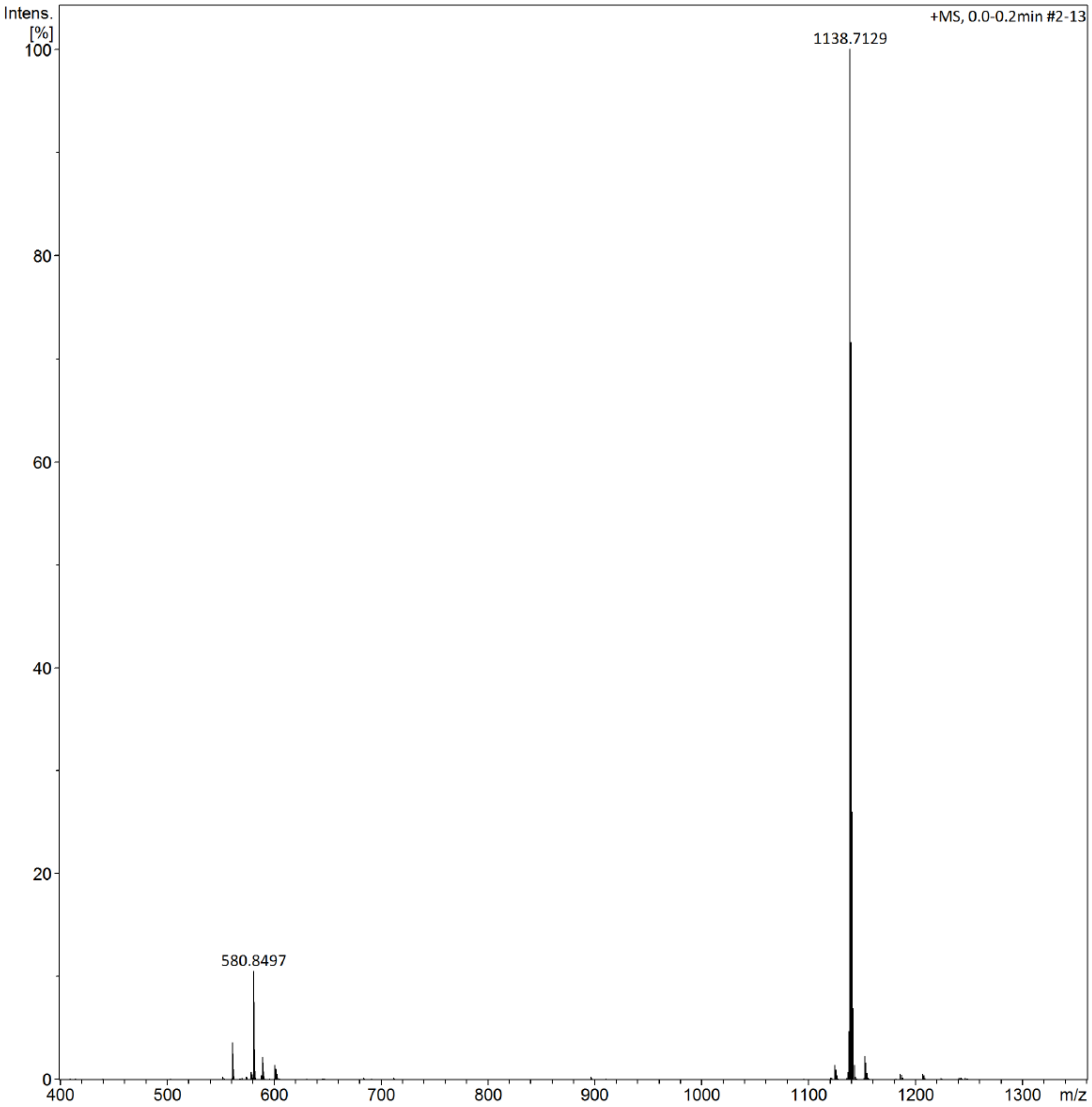

Fig. **S49.** The HR-MS spectra of **5e**.

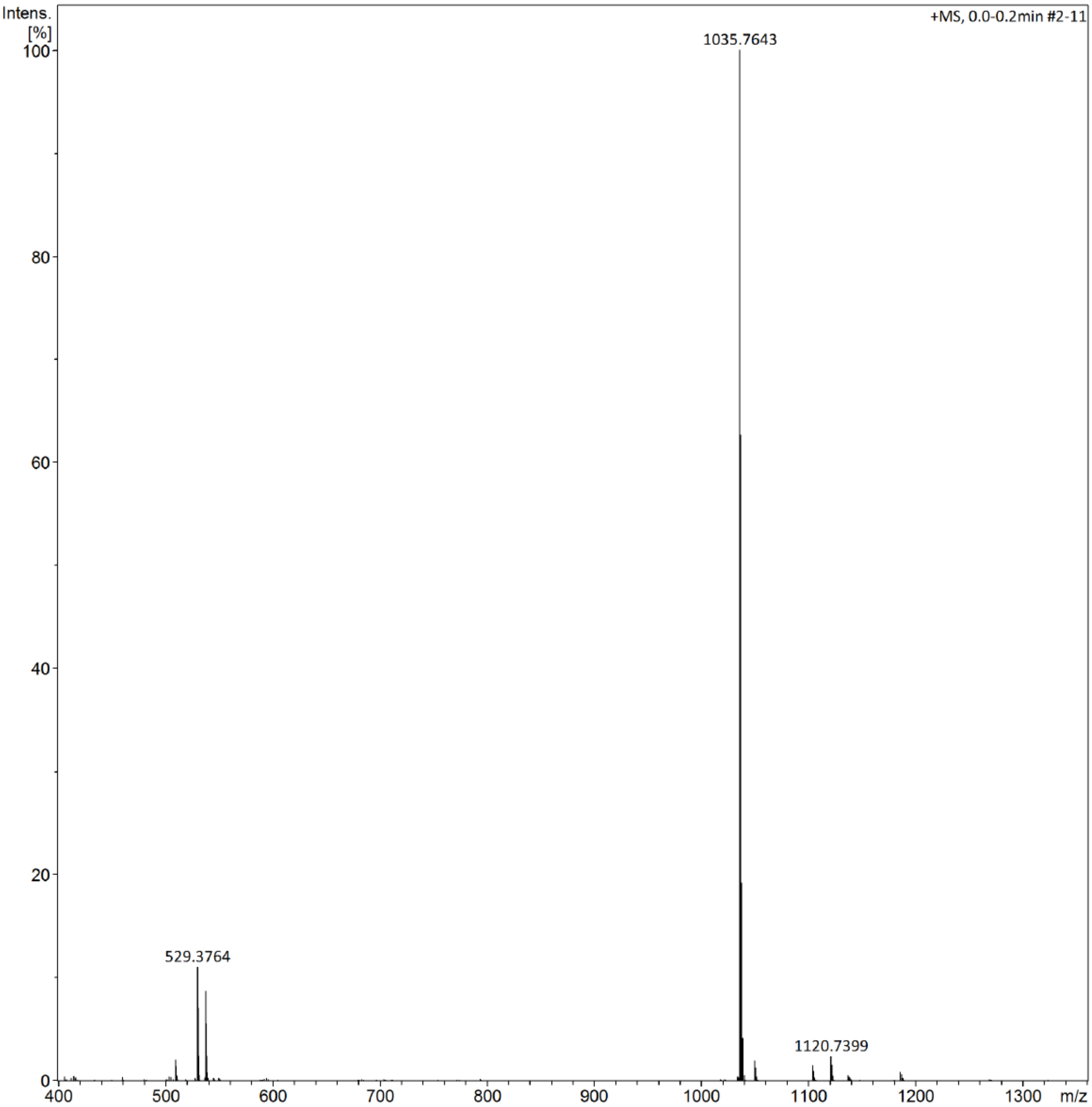

Fig. **S50.** The HR-MS spectra of **5f**.

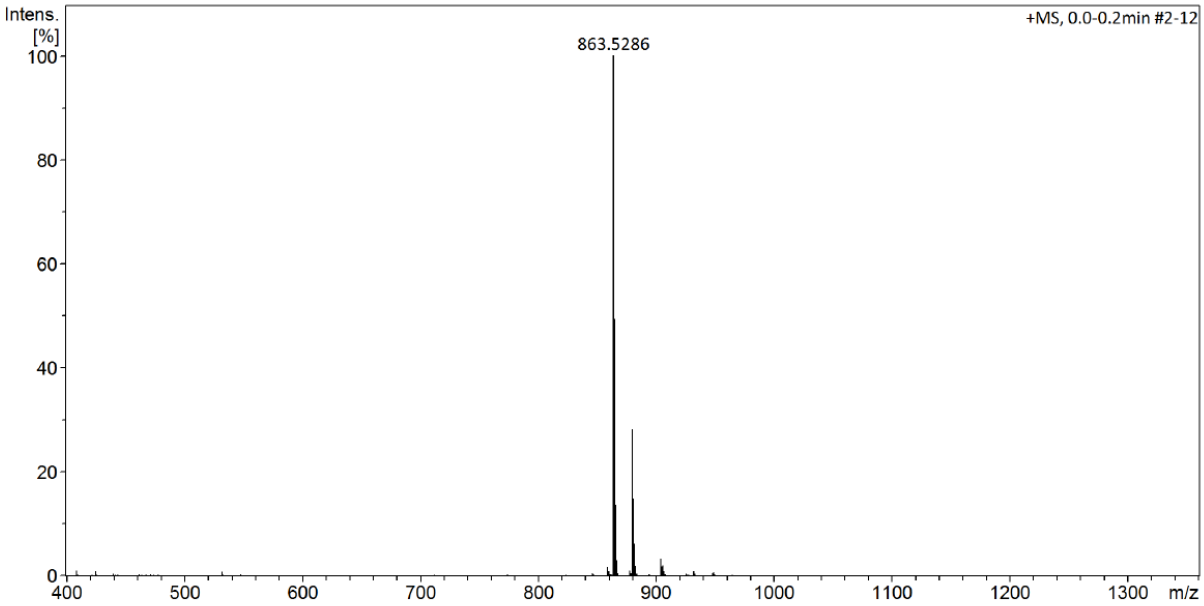

Fig. **S51.** The HR-MS spectra of **6** with $NaClO_4$.

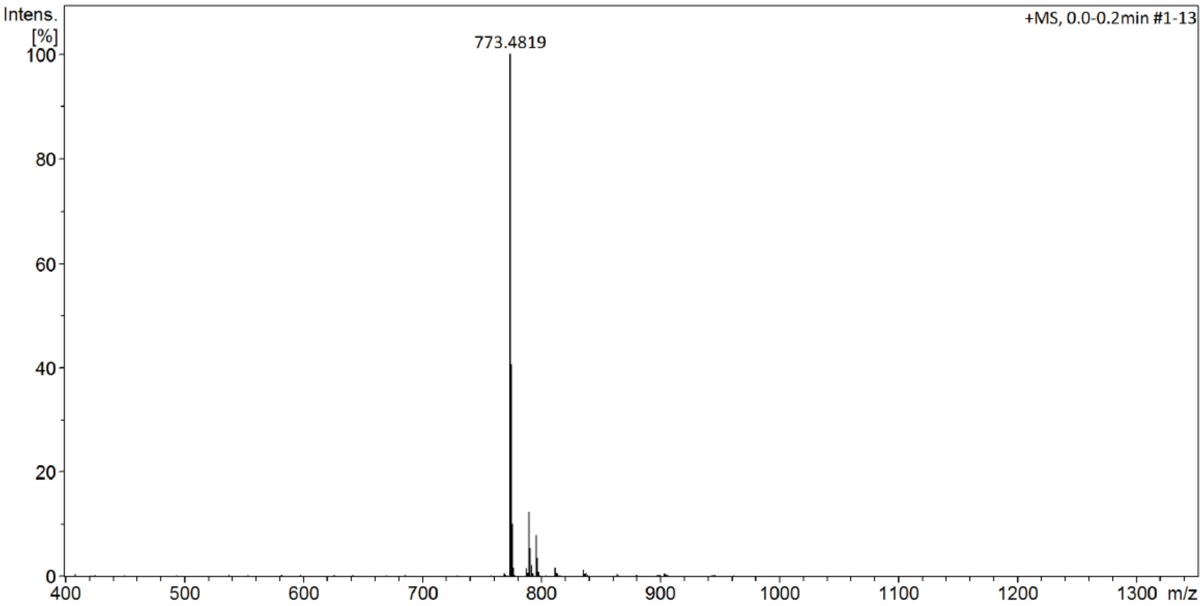

Fig. **S52.** The HR-MS spectra of **SAL** with $NaClO_4$.

OŚWIADCZENIA WSPÓŁAUTORÓW

UNIWERSYTET
IM. ADAMA MICKIEWICZA
W POZNANIU

prof. dr hab. Adam Huczyński
Zakład Chemii Medycznej, Wydział Chemii
Uniwersytet im. Adama Mickiewicza w Poznaniu
ul. Uniwersytetu Poznańskiego 8, 61-614 Poznań

OŚWIADCZENIE

Moja współpraca z mgr Martą Jędrzejczyk układała się znakomicie. To niezwykle samodzielna osoba, doskonała chemiczka łącząca w swoich badaniach pracowitość, sumienność i wytrwałość.

Przy powstawaniu publikacji pełniłem rolę typową dla promotora, wspomagając Doktorantkę radą i pomocą w interpretacji uzyskanych wyników oraz uczestnicząc w dyskusji nad manuskryptami tych publikacji, które w ogromnej większości były przygotowywane przez mgr Martę Jędrzejczyk oraz w dwóch publikacjach pełniłem rolę autora korespondującego.

W związku z ubieganiem się mgr Marty Jędrzejczyk o stopień doktora nauk chemicznych oświadczam, że jestem współautorem następujących publikacji:

- Marta Jędrzejczyk, Michał Sulik, Magdalena Mielczarek-Puta, Gwan Yong Lim, Małgorzata Podsiad, Jakub Hoser, Piotr Bednarczyk, Marta Struga, **Adam Huczyński***; *„Anticancer activity of salinomycin quaternary phosphonium salts”*, European Journal of Medicinal Chemistry, 282 (2024) 117055. Mój udział procentowy stanowi 10%.
- Marta Jędrzejczyk, Jan Janczak, **Adam Huczyński***; *„Molecular structure and spectroscopic studies of the product of acidic degradation of salinomycin and its potassium salt”*, Journal of Molecular Structure, 1263 (2022) 133129· Mój udział procentowy stanowi 15%.
- Yuri N. Antonenko*, Marta Jędrzejczyk, Tatyana I. Rokitskaya, Ljudmila S. Khailova, Elena A. Kotova, **Adam Huczyński**; *„Rate of translocation across lipid bilayer of triphenylphosphonium-linked salinomycin derivatives contributes significantly to their* K^+/H^+ *exchange activity on membranes”*, Bioelectrochemistry, 145 (2022) 108089· Mój udział procentowy stanowi 10%.

Kierownik
Zakładu Chemii Medycznej
Huczyński
prof. dr hab. Adam Huczyński

Wrocław, 8.01.2025

prof. dr hab. Jan Janczak
Instytut Niskich Temperatur i Badań Strukturalnych im. Włodzimierza Trzebiatowskiego
Polskiej Akademii Nauk

OŚWIADCZENIE

W związku z ubieganiem się mgr Marty Jędrzejczyk o stopień doktora nauk chemicznych oświadczam, że jestem współautorem publikacji:
Marta Jędrzejczyk, **Jan Janczak**, Adam Huczyński; „*Molecular structure and spectroscopic studies of the product of acidic degradation of salinomycin and its potassium salt*", Journal of Molecular Structure, 1263 (2022) 133129. Mój udział w przygotowaniu tej publikacji polegał na pomiarze i analizie strukturalnej. Mój udział procentowy stanowi 15%.

Jan Janczak

(czytelny podpis)

Moscow, January 09, 2025

Prof. Yuri N. Antonenko
Belozersky Institute of Physico-Chemical Biology
Lomonosov Moscow State University, Moscow

CO-AUTHOR DECLARATION

In connection with the application of Marta Jędrzejczyk, M.Sc. for the degree of Doctor of Chemical Sciences, I declare that I am a co-author of the publication:
Marta Jędrzejczyk, **Yuri N. Antonenko**, Tatyana I. Rokitskaya, Ljudmila S. Khailova, Elena A. Kotova, Adam Huczyński; *„Rate of translocation across lipid bilayer of triphenylphosphonium-linked salinomycin derivatives contributes significantly to their* K^+/H^+ *exchange activity on membranes"*, Bioelectrochemistry, 145 (2022) 108089. My contribution to the preparation of this publication consisted of running several experiments and writing and editing the manuscript. My percentage contribution can be estimated as 20 %.

Yuri Antonenko
Professor of Biophysics

Moscow, January 10, 2025

Ljudmila S. Khailova
Belozersky Institute of Physico-Chemical Biology
Lomonosov Moscow State University, Moscow

CO-AUTHOR DECLARATION

In connection with the application of Marta Jędrzejczyk, M.Sc. for the degree of Doctor of Chemical Sciences, I declare that I am a co-author of the publication:
Marta Jędrzejczyk, Yuri N. Antonenko, Tatyana I. Rokitskaya, **Ljudmila S. Khailova**, Elena A. Kotova, Adam Huczyński; *„Rate of translocation across lipid bilayer of triphenylphosphonium-linked salinomycin derivatives contributes significantly to their K^+/H^+ exchange activity on membranes"*, Bioelectrochemistry, 145 (2022) 108089. My contribution to the preparation of this publication consisted of running several experiments and editing the manuscript. My percentage contribution can be estimated as 10 %.

Ljudmila Khailova
Senior research investigator

Moscow, January 10, 2025

Elena A. Kotova
Belozersky Institute of Physico-Chemical Biology
Lomonosov Moscow State University, Moscow

CO-AUTHOR DECLARATION

In connection with the application of Marta Jędrzejczyk, M.Sc. for the degree of Doctor of Chemical Sciences, I declare that I am a co-author of the publication:
Marta Jędrzejczyk, Yuri N. Antonenko, Tatyana I. Rokitskaya, Ljudmila S. Khailova, **Elena A. Kotova**, Adam Huczyński; *„Rate of translocation across lipid bilayer of triphenylphosphonium-linked salinomycin derivatives contributes significantly to their* K^+/H^+ *exchange activity on membranes"*, Bioelectrochemistry, 145 (2022) 108089. My contribution to the preparation of this publication consisted of writing and editing the manuscript. My percentage contribution can be estimated as 10 %.

Elena Kotova
Senior research investigator Котова

Moscow, January 10, 2025

Tatyana I. Rokitskaya
Belozersky Institute of Physico-Chemical Biology
Lomonosov Moscow State University, Moscow

CO-AUTHOR DECLARATION

In connection with the application of Marta Jędrzejczyk, M.Sc. for the degree of Doctor of Chemical Sciences, I declare that I am a co-author of the publication:
Marta Jędrzejczyk, Yuri N. Antonenko, **Tatyana I. Rokitskaya**, Ljudmila S. Khailova, Elena A. Kotova, Adam Huczyński; „Rate of translocation across lipid bilayer of triphenylphosphonium-linked salinomycin derivatives contributes significantly to their K^+/H^+ exchange activity on membranes", Bioelectrochemistry, 145 (2022) 108089. My contribution to the preparation of this publication consisted of running several experiments and editing the manuscript. My percentage contribution can be estimated as 10 %.

Tatyana Rokitskaya
Senior research investigator

UNIWERSYTET IM. ADAMA MICKIEWICZA W POZNANIU
Wydział Chemii
Zakład Chemii Medycznej
ul. Uniwersytetu Poznańskiego 8, 61-614 Poznań
tel. 61 829 16 73

Poznań, 4.03.2025 r.

mgr Michał Sulik
Zakład Chemii Medycznej, Wydział Chemii
Uniwersytet im. Adama Mickiewicza w Poznaniu

OŚWIADCZENIE

W związku z ubieganiem się mgr Marty Jędrzejczyk o stopień doktora nauk chemicznych oświadczam, że jestem współautorem publikacji:
Marta Jędrzejczyk, **Michał Sulik**, Magdalena Mielczarek-Puta, Gwan Yong Lim, Małgorzata Podsiad, Jakub Hoser, Piotr Bednarczyk, Marta Struga, Adam Huczyński; *„Anticancer activity of salinomycin quaternary phosphonium salts"*, European Journal of Medicinal Chemistry, 282 (2024) 117055. Mój udział w przygotowaniu tej publikacji polegał na pomocy w izolowaniu odpowiedniej ilości salinomycyny oraz redagowaniu tekstu artykułu. Mój udział procentowy stanowi 5%.

Michał Sulik
(czytelny podpis)

Warszawa, 17.01.25

dr n. med. Magdalena Mielczarek-Puta
Katedra i Zakład Biochemii, Wydział Lekarski
Warszawski Uniwersytet Medyczny

OŚWIADCZENIE

W związku z ubieganiem się mgr Marty Jędrzejczyk o stopień doktora nauk chemicznych oświadczam, że jestem współautorką publikacji:
Marta Jędrzejczyk, Michał Sulik, **Magdalena Mielczarek-Puta**, Gwan Yong Lim, Małgorzata Podsiad, Jakub Hoser, Piotr Bednarczyk, Marta Struga, Adam Huczyński; *„Anticancer activity of salinomycin quaternary phosphonium salts"*, European Journal of Medicinal Chemistry, 282 (2024) 117055. Mój udział w przygotowaniu tej publikacji polegał na wykonaniu badań biologicznych na poziomie komórkowym, analizie i opisie wyników. Mój udział procentowy stanowi 15%.

Magdalena Mielczarek-Puta
(czytelny podpis)

Warsaw, 17.01.25

Gwan Yong Lim
Katedra i Zakład Biochemii, Wydział Lekarski
Warszawski Uniwersytet Medyczny

CO-AUTHOR DECLARATION

In connection with the application of Marta Jędrzejczyk for the degree of doctor of Chemical Sciences, I declare that I am a co-author of the publication:
Marta Jędrzejczyk, Michał Sulik, Magdalena Mielczarek-Puta, **Gwan Yong Lim**, Małgorzata Podsiad, Jakub Hoser, Piotr Bednarczyk, Marta Struga, Adam Huczyński; „*Anticancer activity of salinomycin quaternary phosphonium salts*”, European Journal of Medicinal Chemistry, 282 (2024) 117055. My contribution to the preparation of this publication consisted of cytotoxicity assessment. My percentage contribution is 5%.

Gwan Yong Lim
(signature)

Warszawa, 17.01.25

mgr inż. chem. Małgorzata Podsiad
Katedra i Zakład Biochemii, Wydział Lekarski
Warszawski Uniwersytet Medyczny

OŚWIADCZENIE

W związku z ubieganiem się mgr Marty Jędrzejczyk o stopień doktora nauk chemicznych oświadczam, że jestem współautorką publikacji:
Marta Jędrzejczyk, Michał Sulik, Magdalena Mielczarek-Puta, Gwan Yong Lim, **Małgorzata Podsiad**, Jakub Hoser, Piotr Bednarczyk, Marta Struga, Adam Huczyński; „*Anticancer activity of salinomycin quaternary phosphonium salts*", European Journal of Medicinal Chemistry, 282 (2024) 117055. Mój udział w przygotowaniu tej publikacji polegał na wykonaniu części badań mikrobiologicznych. Mój udział procentowy stanowi 5%.

M. Podsiad
(czytelny podpis)

Warszawa, 03.01.2025

mgr Jakub Hoser
Katedra Fizyki i Biofizyki, Instytut Biologii
Szkoła Główna Gospodarstwa Wiejskiego w Warszawie

OŚWIADCZENIE

W związku z ubieganiem się mgr Marty Jędrzejczyk o stopień doktora nauk chemicznych oświadczam, że jestem współautorem publikacji:
Marta Jędrzejczyk, Michał Sulik, Magdalena Mielczarek-Puta, Gwan Yong Lim, Małgorzata Podsiad, **Jakub Hoser**, Piotr Bednarczyk, Marta Struga, Adam Huczyński; *„Anticancer activity of salinomycin quaternary phosphonium salts”*, European Journal of Medicinal Chemistry, 282 (2024) 117055. Mój udział w przygotowaniu tej publikacji polegał na wykonaniu, a także opracowaniu wyników i opisów eksperymentów biofizycznych- pomiaru transportu jonów w poprzek sztucznej dwuwarstwy lipidowej przy pomocy techniki czarnych błon lipidowych oraz pomiaru zużycia tlenu metodą respirometrii o wysokiej rozdzielczości. Mój udział procentowy stanowi 10%.

..Jakub....Hoser.............

Warszawa, 9 stycznia 2025 r.

prof. SGGW dr hab. Piotr Bednarczyk
Katedra Fizyki i Biofizyki, Instytut Biologii
Szkoła Główna Gospodarstwa Wiejskiego w Warszawie

OŚWIADCZENIE

W związku z ubieganiem się mgr Marty Jędrzejczyk o stopień doktora nauk chemicznych oświadczam, że jestem współautorem publikacji:
Marta Jędrzejczyk, Michał Sulik, Magdalena Mielczarek-Puta, Gwan Yong Lim, Małgorzata Podsiad, Jakub Hoser, **Piotr Bednarczyk**, Marta Struga, Adam Huczyński; *„Anticancer activity of salinomycin quaternary phosphonium salts"*, European Journal of Medicinal Chemistry, 282 (2024) 117055. Mój udział w przygotowaniu tej publikacji polegał na pomocy przy analizie i opisie danych elektrofizjologicznych. Mój udział procentowy stanowi 5%.

Piotr Bednarczyk
(czytelny podpis)

Warszawa, 17.01.25

prof. dr hab. Marta Struga
Katedra i Zakład Biochemii, Wydział Lekarski
Warszawski Uniwersytet Medyczny

OŚWIADCZENIE

W związku z ubieganiem się mgr Marty Jędrzejczyk o stopień doktora nauk chemicznych oświadczam, że jestem współautorką publikacji:
Marta Jędrzejczyk, Michał Sulik, Magdalena Mielczarek-Puta, Gwan Yong Lim, Małgorzata Podsiad, Jakub Hoser, Piotr Bednarczyk, **Marta Struga**, Adam Huczyński; „*Anticancer activity of salinomycin quaternary phosphonium salts*", European Journal of Medicinal Chemistry, 282 (2024) 117055. Mój udział w przygotowaniu tej publikacji polegał na nadzorze merytorycznym nad badaniami biologicznymi. Mój udział procentowy stanowi 5%.

Marta Struga
(czytelny podpis)